Università degli Studi di Padova

Università degli Studi di Padova

centro interdipartimentale *"Centro Ricerche Fusione"*

Universidade Técnica de Lisboa

instituto superior técnico

joint research doctorate in fusion science and engineering

cycle XXVII

Experiments and modelling of active control of MHD instabilities

Coordinator: Ch.mo Prof. Paolo Bettini

Supervisor: Ch.mo Prof. Piero Martin

Supervisor: Dott. Lionello Marrelli

Supervisor: Dott. Paolo Piovesan

Doctoral student: Chiara Piron

Abstract

The plasma in a controlled thermonuclear fusion experiment is a complex non-linear system, whose dynamics can be largely due to the interplay of multiple MagnetoHydroDynamic - MHD instabilities that coexist together. The main aim of this Thesis work is to develop the knowledge on the active control of these instabilities, an important aspect of present controlled fusion research. The possibility to safely operate a plasma near instability limits, or even beyond them in regimes that are unstable without control, has a twofold advantage: it allows not only to extend the operational boundaries of the possible plasma scenarios and their performance, for example towards high normalized pressure or high plasma current, but also to explore new physics, that otherwise would remain veiled.

The main principles of thermonuclear fusion and a brief introduction to the physics of the MHD instabilities investigated in this Thesis, namely Tearing Modes - TMs, Resistive Wall Modes - RWMs and sawteeth, is provided in Chapter 1.

A distinctive feature of this Thesis is its interdisciplinary approach to the active control of MHD instabilities, which has required investigations on both physics and engineering aspects. This approach is necessary for the advance of MHD control, since the scientific progress keeps up with the technological one, and vice versa. This Thesis work has been carried out in three different fusion experiments, all equipped with advanced real-time systems for active MHD control, based both on non axi-symmetric coils and wave heating and current drive. The work has been focused initially on the RFX-mod device at Consorzio RFX, Padua, Italy, and then extended to larger Tokamaks, namely DIII-D at General Atomics, San Diego, USA, and ASDEX Upgrade at Max-Planck-Institute für Plasmaphysik in Garching, Germany. These experiments will be described in Chapter 2.

RFX-mod stands out among other machines for its flexibility: besides being born as a Reversed Field Pinch - RFP, it can operate also as a circular and D-shaped Tokamak. The MHD stability in both magnetic configurations is guaranteed by its sophisticated MHD control system, based on a large number of

independently-controlled saddle coils and a state-of-the-art digital real-time control system, whose recent upgrade allowed to design and test more computationally challenging control algorithms. Chapter 3 describes in particular the integration of the RFX-mod MHD control algorithms in the new Multi-threaded Application Real-Time executor - MARTe framework and its deployment, as well as the development of new control strategies, both performed during this Thesis work. The aim was to develop new control approaches for RWM instabilities based on new sensors and real-time algorithms. These new solutions were tested in the challenging low $q(a) < 2$ Tokamak scenario. Here a very reproducible current-driven RWM is well known to grow and disrupt the discharge if not properly controlled. This regime offered an excellent testbed to test and systematically compare new RWM control schemes then exportable to other Tokamak scenarios, e.g. at high β.

The main experimental results obtained during this Thesis are organized in two parts. The first part, which is titled "3D magnetic fields to control the MHD dynamics in Tokamak plasmas", investigates the interactions between these fields and the plasma dynamics and how they can be exploited to control its stability. In a fusion experiment, 3D fields have a twofold origin. They can appear in the form of small non-axisymmetries called Error Fields - EFs, from a wide range of unavoidable boundary imperfections, or they can be intentionally applied with external non-axisymmetric coils. The role of EFs on the current-driven RWM stability has been investigated in the RFX-mod Ohmic Tokamak plasmas at $q(a) < 2$. The EFs in RFX-mod have been firstly measured with the so-called compass scan technique and then corrected, as it will be discussed in Chapter 4 and Chapter 5, respectively. In the low $q(a)$ regime, the RWM is found to be linearly unstable, different from high β scenarios previously investigated, where the RWMs are usually stabilized by strong kinetic effects. In fact, its growth could not be avoided by simply removing EFs with the so-called Dynamic Error Field Correction - DEFC technique.

The necessity of an active feedback control to guarantee the RWM stabilization in $q(a) < 2$ Tokamak plasmas motivated the development of new control algorithms. Their main aim is to drive the non-axisymmetric coil currents to induce 3D magnetic fields that counteract the growth of this instability. In RFX-mod the RWM stabilization has been successfully achieved with both radial and poloidal magnetic field sensors. The experiments carried out during this Thesis point out the crucial role of the aliasing in the radial magnetic field measurements of sidebands from active coils. Their removal enables the radial magnetic field

sensors to compete with the poloidal ones, previously considered somehow superior and more often used in Tokamaks for RWM control. This result contributes to the scientific debate on the optimal sensors for RWM feedback control. Indeed the harsh environment of future fusion reactors will probably not allow to install poloidal magnetic field sensors inside the vacuum vessel, thus the radial magnetic field ones, which can also be installed outside it, can provide a valuable and feasible alternative. The RFX-mod experiments that test the performance of these control schemes will be discussed in Chapter 6.

Furthermore, external 3D magnetic fields have been applied in RFX-mod low q Tokamak plasmas to investigate their interaction with core MHD and in particular with the sawtooth instability. In these experiments, that will be presented in Chapter 7, 3D fields cause a reduction of both the sawtooth amplitude and period, leading to an overall mitigating effect on this instability. In RFX-mod sawteeth eventually disappear and are replaced by a stationary $m = 1, n = 1$ helical equilibrium without an increase in disruptivity. However toroidal rotation is significantly reduced in these plasmas too, thus it is likely that the sawtooth mitigation in these experiments is due to the combination of the helically deformed core and the reduced rotation. The results are qualitatively well reproduced by nonlinear MHD simulations performed with the PIXIE3D code.

The results obtained in these RFX-mod experiments motivated similar ones in DIII-D L-mode diverted Tokamak plasmas with low q_{95}. These experiments, that will be presented in Chapter 8, succeeded in reproducing the sawtooth mitigation with the approach developed in RFX-mod. In DIII-D this effect is correlated with a clear increase of the $n = 1$ plasma response, that indicates an enhancement of the coupling to the marginally stable $n = 1$ external kink, as simulations with the linear MHD code IPEC suggest. A significant rotation braking in the plasma core is also observed in DIII-D. Numerical calculations of the Neoclassical Toroidal Viscosity - NTV carried out with PENT identify this torque as a possible candidate for this effect.

In the future, fusion reactors will bring new scientific and technological challenges for plasma control, which will probably require an integrated, model-based approach. Indeed, the high performance of these fusion devices can be supported if an accurate control of internal profiles is well coordinated with the active control of MHD instabilities using multiple actuators, so that disruptions can be detected in time and avoided with preventive actions. The second part of this work, "A model-based active control of the sawtooth instability" describes how this Thesis

has contributed to this innovative integrated approach. Chapter 9 will introduce the RApid Plasma Transport simulator - RAPTOR, a real-time state observer algorithm that allows to reconstruct the plasma state by combining diagnostic measurements with the predictions of a simplified transport model. This code has been recently embedded in the ASDEX Upgrade control system, where it provides in real-time the time evolution of many plasma profiles, like for example the safety factor or the electron temperature ones, which are useful to monitor and control the plasma dynamics, and in particular instabilities like sawteeth and Neoclassical Tearing Modes - NTMs.

During this Thesis work, the potentialities of RAPTOR have been widened with the integration of a new module that evolves the Porcelli's sawtooth model to reproduce the effects of sawteeth on the plasma state reconstruction and in particular on profiles. The simulations of some ASDEX Upgrade discharges show that the new sawtooth model is able to predict in real-time the average sawtooth period and the effect of the sawtooth crash on internal profiles, for example on the safety factor one. Thanks to this new module, RAPTOR can now be used to design and control sawtooth locking or pacing experiments using Electron Cyclotron Resonance Heating - ECRH, with the aim to avoid NTMs, whose seed islands can be provided by sawteeth. But it can also be used to improve direct NTM control with Electron Cyclotron Current Drive - ECCD due to an improved estimate of the safety factor profile. These results will be presented in Chapter 10.

The interdisciplinary approach of this Thesis, that allowed to gain both physics and engineering competences, has deepen the insight into the physics and the control of the MHD instabilities in different fusion experiments. Initial work on the integration of different control strategies, that combine into a single model-based framework both 3D physics, like for instance the effect of sawteeth, and profile control aspects, has been described, but it will certainly need to be further investigated in next years. This should make possible to combine in a single real-time control framework different actuators, that are now exploited separately. The main results of this work together with its possible future developments will be summarized in the final Chapter Conclusions and future work.

Prefazione

Il plasma, in un esperimento di fusione termonucleare controllata, è un sistema complesso e non lineare, la cui dinamica è il risultato di una interazione di multiple instabilità magnetoidrodinamiche (MHD) che coesistono. Il principale scopo di questo lavoro di Tesi mira a sviluppare la comprensione del controllo attivo di queste instabilità, tematica di principale interesse nella ricerca della fusione controllata. La possibilità di produrre un plasma vicino ai limiti che possono indurre delle instabilità in maniera sicura, o spingersi oltre i confini di tali regimi che sono instabili senza controllo attivo, ha un doppio vantaggio: permette infatti non solo di estendere i limiti operazionali dei possibili scenari e le relative performance - ne sono esempi i regimi ad alte pressione o alta corrente di plasma - ma anche di esplorare nuova fisica, che non potrebbe essere altrimenti indagata.

I principi fondamentali della fusione termonucleare e una breve introduzione della fisica delle instabilità MHD - ovvero i modi tearing (TM), i modi resistivi in presenza di conduttore passivo (RWM) e i denti di sega . analizzati in questa Tesi verranno presentati nel Capitolo 1.

Una caratteristica distintiva di questo lavoro è l'approccio interdisciplinare nello studio del controllo delle instabilità MHD. Ciò ha richiesto approfondimenti sia di carattere fisico che ingegneristico. Questo approccio è necessario per i controlli MHD avanzati, dal momento che il progresso scientifico va di pari passo con quello tecnologico e viceversa. Questo lavoro di Tesi è stato condotto in tre esperimenti a fusione, caratterizzati dalla presenza di un sistema di controllo MHD avanzato, basato su bobine non assial-simmetriche, riscaldamenti ad onde e generazione di corrente di plasma. La Tesi è stata focalizzata inizialmente sull'esperimento RFX-mod situato presso il Consorzio RFX di Padova in Italia. Successivamente il lavoro è stato esteso ad esperimenti Tokamak più grandi, ovvero DIII-D presso la General Atomics, a San Diego, USA e ASDEX Upgrade presso il Max-Planck-Institute für Plasmaphysik in Garching, Germania. Tali esperimenti verranno descritti nel Capitolo 2.

RFX-mod si distingue dagli altri esperimenti sopra citati per la sua flessibilità: nonostante fosse stato originariamente progettato con una configurazione a campo magnetico rovesciato (RFP), può operare anche in configurazione Tokamak sia a forma circolare che a D. La stabilità MHD in entrambe le configurazioni magnetiche è assicurata dalla presenza di un sistema di controllo MHD d'avanguardia, basato su un un gran numero di bobine alimentate in maniera indipendente e da un controllo digitale in tempo reale, le cui recenti modifiche hanno consentito di sviluppare e testare algoritmi di controllo più complessi. Il Capitolo 3 descrive in quale modo il sistema di controllo MHD di RFX-mod è stato integrato nell'infrastruttura real-time MARTe, quale sia stato il suo utilizzo e l'implementazione di nuove strategie di controllo. Quanto descritto è stato oggetto di questo lavoro di Tesi. Scopo principale è stato quello di sviluppare strategie di controllo per le instabilità RWM che usano nuovi sensori e algoritmi. Queste nuove alternative sono state testate su scenari interessanti con $q(a)$ minore di 2. In questi scenari un modo RWM destabilizzato da gradienti di corrente compare con alta riproducibilità e cresce inducendo una disruzione se non viene controllato in maniera opportuna. Questo regime ha offerto un banco di prova eccellente per testare e confrontare nuovi schemi di controllo per l'RWM riutilizzabili in altri scenari Tokamak, ad esempio ad alto β.

I principali risultati sperimentali ottenuti durante la Tesi saranno presentati nella seconda e terza parte del lavoro. La prima parte - intitolata "Campi magnetici 3D per il controllo della dinamica MHD in plasmi di tipo Tokamak" - studia l'interazione tra questi campi e la dinamica di plasma e come questa possa essere sfruttata per il controllo della sua stabilità. In un esperimento di fusione, i campi 3D possono avere una doppia natura: possono essere associati a piccole non-assialsimmetrie chiamate campi errori (EFs) dovuti a vari ed inevitabili tipi di imperfezioni nella superficie esterna al plasma, o possono essere intenzionalmente applicati tramite l'utilizzo di bobine esterne non-assialsimmetriche. Il ruolo degli EFs nella stabilità degli RWM indotti da gradienti di corrente è stato studiato in plasmi Ohmici in RFX-mod con $q(a) < 2$. Gli EFs in RFX-mod sono stati inizialmente misurati con la tecnica chiamata compass scan e poi corretti, come verrà illustrato nel Capitolo 4 e nel Capitolo 5. Nel regime a basso $q(a)$, il modo RWM risulta linearmente instabile, a differenza degli scenari ad alto β studiati in precedenza, ove gli RWMs sono di solito stabilizzati da importanti effetti cinetici. La crescita del modo non può infatti essere evitata semplicemente rimuovendo gli EFs con la tecnica chiamata Dynamic Error Field Correction (DEFC).

La necessità di un controllo attivo in feedback per garantire la stabilizzazione dell'RWM nei plasmi di tipo Tokamak con $q(a) < 2$ ha motivato lo sviluppo di nuovi algoritmi di controllo. Il loro principale scopo è quello di generare delle correnti nelle bobine non-assialsimmentriche, inducendo campi magnetici 3D che evitano la crescita di questa instabilità. In RFX-mod, la stabilizzazione dell'RWM è stata ottenuta con successo utilizzando sia i sensori di campo magnetico radiale che poloidale. Gli esperimenti eseguiti durante questa Tesi hanno fatto emergere il ruolo cruciale dell'aliasing delle sidebands nelle misure di campo magnetico radiale generate dalle bobine attive. La loro rimozione ha consentito ai sensori di campo magnetico radiale di competere con quelli poloidali, i quali erano precedentemente considerati più efficaci e molto più usati nei Tomamak per il controllo RWM. Questo risultato contribuisce al dibattito scientifico su quale sia la scelta ottimale dei sensori per il controllo in feedback degli RWM. L'ambiente ostile dei futuri reattori a fusione probabilmente non consentirà di installare sensori di campo magnetico poloidale nella camera da vuoto, dunque quelli radiali, che comunque possono essere posizionati al di fuori di essa, possono fornire un'alternativa valida e fattibile. Gli esperimenti fatti a RFX-mod in cui è stata testata la performance degli schemi di controllo verranno presentati nel Capitolo 6.

Inoltre, i campi magnetici 3D esterni sono stati utilizzati in RFX-mod in plasmi Tokamak a basso fattore di sicurezza per studiare la loro interazione con l'attività MHD nel centro del plasma e in particolare con l'instabilità a dente di sega. In questi esperimenti, che verranno discussi nel Capitolo 7, i campi 3D causano una riduzione sia dell'ampiezza che del periodo del dente di sega, inducendo un effetto di mitigazione di questa instabilità. In RFX-mod, i denti di sega vengono mitigati e sono sostituiti da una equilibrio stazionario con elicità $m = 1, n = 1$ senza rischio di disruzione. La rotazione toroidale è significativamente ridotta in questi plasmi. Dunque la mitigazione del dente di sega in questi esperimenti è il risultato di un effetto combinato dovuto alla deformazione elicoidale nel centro del plasma e alla riduzione della rotazione. Questi risultati sono qualitativamente ben riprodotti da simulazioni MHD non lineari fatte con il codice PIXIE3D.

I risultati ottenuti ad RFX-mod hanno motivato esperimenti simili nel Tokamak DIII-D in plasmi in modo L, in configurazione divertore e con basso q95. Questi esperimenti, illustrati nel Capitolo 8, hanno riprodotto la mitigazione dei denti di sega con la tecnica sviluppata ad RFX-mod. A DIII-D questo effetto è correlato con un aumento evidente della risposta di plasma per la componente $n = 1$, che indica un accoppiamento con il kink esterno $n = 1$, marginalmente stabile, così

come predetto dal codice ad MHD lineare IPEC. Una significativa decelerazione della rotazione di plasma nel centro è stata inoltre osservata a DIII-D. Calcoli numerici della Neoclassical Toroidal Viscosity (NTV) eseguiti con il codice PENT hanno identificato questa sorgente di momento come possibile responsabile di tale evidenza.

Nel futuro, i reattori a fusione proporranno sfide sia in campo scientifico che tecnologico per il controllo del plasma e ciò probabilmente richiederà un approccio integrato e modellizzato. L'alta performance di questi esperimenti a fusione può essere infatti garantita se un controllo accurato di profili interni sarà ben coordinato con il controllo attivo di instabilità MHD usando molteplici attuatori, in modo tale da diagnosticare in tempo le disruzioni ed evitarle con azioni preventive. La seconda parte di questo lavoro - "Controllo attivo basato su modello di instabilità a dente di sega" - descrive il contributo di questa Tesi a questo approccio integrato ed innovativo. Il Capitolo 9 descriverà il codice Rapid Plasma Transport simulatOR (RAPTOR), un algoritmo che consente la ricostruzione in tempo reale dello stato di plasma usando misure combinate di diagnostiche e un modello semplificato di trasporto nel plasma. Questo codice è stato recentemente inserito nel sistema di controllo di ASDEX-Upgrade, dove produce in tempo reale l'evoluzione di molteplici profili di plasma - come ad esempio il fattore di sicurezza o la temperatura elettronica - importanti per monitorare e controllare la dinamica del plasma, e in particolare instabilità quali i denti di sega e Neoclassical Tearing Modes (NTMs).

Durante questo lavoro di Tesi, le potenzialità di RAPTOR sono state estese con l'integrazione di un nuovo modulo che, utilizzando il modello di Porcelli per i denti di sega, riproduce gli effetti di questa instabilità nella ricostruzione dello stato di plasma e in particolare nei profili. Le simulazioni di alcuni plasmi di ASDEX Upgrade mostrano che il nuovo modello è capace di predire in tempo reale il periodo medio dei denti di sega e l'effetto del suo crash sui profili interni, come per esempio sul fattore di sicurezza. Grazie a questo nuovo modulo, RAPTOR può essere ora usato per progettare e controllare esperimenti di sawtooth locking o pacing, usando l'Electron Cyclotron Resonance Heating (ECRH), ma può anche essere usato per migliorare il controllo diretto degli NTM con Electron Cyclotron Current Drive (ECCD) grazie ad una migliore stima del profilo del fattore di sicurezza. Tali risultati verranno presentati nel Capitolo 10.

L'approccio interdisciplinare adottato in questa Tesi ha consentito di acquisire competenze sia in ambito fisico che ingegneristico ed ha approfondito la fisica e il

controllo delle instabilità MHD in diversi esperimenti di fusione. Lo studio iniziale sull'integrazione di diverse strategie di controllo, che coordina sia la fisica 3D, come per esempio l'effetto dei denti di sega, che gli aspetti legati al controllo dei profili, è stato descritto in questo lavoro, ma certamente necessiterà di ulteriori approfondimenti nei prossimi anni. Ciò dovrebbe consentire di unificare in un unico controllo integrato in tempo reale diversi attuatori attualmente utilizzati separatamente. I risultati rilevanti di questo lavoro con i possibili futuri sviluppi saranno riassunti nel Capitolo Conclusioni e sviluppi futuri.

Contents

1

Introduction

Thermonuclear fusion is a promising candidate for safe and clean energy production. The fuel of this reaction is a plasma of light nuclei that release energy while they fuse together. High plasma thermal energy and long confinement time are necessary to overcome the Columb repulsion and to increase the likelihood of this reaction. A fusion plasma is confined by magnetic fields, giving rise to MagnetoHydroDynamics - MHD equilibrium states. Nevertheless, in some cases plasma confinement can be severely threatened by the onset of MHD instabilities. The main aim of this Thesis work is to investigate their dynamics and to develop schemes to control them and thus maximize fusion performance. This Chapter introduces the main principles of thermonuclear fusion, the magnetic equilibrium of the toroidal devices that confine the plasma, as well as the MHD instabilities that have been investigated in this Thesis work.

1.1 Principles of thermonuclear fusion

Nowadays, limited energy resources and the environmental impact of the existing energy production techniques are problems that have to be urgently solved. Thermonuclear fusion, besides being a widespread phenomenon in Nature, is a promising candidate for a safe and renewable energy production. Fusion offers a practically inexhaustible and clean source of energy, without producing neither greenhouse gases nor long-lived radioactive waste [1].

In a thermonuclear fusion reaction two light nuclei fuse together to generate a heavier one plus other products, like neutrons. Due to the mass difference Δm between the reactants and the products of the reaction, an amount of energy equal to $\Delta E = \Delta m c^2$, where c is the speed of light, is released in the form of the kinetic energy of the particles that are produced during the reaction. The average binding energy per nucleon is a monotonically increasing function of the atomic mass number up to Fe^{56} with a very steep increasing rate for light nuclei [2], as it is shown in Fig. 1.1. This figure shows the binding energy for a single nucleon as a function of the mass number A.

Thus fusing two nuclei of very small mass, such as Hydrogen - H or its isotopes, will originate a significant amount of energy. Indeed, if a nucleus of Deuterium - D fuses with a nucleus of Tritium - T, an amount of $17.6 MeV$ of energy is released

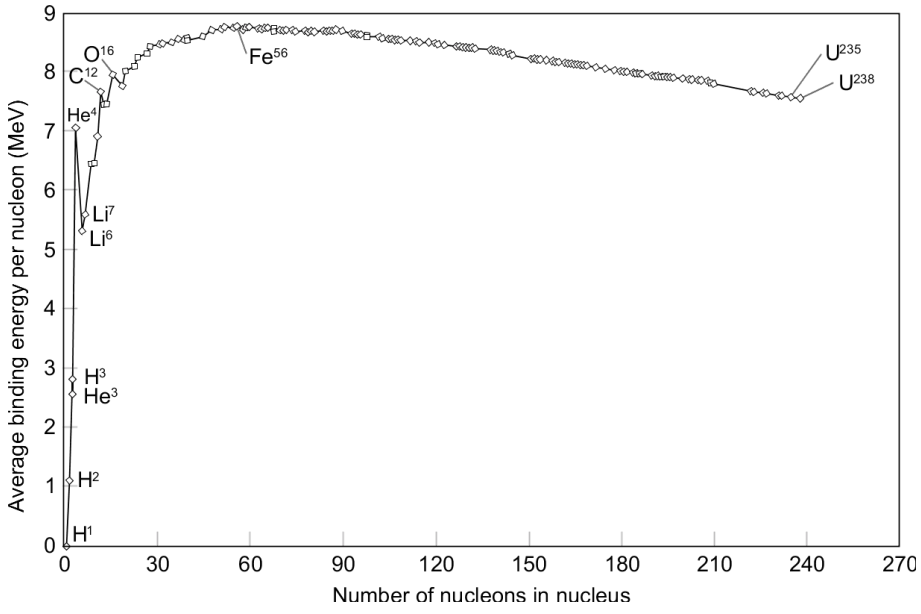

Figure 1.1: Nucleon bond energy as a function of the mass number. (This figure is taken from [2]).

during a single fusion reaction. Macroscopically, this means that just $1kg$ of this fuel would produce $10^8 kWh$ of energy, that equals the requirements of a $1GW$ power station for a day [2].

The idea to exploit thermonuclear reactions as the basis for a renewable energy source was suggested by stars, where these reactions supply them with their light. In the Universe Hydrogen fuses to form Helium - He through a chain of reactions, that involve the weak interaction of a β-decay. Since the latter has a very small cross section, this chain would not be efficient on Earth. For this reason alternative reactions that involves the isotopes of the Hydrogen, namely Deuterium - D and Tritium - T, were taken into account. Eventually the one with the maximum cross section at the lowest Deuterium kinetic energy was chosen, namely:

$$ {}^2_1D + {}^3_1T \longrightarrow {}^4_2He(3.56MeV) + {}^1_0n(14.03MeV). \tag{1.1} $$

Deuterium resources on Earth are almost endless since a litre of seawater contains $33mg$ of Deuterium, whereas Tritium does not virtually exist in Nature, because of its radioactive half time of 12.3 years [2]. Nonetheless, Tritium can be produced from Lithium exploiting neutron-induced fission reactions:

$$ {}^6_3Li + {}^1_0n \longrightarrow {}^4_2He + {}^3_1T + 4.8MeV, \tag{1.2} $$

$$ {}^7_3Li + {}^1_0n \longrightarrow {}^4_2He + {}^3_1T + {}^1_0n - 2.5MeV. \tag{1.3} $$

A thermonuclear fusion reactor is designed to maximize the likelihood of all these reactions and to provide a self-sustaining energy production system. Indeed, the main obstacle for a fusion reaction is the Coulomb repulsion of the positively charged nuclei, that however can be overcome at high kinetic energies. The highest cross section for the D-T reaction corresponds to a Deuterium energy of $100keV$. Nevertheless the probability of Columb scattering is still greater than the fusion reaction one at this energy, hence nuclei with sufficient energy have to be confined for many elastic collision times. Operationally, the most promising solution is to heat a D-T mixture until the thermal velocities are sufficiently high for fusion reactions to become likely, keeping it confined for a sufficient long time. At this temperature Hydrogen isotopes are fully ionized, but the electrostatic charge of the ions is neutralized by that of the electrons, and the final result is a quasi-neutral gas called *plasma* [3].

Actually, two different laboratory confinement techniques are available: the magnetic confinement and the inertial one. The basic idea of the former technique

is to confine the plasma in a closed geometry device where strong magnetic fields are applied. In so doing the confinement is provided by the Lorentz's force that pushes the charged particles to move around the magnetic field lines following a spiralling path. Conversely in the inertial confinement, high power lasers from different directions fire against a small volume of solid fuel, so that both temperature and density are increased up to the critical values that are necessary to overcome the Coulomb's barrier and trigger the fusion reactions.

The expertise gained in many years of fusion research in several magnetic confinement experiments provided the physics and technological basis for the design of a burning plasma experiment that will offer the possibility of studying several reactor relevant scientific and technological issues, which are beyond the present experimental capabilities. This experiment is called International Thermonuclear Experimental Reactor - ITER [4] and it is under construction in Cadarache, France. A schematic view of ITER is shown in Fig. 1.2.

This Thesis work deals with magnetically confined fusion plasmas, thus the basic concepts regarding this approach and the underlying plasma physics will be provided in the remaining part of this Chapter.

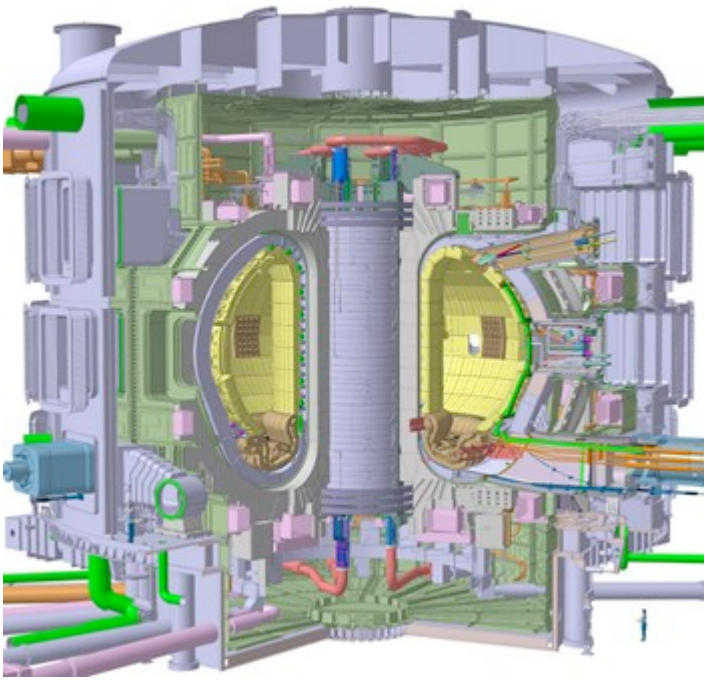

Figure 1.2: Scheme of the International Thermonuclear Experimental Reactor - ITER design.

1.2 Magnetic plasma confinement

In early years, fusion research has investigated different magnetic field geometries and the toroidal one resulted to be the most effective in terms of confinement. This Section will provide a brief introduction to the principles of magnetic plasma confinement in toroidal devices. Fig. 1.3 shows the coordinate system (r, θ, ϕ) of the toroidal geometry that will be used in the rest of this Thesis: r is the radial coordinate, θ and ϕ are the poloidal and the toroidal angle, respectively. R represents the major radius of the torus, a the minor one.

The magnetic field in toroidal experiments has both a poloidal component, B_θ, and a toroidal component, B_ϕ. Their relative amplitudes and the mechanisms that originate these field components depend on the particular magnetic configuration of the device. The three main families are: Tokamak, Reversed Field Pinch - RFP and Stellarator. In the former two the poloidal magnetic field is mainly induced by a plasma current that flows in the toroidal direction, while the toroidal magnetic field component is originated from the currents that flow in external windings. The main difference between the two magnetic equilibria is that in the RFP these external currents produce only a small part of the total toroidal magnetic field and indeed the plasma itself produces a large fraction of it through the dynamo effect [5, 6, 7, 8]. In addition, the two configurations are distinguished from the relative amplitude of B_θ and B_ϕ, as it will be described in details in the next Section.

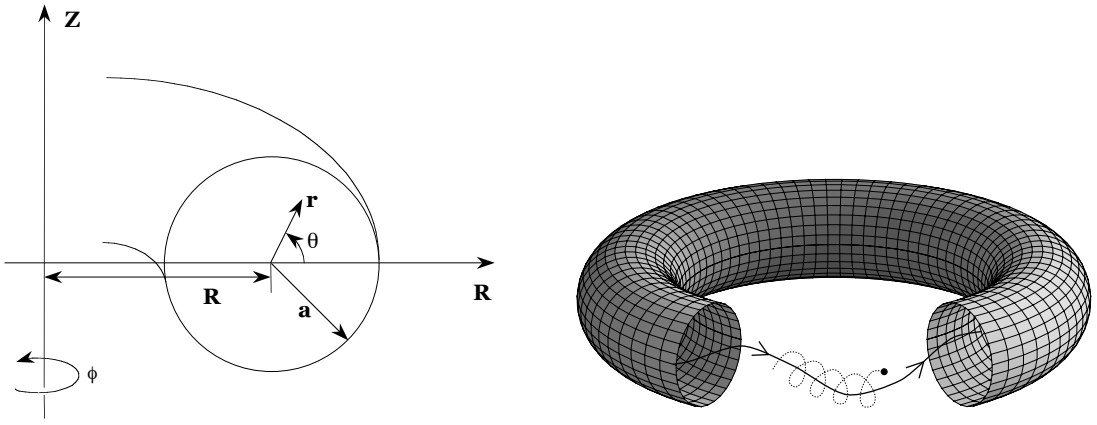

Figure 1.3: The system of toroidal (r, θ, ϕ) and cylindrical coordinates (R, ϕ, Z) (on the left). A scheme showing the principle of toroidal confinement (on the right): a charged particle gyrates around a helical magnetic field line and is thus confined within a toroidal vacuum vessel. (This figure was taken from [2]).

Differently from the previous configurations, both magnetic field components in a Stellarator are completely induced by currents flowing in external coils, that have a very complex 3D geometry to accomplish this task. In this Thesis work only the former two magnetic configurations have been investigated. Further information on Stellarator can be found in [9].

The external winding that supplies for the magnetic field in RFP and Tokamak is sketched in Fig. 1.4 and it is made up by:

The inner poloidal field coils They act as the primary of a transformer circuit to induce a toroidal current in the plasma, that acts as the secondary circuit. These coils are depicted in green in Fig. 1.4.

The outer poloidal field coils In these coils flows a current parallel to the plasma one, that is used to control both its shape and position. They are depicted in grey in Fig. 1.4 .

The toroidal field coils These coils approximate a toroidal solenoid and their design is a compromise between cost and engineering constraints. Indeed

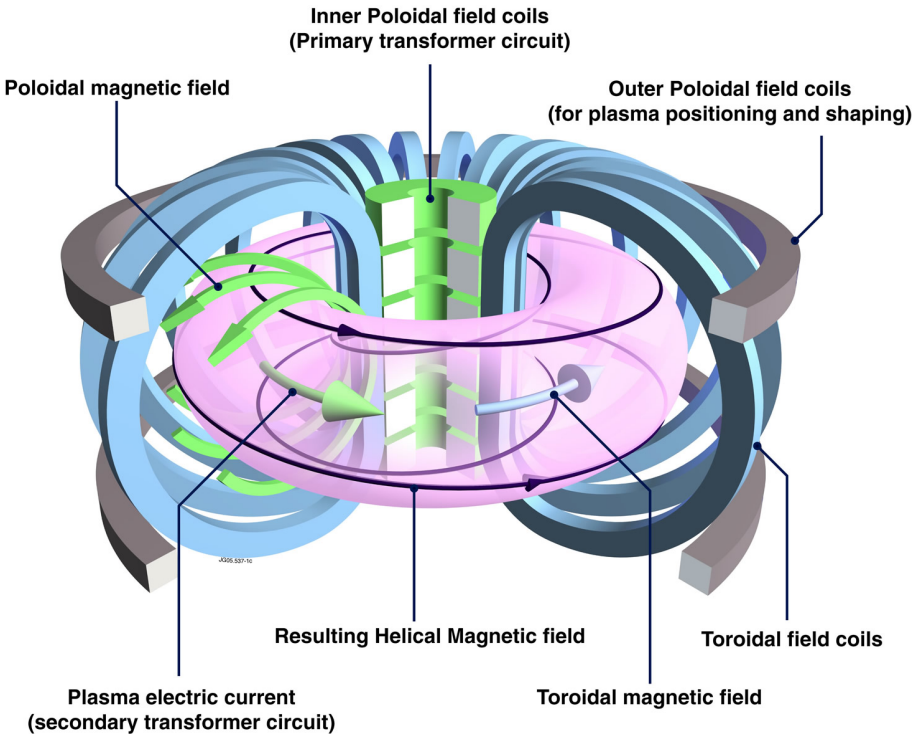

Figure 1.4: Sketch of the external winding system in RFP and Tokamak devices. Toroidal field coils (blue), the outer (grey) and inner (green) poloidal field coils. (This figure was taken from [10])

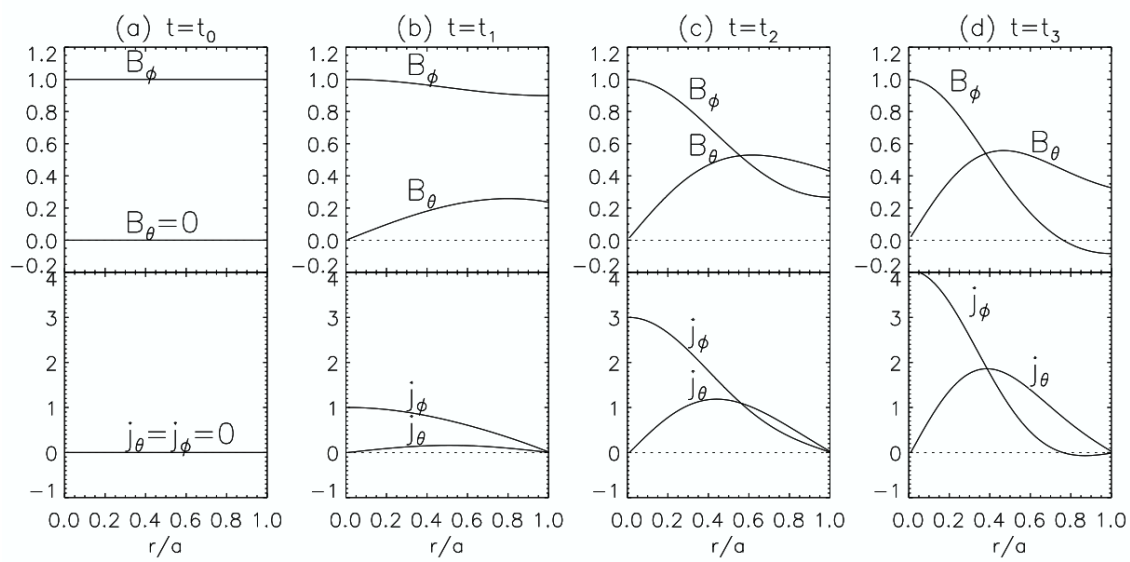

Figure 1.5: Qualitative illustration of time evolution of the normalized magnetic field and current density profiles in a pinch plasma when the electric field is increased in sequence. (a) initial state where only toroidal field exists; (b) a small electric field to drive mainly toroidal current in Tokamaks; (c) a modest electric field to significantly drive both toroidal and poloidal current components, (d) the RFP configuration is realized when toroidal magnetic field reverses its direction. (This figure is taken from [11])

the higher the number of the coils, the lower the toroidal ripple, but this comes at the price of a reduced access to the plasma for the diagnostic and auxiliary heating systems. These coils are depicted in blue in Fig. 1.4.

The non-axisymmetric coils In addition to these axisymmetric coils, modern fusion devices use non-axisymmetric coils to apply 3D fields of small amplitude. They can be used to control plasma stability in different ways, as it will be discussed in the next Chapters.

1.3 Tokamak and RFP magnetic equilibrium

As it has been anticipated in the previous Section, the Tokamak and RFP magnetic configurations differ for the relative amplitude of the poloidal and the toroidal magnetic field components. Fig. 1.5 illustrates this difference by reporting the qualitative time evolution of the magnetic field and the current density profiles in a Tokamak discharge that eventually evolves into a RFP one.

At $t = t_0$ the discharge is driven by the currents that flow in the primary

circuit. Their increasing amplitude induces a change in the magnetic flux that is concatenated with the torus and eventually an electric field that forces plasma particles to propagate in the toroidal direction, while gyrating around magnetic field lines. At $t = t_1$ an electric current originates in the plasma column and in turn it induces a magnetic field in the poloidal direction, as it is reported in panels b). At this time, the poloidal magnetic field component is much smaller than the toroidal one, this magnetic configuration is called *Tokamak*. If the applied toroidal electric field is raised further, the amplitude of both toroidal and poloidal currents increases and further modify the field profiles. Eventually the *Reversed Field Pinch - RFP* configuration is achieved $t = t_3$, as it is shown in panels d). In this magnetic equilibrium, the poloidal magnetic field amplitude becomes comparable with the toroidal one while the latter component reverses its direction at the edge. It is worth to note here that, according to Cowling's theorem [12], the current density and the magnetic field profiles of the RFP, in particular the reversal of the toroidal magnetic component, can not be preserved against resistive diffusion in a steady state toroidally symmetric plasma. In RFP the sustainment of the magnetic equilibrium is provided by the plasma itself through the *dynamo effect*, that that converts part of the poloidal magnetic field to the toroidal one [5, 6, 7, 8].

1.4 MagnetoHydroDynamic - MHD description of a plasma

The magnetic equilibria that confine a thermonuclear plasma and several MHD instabilities that are allied with them can be described by a fluid model called *resistive MagnetoHydroDynamics - MHD*. In this model, the plasma dynamics is described by a set of equations that are obtained combining a hydrodynamic description of the plasma, that is treated as a mixture of two oppositely charged fluids, with Maxwell's equations. Plasma resistivity is taken into account as well. A full description of this model can be found in [1, 2, 3], its equations are summarized in the following:

$$\begin{aligned} &\frac{\partial \rho}{\partial t} + \nabla \cdot (\rho \mathbf{u}) = 0 && \nabla \times \mathbf{B} = \mu_0 \mathbf{j} \\ &\rho \left(\frac{\partial \mathbf{u}}{\partial t} + \mathbf{u} \cdot \nabla \mathbf{u} \right) = \mathbf{j} \times \mathbf{B} - \nabla p && \nabla \cdot \mathbf{B} = 0 \\ &\mathbf{E} + \mathbf{u} \times \mathbf{B} = \eta \mathbf{j} && \nabla \times \mathbf{E} = -\frac{\partial \mathbf{B}}{\partial t} \quad . \end{aligned} \tag{1.4}$$

where ρ is the mass density, $\mathbf{u}$ the fluid velocity, p the plasma pressure and $\mathbf{j}, \mathbf{E}, \mathbf{B}$ have the usual meaning. A good estimation of the plasma resistivity η for a fully ionized plasma with ions of charge Ze is given by the Spitzer resistivity, formulated as:

$$\eta = \frac{\pi^{3/2} m_e^{1/2} Z e^2}{\gamma_E 2(2k_B T)^{3/2}} ln\Lambda, \tag{1.5}$$

where γ_E is a numerical factor depending on the atomic number Z, which turns out to be $\gamma_E = 0.582$ for $Z = 1$, while Λ reads:

$$\Lambda = \frac{3}{2Ze^2}\sqrt{\frac{k_B^3 T^3}{\pi n}}.$$

By combining Faraday's law and Ohm's law ones obtains the following equation, that describes the coupled dynamics of the magnetic and fluid velocity fields in the resistive MHD framework:

$$\frac{\partial \mathbf{B}}{\partial t} = \nabla \times (\mathbf{u} \times \mathbf{B}) + \frac{\eta}{\mu_0}\nabla^2 \mathbf{B}. \tag{1.6}$$

The first term on the right-hand side in Eq. 1.6 describes convection of the magnetic field with the plasma and its amplification or reduction due to compressive motion perpendicular to the magnetic field. Starting from this equation, it is possible to show that, in the *ideal* MHD limit, i.e. in the case where the resistivity η is negligible, the magnetic field lines move like if they were *frozen* to the plasma. Conversely, if $\eta \neq 0$ they can reconnect. The second term describes instead resistive diffusion of the field across the plasma.

In stationary ($\partial/\partial t = 0$) and static ($\mathbf{u} = 0$) conditions, the following equilibrium equation follows from the single-fluid MHD equation of motion:

$$\mathbf{j} \times \mathbf{B} = \nabla p.. \tag{1.7}$$

This equation is often used to describe the balance among the confining magnetic force and the thermal expansion force in a plasma.

1.5 Stability of RFP and Tokamak plasmas

In both RFP and Tokamak equilibrium the magnetic field lines helically wind inside the torus. A magnetic field line travels m turns in the poloidal direction and n in the toroidal one, the ratio of these two quantities is called *safety factor, q*.

While the inverse of this quantity is usually called *iota*, $\iota = 1/q$. Rational values of q play an important role in stability, thus the origin of the name. Indeed Eqs. 1.5 predict that like a neutral fluid, a perturbation $\tilde{\mathbf{A}}$ of a plasma quantity, like the magnetic field or the density, can grow unstable if the current or the pressure gradient provides the necessary free-energy. $\mathbf{A}$ can be decomposed into a Fourier series as follows:

$$\tilde{\mathbf{A}}(\mathbf{r},t) = \sum_{\mathbf{k}} \tilde{\mathbf{A}}_{\mathbf{k}}(r,t) e^{i(\mathbf{k}\cdot\mathbf{r}-\omega t)} = \sum_{m,n} \tilde{\mathbf{A}}_{m,n}(r,t) e^{i(m\theta+n\phi-\omega t)}, \tag{1.8}$$

where $\mathbf{k} = (k_r, k_\theta, k_\phi) = (k_r, m/r, n/R_0)$ is the wave vector in toroidal coordinates and m and n are the *poloidal* and *toroidal mode numbers*, respectively. Each couple of mode numbers (m,n) represents a helical perturbation. The angular frequency $\omega = \omega_\Re + i\omega_\Im$ is a complex variable. The real part accounts for the propagation velocity while the imaginary one describes an exponential growth if $\omega_\Im > 0$, or a damping if $\omega_\Im < 0$, of the perturbation amplitude. A helical magnetic perturbation can become unstable if its wave vector $\mathbf{k}$ satisfies the resonance condition $\mathbf{k}\cdot\mathbf{B} = 0$, where $\mathbf{B} = (0, B_\theta, B_\phi)$ is the equilibrium magnetic field, the radial component being zero due to its symmetry. The above resonance condition can be rewritten for a large aspect ratio device $R/a \gg 1$ as follows:

$$\mathbf{k}\cdot\mathbf{B} = \frac{m}{r}B_\theta + \frac{n}{R_0}B_\phi = 0 \qquad \Rightarrow \qquad q(r) = \frac{r}{R_0}\frac{B_\phi(r)}{B_\theta(r)} = -\frac{m}{n}. \tag{1.9}$$

On the contrary, a perturbation with $\mathbf{k}\cdot\mathbf{B} \neq 0$ has not a constant phase along the field lines on rational surfaces with integer (m,n) number. As a result, the magnetic field lines bend and this has a stabilizing effect on the plasma, since it increases its potential energy. In the opposite case the perturbation is free to grow on the corresponding *resonant surface*.

The safety factor profile in RFP and Tokamak plasmas is quite different, as Fig. 1.6 shows. In RFP $q \simeq a/(2R)$ in the centre and decreases towards small negative values at the edge. Whereas in Tokamak q remains typically around unity in the centre and rises beyond 2 as long as r approaches the edge. The horizontal lines identify the $m = 1$ rational surfaces. In Tokamak plasmas there is only one such unstable mode, the $m = 1,\ n = 1$ *internal kink mode*. Whereas in RFP, that is an intrinsically low-q device, a broader spectrum of $m = 1,\ n \simeq 2R/a$ modes is resonant throughout the plasma radius while the $m = 0,\ n \geq 1$ modes, that are

not reported here, are resonant at the reversal one.

An overview of the MHD instabilities that have been investigated in this Thesis work will be provided in the next Section.

1.6 Classification of MHD instabilities

A possible classification of the MHD instabilities can be based on three aspects: if it can be described by the ideal or the resistive MHD model, its driving mechanism and the localization of its effects along the minor radius.

An *ideal* MHD instability is potentially the strongest one, indeed it grows on a very short timescale of the order of the Alfvén time, defined as:

$$\tau_A = \frac{a\sqrt{\mu_0 \rho}}{B}. \tag{1.10}$$

Being $\tau_A \sim \mu s$ in a typical fusion plasma, this kind of instabilities sets the ultimate operational limit for the plasma confinement in any device. As an example, the kink instability is an ideal MHD mode that literally kinks the magnetic surfaces, while preserving their topology, as it is required by ideal MHD [2].

Conversely, when finite resistivity is taken into account as in Eqs. 1.5, a *resistive* instability allows the reconnection of the magnetic field lines in a small plasma

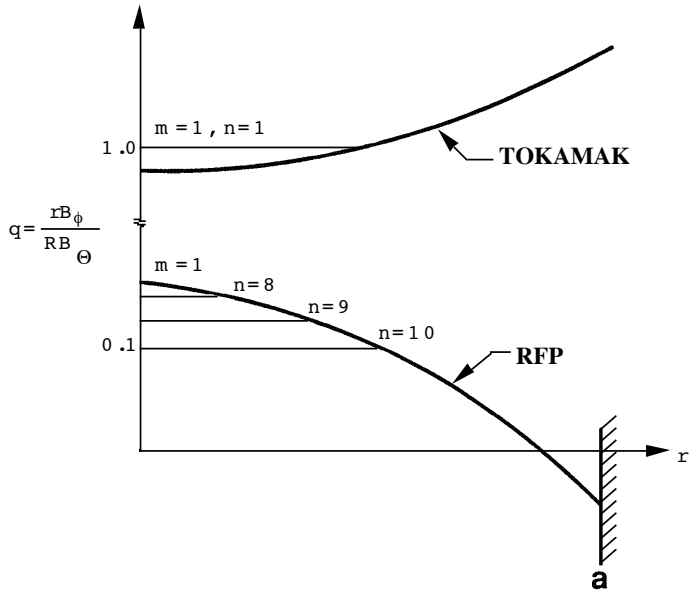

Figure 1.6: Safety factor profiles for a Tokamak and a RFP. Horizontal lines indicate the $(m = 1, n)$ rational radii.

volume, that however can have a dramatic impact on the global equilibrium. The typical time scale for the resistive instability lays between the Alfvén time and the magnetic reconnection time [13], that is defined as:

$$\tau_\eta = \frac{\mu_0 l^2}{\eta}, \tag{1.11}$$

where η is the plasma resistivity and $l \ll a$ the width of the reconnection volume.

As it has been anticipated before, both current and pressure gradients can supply the free energy that is necessary for a perturbation to grow unstable. The distinction between *pressure* and *current-driven* MHD instabilities is allied with the efficiency of confinement of plasma pressure p by the magnetic field, that is defined as:

$$\beta = \frac{p}{B^2/2\mu_0}, \tag{1.12}$$

or the normalized one:

$$\beta_N = \frac{\beta(\%)}{I(MA)/a(m)B(T)}, \tag{1.13}$$

where I is the plasma current. In high β plasmas an MHD instability can be typically triggered by a finite pressure gradient, in low-β regimes by a toroidal current density one. Both pressure and current-driven instabilities set hard operational limits, if they are not controlled. In Tokamak plasmas the onset of pressure-driven instabilities constraints the maximum achievable β_N, while current-driven ones limit the maximum plasma current. The former limit is commonly referred to as the Troyon or ideal MHD β limit [2]. Experiments in a broad range of Tokamaks have revealed that its upper bound depends on both plasma shape and the degree of the radial peaking of the plasma current density profile [14]. Thus a general definition for this limit reads as $\beta_N \leq 4l_i$ [15], where l_i is the plasma internal inductance that is a measure of the profile peaking. The plasma current limit can be defined as $q_{edge} < 2$, beyond it an $m = 2, n = 1$ kink mode instability leads to the disruption of the discharge [16].

Eventually, an MHD instability can develop inside the plasma or at its boundaries, so that *internal* and *external* instabilities can be distinguished. However, it is worth to note here that sometimes this classification does not strictly apply. Indeed toroidicity couples different m modes with the same toroidal number n. These secondary modes have components at the plasma boundary even if the

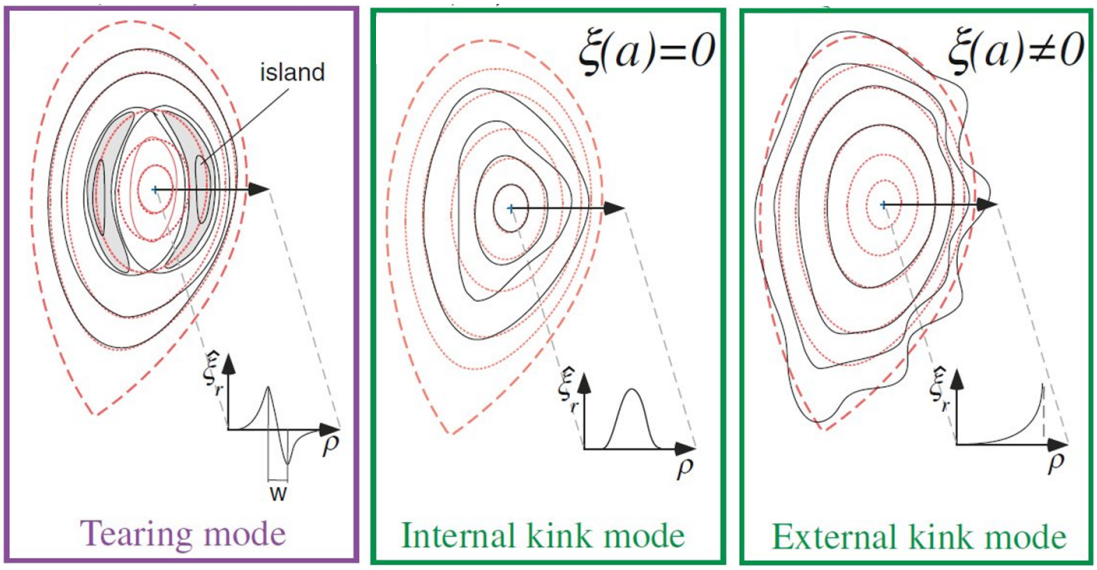

Figure 1.7: A basic classification of the MHD instabilities. (This figure is taken from [13])

dominant mode is purely internal.

Fig. 1.7 depicts the three main resistive MHD instabilities that have been investigated during this Thesis work and that will be described in the next Section, namely the Tearing Modes - TM, the internal kink mode, that is responsible for the *sawtooth oscillations* [2, 14, 17], and the external kink mode, that converts to a *Resistive Wall Mode - RWM* in the presence of a conducting wall with finite resistivity.

1.6.1. Tearing Mode - TM

Tearing modes are resistive instabilities that are driven by a gradient in the current density parallel to the magnetic field. The name comes after the effect of such instability on the magnetic field lines, that actually tear and reconnect. The tearing instabilities grow on a timescale between the fast Alfvén time, Eq. 1.10, and the relatively longer reconnection time, Eq. 1.11. They are unstable in both Tokamak and RFP plasmas, where they cause the degradation of the energy confinement time because heat and particles are able to travel radially from one side of an island chain to the other by flowing along the field lines, which is a faster process compared to the classical diffusion across the magnetic flux surfaces due to collisional transport. Nonetheless, in RFP plasmas the non linear interaction

of several tearing modes can be useful because it contributes to the sustainment of the magnetic equilibrium through the dynamo effect [18, 6, 7]. After its onset, magnetic feedback control can be used to hinder the growth of a tearing mode. Indeed the island chains naturally lock to a resonant perturbation that can have a destabilizing effect on it, if it is in phase. A fast feedback control can be exploited to modify the phase of the applied magnetic perturbation to maintain a stabilizing phase relation on a timescale of the order of $\sim ms$ [19, 20].

Another type of Tearing Modes, called Neoclassical Tearing Modes - NTMs, are found to seriously threatens the stability of toroidal plasmas, especially at high β [21, 22]. Indeed, in these plasmas the particles do not follow the magnetic field lines exactly, but exhibit a finite drift as a consequence of the magnetic field curvature and inhomogeneity [2]. The drift traps a fraction of the particles in banana shaped orbits that are located in the low field side of the torus. In the presence of a finite density gradient, an imbalance arises between the trapped particles moving in co and counter-current direction. This imbalance originates the *bootstrap current* that is eventually transferred to the passing particle by collisions. A NTM is a typically metastable mode but it can be triggered by perturbation of the bootstrap current profile that can occur in the presence of a seed island. Indeed, since parallel transport in a toroidal plasma is more efficient than perpendicular one, the conduction is good across the island and the pressure profile flattens. As a consequence, the boostrap current, that can be written as:

$$\mathbf{j}_{BS} = -\frac{1}{B_\theta}\frac{dp}{dr} \tag{1.14}$$

decreases, being proportional to the pressure gradient. This loss causes a helical hole across the current density profile that eventually favors the growth of the island. The result of such growth is a large island with appreciable width that affects energy and transport and that may trigger a disruption if it is large enough. Typically the major NTM instability $m = 2,\ n = 1$ represents a hard operational limit for Tokamaks, if not opportunely hindered.

Indeed the success of many advanced Tokamak scenarios relies on the steady state operation at high normalized β_N. This regime is desirable because it guarantees high fusion power density p_F and a consistent fraction of self-generated boostrap current f_{BS}. The relation of β_N with these two quantities, which are strongly critical for the economy and the performance of a future nuclear reactor, can be described as follows. The fusion density power scales as $p_F \propto \beta^2 B_T^4$ while

the bootstrap current fraction as $f_{BS} \propto q\beta_p$, where the poloidal β_p is the ratio of the plasma pressure and the poloidal magnetic field one. The higher β_N the higher both latter quantities, since $\beta_N^2 \propto \beta\beta_p$.

Several techniques have been developed to counteract the NTM instability in order to allow a safe plasma operation at high β values. Seed islands can be prevented by quenching the other instabilities that originate them, like the sawtooth one [23, 24], that will be discussed in the next Section. Alternative methods aim to actively drive current in order to supply for the missing bootstrap current in the helical hole [25, 26, 27].

1.6.2. Sawtooth instability

The phenomenology of this instability consists in a repeated and regular collapse of the central electron temperature together with a heat pulse propagation from inside the $q = 1$ surface to the plasma edge. Since each rapid collapse is followed by a slow recovery that shapes the soft X-ray and the electron temperature time traces with a sawtooth pattern, the instability was dubbed *sawtooth instability* [2, 13, 28].

Sawteeth originate in Tokamak plasmas in the proximity of the axis region, where the safety factor q is less or equal to unity. The underlying mechanism that triggers a crash is the destabilization of the $m = 1, n = 1$ internal kink mode, whose dynamics can be described as follows. An axisymmetric Tokamak plasma consists in nested toroidal flux surfaces along which the electron temperature T_e is assumed constant. If the T_e profile peaks, then generally a more peaked current profile will be observed because of a higher Spitzer conductivity Eq. 1.5. The resultant strong peaking in the toroidal current density profile makes the plasma unstable to a helical internal kink mode, which develops near the $q = 1$ resonant flux surface. Due to the presence of a local finite resistivity, the kink mode evolves into a tearing one and the helical deformation of the plasma in the proximity of this surface relaxes towards a lower energy state by reconnecting the nearby magnetic flux surfaces. This magnetic reconnection event is followed by a fast mixing of particles and energy in the axial and peripheral regions of the plasma core. A more detailed description of the models that describe this event will be provided in Chapter 10. The mixing effect is constrained within the so-called *sawtooth mixing radius* r_{mix}, which lies outside the $q = 1$ surface typically at $25 - 50\%$ of the minor radius, as depicted in Fig. 1.8 b). The remaining panels of Fig.

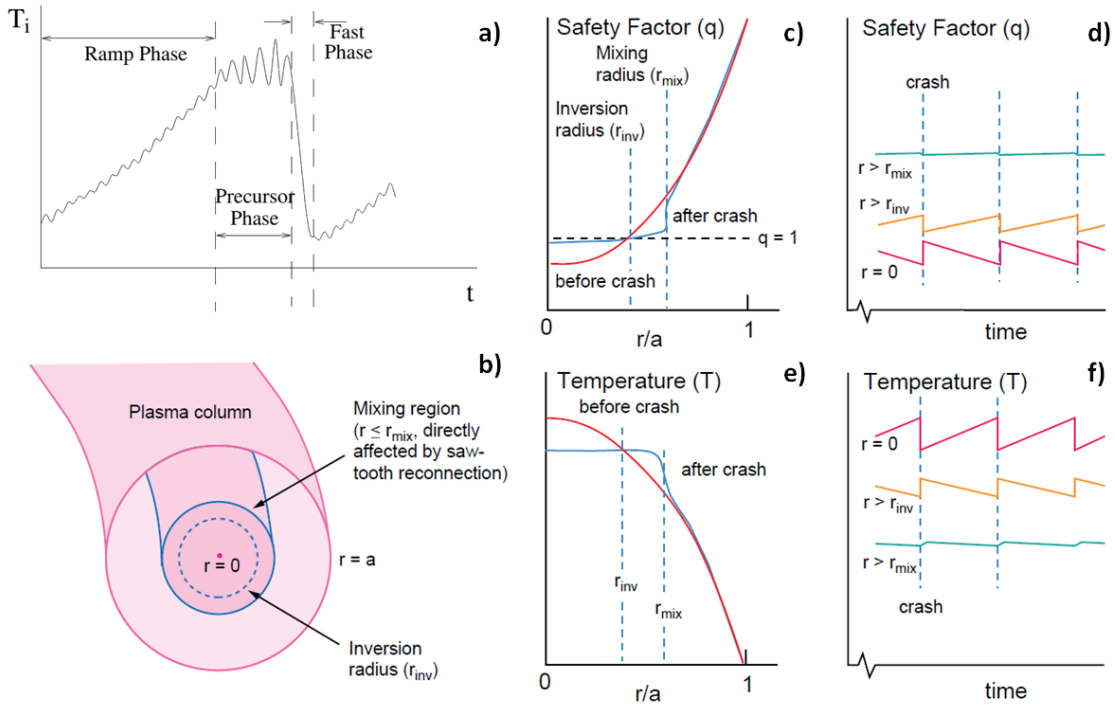

Figure 1.8: Schematic illustration of sawtooth oscillation features. a)Sketch of the time trace of a sawtooth instability in a Tokamak. The ramp phase, the precursor phase and the fast collapse phase are highlighted. (This figure is taken from [29]). b-f) Temperature and safety factor profile waveforms and evolution in an idealized circular cross-section Tokamak plasma. (This figure is taken from [14]).

1.8 show the safety factor and the plasma temperature profiles c), e) and time evolution d), f), respectively. The phase of both signals reverses at the sawtooth inversion radius, that is close to the $q = 1$ surface. This sign inversion points out that the energy and the current inside the $q = 1$ surface are rapidly ejected towards the $q > 1$ portion of the mixing radius whenever a sawtooth crash takes place. While the fluctuations in the plasma core are appreciable, the outer plasma region is quite unaffected.

The dynamics of a single sawtooth oscillation can be divided into three phases: the sawtooth ramp, precursor and fast collapse phase as shown in Fig. 1.8 a). The *sawtooth ramp phase* is a quiescent period during which the plasma density and temperature increase approximately linearly with time in the plasma core. During the *precursor oscillation phase* a helical magnetic perturbation grows and, due to toroidal rotation of the plasma, it is revealed as an increasing oscillatory behavior in many diagnostic signals such as in the soft X-ray emission, in the Electron Cyclotron Emission - ECE or in interferometric data. The last two measurements

detect the electron temperature and density, respectively. The third and last part coincides with the *collapse phase*, in which all the previous quantities fall rapidly to lower values. The effects on the safety factor and the temperature profiles are depicted in Fig. 1.8 c, e), the former straightens towards 1 in the plasma region within the mixing radius, the latter flattens accordingly.

Frequent small amplitude sawtooth oscillations can be benign for the plasma confinement. The benefit comes from the ability to counteract the accumulation of high-Z impurities in the core that can be responsible for excessive energy radiation. However this instability can be deleterious as well, because it can couple with other resistive MHD instabilities. One of the most deleterious ones, that concerns also the future ITER operation, is the NTM. As it has been discussed in the previous Section, this instability relies on a seed island to develop and the latter can be likely provided by the sawtooth instability [30].

Sawtooth oscillations can be tailored in many ways. By changing the distribution of energetic ions in the plasma [31] or by locally modifying the radial profiles of the plasma current and pressure near the $q = 1$ surface [32], by rotating [33] or shaping [34] the plasma as well as by heating the electrons inside the $q = 1$ surface [35]. The Electron Cyclotron Resonance Heating and Current Drive - ECRH and ECCD, the Ion Cyclotron Resonance Heating - ICRH and the Neutral Beam Injection - NBI, are the main actuators of the sawtooth control strategies that are listed above.

The safety factor profile in RFP plasmas is intrinsically low, as Fig. 1.6 shows, thus the sawtooth instability does not appear. Nonetheless high-currents RFP plasmas ($I_p \gtrsim 1MA$) are found to spontaneously self-organize in a Quasi Single Helicity - QSH state, where the magnetic dynamics is dominated by the innermost $m = 1$ resonant mode [36]. Magnetic reconnection is the mechanism at the basis of the intermittent QSH organization, that is reminiscent of the sawtooth activity of the Tokamak $m = 1$, $n = 1$ mode. Internal $m = 1$ modes can produce both in Tokamaks and RFPs stationary helical equilibria called snakes or Single Helical aXis states - SHAx [37].

1.6.3. Resistive Wall Mode - RWM

A RWM is an ideal external MHD instability that has a finite growth rate in the presence of conducting structures at the plasma boundary [38]. This instability can be driven by either pressure or current gradients.

Pressure-driven RWM

If the NTMs are stable or are actively stabilized, the ultimate limit for the maximum achievable β_N in the absence of any stabilizing conductive wall is the so-called *no-wall β limit*, that is the critical β value at which an external $n = 1$ kink mode becomes unstable and triggers the unwanted β collapse. This threshold can be increased by a perfectly conducting wall surrounding the plasma, in this case the limit for the external kink instability is called *ideal wall limit* and the stabilization is provided by the eddy currents that, flowing into the wall, counteract the penetration of the kinked magnetic surfaces. In both cases the RWM grows on the fast Alfvén timescale once the limit is overcome.

In any real experiment the wall that surrounds the plasma has a finite resistivity. In this condition the RWM is stable with β below the no-wall limit and highly unstable above the ideal wall one [39, 40]. This evidence is documented in Fig. 1.9. This is a DIII-D discharge where β_N reaches twice the value of $\beta_N^{no-wall}$ at $t \simeq 2100ms$, when the plasma disrupts due to a rapidly growing instability. This instability has been found to be consistent with an $n = 1$ kink mode occurring at the stability limit calculated with an ideal wall [41]. Just before the onset of this instability, the Mirnov coils detect an $n = 1$ structure that rotates at $1kHz$ with a growth time of $0.3ms$. Both these values are almost an order of magnitude larger than the ones expected on for a RWM. This evidence suggests that the dynamics of this instability would be the same in the presence of an ideal wall. The MHD calculations on the $n = 1$ stability have been carried out with an ideal wall that closely reproduces the geometry of the DIII-D one. Its minor radius is a free parameter of this simulation, thus the effect of the plasma-wall separation on the instability can be investigated. The results are summarized in panel d). The plasma is found to be stable (black line) at $t = 2040ms$ with the ideal wall located at the DIII-D vacuum vessel position, but unstable if β_N is slightly increased (dark and light grey lines). This means that the experimental equilibrium is very close to the stability limit with respect to both wall position and β_N. Moreover, the measured growth time is compatible with the one evaluated by the electromagnetic code VALEN [42].

In the intermediate range $\beta_{no-wall} < \beta_N < \beta_{idealwall}$, the instability splits into two branches. The faster one is stable because it rotates at such a high frequency that the resistive wall acts as if it was perfectly conducting. The slower branch is unstable because the instability can penetrate the wall and grow on the resis-

tive diffusion timescale. Luckily $\tau_\eta \gg \tau_A$ thus the RWM stabilization becomes operationally possible.

Pressure-driven RWMs can be both actively or passively stabilized. The passive control consists in enhancing the toroidal plasma rotation by injecting additional angular momentum with NBI [40]. Early theories predict that plasma rotation ω can be effective in counteracting the RWM instability if it is larger than a critical value $\Omega_c \sim \%(1/\tau_A)$. Further theoretical developments [43] as well as experimental evidences [44], confirm that this threshold can be reduced, and even overthrew,

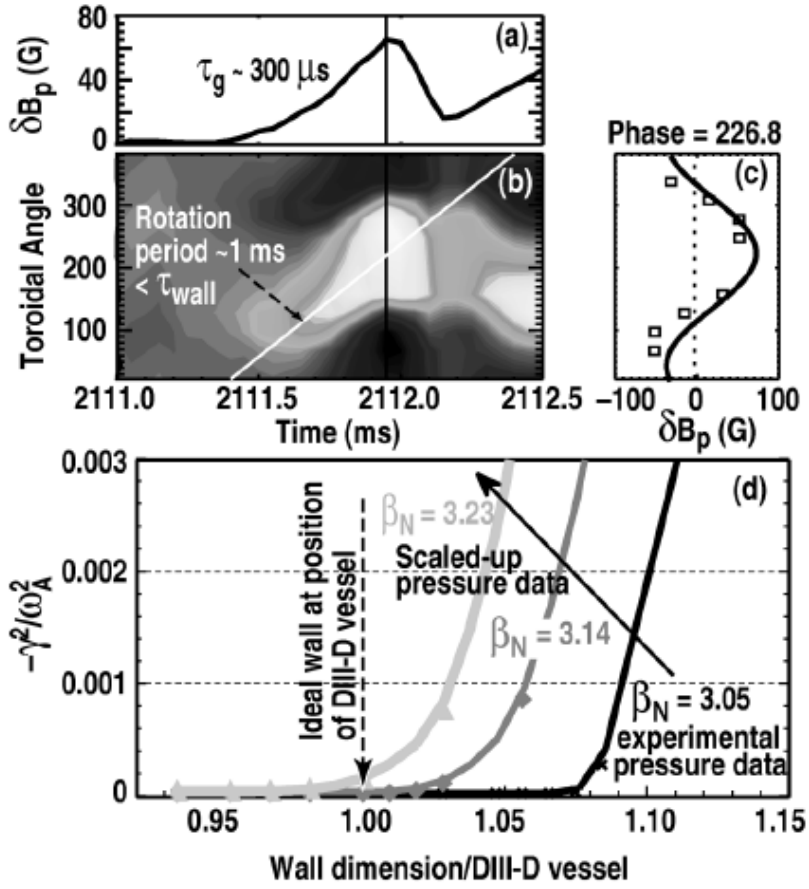

Figure 1.9: Shot: #106535. Magnetic measurements of the fast growing $n = 1$ MHD instability at $\beta_N \simeq 2\beta_N^{no-wall}$. a) Time trace of the $n = 1$ amplitude obtained from a midplane array of Mirnov probes. b) Contour plot of all the Mirnov probe signals vs time and toroidal angle. c) Same signals vs toroidal angle at time of peak amplitude. d) Calculated growth rate of the $n = 1$ kink mode vs assumed position of a perfectly conducting wall for equilibrium reconstructions at $\sim 60ms$ before the instability. Reconstructions are calculated using the experimental pressure profile (black curve), or with the measured pressure profile scaled up by $\sim 3\%$ (dark gray) and by $\sim 6\%$ (light gray). (This figure is taken from [41]).

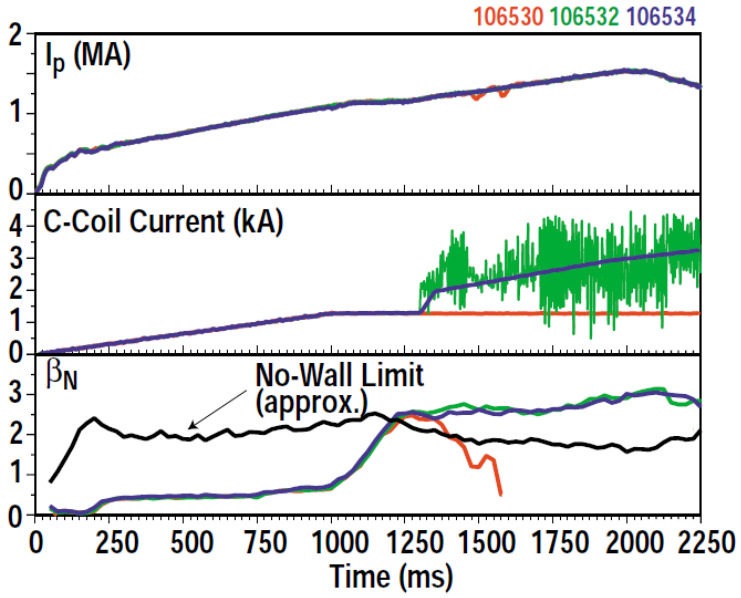

Figure 1.10: Comparison of C-coil current and β for discharges without optimum error field correction (106530, red curves), with feedback-controlled error field correction (106532, green curves), and error correction currents pre-programmed to approximate the feedback controlled currents (106534, blue currents). (This figure is taken from [39]).

if the kinetic effects, that are due to the resonance of plasma rotation frequency with the precession and the bounce frequencies of the passing and trapped ions, are taken into account as the main energy dissipation channel. Conversely, the stabilizing kinetic effect seems not to be so effective in changing the RWM growth rate in RFP plasmas [45].

The active RWM control exploits a set of external coils to minimize the magnetic field asymmetries, since it has been observed that once they are annihilated the plasma rotation drag is prevented above the no wall β limit and a more stable plasma operation is achieved, compared to rotationally stabilized plasmas [39]. This is illustrated in Fig. 1.10, that compares three discharges: without optimum error field correction, with feedback-controlled correction and with pre-programmed error correction currents, that are inferred from the feedback ones.

They are plotted in red, green and blue respectively. These discharges are similar, as the time evolution of the plasma current, that is reported in the first panel, shows. The main difference is in the plasma performance above the no-wall β limit, that is plotted in the last panel. The discharge without any error field correction suffers of a β collapse as soon as the threshold is exceeded. Conversely,

the feedback control succeeds in maintaining a stable plasma operation well above the limit. Interestingly, the pre-programmed currents that mimic the slow varying component of the feedback ones, result to be equally effective in stabilizing the plasma. This experiment reveals that the pressure-driven RWM is actually linearly stable.

Current-driven RWM

Current gradients can drive a RWM instability as well as pressure ones. Similarly to what happens for the upper limit in β, the highest plasma current that can be achieved in a Tokamak is constrained by an external kink mode that is triggered whenever the ratio between the plasma current and the toroidal magnetic field exceeds a critical value. This threshold is conveniently expressed in a circular plasma in terms of the safety factor with the condition $q(a) > 2$. The same limit seems to hold for a diverted plasma if the edge safety factor is replaced by q_{95}, that is the edge safety factor value at the 95% magnetic flux surface.

This regime shares many similarities with the high β one. Firstly, the current-driven kink evolves into a RWM if the plasma is surrounded by conducting structures with finite resistivity, as the pressure-driven one does. Secondly, similarly to the high β regime in DIII-D, the amplification of the plasma response is evidenced also in low-q Tokamak plasmas as the safety factor approaches the $q(a) = 2$ current limit [46]. Thirdly, the structure of a current-driven RWM at the plasma boundary is similar to the pressure-driven one, however the latter has a quite different eigenfunction in the plasma core with higher amplitudes of the internal components and a much richer poloidal spectrum [47].

The RWM in RFP plasmas is a current-driven instability as well and, like in Tokamak ones, it is usually stabilized by actively controlling their amplitude with non-axisymmetric magnetic coils [48]. An example is reported in Fig. 1.11, that compares the dynamics of this instability in an Ohmic Tokamak plasma and in a RFP one. In both cases, the uncontrolled discharge, that is plotted in red, is characterized by the presence of a current RWM, a $m = 2, n = 1$ RWM in the Tokamak and a $m = 1, n = -6$ one in the RFP, which increases in amplitude with the characteristic exponential growth up to a certain level which induces a disruption, as it is shown in the bottom panels. Conversely, with magnetic feedback control the mode amplitude is kept at very small values and the instability is completely suppressed, as it is shown in the plasma experiments reported in blue. This

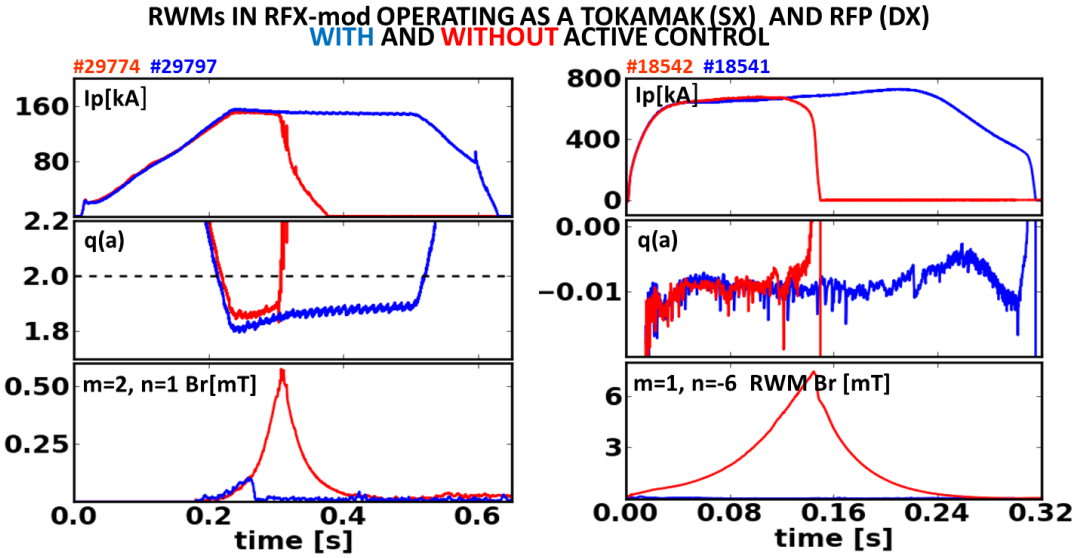

Figure 1.11: RWM in RFX-mod running as an Ohmic circular Tokamak and a RFP with (blue) and without (red) feedback control. Time evolution of a) the plasma current, b) the edge safety factor and c) the RWM radial magnetic field amplitude.

instability has a very similar dynamics in these two magnetic configurations, thus RFX-mod is a suitable testbench to investigate the interaction of this instability with external currents and wall.

2

RFX-mod, DIII-D and ASDEX Upgrade experiments

The active control of MHD instabilities has been investigated during this Thesis work in three different fusion experiments: RFX-mod, DIII-D and ASDEX Upgrade. In RFX-mod at Consorzio RFX in Padua (Italy) the work deals with the integration and the development of its MHD control system in the new real-time MARTe framework, that has been recently adopted in this device. The results obtained on RWM and sawtooth control during this Thesis work in RFX-mod suggested similar ones in DIII-D at General Atomics in San Diego (USA) as well. Eventually the development of a real-time model for sawtooth control using the RAPTOR code has been carried out in ASDEX Upgrade at IPP in Garching (Germany). This Chapter introduces these three machines and in particular the aspects relevant to this Thesis.

2.1 RFX-mod experiment

The Reversed Field eXperiment-mod - RFX-mod is currently the largest RFP experiment in the world, with an aspect ratio $R_0/a = 2/0.459 \simeq 4.4$, where $R_0 = 2m$ and $a = 0.495m$ are respectively the major and the minor radius of the machine. This experiment is an upgrade of the previous RFX experiment [49], whose design modifications were aimed at increasing the capability of actively controlling the MHD dynamics on timescales much shorter than pulse duration, that is of the order of $0.5s$. Doing so, energy loss and intense plasma-wall interactions caused by magnetic field errors and internally resonant tearing modes that are locked to the wall can be significantly reduced [50]. The main RFX-mod parameters are listed in Table 2.1 while a picture of this experiment is shown in Fig. 2.1. The description of the main improvements made on RFX is presented in the following.

First wall As in the RFX experiment, the inner surface of the vacuum vessel is fully covered with 2016 graphite tiles. The shape of the tiles was modified in order to improve the protection of the vacuum vessel, to increase the uniformity of the power distribution and to house a large number of sensors between the tiles and the vacuum vessel [51].

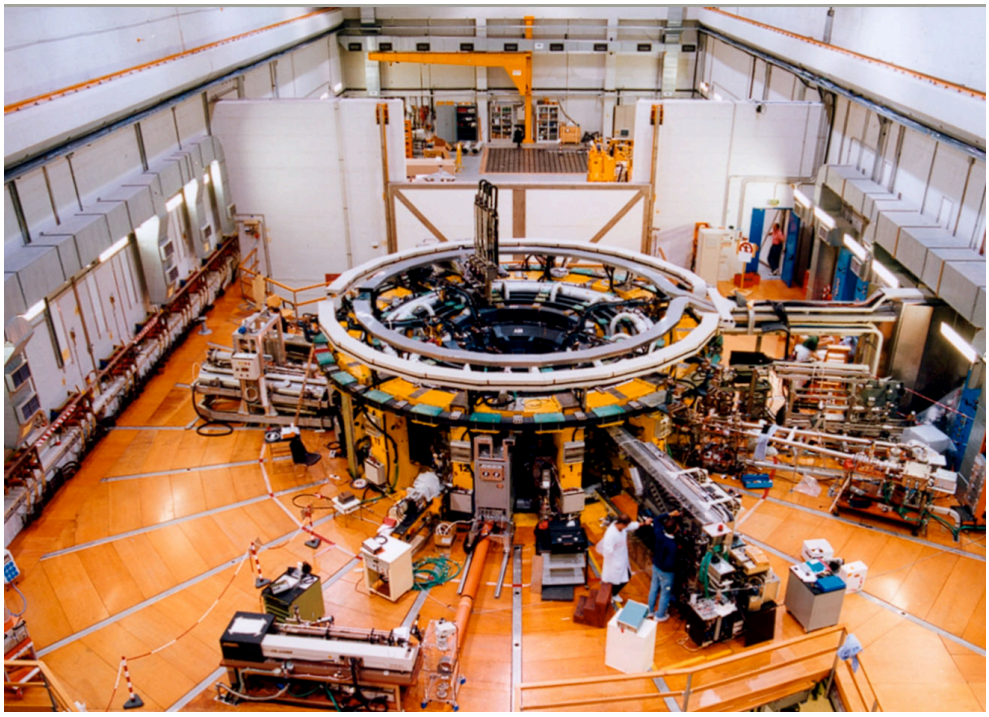

Figure 2.1: The RFX-mod experiment.

Major radius R	2m
Minor radius a	0.459m
Maximum plasma current	2.0MA
Maximum applied toroidal field	0.7T
Flat-top time	0.5s
Core flux swing	15Vs

Table 2.1: Main parameters of RFX-mod machine.

Stabilizing shell RFX-mod is equipped with a new shell made of copper $3mm$ thick. Copper was chosen to minimize the overall radial thickness, once fixed the shell resistive penetration characteristics. The resistive penetration time for the $m = 1,\ n = 0$ vertical magnetic field is about $50ms$, that is much shorter than the discharge duration. In RFX a $65mm$ thick aluminium shell supported the vacuum vessel and all the magnetic diagnostics, while in RFX-mod this task is fulfilled by the Toroidal Support Structure (TSS). The TTS is made of stainless steel and it is $47mm$ thick. Its structure consists of 4 parts and it has two insulated butt joint poloidal gaps and one insulated equatorial gap (the inner one). The TTS houses the vacuum vessel and the copper shell on its inside, instead the saddle coil system, the toroidal field windings and the rings, that support the field shaping coils are located externally. The TTS structure is plotted in dark grey in Fig. 2.2

Vacuum Vessel This is the toroidal chamber containing the plasma. It is an all-welded, rigid structure made of INCONEL 625, composed of 72 elements welded together. The vacuum vessel is also an interface between the plasma and the outside. It is equipped with 96 ports for gas input, vacuum pumping and diagnostic systems. It is depicted in light grey in Fig. 2.2

Axisymmetric coils The *inner poloidal field coils*, that are sketched in yellow in Fig. 2.2, provide the time-varying poloidal magnetic flux that induces the toroidal loop voltage during the discharge. The magnetizing windings can carry a maximum current of $50kA$ and produce a $15Wb$ maximum flux. No iron core has been adopted, even though it would have reduced the coil dimensions, power demand and costs, in order to avoid magnetic field asymmetries and improve the accessibility.

The *toroidal field winding* system, in blue in Fig. 2.2, consists of 48 coils uniformly distributed along the toroidal direction, that surround the vessel

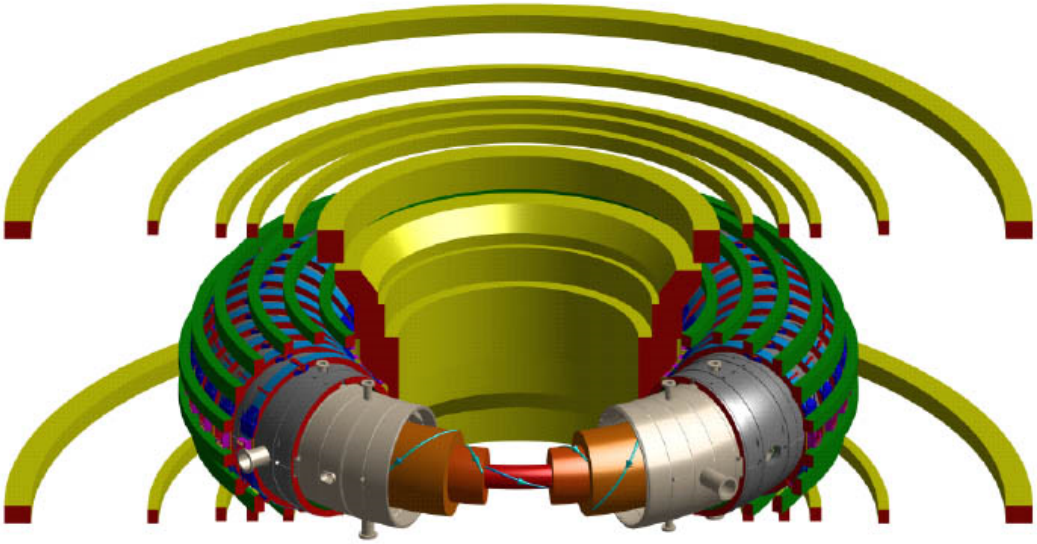

Figure 2.2: 3D view of the RFX-mod axisymmetric coil system. Inner poloidal field coils (yellow), toroidal field coils (blue), outer poloidal field coils (green). TTS (dark grey) and vacuum vessel (light grey) are sketched as well.

and the shell. They are designed to generate the toroidal magnetic field needed to set-up and maintain the discharge. The coils are series-connected in 12 groups of 4: each group is connected to an independently controlled power supply unit. During standard operations, the toroidal field coils can produce a maximum toroidal bias field $B_\phi = 0.7T$, that allows to operate RFX-mod as a Tokamak too. In the RFP configuration the toroidal field is much smaller, but it can be reversed at the edge down to $B_\phi(a) = 0.44T$ during the plasma current flat-top.

The 16 outer *poloidal field coils* are routinely used to control the plasma position and shape and they have also been recently exploited to control D-shaped Tokamak plasmas, as it will be described in the next Section. They are depicted in green in Fig. 2.2.

Non-axisymmetric active coils The TTS support structure sustains the 192 active coils that are divided in 48 poloidal arrays of 4 coils, as it is shown in Fig. 2.3. Each coil has 60-turns, has an average surface of $0.27m^2$ and extends $90deg$ poloidally and $7.5deg$ in the toroidal direction. A single coil

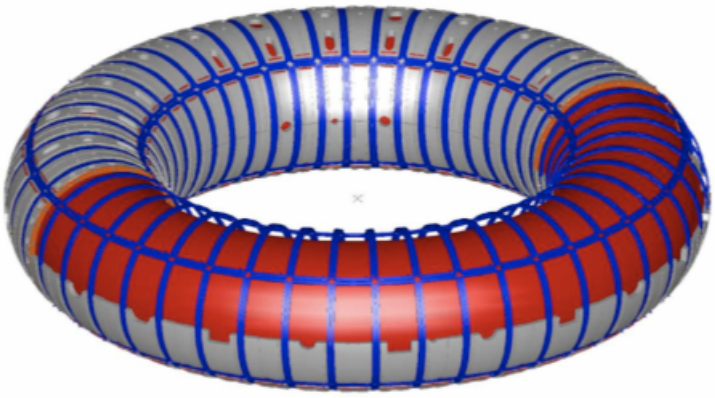

Figure 2.3: Scheme of the RFX-mod non-axisymmetric coils: 192 active coils (in blue), located external to the TTS support structure (in grey), which fully covers the torus surface.

can carry a maximum total current of $400A$ for $300ms$ producing a maximum local DC radial field $B_r \simeq 50mT$ at the plasma surface. Each coil is fed by its own power supply, which can perform an independent control of the current in the coil. This feature, allied with the flexibility of the new real-time MARTe framework, that will described in Chapter 3, allows to change arbitrarily the original configuration of the active coils obtaining any user-defined partial coverage of the plasma surface. The possibility to switch off the single coils and to join some consecutive ones in a so-called *super coil* allows to test new active coil geometries and to validate the results obtained in other experiments, as it is described in [48].

The magnetic probe system The RFX-mod magnetic measurements mainly come from a system of 192 biaxial pick-up probes and an equal number of radial saddle coils, both regularly distributed all over the surface of the torus, as it is shown in Fig. 2.4. The former are depicted with white squares in the 2D plot, while with blue ones in the 3D section. They are installed on the shell, in the middle of each active coil. They provide measurements of both toroidal and poloidal magnetic field components. The saddle loops, that measure the radial component of the magnetic field, are depicted in red and are located on the outer surface of the TTS. Both toroidal and the radial magnetic field measurements are available in real-time and they are routinely used in many MHD control schemes, as it will be discussed in Chapter 3. During this Thesis work 32 poloidal sensors, divided into 4 poloidal arrays

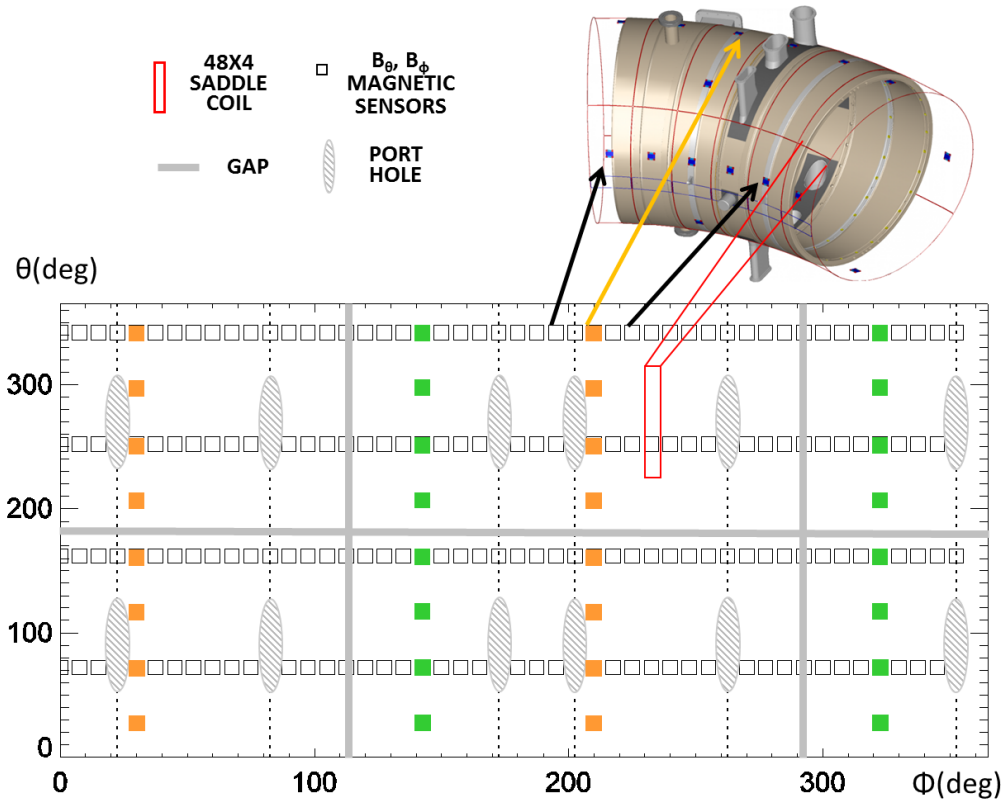

Figure 2.4: The magnetic sensors in RFX-mod. 192 bi-axial pick-up coils, measuring the toroidal and poloidal magnetic field components (white squares), 32 brand-new sensors for the poloidal magnetic field component (orange and green squares) and 192 saddle coils for the radial ones (red). Broken saddle coils (violet), gaps (grey lines) and portholes (grey ellipses) are reported as well.

of 8 sensors each, have been embedded in real-time and integrated in a dedicated MHD control scheme, they offer significant advantages as it will be discussed in Chapter 6. They are plotted with orange and green squares in Fig. 2.4. All the magnetic sensors have a bandwidth that is limited by the vacuum vessel eddy currents at about $1kHz$, while the sampling frequency is $10 - 20kHz$.

The MHD control system The RFX-mod real-time control system has recently been moved to the real-time MARTe framework [52], that will be described in Chapter 3. The RFX-mod MHD control is highly configurable and several equilibrium and MHD control schemes are available. According to the user-defined choice, at each time step the digital controller performs

the FFT of the 192 toroidal and radial sensors or of the 32 poloidal ones. Further computations are carried out to obtain an optimized estimate of the feedback variable, that eventually is minimized or kept at a finite value by a Proportional Integral Derivative - PID controller. The currents that it prescribes are supplied by the 192 active coils or by a subset of them if a coil reconfiguration option is activated.

2.1.1. Flexibility of RFX-mod

Thanks to the flexibility of its feedback control system and to the capabilities of its power supplies, RFX-mod is the only experiment in the world that can operate the plasma in two different magnetic configurations: as an RFP and as an Ohmic circular and D-shaped Tokamak. Three demonstrative examples of these configurations are reported in Fig. 2.5, that shows the time history of the plasma current and the safety factor for an RFP plasma in panels a) and b) and the ones for the two Tokamak plasmas, circular in blue and D-shaped in green, in panels c) and d). The last two panels e) and f) report the plasma shape in the two Tokamak experiments, the poloidal sections show the Last Closed Flux Surface - LCFS plotted with a continuous line, while the magnetic flux surface that encloses the 95% of the poloidal flux with a dashed one.

The RFX-mod can operate RFP plasmas up to currents of $2MA$, as it is shown in panel a). This is a remarkable and unique feature of this experiment. Note that the discharge duration is around $0.5s$. This result has been obtained thanks to magnetic feedback control of both RWM [48, 53] and tearing mode instabilities [20, 54]. The study of these high current regimes allowed the discovery of a new helical state called *Single Helical aXis State - SHAx state*, which naturally develops thanks to a self-organization process [37] and shares interesting commonalities with Tokamak helical states and Stellarators.

As it has been anticipated above, the machine can be also operated as an Ohmic circular Tokamak. In this magnetic configuration, the plasma can be driven and safely maintained at edge safety factor values $q(a) < 2$ for the entire discharge. An example is plotted in blue in panels c) and d), that report the time evolution of the plasma current and of the edge safety factor, respectively.

As it will be explained in Chapter 3, this result is not trivial, since Tokamak plasmas are highly unstable in this regime due to the presence of a high disruptive kink mode, which is successfully controlled in RFX-mod thanks to its active MHD

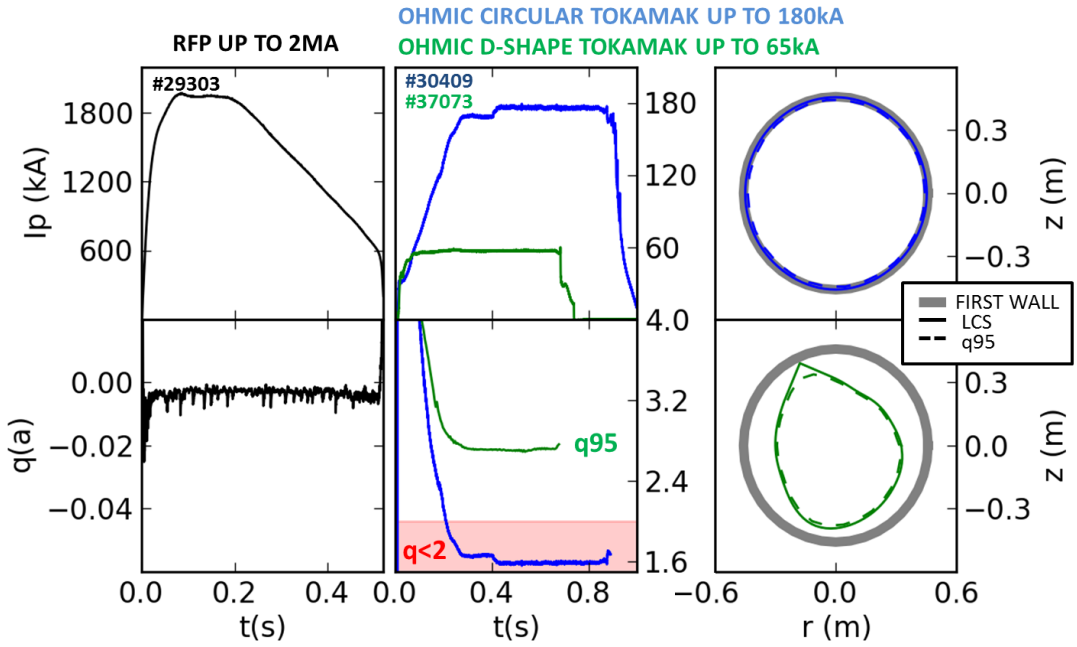

Figure 2.5: RFX-mod magnetic configurations: RFP, ohmic circular Tokamak and ohmic D-shaped Tokamak. Time evolution of the plasma current and the safety factor. The plasma shape for the two Tokamak discharges is reported on the right.

control [55, 56]. The expertise acquired in RFX-mod promoted similar experiments in the DIII-D Tokamak, where this regime has been successfully explored as well. [46, 57].

Recently, single null D-shaped Tokamak plasma operation has been also obtained. Panels c) and d) compare a D-shaped Tokamak plasma discharge, that is plotted in green, with a circular one. A single null Tokamak plasma can be obtained from a circular one by controlling the plasma shape either with pre-programmed currents or with a closed-loop controller. In this discharge the transition to the single null configuration occurs at around $t = 0.2s$, when the currents in the field shaping coils are opportunely driven by the feedback controller to create the X-point inside the vacuum chamber.

Fig. 2.6 highlights the main features of the circular Tokamak discharge that is plotted in blue in Fig. 2.5. In a typical RFX-mod Tokamak discharge the plasma current is ramped up to a target edge safety factor value $q(a)$ and a pre-programmed receipt of gas puffing is set to sustain the plasma density. In the

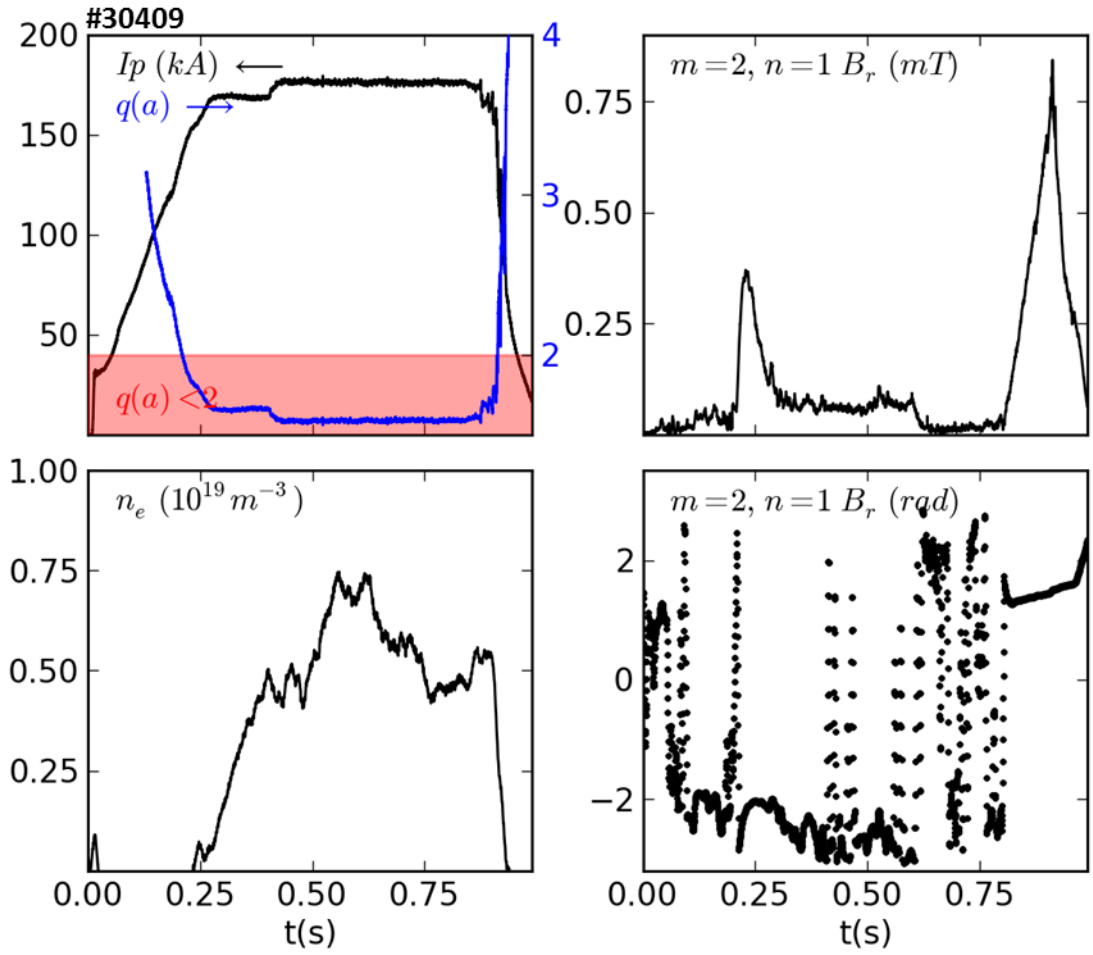

Figure 2.6: A typical RFX-mod Tokamak discharge. Time evolution of the plasma current, edge safety factor and the electron density on the left, $m = 2, n = 1$ poloidal magnetic field amplitude and phase on the right.

example reported in this figure, which corresponds to a circular Tokamak discharge, the target safety factor is around 1.6 and the plasma density, which is $n_e \simeq 0.3 n_G$, where $n_G = \frac{I_p}{\pi a^2}$ is the Greenwald density, is shown in the bottom panel on the left. During the plasma current ramp phase, the safety factor profile assumes rational values and, as it has been described in Chapter 1, different modes can be excited. In particular, in the experiment presented here, when the safety factor equals 2 around $t = 0.2s$, a $m = 2,\ n = 1$ tearing mode is detected with the magnetic field sensors, that have been described previously in this Chapter. A Fourier analysis of radial magnetic field sensors located outside the vessel has been performed to calculate the amplitude and phase of the $m = 2,\ n = 1$ radial magnetic field component. The result is reported in the upper and lower panels on the right,

respectively. The $m = 2,\ n = 1$ tearing mode initially rotates at around $\sim 1kHz$ and then it slows down to $100Hz$. Its frequency value is controlled by the magnetic feedback system that keeps the mode amplitude at the lowest possible value with a pure proportional gain. When the plasma current is further increased, and the desired safety factor value is reached, the plasma current is maintained constant and the $q(a) < 2$ regime is explored. As it will be discussed in Chapter 5, such regime can be investigated only thanks to magnetic feedback control. When $q(a)$ is below 2 in fact, a $m = 2,\ n = 1$ kink mode is present in the plasma and it is converted to a resistive wall mode in the presence of a conducting shell as in RFX-mod. From $t = 0.27s$ to $t = 0.8s$, a controlled $m = 2,\ n = 1$ RWM appears in the plasma, its amplitude reported in panel c) is minimized down to ~ 0 towards the end of the discharge, where the proportional gain is changed. The mode does not rotate, as reported in the bottom panel. As soon as the magnetic feedback control system is switched off, starting from $t = 0.8s$, the $m = 2,\ n = 1$ resistive wall mode grows unstable and leads to a disruption.

2.2 DIII-D Tokamak

The DIII-D Tokamak is located in San Diego, CA, USA and it is operated by General Atomics. The "D" suffix in the name comes from the D-shaped cross-section of the vacuum vessel, having a major radius of $1.66m$ and a minor radius of $0.67m$ [58]. Fig. 2.7 sketches a poloidal view of this Tokamak together with contours of constant magnetic flux shown to illustrate a typical plasma shape.

Major radius R	1.66m
Minor radius a	0.67m
Maximum plasma current	3.0MA
Maximum applied toroidal field	2.2T
Flat-top time	5s
Core flux swing	10.5Vs

Table 2.2: Main parameters of DIII-D machine.

DIII-D is one of the main contributors to the ITER project, as far as both its shape and operation are concerned. Indeed this experiment is approximately one-fourth the size of ITER and its plasmas have ITER-relevant characteristics, like collisionality and β_N. The main DIII-D features are described in the following.

Vacuum vessel The vacuum vessel resistive penetration time τ_W is in the order

of few ms. The graphite tiles that cover its inner surface heat up during the discharge, but they are cooled down by the water that passes through the channels in the vessel wall between two consecutive discharges. In the high heat flux areas of the upper and lower divertor regions the edge-to-edge tile misalignment and the tile gaps are less than $0.25mm$, to reduce erosion and provide axisymmetry.

Axisymmetric coils The electric field necessary for the plasma breakdown is provided by the so-called Ohmic heating coil, that supplies also Ohmic power, once the plasma is formed. These coils are coloured in magenta in Fig. 2.7. The plasma shape and position are controlled by 18 poloidal field coils, labelled F-coils and plotted in orange in Figure 2.7.

Non-axisymmetric coils These coils in DIII-D are mainly devoted to error field correction and to the stabilization of the $n = 1$ RWM [39, 59]. But they have been also exploited to apply resonant magnetic field perturbations for ELM mitigation [60], and to produce forced NTM rotation to avoid disruption [61].

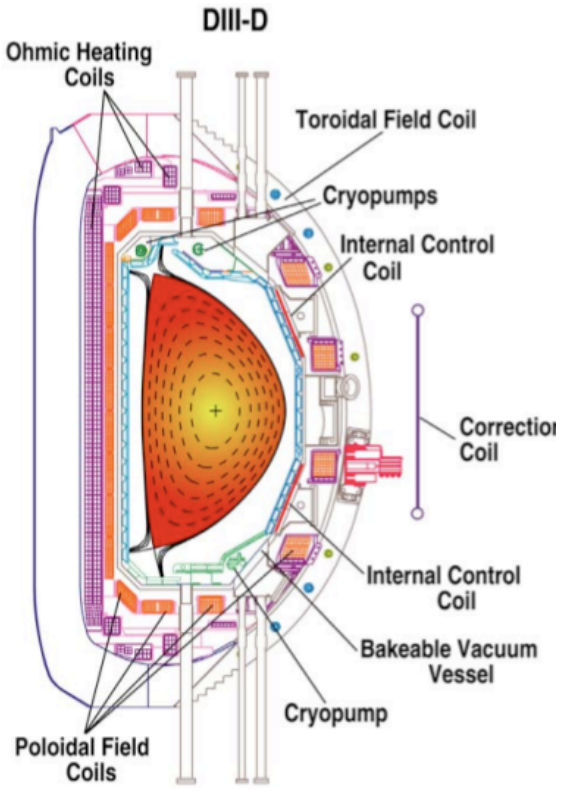

Figure 2.7: Cross-section view of the DIII-D Tokamak.

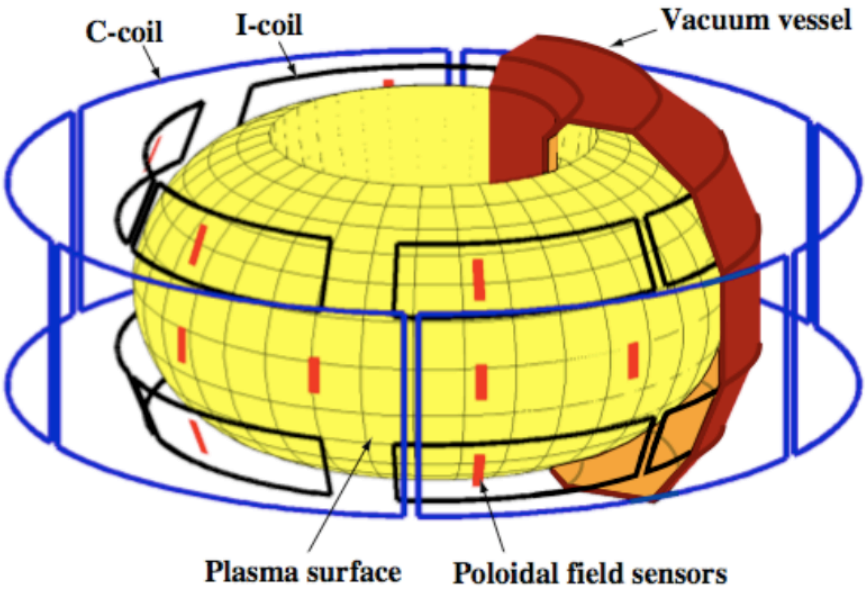

Figure 2.8: Locations of the C-coils and I-coils and poloidal magnetic field sensors used for magnetic feedback.

The first group of coils, that are shown in blue in Fig. 2.8 are named C-coils. They are located outside the vessel at the midplane. They can induce a radial magnetic field up to $15G$ at the plasma surface and they can apply magnetic perturbations with toroidal mode number up to $n = 3$. The second group, the so called I-coils, that are shown in black in the same figure, were installed in 2003. This is a set of 12 coils located between the vacuum vessel and the carbon tiles, six above and six below the midplane. The poloidal magnetic spectra that are applied with the I-coils can be modified by varying the toroidal phase difference between the currents in the upper and lower arrays. A further advantage in addition to the latter one, compared to the C-coils, is the improved coupling with the plasma, thanks to their closer proximity to it. The two coil sets can be powered using different power supply configurations that allow operation nearly up to the design current limits of $7kA$.

The magnetic probe sensors More than 50 poloidal field probes and radial flux loops are installed both inside and outside the vacuum vessel. The poloidal sensors normally used for MHD control are grouped in four couples located $180deg$ apart at $\phi = [67, 97, 127, 157]deg$. Radial magnetic field sensors are available as well. The DIII-D Tokamak magnetic diagnostic has been recently upgraded with further 101 magnetic sensors that allow resolution of toroidal

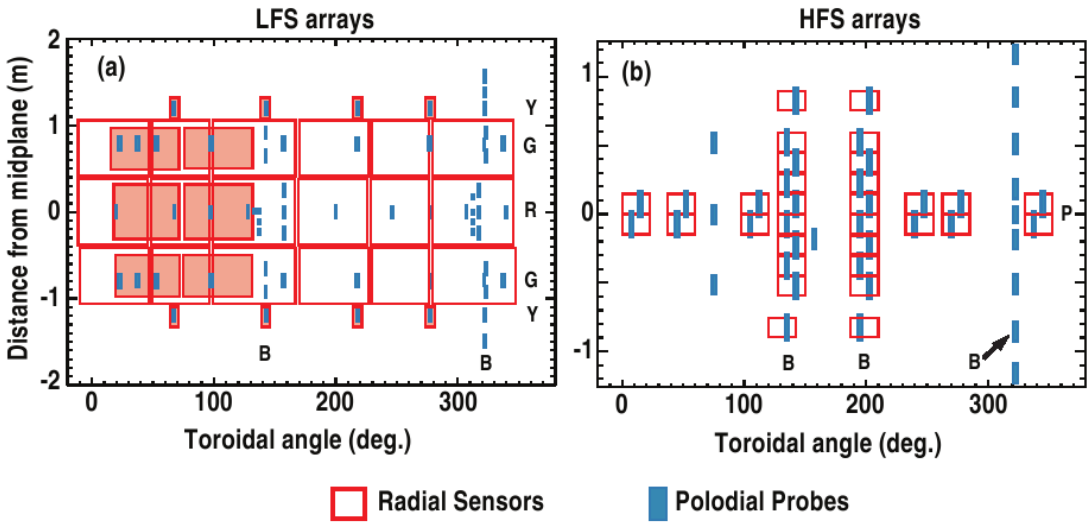

Figure 2.9: Vacuum vessel wall of DIII-D showing internal magnetic diagnostics relevant to non-axisymmetric measurement: radial field sensors (open rectangles), poloidal field probes (solid rectangles). The vessel wall is presented as unwrapped with the vertical axis representing the poloidal distance from the midplane for both (a) LFS and (b) HFS.(This figure is taken from [62]).

mode numbers $1 \leq n \leq 3$ [62]. The updated magnetic probe location is depicted in Fig. 2.9 that shows all the poloidal (blue) and radial (red) probes.

MHD control system It provides a state-of-the-art high-speed, digital control of the magnetic configuration and of various plasma parameters that influence the discharge performance. The system can control the plasma shape, density, pressure, current profile, and toroidal rotation, as well as perform feedback stabilization on the neoclassical tearing mode, resistive wall mode, and apply pre-programmed error field correction [59, 63].

Auxiliary heating systems Auxiliary heating and current drive in DIII-D are mainly provided by the Neutral Beam Injection system - NBI and the Electron Cyclotron Resonance Heating - ECRH. In the former 7 neutral beams are routinely used in most experiments to provide $14MW$ for $5s$ or $17.5MW$ for $3.8s$. The possibility to module the power sources in the co-I_p and counter-I_p directions allows both injected power and momentum to be continuously and independently controlled. ECRH consists of 6 $110GHz$ gyrotrons that can inject up to $3.5MW$ for pulses up to $5s$ in length. This system, that can provide also current drive like the NBI, is used for both

NTMs [64] and sawtooth control [65].

2.3 ASDEX Upgrade Tokamak

ASDEX Upgrade, that originated from an upgrade of the previous Axial Symmetric Divertor Experiment - ASDEX experiment, is one of the leading fusion experiments worldwide [66].

Vacuum vessel The plasma vessel is a self-sustaining rigid structure made of austenitic steel. It is composed of 16 D-shaped sectors and it allows to access the plasma through more than 130 ports. The original graphite tiles, that covered the inner vessel surface, were replaced with tungsten plasma facing components.

Axisymmetric coils A poloidal cross-section of the axisymmetric coils is sketched in Fig. 2.11. The inner poloidal field coil system is made up by the Ohmic heating coils, that are labelled OH1-2, and are used to induce the loop voltage necessary for the plasma breakdown. The toroidal field is induced by

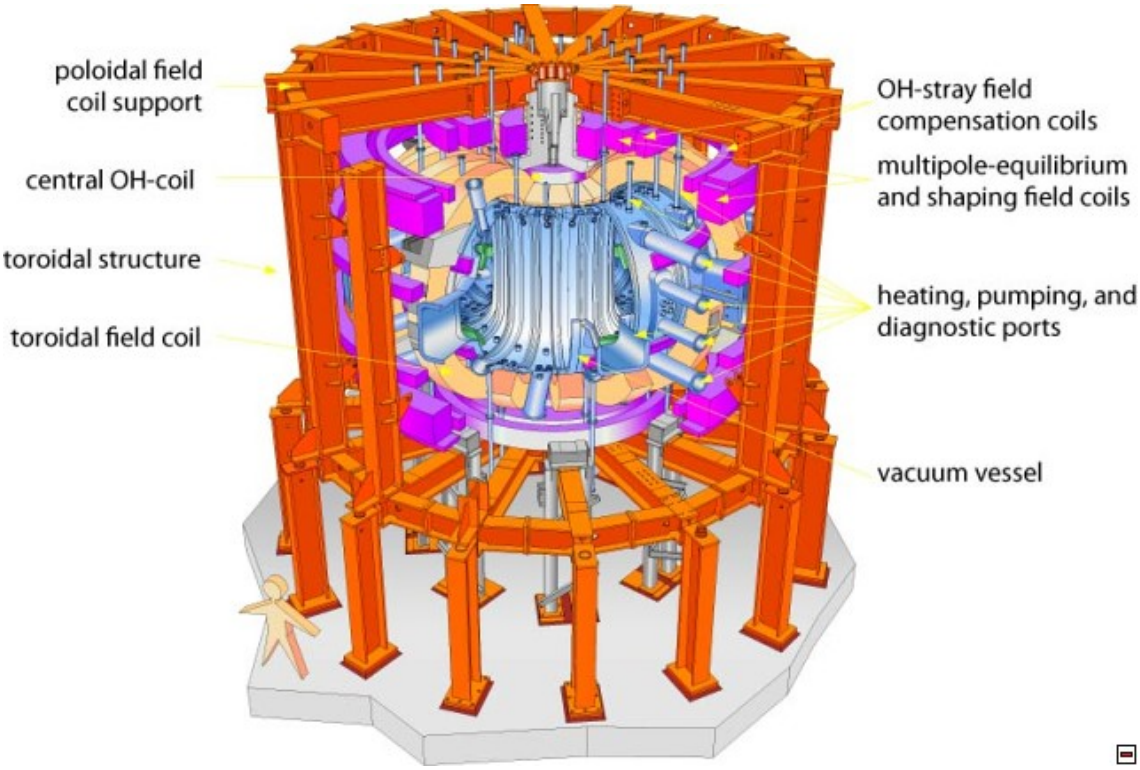

Figure 2.10: 3D view of the ASDEX Upgrade Tokamak. (This figure was taken from [67]).

Major radius R	1.65m
Minor radius a	0.5m
Maximum plasma current	0.6-1.2MA
Maximum applied toroidal field	3.1T
Flat-top time	10s
Core flux swing	9.5Vs

Table 2.3: Main parameters of ASDEX Upgrade machine.

16 double pancake coils that are housed, together with the cooling system, in the so called Turn Over Structure - TOS. These coils, that are shown in green in Fig. 2.11, are able to induce a stationary magnetic field up to $3.1T$ on the torus axis at $R = 1.65m$, while the toroidal field ripple amplitude at

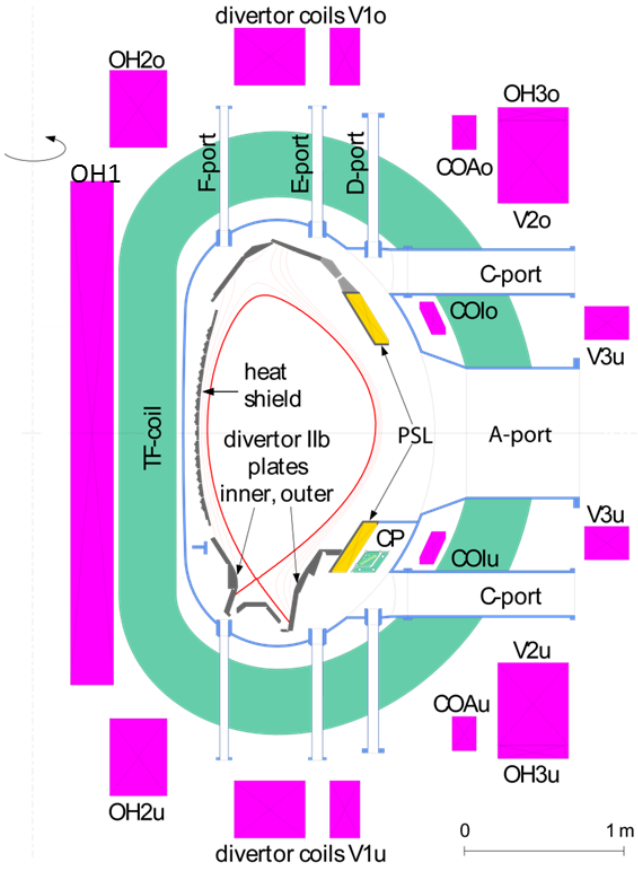

Figure 2.11: Poloidal cross section of the ASDEX Upgrade axisymmetric coil system (This figure was taken from [67]).

the outer plasma edge is 1%. The outer poloidal field coil system is used to control the plasma shape, its position and the divertor configuration. They are divided into two groups: the vertical field coils are tagged V1-2-3 while the remaining ones CoI, CoA, CoOH. Plasma movements on the timescale of $\sim ms$ are damped by a copper coil called Passive Stabilizing Loop - PSL.

Non-axisymmetric coils The 16 saddle coils are divided into two groups of 8 coils each, that are called BU and BI, respectively. They located in the upper and lower Tokamak midplane. These coils, together with the A-ones that have been proposed as a possible upgrade [68], are reported in Fig. 2.12. Both of them are 5-turn coils and can produce magnetic perturbations with toroidal mode numbers $n = 1, 2, 4$ either resonant or non-resonant inside the plasma.

The magnetic probe sensors The poloidal magnetic field is measured by 2 poloidal sets of 30 Mirnov coils each and by additional 6 coils located at different toroidal positions in the midplane, they are plotted in green in Fig. 2.13. The radial component of the magnetic field is measured by a toroidal

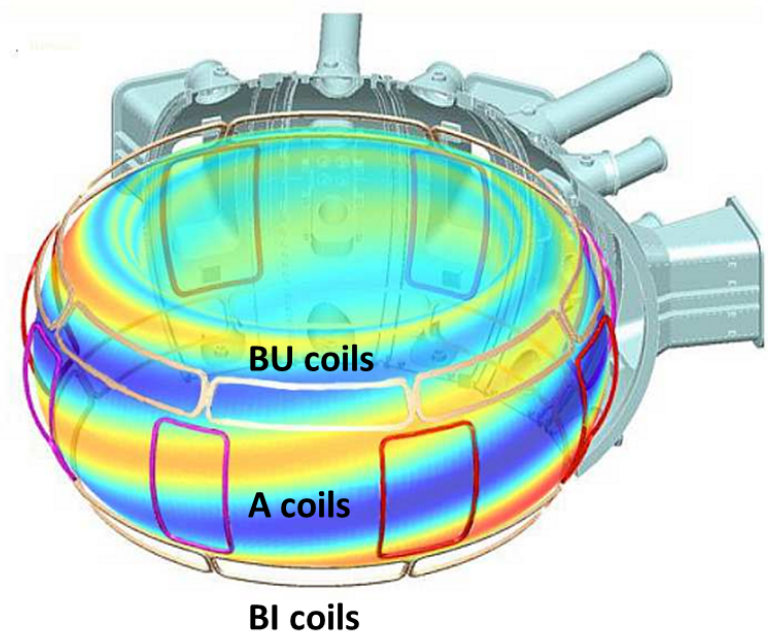

Figure 2.12: The ASDEX Upgrade non-axisymmetric coil system. (This figure was taken from [67]).

set of the so called BAL-coils, that are reported in red in the figure, and by 2 saddle loops located at the high-field side of the vessel.

MHD control system The MHD control system, that integrates multivariable feedback schemes, is embedded in the so called Discharge Control System - DCS, a digital control system that has many functionalities, from real-time diagnostic, to actuator management including load distribution schemes and powerful monitoring tools [69].

Auxiliary Heating System It includes Neutral Beam Injector - NBI and both Ion - ICRH and Electron Cyclotron Resonance Heating - ECRH systems. The former consists in two groups of four neutral beam sources each. In

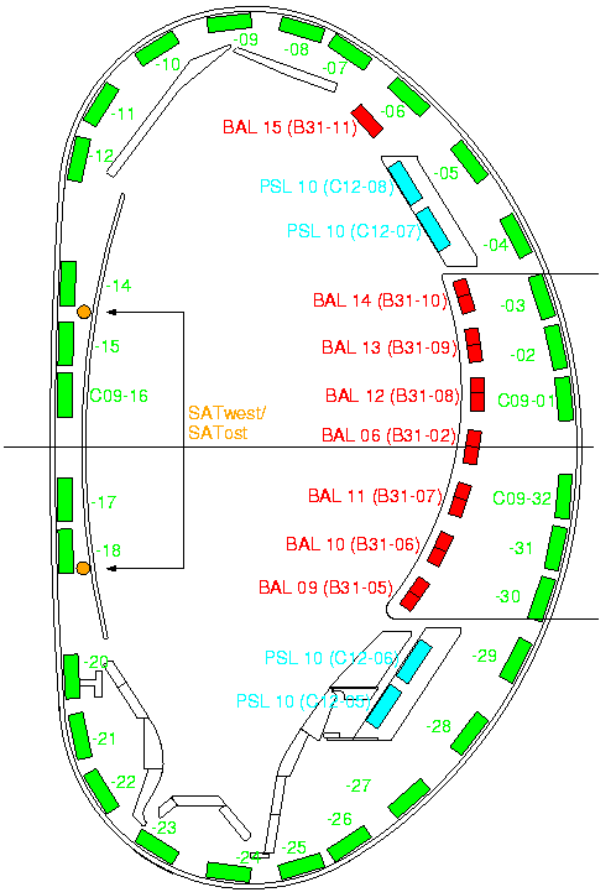

Figure 2.13: The ASDEX Upgrade magnetic sensor system. Poloidal magnetic field sensors (green), radial magnetic sensors (red) and the PLS coils (cyan). (This figure was taken from [67]).

Deuterium each source delivers a neutral beam power of $2.5MW$, thus the total installed neutral beam power is $20MW$ in Deuterium and somewhat lower at $13MW$ for Hydrogen. The ICRH supplies about $6MW$ to the plasma from 4 generators of $2MW$ each. The ECRH gyrotrons have similar power characteristic and they are designed to achieve a very localized heating and current drive deposition.

3

RFX-mod feedback control system in the new real-time MARTe framework

The entire RFX-mod feedback control system including both equilibrium and MHD control has been recently integrated in the real-time Multi-threaded Application Real-Time executor - MARTe framework, whose potentialities allow now to design and test new and more computationally challenging equilibrium shape and MHD control algorithms in a very flexible and efficient way. Hardware innovations in the real-time communication system have been introduced as well. This Chapter describes in particular the overall upgrade of the RFX-mod MHD control system, as well as the new magnetic feedback control schemes that have been developed during this Thesis work and made possible the experiments described in the following Chapters.

3.1 Hardware and software innovations of the RFX-mod real-time control system

The real-time control system that has been used since its beginning in RFX-mod was based on a C-procedural code and was initially implemented as a network of eight VME racks that handled about 700 input signals and produced around 250 reference waveforms. The latter drove the power supplies of the coils for the plasma position and the MHD control. This system used to operate at a rate of $2.5kHz$ with an overall latency of $1.5ms$. Over time new and more computationally demanding control algorithms have been developed and the system has been pushed to its limits [70]. Therefore a complete re-design has been carrying out since 2012 [52, 71, 72].

Both hardware and software innovations were introduced to get rid of the two main bottlenecks of the system, namely the limited processor power and the network communication latency, that was due to the distributed nature of the system. The upgraded system has then been exploited to develop and test new computationally challenging feedback algorithms based on the toroidal, poloidal and radial magnetic field measurements, whose sensors have been described in Chapter 2, to control the MHD stability of both RFP and Tokamak plasmas.

3.1.1. Hardware architecture: a brand-new multi-core server

In the updated version of the RFX-mod control system, a single multi-core server connected to Analog to Digital - ADC and Digital to Analog - DAC converters via fiber-optic bus extenders was adopted. This solution effectively reduced the communication latency, as it will be shown further on in this Chapter. This solution not only improved data exchange, that is now performed over shared memory, but also overcame the limit in processor power. The upgraded multi-core server can now keep pace with the rapid development of the technology and moreover it allows a wise distribution of the computational efforts through all the available cores.

Fig. 3.1 sketches the whole hardware architecture of the new RFX-mod control system including equilibrium and MHD control. The new system is based on a multi-core server hosting 12 $2.8GHz$ cores with $12GB$ RAM. The server is connected to 4 PXI racks via fiber-optics based bus extenders. In the original project, both VME processors supervising the data acquisition and the ones generating the

reference waveforms were supposed to be replaced with an equal number of cores for I/O management [72]. Due to budget restrictions, the former were temporarily retained and with them the latency of the transmission to the network of the raw packets of data. Nonetheless the original project is expected to be completed in the next future.

Two sets of DAC devices, hosted in two different PXI racks, drive the generation of the 192 reference waveforms for the active non-axisymmetric coils devoted to MHD control. The use of two different PXI racks in place of a single one allows to parellelize the generation of the output signals and to reduce the latency due to the DAC conversion time (0.6 μs for each channel). Other two PXI racks host the DAC devices for the generation of the reference waveforms for axisymmetric control, respectively. The data acquired by the old VME ADC devices include the measured radial, toroidal and poloidal magnetic field at the coil positions.

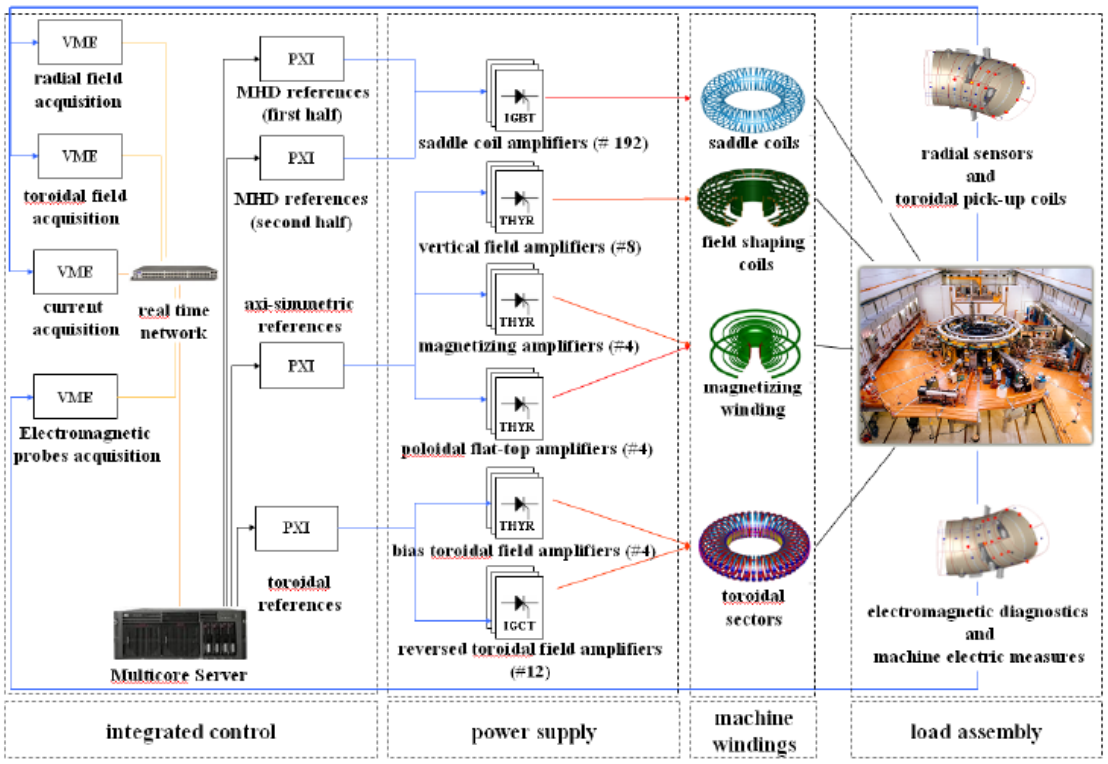

Figure 3.1: The hardware organization of the real-time control system of RFX-mod. (This figure is taken from [52]).

3.1.2. Software architecture: The MARTe framework for RFX-mod

The VxWorks software framework used in the previous control system was ported to real-time Linux, to take advantage of the real-time performances of this OS, the free cost license and the wider community of users. This choice, together with the necessity to manage the new hardware architecture, motivated the adoption of the Multi-threaded Application Real-Time executor - MARTe [52, 70].

MARTe provides a modular development environment for the design, the simulator and the implementation of real-time applications like control systems [73]. The appealing features of this new framework are its capability to maximize code reuse, its maintainability and portability without compromising the application performances. MARTe has been adopted in several fusion experiments. It manages the Vertical Stabilization and the Error Field Control Coils system - EFCC in JET, the plasma control system in COMPASS, the real-time tomography equilibrium reconstruction in ISTTOK and the Lower Hybrid - LH reflected power system in the FTU experiment [74].

New components, performing system-specific tasks, like management of I/O and control computation and the essential inter-thread communication, that was not natively provided by the MARTe framework, have been developed in RFX-mod [72]. These components manage the reception of the raw data packets over Ethernet and the generation of the reference waveforms via PXI DAC devices.

The basis of the MARTe framework is BaseLib2, a C++ multi-platform real-time library, while the bricks for MHD and equilibrium control are the so called Generic Application Modules - GAMs, that have been developed in RFX-mod as well. A GAM is a block of code that implements an interface specified in the BaseLib2 library. Each module is self-consistent because it has no awareness about the other modules, despite extensively exchanging data with them.

A module includes three communication points: one for the configuration of the processed data, one for the input and the last one for the output. In the initialization, that is performed before the real-time execution of the code, the modules declare which data are going to receive and to produce and how these signals are configured. This standardization of the I/O signals, that is known a priori, allows to chain all the independent GAMs. Their functionalities are wide, among them the interface with the hardware, the data acquisition and storage, the execution of algorithms, the ability to take decisions based on the current state of the system or the debug of the internal states.

3.1.3. Overall organization of the RFX-mod control code

MARTe is an Object-Oriented framework. As a consequence the code for the MHD and equilibrium control in RFX-mod has been organized into a hierarchy of classes that reflect the logic of this new real-time architecture [75]. Fig. 3.2 is a schematic picture of how the MARTe framework has been configured to provide the RFX-mod real-time control of both equilibrium and the MHD stability. The pillars of this configuration are four real-time threads that supervise the acquisition and pre-elaborate the signals from a large number of sensors. Two sets of 192 signals come from the radial and toroidal magnetic field probes, other 192 signals from the reference correction coil currents. A fourth set of 128 signals collect the data from other electromagnetic probes mostly used for equilibrium control. During this Thesis work 34 additional real-time signals, that come from an equal number of poloidal magnetic field sensors, have been embedded in the system as well, as it will be described further on.

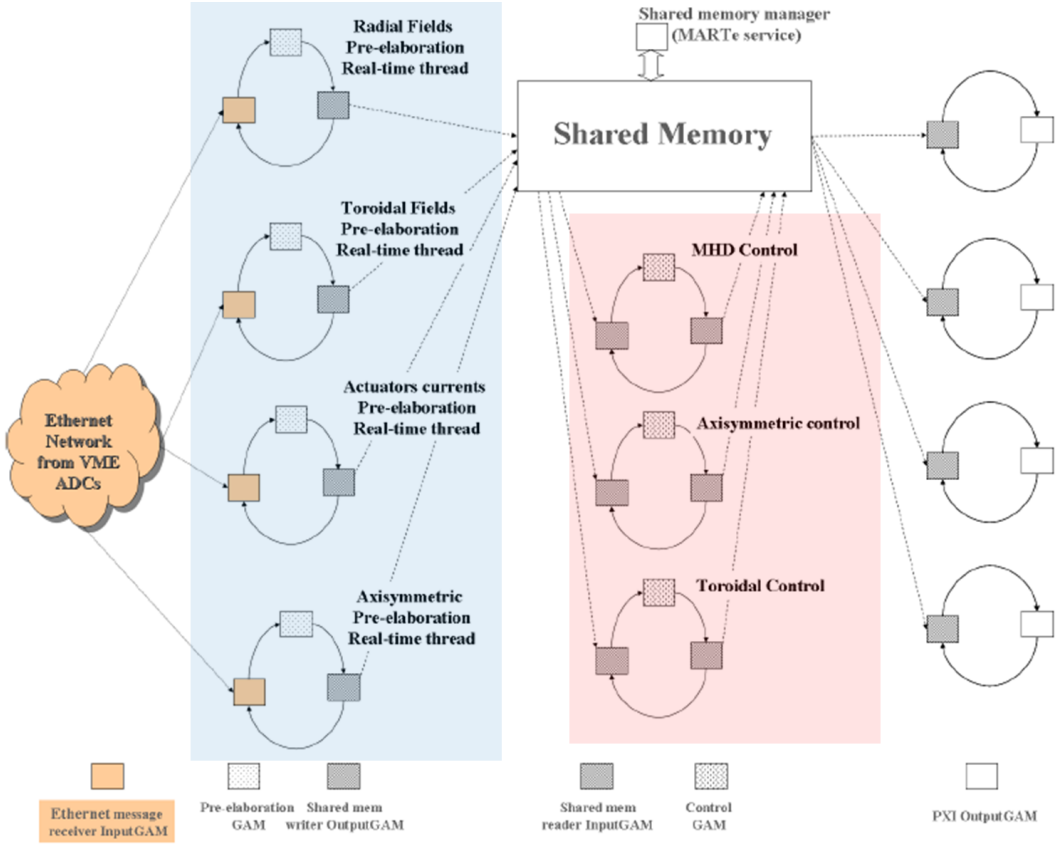

Figure 3.2: The MARTe configuration for the RFX-mod real-time control. (This figure was taken from [70])

Each thread is made up by three GAMs: an InputGAM, that is represented here with a yellow square, is devoted to monitor the network for incoming raw data packets that come from the ADC modules. A pre-elaboration GAM, the white square, conditions the signals that are eventually stored in the DATApool, a shared memory stack, by an Output-GAM, that is sketched with a grey square.

Three similar GAMs made up the core of the system, namely the three threads that guarantee the MHD, the axisymmetric and the toroidal field control. In this second stage the pre-elaboration GAM produces the inputs for the feedback algorithms, namely the spatial bidimensional Fourier components of the magnetic field measurements. The computed spectra corresponds to the circles labelled with *Equ, MhdBr, MhdBt, MhdI* in Fig. 3.3, that is a detailed zoom of Fig. 3.2.

The three control threads labelled *EquCtrl, TorCtr* and *MhdCtrl* prescribe the reference waveforms for the power supply system. Finally, the DAC conversion is performed by four PXI racks, each supervised by one of the four real-time threads in Fig. 3.2 on the right and the analog signals are then sent to the actuators.

3.1.4. Implementation of control algorithms: the RFX-mod MHD control thread

Fig. 3.4 blows up the red rectangle in Fig. 3.3. This figure is a simplified flowchart that summarizes the functionalities of the GAMs devoted to manage and exe-

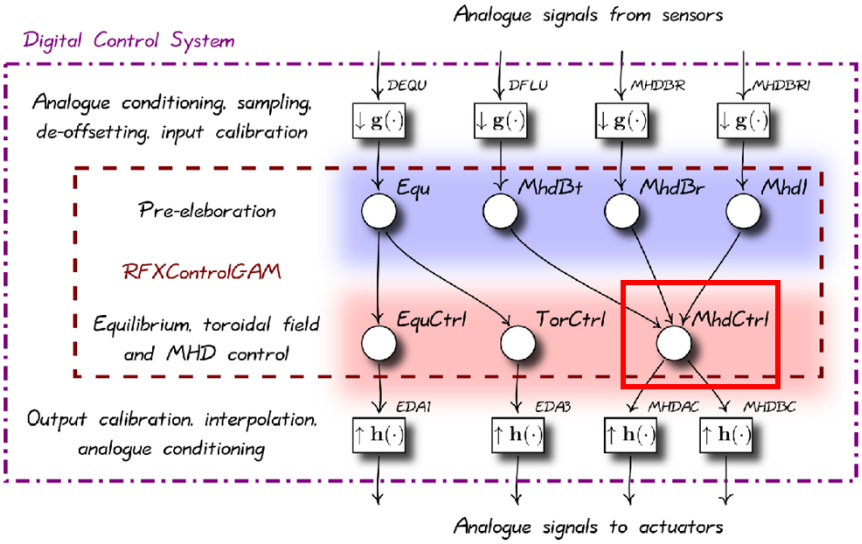

Figure 3.3: Data flow of the new RFX-mod control system. (This figure was taken from [70])

cute the MHD control algorithms. Thanks to the flexibility of the new MARTe framework, each of the 192 modes, that are obtained from the magnetic sensor measurements, can be processed with user-defined feedback algorithms.

Originally only two algorithms for the radial magnetic field component were available, namely the Raw Mode Control - RMC and the Clean Mode Control - CMC. During this Thesis work these control schemes have not only been integrated in the new MARTe framework, but also brand-new ones have been developed. The Plasma Response and the Double Shell Clean Mode Control are based on the radial magnetic field measurements, the Poloidal Control on the new poloidal magnetic field sensors that have been integrated in the framework during this Thesis as well. All these control schemes will be extensively discussed further on in this Chapter.

It is worth to note here that code redundancy is strictly avoided, thanks to the modularity of MARTe. For example, the cleaning of the sideband aliasing, that comes from the finite number of radial sensors, is performed in all the algorithms

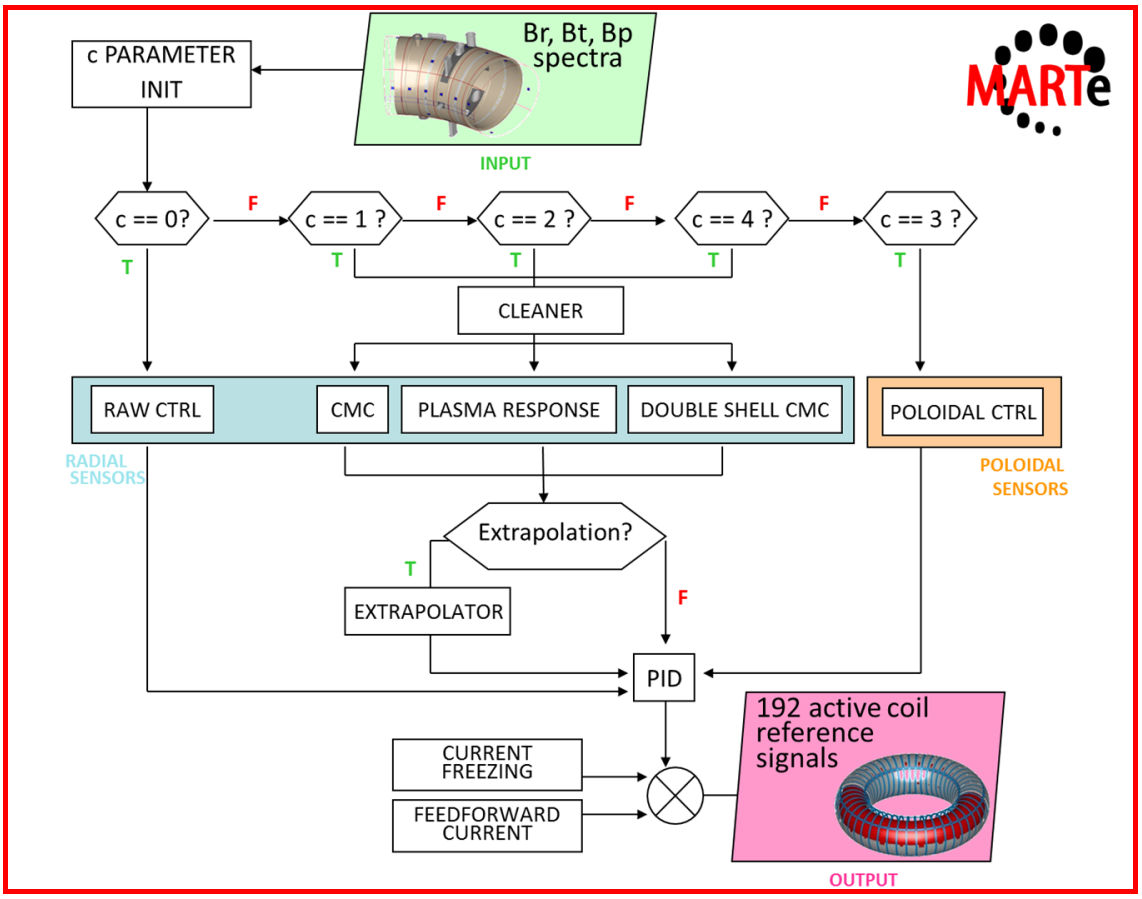

Figure 3.4: The RFX-mod MHD control flowchart.

that deals with the radial magnetic field by the same procedure called *Cleaner*. Similarly the *Extrapolator* evaluates the computed harmonics at an user-defined radial position, that can go from the plasma edge to the sensor location.

The MARTe flexibility allows to control simultaneously different magnetic modes with different control schemes, while the increased computational power, that comes from the new multi-core architecture, allows in principle to extend the magnetic feedback control over the entire radial magnetic field spectrum, namely 192 modes, without introducing significant delays in the real-time system, as it will be discussed further on in this Chapter. According to the selected MHD control scheme, the PID prescribes at each time step the 192 reference waveforms for the active saddle coils. These currents can be used not only to minimize the amplitude of the controlled modes but also to keep it at a finite value.

At present the RFX-mod MHD control system allows to configure a huge number of parameters, namely three sets of 192 proportional, derivative and integral gains and a cut-off frequency for a low-pass single pole Butterworth filter, that will be described further on in this Chapter, for each of the 8 time windows that can be set. At the very end of the chain pre-programmed current signals can be added to the reference ones.

3.1.5. Deployment of the MHD control thread

Besides the modularity and the flexibility, a further advantage of the MARTe framework is the possibility to simulate the whole coded project, or even a part of it, without interfering with the plant, where it is installed. This feature is essential for a phased commissioning, like the one that has been done to port the old RFX C-procedural control code to the new RFX-mod C++ object-oriented one.

In RFX-mod the commissioning of the entire code was carried out step by step during this Thesis work. In a first stage the new system was entirely tested offline by replacing the Input GAMs, whose action is to receive the raw data packets from the diagnostics, with simulation GAMs, that read the raw data stored in pulse files during previous plasma discharges. Thanks to the modularity of the framework, this replacement was the only change in the configuration for simulating the system. All the other components were exactly the same of the final control system, including the parameter readout and the storage of signals in dummy pulse files. Fig. 3.5 shows an example of this last appealing feature. The output of the simulation is stored in the #345900 bogus shot, that is fully equivalent to a standard

RFX-mod one. Thanks to this, both shots can be easily visualized with jScope, a Java tool for data visualization that is routinely used in the RFX-mod control room to monitor plasma parameters and signals during its operation. The figure, that is indeed a jScope snapshot, compares the output of the simulation, here plotted in red, with the original shot (#34590), in black. The simulated shot is a Tokamak discharge at $q(a) < 2$, whose stability is maintained by a pure proportional feedback control of the $m = 2,\ n = 1$ mode with poloidal sensors. The time history of the main plasma parameters, namely the plasma current, the edge safety factor and the electron density are plotted on the left column, while in the middle and the right one are reported the $m = 2,\ n = 1$ amplitude and phase of the coil currents, the radial magnetic field, that has been cleaned by the sideband aliasing, and the poloidal ones. The simulated and the real signals are extremely similar, as the zoom in the blue rectangle shows.

The RFX-mod control system has been tested incrementally, namely starting from a single thread with a single GAM and then adding all the other GAMs and the remaining threads, one by one.

In a second stage, the system has been activated in parallel with the old one

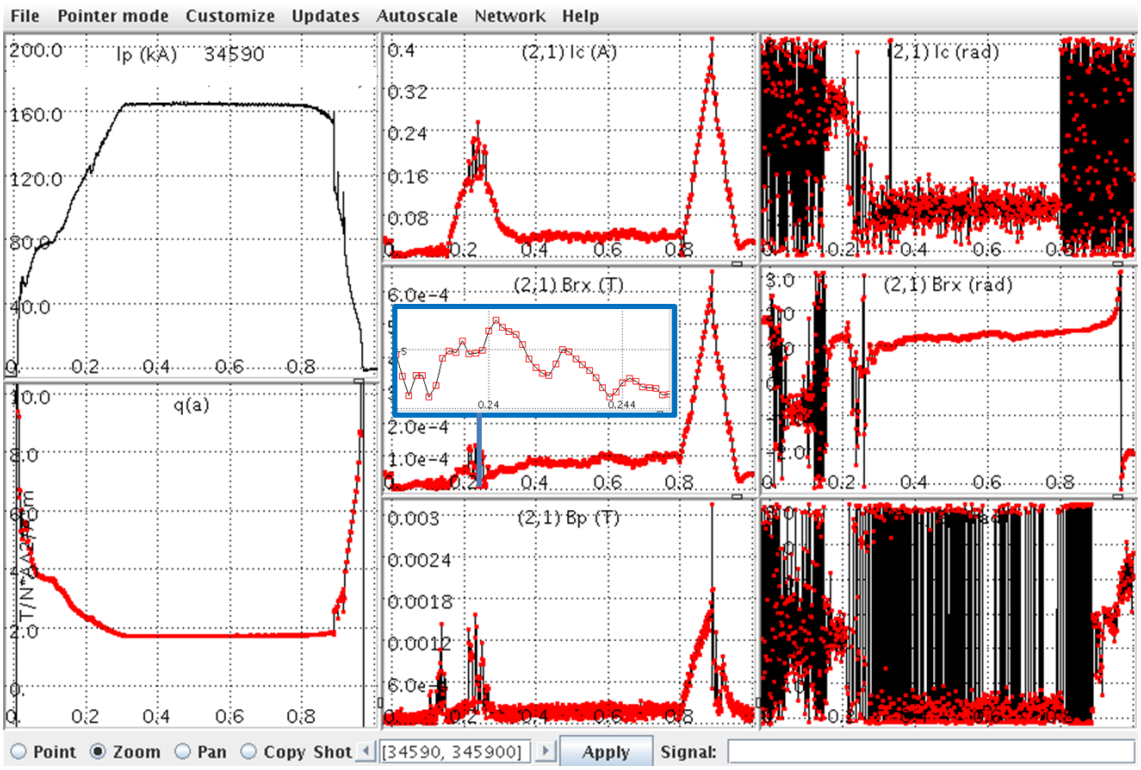

Figure 3.5: Comparison of a real (black) and a simulated (red) Tokamak shot in RFX-mod. The latter signals are the output of the MARTe simulator.

during standard operations, so that its output signals could be compared with the ones that it would have replaced. A series of commissioning shots have been performed in this preliminary phase of the migration from the old to the new control code. Thanks to the possibility to run the two codes simultaneously the output could be easily compared, as it is shown in Fig. 3.6. In this shot three rotating perturbations with finite amplitude and $m = 1, n = 6$, $m = 0, n = 7$, $m = 1, n = -7$ helicity were maintained by feedback controlling the corresponding raw radial magnetic field amplitude and phase. The amplitude and phase of the former perturbation are plotted in panel a) and b), respectively. The blue signals are the MARTe ones, while the red are computed by the old control system. A remarkable matching was obtained thanks to the extensive debug that was performed before the experimental commissioning.

In the last stage, the old control system was entirely substituted with the new MARTe framework and dedicated shots were performed to check all its functionalities and to characterize the new performances.

It is worth to note here that the MARTe simulator proves to be a really useful and essential tool whenever some brand-new code, a new GAM or its development for instance, needs to be embedded in the system. The possibility to debug

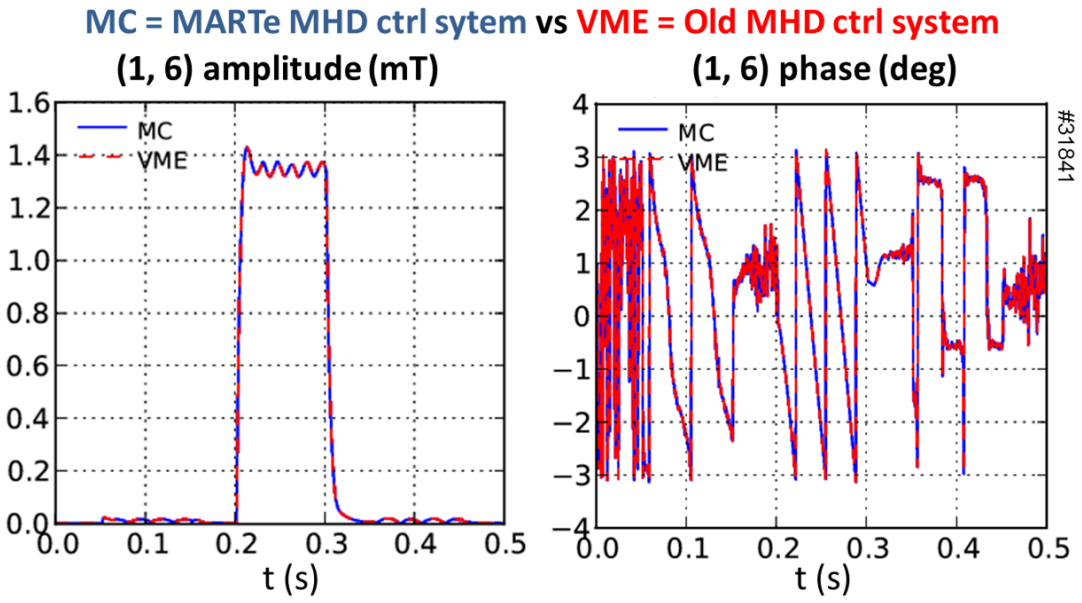

Figure 3.6: Comparison between the old MHD control system in red and the new MARTe one in blue. Amplitude and phase of a feedback controlled magnetic perturbation applied while both systems are running in parallel.

the code completely offline and to track all the possible bottlenecks in the data streaming and processing, allows to fully optimize the new algorithms and save both experimental time and power resources.

Timing and performance

Among the appealing features of the new MARTe frameworks, there is the possibility to monitor in real-time the execution times of each thread. The timing is measured by an internal clock, whose time lapses can be set by the thread triggers. This powerful tool allows to easily and promptly identify and locate a possible bottleneck and it suggests where the code needs to be optimized [76].

Moreover, latency, the ability to deliver a timely and regular response, is a critical aspect of any feedback control system [77] because it can cause a feedback loop to become noisy or unstable. The new MARTe framework reduces substantially this parameter in RFX-mod. The latency of the MHD control system in RFX-mod has been measured by evaluating the cross-correlation between the real-time coil current references and the corresponding offline signals, that are not affected by any delay apart from the one that comes from the data acquisition and storage. The real and imaginary part of both signals are plotted in the two panels on the left of Fig. 3.7, in red and black respectively.The two cross-correlation curves on the right estimate a delay of $\Delta t \simeq 0.95ms$ in both cases.

This analysis has been extended to an ensemble of shots that were performed both before and after the RFX-mod MHD control upgrade, as it is reported in Fig. 3.8. This figure shows that the upgrade allows a latency reduction of 30%. This value is expected to further reduce when the upgrade will be completed with the new acquisition modules.

3.2 Magnetic feedback schemes

3.2.1. New poloidal magnetic field sensors for real-time MHD feedback control

One of the most appealing features of MARTe is its user-friendly framework, that incredibly simplifies the development of brand-new control tools. As a demonstrative example, this Section will discuss the integration of a new feedback control scheme, from the magnetic sensor embedding to the final experiments, where Toka-

mak plasma discharges have been driven and sustained in the unstable $q(a) < 2$ regime.

In RFX-mod no measurement of the poloidal magnetic field component was available in real-time before this Thesis work. Tokamak plasma operation was always performed using the 192 radial sensors, as it was documented in Fig. 2.6 of Chapter 2. Nonetheless, poloidal sensors are largely used in Tokamaks, due to their better coupling with the plasma, as it will be discussed in Chapter 6.

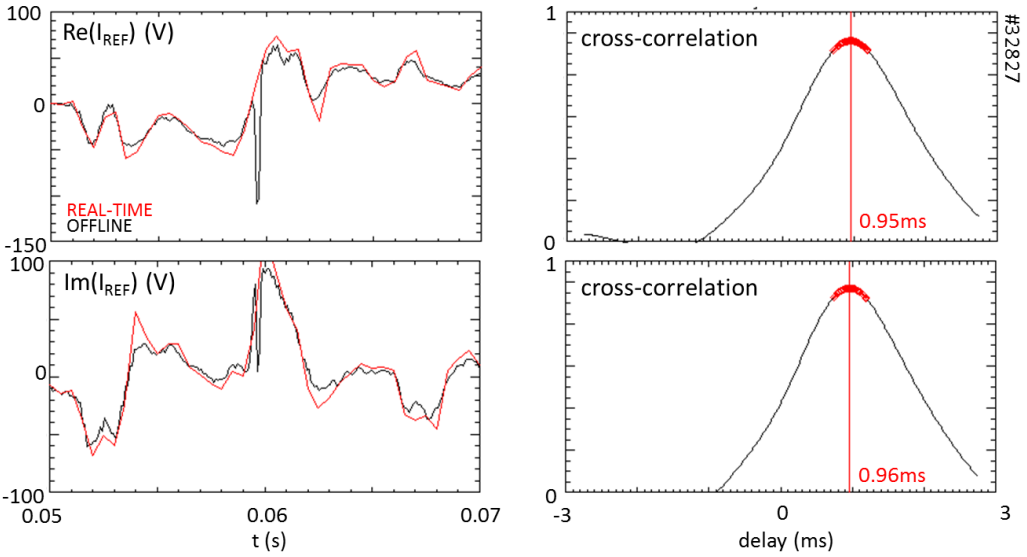

Figure 3.7: Real and imaginary part of a reference power supply signal on the left, cross-correlation analyses on the right.

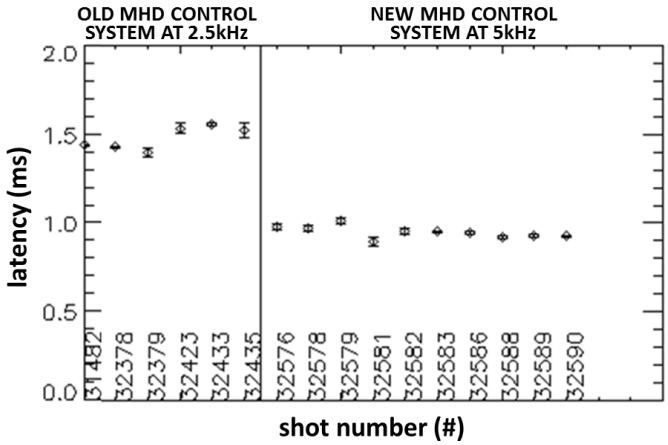

Figure 3.8: Latency of the MHD control system in RFX-mod before and after the introduction of the MARTe framework.

The new poloidal pick-up probes that have been embedded in the real-time framework are the 32 ones represented with coloured squares in Fig. 2.4. The sensors are distributed in four toroidal arrays of eight probes each. Due to engineering constraints, the toroidal arrays are not equally spaced thus the spectrum can not be computed with a straight Fast Fourier Transform - FFT algorithm.

The first step consisted in embedding the poloidal sensor measurements in the real-time framework. Since the poloidal magnetic field measurements can be useful both for the MHD and the magnetic equilibrium control the new signals were stored in the real-time thread of the toroidal field equilibrium that has been modified with all its GAMs to acquire, store and distribute among the other threads the new signals. The latter task is particularly useful since it minimizes the code redundancy and widens the data availability.

In the second step two C++ classes were implemented to process the raw data. The first class was devoted to perform a real-time DC compensation of the signals. Indeed if the magnetic probes are slightly tilted then they detect an unwanted pick-up field that is induced by the currents that flow in the toroidal field coils. The optimal correction eventually reads as:

$$B_\theta^{corr} = B_\theta^{raw} - C\langle I_\phi \rangle \tag{3.1}$$

where B_θ^{corr} is the compensated signal, B_θ^{raw} is the raw sensor measurement, $\langle I_\phi \rangle$ is the average of the currents that flow in the 12 sectors of the toroidal field coil system and C is an array of 32 coefficients, that can be configured as user-defined parameters. A further functionality of this class is the real-time correction of one of the poloidal sensor signals, the one at $\theta = 252deg, \phi = 322.5deg$, whose acquisition channel is corrupted. The signal is reconstructed as a linear interpolation of the two adjacent sensors, in the poloidal direction. Fig. 3.9 shows how the signals are conditioned by this first class. The figure reports the signals of the four poloidal magnetic sensors that are located at $\phi = 322.5deg$ and in the poloidal angular range $\theta = [207, 342]deg$. The blue and red curves correspond to the raw signals that are stored offline and in real-time, respectively. The corrupted signal is reported in the third panel. The green data are the output of the class discussed so far. It is worth to note here that the real-time correction can be negligible for some sensors but significant for others, like the one in the first top panel.

The second C++ class performs the computation of the magnetic harmonics. As anticipated, the sensors are not evenly spaced so a Discrete Fourier Transform

algorithm was implemented and a $\pi/2$ phase difference was hard coded to match the poloidal magnetic field harmonics with the active coils, that apply a radial magnetic field. The algorithm evaluates the amplitude and the phase of 12 modes namely the ones with $m = [0, 3], n = [0, 2]$. Fig. 3.10 reports the time history of the $m = 2, n = 1$ poloidal field amplitude during a Tokamak discharge at $q(a) < 2$. The green and the blue curves are the output of this second class with and without the signal conditioning performed by the first one. The comparison of the two outputs points out the necessity to pre-elaborate the raw poloidal measurements, indeed only the green signal shows clearly both fast tearing activity in the beginning of the discharge and the slower exponentially growth of the $m = 2, n = 1$ RWM as soon as the feedback control is switched off at $t = 0.8s$. Whereas the toroidal field

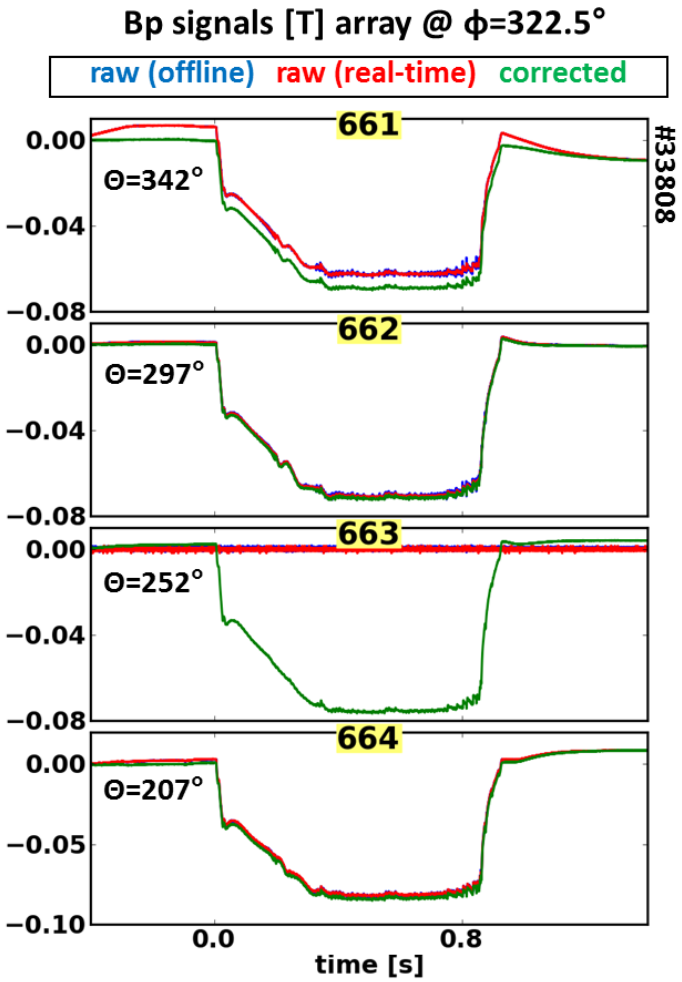

Figure 3.9: Real-time DC-compensation and correction of the poloidal sensor signals in RFX-mod.

pick-up completely masks this dynamics in the blue case.

The spectrum of the poloidal magnetic field is then stored in the shared memory DATApool, so that it can be further processed by both plasma equilibrium thread and the MHD control one. The former exploits it to control the plasma shape, the latter to maintain the plasma stability. The 12 poloidal modes add to the 192 radial ones in the range of the possible feedback variables that the PID will minimize.

The offline simulator allowed to monitor the data flow and the absence of unforeseen bottlenecks, while dedicated experiments were devoted to test and characterize the performances of the brand-new feedback control with poloidal magnetic sensors in circular Tokamak plasmas at $q(a) < 2$. Fig. 3.11 shows a proportional gain scan experiment that was performed by running RFX-mod as a circular Tokamak at $q(a) \simeq 1.8$, as panel a) shows. The $m = 2, n = 1$ component of the poloidal magnetic field was used as the feedback variable and the proportional gain was progressively increased in consecutive time windows, with the aim to find out the minimal value that stabilizes the discharge. The zoom that is reported in panel b) shows that this value is $K_p \simeq 6000(a.u)$ since in the corresponding green time window the RWM amplitude saturates, meaning that a stable regime is obtained.

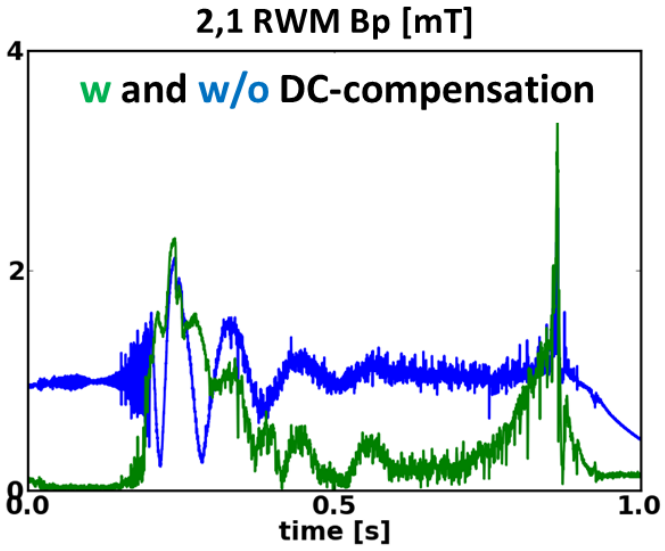

Figure 3.10: Shot: #33808. Time evolution of the $m = 2, n = 1$ poloidal magnetic field amplitude with (in green) and without (in blue) the real-time DC-compensation and correction of the raw poloidal sensor signals in RFX-mod.

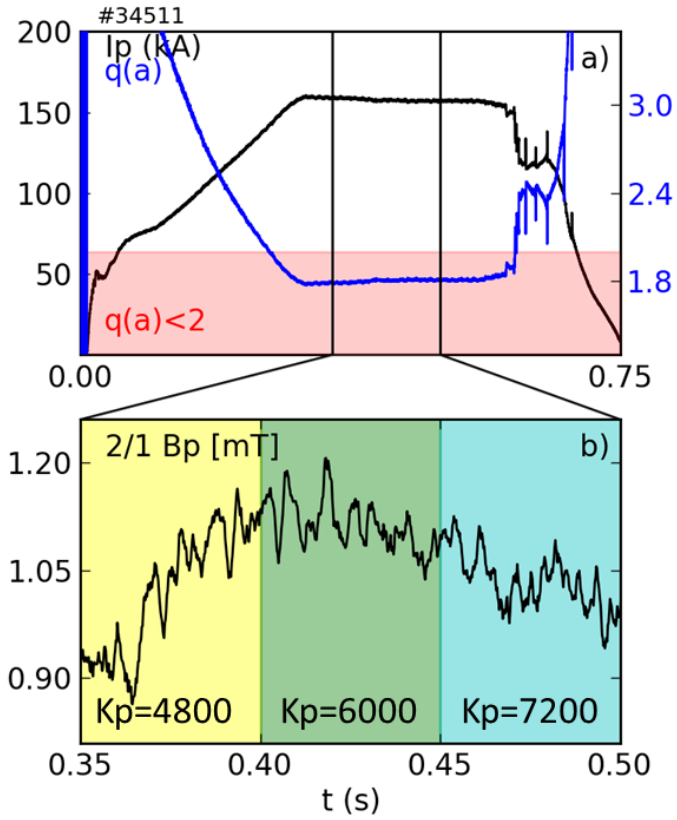

Figure 3.11: Proportional gain scan experiment with the poloidal feedback control in RFX-mod. Time evolution of a) the plasma current in black and the edge safety factor in blue, b) a zoom of the $m = 2, n = 1$ poloidal field amplitude and three consecutive time windows with increasing proportional gain values.

Due to coil safety constraints, the corresponding upper limit, namely the maximum proportional gain value that does not trigger a high-gain instability, could not be determined. However Tokamak discharges with K_p up to 40000 have been safely performed with no sign of instabilities. Finally, an optimized feedback control with poloidal sensors was obtained. Fig. 3.12 is a demonstrative example of it. A circular Tokamak discharge can be driven and maintained well above the current limit, since the brand-new control is able to quench both fast tearing mode activity and the $m = 2, n = 1$ RWM growth as soon as the $q(a) < 2$ threshold is overcome.

3.2.2. Feedback control schemes with radial and toroidal magnetic field sensors

In addition to the real-time feedback control with poloidal sensors, that has been extensively described in the previous Section, other control schemes that are based on the 192 radial saddle coil measurements are available in the RFX-mod control system, as it is sketched in Fig. 3.4. The raw mode control and the Clean mode control were ported from the old control system, while the Explicit Mode Control and the Double Shell Clean Mode Control, together with the Poloidal Control, have been embedded ex novo. In this Section an overview on these algorithms will be provided, while the experimental results will be discussed in Chapter 6

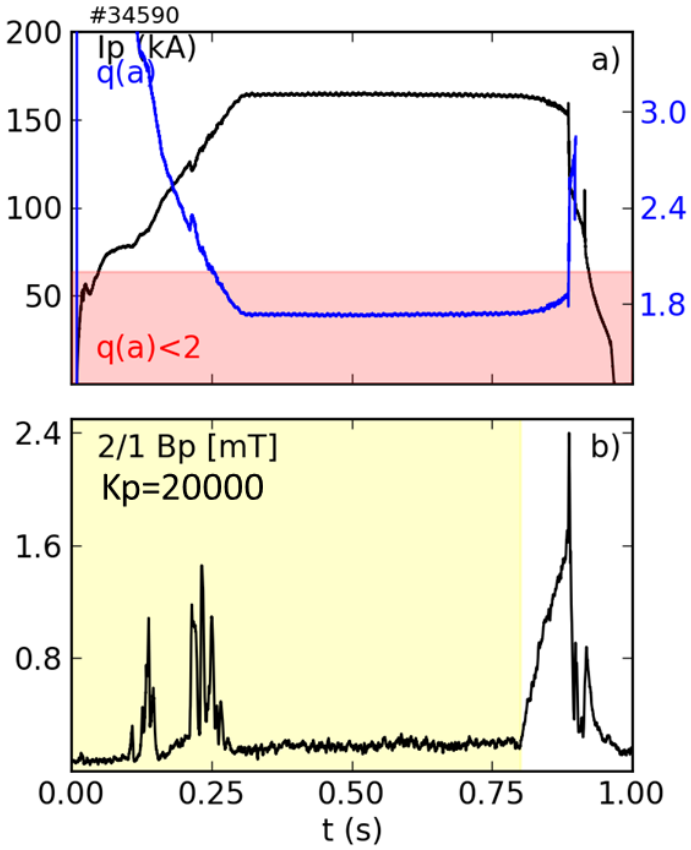

Figure 3.12: The brand-new feedback control with poloidal sensors guarantees the stability of a RFX-mod circular Tokamak discharge at $q(a) \simeq 1.8$. Time evolution of a) the plasma current in black and the edge safety factor in blue, b) the $m = 2, n = 1$ poloidal field amplitude and the yellow time window during which the feedback control is switched on.

Raw Mode Control - RMC

With this control scheme the variable processed by the PID is the spectrum of the radial saddle coil sensors, namely:

$$b_{r,DFT}^{m,n} = \frac{1}{MN} \sum_{i=1,Mj=1,N} b_r^{i,j} e^{-i(m\theta + n\phi_j)},$$

where $M = 4, N = 48$ are the number of the sensors in the poloidal and toroidal direction respectively and m, n the poloidal and toroidal wave number. In MARTe, the harmonics are evaluated using the Fastest Fourier Transform in the West - FFTW [78], that is a C subroutine library designed to compute the Discrete Fourier Transform - DFT in one or more dimensions, of arbitrary input size and of both real and complex data. The support for the code parallelization and the portability to any platform with a C compiler, were the bases on which it was chosen. Unluckily, the DFT harmonics are polluted by sideband aliasing, as it will be discussed in the next Section, thus this control scheme can not robustly maintain the plasma stability, because the perfect cancellation of the raw radial magnetic field does not correspond to the cancellation of the instability harmonics at the sensor radius, as it is discussed in [79].

Clean Mode Control - CMC

As it has been described in Chapter 2, the radial magnetic field sensors in RFX-mod are grouped in 48 toroidal arrays of 4 coils each, both evenly distributed on the torus surface. The sidebands above the Nyquist limit can not be resolved and thus they are aliased in the measurements of the lower mode number harmonics.

To overcome the aliasing problem, an algorithm that computes and subtracts the sidebands from the measurements has been implemented in real-time. The sidebands are estimated from the feedback coil currents, using a cylindrical model of the active coils. The sideband computation takes into account the copper shell as the only passive structure between the active coils and the plasma. To incorporate the additional shielding effect of the support structure, the shell time constant is artificially increased from $100ms$ to $124ms$. The sideband contribution can be evaluated as:

$$b_{r,DFT}^{m,n} = \sum_{\{l,k\} \in Z} b_r^{p,q}(r_s) f(p,q),$$

where $p = m + lM, q = n + kN$ identify the polluting sidebands and $f(p,q)$ is the shape factor that is due to the finite sensor geometry:

$$f(p,q) = \frac{sin\left(q\frac{\Delta\phi}{2}\right)}{q\frac{\Delta\phi}{2}} \frac{sin\left(p\frac{\Delta\theta}{2}\right)}{p\frac{\Delta\theta}{2}}.$$

Sidebands, in general, do not correspond to unstable plasma modes, thus their vacuum approximation, corrected from the shielding effect of the passive structures, is justified. The cleaned harmonics obtained in this way are used as the feedback variable of a control scheme, named Clean Mode Control - CMC. The latter reads as:

$$b^{m,n}_{r(r_s)} = \frac{1}{f(p,q)}[b^{m,n}_{r,DFT} + \sum_{\{l,k\}\in Z-\{0,0\}} b^{p,q}_c(r_s) f(p,q)], \tag{3.2}$$

where the time evolution of $b_c(r_s)^{p,q}$ is determined by the following equation:

$$\frac{dbc^{p,q}}{dt} = A^{p,q}[b^{p,q}_c + \lambda(m,l,n,k) I^{m,n}_{DFT}(t)].$$

The constants $A^{p,q}$ and λ are defined in [79], while $I^{m,n}_{DFT}(t)$ is the Discrete Fourier Transform of the coil currents. This equation, that describes the time evolution of the magnetic field, is discretized in the algorithm so that a new value is evaluated at each cycle. The feedback action is applied to cancel independently each harmonic, that can also be extrapolated at any radial position, between the sensor radius and the plasma edge one. To do so the toroidal magnetic field measurements are required as well, indeed the extrapolated harmonic at the radius r is evaluated as:

$$b_r(r)^{m,n} = \alpha^{m,n} I'_m\left(\frac{|n|r}{R_0}\right) + \beta^{m,n} K'_m\left(\frac{|n|r}{R_0}\right),$$

where $\alpha^{m,n}$ and $\beta^{m,n}$ are functions of the radial and toroidal magnetic field harmonics, as it is described in [55], while I'_m and K'_m are modified Bessel functions. The relative contribution of the sidebands and the effect of the extrapolation at the plasma radius are shown in Fig. 3.13. This figure reports the amplitude of the $m = 1,\ n = -7$ mode, that is the inner resonant one in the RFX-mod operating as a RFP. Its amplitude is maintained at a finite value by the feedback control. The raw harmonic, namely the one that is obtained by a straightforward Fourier decomposition of the 192 radial magnetic field measurements, is plotted in blue. The comparison with the green curve, that corresponds to the cleaned harmonic, highlights that the sideband contribution is about 30% in this discharge. The red

case represents the cleaned harmonic extrapolated at the plasma radius.

Explicit Mode Control - EMC

This feedback control algorithm is a good approximation of the plasma response control, namely the difference between the measured field harmonics and the ones produced by the active coils in vacuum. To achieve this together with the sideband cleaning, the sideband subtraction of Eq. 3.2 is extended also to the vacuum harmonic $m, n = 0, 0$. In Tokamak plasmas, the RWM stabilization can be achieved with this control scheme and radial magnetic sensors if the unstable mode has a low growth rate, whereas any constraint holds for the poloidal magnetic field ones [39]. The inefficiency of the radial magnetic field sensors with this control scheme was predicted by some theoretical model in RFX-mod [55] as well, but it has never been experimentally validated. This motivated the implementation of the EMC control scheme during this Thesis work.

Double Shell Clean Mode Control - DSCMC

The upgraded capability of the new control system allowed a refinement of the CMC algorithm, that could not be implemented before due to its demanding com-

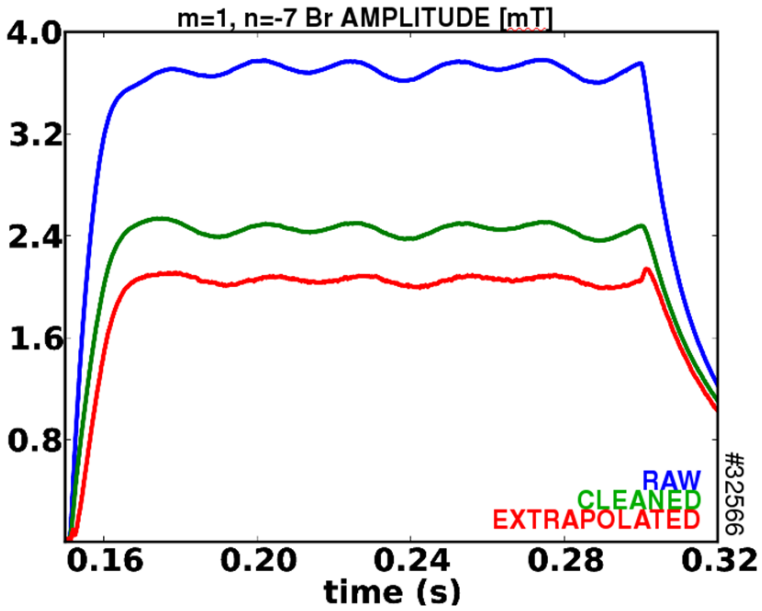

Figure 3.13: $m = 1$, $n = -7$ amplitude in the RFX-mod RFP, raw radial magnetic field harmonic (blue), radial magnetic field harmonic cleaned from the sideband aliasing (green) and extrapolated at the plasma radius (red).

putational effort. In this new algorithm, that has been implemented during this Thesis work, the sideband computation is performed by modelling the field shielding of the copper shell and the mechanical structure that supports the active coils, separately. Differently from the CMC, the sidebands computation reads as:

$$b_c^{p,q}(r_g) = \lambda_r^{p,q}[-Y_v^{p,q} + iX_v^{p,q}],$$

where $\lambda_r^{p,q}$ is a real constant and $X_v^{p,q}, Y_v^{p,q}$ are the real and the imaginary part, respectively, of the complex function that represents the magnetic field spectrum, whose time evolution is obtained by resolving the following coupled differential equations

$$\tau_v \frac{dX_v^{p,q}}{dt} = E_v^{p,q} X_v^{p,q} + E_{bv}^{p,q} X_b^{p,q}, \tag{3.3}$$

$$\tau_v \frac{dY_v^{p,q}}{dt} = E_v^{p,q} Y_v^{p,q} + E_{bv}^{p,q} Y_b^{p,q}, \tag{3.4}$$

$$\tau_b \frac{dX_b^{p,q}}{dt} = E_{vb}^{p,q} X_v^{p,q} + E_b^{p,q} X_b^{p,q} - \mu_0 L^{p,q} I_m(I_c^{m,n}), \tag{3.5}$$

$$\tau_b \frac{dY_b^{p,q}}{dt} = E_{vb}^{p,q} Y_v^{p,q} + E_b^{p,q} Y_b^{p,q} - \mu_0 L^{p,q} R_e(I_c^{m,n}). \tag{3.6}$$

The b and v subscripts refer to the copper shell and the mechanical structure, respectively. While the constants E_* model the interaction of the magnetic field with the conducting components. The time constants are $\tau_b = 0.024s$ and $\tau_v = 0.1s$, respectively. In addition, a different choice of the sidebands, compared to the standard CMC, that have to be subtracted, is performed. Indeed in the CMC control scheme the sidebands are evaluated up to the second poloidal order and to the first toroidal order for the $m = 1, 2$ modes only, for a total of 14 harmonics. In the new algorithm 20 sidebands are taken into account as Fig. 3.14 sketches.

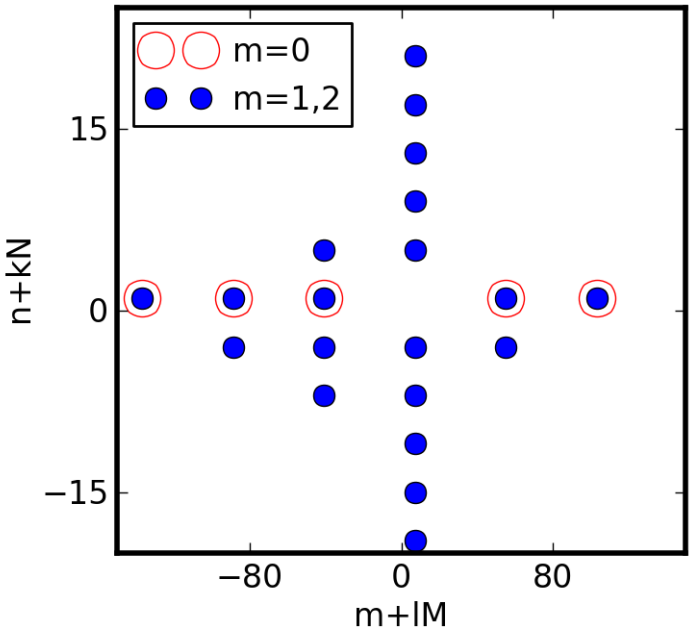

Figure 3.14: Sideband subtraction in the Double Shell Clean Mode Control feedback algorithm.

I

3D MAGNETIC FIELDS TO CONTROL THE MHD DYNAMICS IN TOKAMAK PLASMAS

4

Error field measurement in RFX-mod

Deviations of the machines structures and coils from a perfect axisymmetry, that can hardly be fulfilled in experiments, origin small non-axisymmetric magnetic fields that are called error fields. In general, the effects of these error fields are deleterious for the plasma stability and indeed they can lead to the formation of locked modes and the consequent reduction of the energy confinement or even to the plasma disruption. Therefore, it is essential to measure these error fields and to annihilate the components resonate most with internal MHD instabilities and that have the worst effects on the plasma performance. This Chapter describes how the error fields have been measured in RFX-mod circular and D-shaped Tokamak plasmas. The large number of correction coils in the toroidal direction made possible the use of proxy EF to validate in a clean way the EF measurement techniques against a known error field source.

4.1 Impact of error fields on Tokamak operation

The equilibrium magnetic field of a Tokamak is ideally toroidally symmetric, but unluckily slight deviations from the toroidal symmetry are always present in every device due to a wide range of unavoidable boundary imperfections. The latter can be the seeds of small non-axisymmetric magnetic fields that are commonly referred to as *Error Fields - EFs*. The typical magnitude of the EFs is generally of the order of $10^{-4}T$ in present day Tokamak experiments, but besides being a very small fraction of the equilibrium magnetic field, it can have disruptive effects.

One of the main contributions to the EFs comes from the misalignment and the shape imperfections of the axisymmetric field coils, like the poloidal or toroidal field ones. And indeed, the lowest order and the most effective $n = 1$ asymmetry can be simply induced by a shift and a tilt of the axis of a circular coil with respect to the symmetry axis of the Tokamak. The finite number of toroidal field coils, that induces a toroidal modulation in the magnetic field amplitude, known as *toroidal field ripple*, can contribute to the EFs, as well as asymmetries in the conducting structures, like gaps and portholes in the vacuum vessel. EFs can also have a dynamical nature, namely the electromagnetic and thermal forces that rise on the axisymmetric coils during plasma operations. Eventually, non-axisymmetric magnetic fields, that are intentionally applied to control or study the plasma instabilities, like magnetic perturbations that suppress the Edge Localized Modes - ELMs [60, 80] or that probe the long wavelength kink mode stability [81], are often referred to error fields as well.

The Fourier's harmonics of the error fields can then be divided into resonant and non-resonant components, according to the presence, or the absence, of a rational magnetic flux surface inside the plasma such that $\mathbf{k} \cdot \mathbf{B} = 0$, where $\mathbf{k}$ is the wave vector associated with the error field harmonic. Both components induce a non-axisymmetric displacement of the plasma magnetic flux surfaces but it deteriorates the energy confinement only in the resonant case. Indeed, the EF resonant components can trigger the magnetic reconnection of the field lines in the proximity of the displaced surfaces and, if the resulting magnetic islands become too large either in dimension or number, then an unaffordable loss of energy occurs and the plasma eventually disrupts. This process is called *mode penetration* [82]. In a rotating plasma, the currents flowing on the rational surfaces naturally shield the $n = 1$ component of the error field that attempts to drive the magnetic islands. These currents however originate a torque that slows the plasma rotation. When

the plasma is sufficiently braked, a loss of torque balance occurs and the dissipation of the shielding currents triggers a large stationary island. At higher values of β_N, the EFs can even be amplified if they couple to a marginally stable kink mode [83], like the RWM, in the so-called *resonant field amplification* - *RFA* [40].

Since the error fields are partially originated by the geometry uncertainties of the device, it is not possible to know them a priori. However several techniques have been developed to measure them. For instance, magnetic feedback control can be used to infer the component of the error field that couples with the marginally stable $n = 1$ kink mode, from the measure of its linear plasma response [84, 85]. In low-β plasmas the EFs involves the onset of a locked tearing mode, thus they can be measured with the so-called *compass scan technique* where an external $n = 1$ magnetic perturbation is ramped until the error field penetration triggers the growth of a locked mode [86]. This method has been applied in this Thesis work to measure the error fields in RFX-mod both circular and D-shaped Tokamak plasmas, as it will be described in the next Section. The error field can be estimated also from the measurements of the torque balance on a saturated magnetic island or from the braking of plasma rotation [87]. Eventually the amplitude modulation of the kink modes, that is observed when rotating magnetic perturbations are applied to plasmas [88], can be used as well.

Nonetheless it is important to bare in mind that it is not possible to achieve a full error field correction, even if one succeeds in perfectly measuring it. Indeed the active coils, that are devoted to their correction, hardly have the same geometry of the error fields, thus they can just compensate part of its components, hopefully those resonating most with the plasma.

4.2 Compass scan EF measurement approach

One of the most extensively used method to measure the error fields in a device is the so-called *compass scan*. This technique has been applied to measure the error fields in DIII-D [89], JET [90] as well as C-mod [91].

The method is based on the assumption that the locked-mode onset during the EF penetration process depends only on the amplitude of the total external non-axisymmetric field $\delta B_{ext} = \delta B_{app} + \delta B_{EF}$, that is the sum of the non-axisymmetric components of the externally applied magnetic field δB_{app} and the error field ones δB_{EF}. Therefore the critical threshold value of δB_{ext} should lay on a circle in

the complex $(Re(\delta B_{ext}), Im(\delta B_{ext}))$ plane. The error field is inferred from the possible shift of this circle that is obtained by measuring the critical amplitude of the applied field as it is ramped with several different toroidal phases. Interestingly, this method directly yields the coil currents that are needed to correct them, as well. This method is pretty simple and allows a straightforward measure of the error fields, but it has also some drawbacks. Firstly, it requires several reproducible discharges, at least three, thus it is a time consuming method. Secondly, it will not be feasible in ITER since a locked mode can eventually trigger a plasma disruption, and several of them can not be tolerated in ITER since local thermal loads during a plasma disruption can significantly exceed the melting threshold of divertor targets and first wall panels especially in high current operation [92].

Nonetheless in standard Tokamak experiments this method can be safely applied. Several compass scan experiments have been performed in RFX-mod both in circular and D-shaped single null Tokamak configurations to estimate the intrinsic error fields. Moreover, in this experiment the large number of non-axisymmetric coils in toroidal direction allows to apply known proxy error field, that can be measured with this technique to verify its reliability. The results of these experiments will be presented in the next two Sections.

4.2.1. Compass scan experiments in circular RFX-mod Tokamak plasmas

The error fields in RFX-mod running as a circular Tokamak have been measured at two low edge safety factor values, namely $q(a) \simeq 2.8$ and $q(a) \simeq 2.4$. In both experiments all the 192 active coils have been used to apply a $m = 2$, $n = 1$ magnetic perturbation with linearly increasing amplitude, in the former case the coil currents have been increased up to $6A$, while in the latter up to $5A$. In the latter regime the plasma response to the applied magnetic perturbation is expected to be higher because the plasma is closer to the $q(a) = 2$ stability limit [46]. In both experiments, the critical threshold for the error field penetration has been measured at a constant plasma density of about $n_e \sim 10^{19} m^{-3}$ and at different toroidal phases of the $m = 2, n = 1$ coil current perturbation, as it is required by the compass scan technique.

Fig. 4.1 shows the results of the compass scan experiment that was performed at $q(a) \simeq 2.8$. Panel a) reports the time evolution of the plasma current. The instant when the disruption occurs depends on the phase of the applied magnetic perturbation, as it is shown in panel b) together with the probing amplitude,

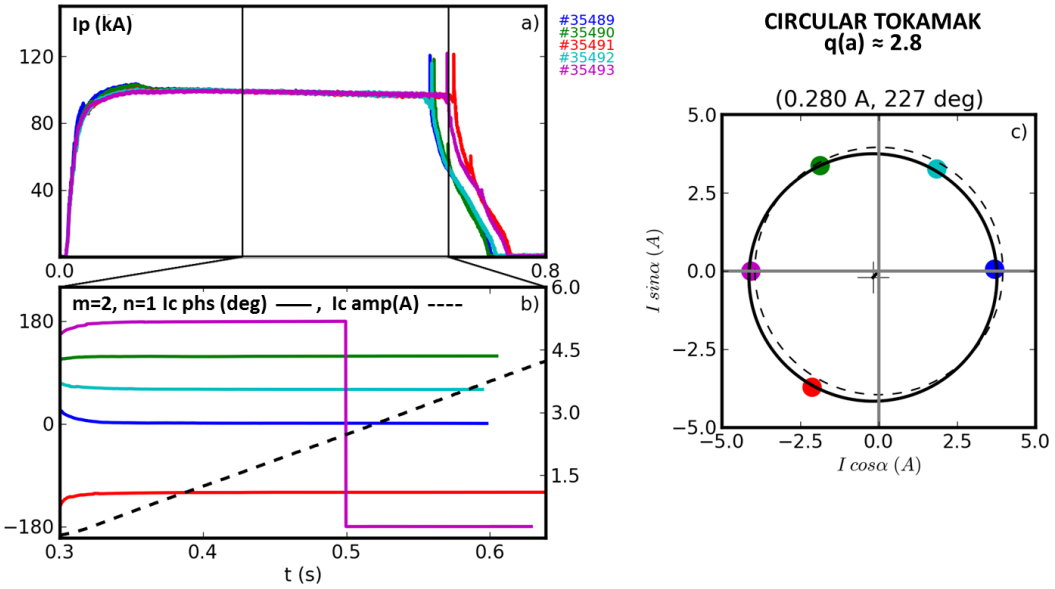

Figure 4.1: Compass scan in RFX-mod circular Tokamak at $q(a) \simeq 2.8$. Time history of a) the plasma current, b) the $m = 2, n = 1$ coil current phase and amplitude in the primary and secondary axis respectively, c) the compass scan analysis.

plotted with a black dashed line in the secondary y-axis.

The error field are inferred from the value of the coil current amplitude at the disrupting instant for the different phases. The compass scan analysis is reported in panel c). In the absence of any error fields the experimental points should lay on the dashed circle, that is centred in the origin. Due to the error fields, they define a new circle, the one represented with a continuous black line that has been obtained as a least square fit of the experimental data. The new centre of the circle gives an estimate the error fields, that in this case is pretty small, namely $0.280A$ at about $227deg$.

As anticipated, the error field measurement has been repeated at a lower value of the edge safety factor, namely at $q(a) \simeq 2.4$. Fig. 4.2 compares the error field measurement in the two experiments. The estimate of the error field is very similar in the two cases and it results to be $\simeq 0.3A$ at $\simeq 230deg$. It is worth to note here that in this lower q regime, the onset of the locked-mode, that eventually triggers the plasma disruptions, occurs at lower amplitudes of the $m = 2, n = 1$ coil current perturbation compared to the experiment at $q(a) \simeq 2.8$. This can be due to the plasma response that increases as the $q(a) = 2$ limit is approached [46].

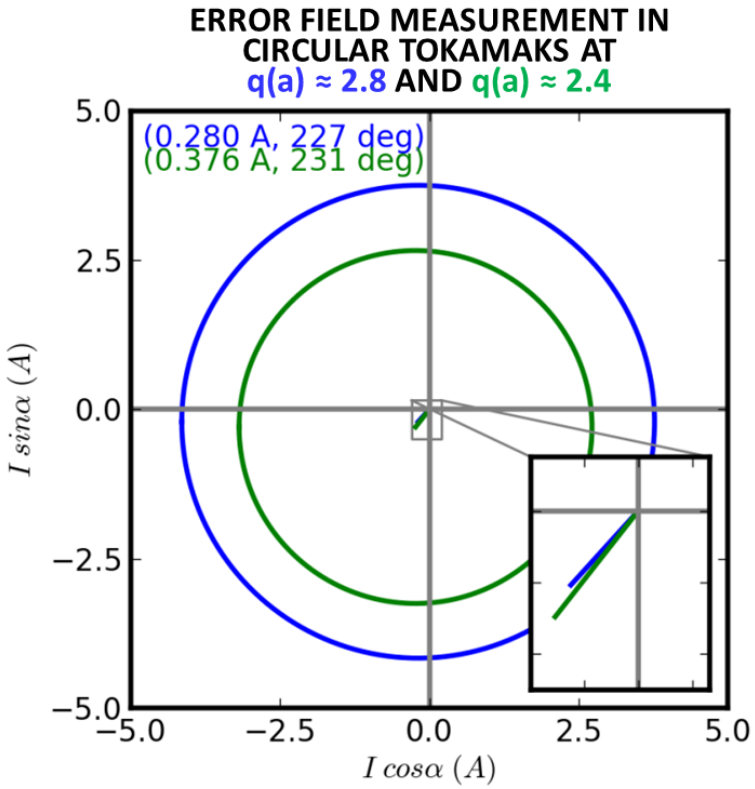

Figure 4.2: Error field measurements in RFX-mod circular Tokamak plasmas at $q(a) \simeq 2.8$ in blue and at $q(a) \simeq 2.4$ in green.

4.2.2. Compass scan experiments in D-shaped RFX-mod Tokamak plasmas

As it has been described in Chapter 2, RFX-mod has recently performed Tokamak discharges with single null D-shaped equilibria. This magnetic configuration can be obtained starting from the circular one either with pre-programmed currents or with a more sophisticated magnetic feedback controller. In the latter case a compass scan was performed at around $q_{95} \simeq 2.7$ and at a constant density of about $n_e \sim 10^{19} m^{-3}$ by applying $n = 1$ probing magnetic perturbations using only the active coils at the outer midplane to mimic a situation typical of modern Tokamaks where the error fields have geometries different from the non-axisymmetric coil one. Fig. 4.3 shows the results of the error field measurement for these Tokamak plasmas. It is worth to note here the accuracy of these compass scan experiments, where the error field penetration has been measured at 8 different toroidal phases.

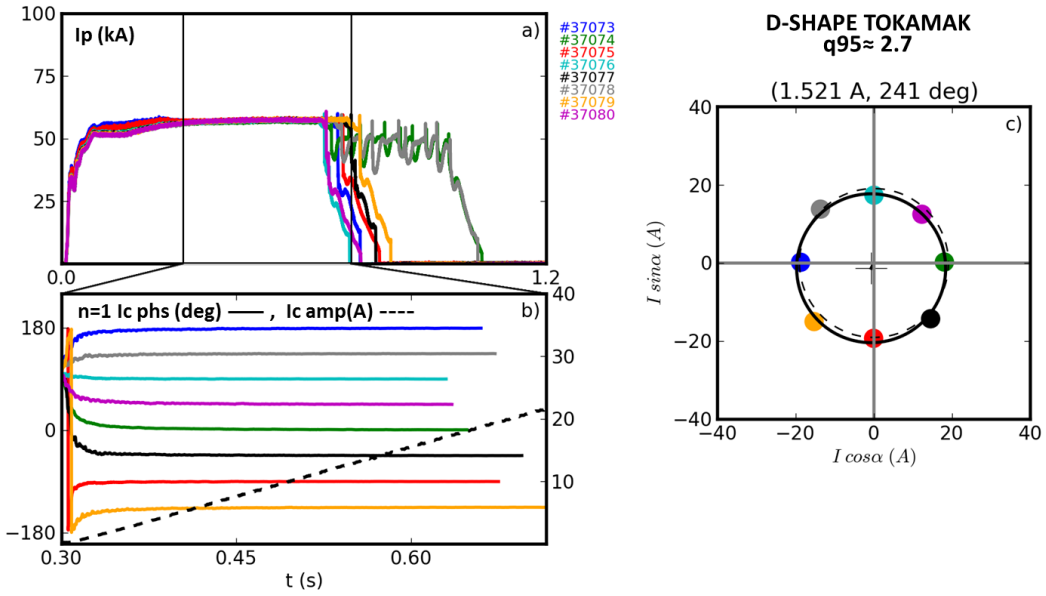

Figure 4.3: Compass scan experiments in D-shaped RFX-mod Tokamak plasmas, where the plasma shape is feedback controlled.

The estimate of the error fields is $1.521A$ at $241deg$. The phase of the error fields in this experiment is highly compatible with the one measured in the circular Tokamak compass scan experiments, meaning that the plasma response to the error fields in RFX-mod is not influenced by the plasma shape. Whereas, the error field amplitude in D-shaped Tokamak is larger than in the circular one because in the former case the estimate has been inferred from the $n = 1$ amplitude of the coil currents, rather than from the single $m = 2, n = 1$ harmonic.

4.2.3. Validation of the compass scan technique in RFX-mod

In order to verify if the compass scan is a reliable tool to measure the magnetic field asymmetries in RFX-mod, the large number of non-axisymmetric coils in the toroidal direction and the flexibility of its MHD control system have been exploited to re-configure the active coils to intentionally apply a couple of user-defined proxy error fields that have then been measured with this technique. Fig. 4.4 sketches how the proxy error fields have been applied in the two experiments. In the former, that is reported in panel a), the outer midplane coils both apply and measure the $n = 1$ proxy error field, while the remaining ones were switched off as the grey colour suggests. In the second experiment, that is depicted in panel b), the lower

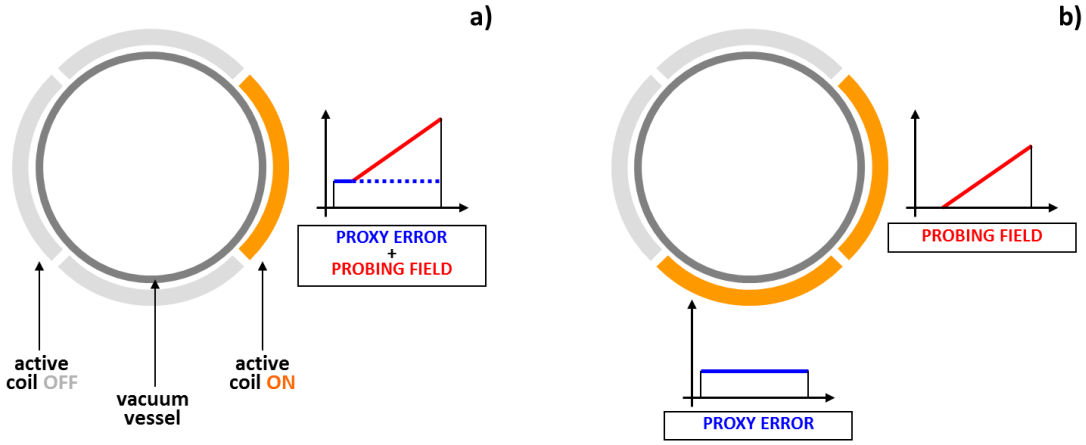

Figure 4.4: Sketches of the proxy error field measurements. The $n = 1$ proxy error field is applied and measured with the outer middle plane coils, in panel a), while it is applied with the lower plane coils and measured with the outer middle ones, in panel b).

active coils apply a $n = 1$ proxy error field with a $90deg$ phase, while the ones in the outer midplane probe it with the usual $n = 1$ increasing amplitude method. In both cases the $n = 1$ amplitude of the applied proxy error field is $10A$.

Fig. 4.5 reports the results of the experiments that are sketched in panel b) of Fig. 4.4. Panel a) reports the time evolution of the plasma current, while panel b) the $n = 1$ phase of the outer midplane coil currents, together with the amplitude that is plotted with a black dashed line. The circle, from which the proxy error field is estimated, is shifted of about $8A$ at $90deg$. The phase is compatible with the applied proxy error field.

Fig. 4.6 summarizes the results of the compass scan analyses for the two experiments. The former case is plotted in cyan, while the latter in orange. In both cases the amplitude of the measured proxy error field is slightly smaller than the applied magnetic perturbation. Besides this, the phase is compatible with the value set.

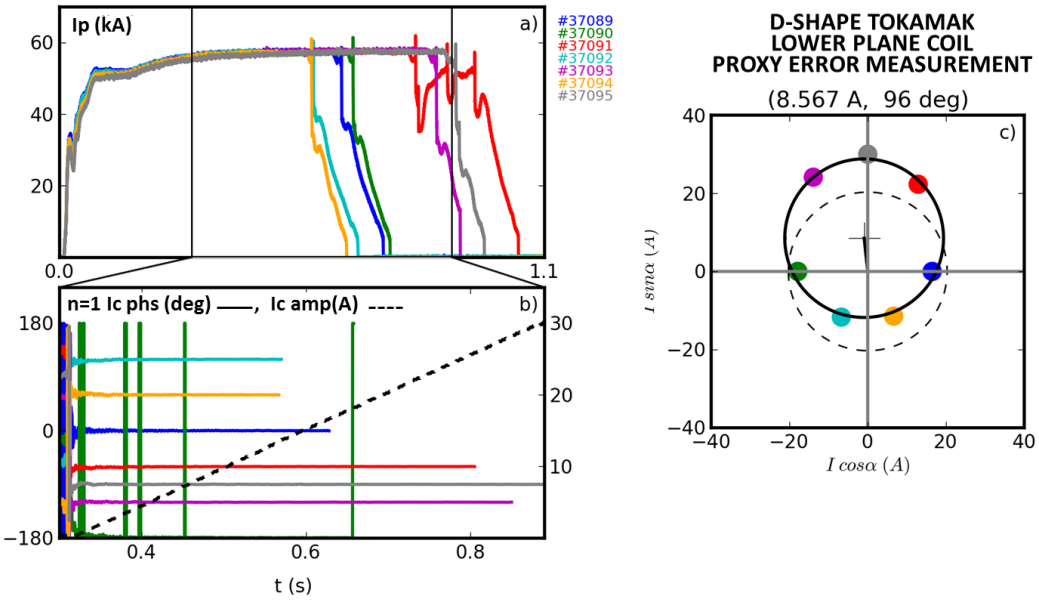

Figure 4.5: Compass scan measure of a proxy error field applied with the lower coils in RFX-mod D-shaped Tokamak. Time history of a) the plasma current, b) the $n = 1$ coil current phase and amplitude in the primary and secondary axis respectively, c) the compass scan analysis.

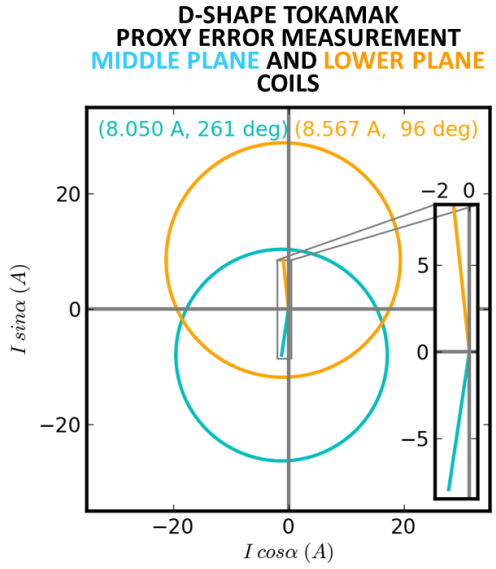

Figure 4.6: Compass scan with proxy error fields in D-shaped RFX-mod Tokamak plasmas.

5

Error Field Correction in RFX-mod Tokamak plasmas

The Dynamic Error Field Correction - DEFC approach, previously developed in high β plasmas, successfully avoids the error field penetration and the consequent onset of a pressure-driven RWM, revealing that this is a marginally stable mode in this regime. This technique, that consists in compensating the magnetic asymmetries with pre-programmed currents suggested by slow magnetic feedback, was tested for the first time in the RFX-mod in $q(a) < 2$ Tokamak plasmas. The experiments that will be discussed in this Chapter show that, differently from the pressure-driven RWM, the current-driven one is an intrinsically unstable mode that requires an active feedback control for its stabilization.

5.1 Dynamic Error Field Correction - DEFC technique

As it has been anticipated in Chapter 1, the active stabilization of a pressure-driven RWM in high β plasmas can be achieved if the non-axisymmetric coils are used to supply currents that minimize the $n = 1$ component of the error fields. In order for the feedback control with gain G to prescribe the correct coil currents for the error field symmetrization, both high proportional gain and decoupled sensors are needed, as it will be explained in the following. The measured plasma response, that is used as feedback variable, can be described as a linear amplification of the external field component that resonates with the kink mode, B_K^{ext}.

$$B^{pl} = \alpha B_K^{ext}, \tag{5.1}$$

where α is the complex proportional constant that takes into account an eventual toroidal phase shift between the external EF and the plasma response. This value can then be used by a proportional feedback controller to prescribe the currents I_c that nullify the plasma response:

$$I_c = -GB^{pl}. \tag{5.2}$$

All the resonant components, both those of the error fields and the ones of the field applied by the non-axisymmetric coils, are amplified by the plasma. If one describes the latter contribution with an effective mutual inductance $M_{K,c}$, then the external field component resonant with the kink mode reads as:

$$B_K^{ext} = B_K^{EF} + M_{K,c} I_c. \tag{5.3}$$

Once the feedback loop is closed, the coil currents can be described as:

$$I_c = -\frac{G\alpha}{1 + G\alpha M_{K,c}} B_K^{EF}. \tag{5.4}$$

If the proportional gain is large enough, $G \gg 1$ then the feedback currents are potentially able to completely annihilate the kink mode resonant component of the external field $B_K^{EF} = -M_{K,c} I_c$.

The sensor decoupling is necessary to fully compensate the error fields. Indeed if one models the coupling between the magnetic sensors and the active coils with a coefficient $\epsilon = [0, 1]$ then its contribution modifies Eq. 5.3 as:

$$B_K^{ext} = B_K^{EF} + M_{K,c} I_c + \epsilon M_{K,c} I_c. \tag{5.5}$$

Solving for the coil currents, as it has been done before, one obtains:

$$I_c = -\frac{G\alpha}{1 + G\alpha(1+\epsilon)M_{K,c}} B_K^{EF}. \tag{5.6}$$

If the coupling between the sensors and the active coils is negligible, $\epsilon \approx 0$, then the solution that has been discussed above still hold. But if $\epsilon \sim 1$ and the proportional gain is large enough, $G \gg 1$, then $I_c = -B_K^{EF}/2$, namely the error field correction with coupled sensors is only able to compensate half of the error field.

In DIII-D the decoupling is achieved by measuring the plasma response with the poloidal sensors that are installed in the outer midplane . The error field amplification is counteracted with the I-coils. This approach is successful because these sensors are geometrically decoupled from the non-axisymmetric coils and they are also DC-compensated to minimize the residual coupling [93].

Arbitrarily large proportional gain values can not be used in any feedback system due to the high gain instability. However, the effect of an infinite proportional gain can be obtained with finite ones if the minimization of the feedback variable is somewhat helped. In the so called *Dynamic Error Field Correction - DEFC* technique [40], that has been developed in DIII-D, pre-programmed currents, that are evaluated as time averages of the feedback ones, are iteratively added in feed-forward while the feedback control is switched on to achieve a a progressive error minimization. This process lastly converges to the prescription of highly optimized error field correction currents.

5.2 Error field correction in low-q RFX-mod circular Tokamak plasmas

Reproducible current-driven RWMs in low-q Ohmic discharges provide a simple system where to study RWM control issues, as well as a challenging testbed for those MHD control schemes that are originally developed to counteract the pressure-driven ones. Indeed similarly to the high β limit, the $q(a) < 2$ one is set by an ideal kink mode that eventually evolves into a RWM, as it has been experimentally verified both in RFX-mod [46] and DIII-D [57]. All these analogies suggested to test the Dynamic Error Field Correction technique in the RFX-mod Ohmic circular Tokamak at $q(a) < 2$.

It is worth to notice here that, while the interaction between the $n = 1$ component of the error fields and the RWM onset has been extensively investigated in high β plasmas, due to the significant relevance of this operational regime, a similar study in low-q plasmas has never been carried out before this Thesis work. Nonetheless, plasma operation at low-q values offers a different ground where the inner plasma physics of this instability can be investigated. Of course, the high β and the high current limit have their own peculiarities but, thanks to their similarities, the optimization of the plasma performance in one regime can benefit from the advance in the plasma physics achieved in the other.

These premises motivated experiments in RFX-mod with the aim to understand, and possibly to characterize, the role played by the error fields in settling the current limit, if any exists. Indeed, similarly to the high β regime, the $m = 2, n = 1$ RWM, that routinely appears as soon as the safety factor approaches 2, could be originated by the resonant amplification of the $n = 1$ error field component. The experiments that will be described in the following will reject this hypothesis.

5.2.1. "Current-Freezing" technique

The error field correction in RFX-mod was carried out with the so called *current freezing* approach. This technique was designed to investigate the role of the error fields on the onset of the current-driven RWM in a more straightforward way. In this method, the magnetic feedback control is used to drive the plasma above the current limit and to sustain its stability till stationary plasma conditions are reached. At this point, the feedback control is switched off and its action is replaced by the pre-programmed currents that are obtained as an average of the feedback ones over $50ms$ before its turning off. Since the error fields have components that specifically depend on the plasma dynamics itself, this method allow to apply exactly the correction that the plasma asks for.

Initially, 192 radial magnetic field sensors have been used during the feedback controlled phase of this technique. The result of one of these experiments is reported in Fig. 5.1 on the left. Panel a) reports the time history of the plasma current and the edge safety factor, that is maintained at $q(a) \simeq 1.8$ during the whole discharge. The Clean Mode Control feedback algorithm, that has been introduced in Chapter 3, has been used to control the fast tearing mode activity in the initial part of the discharge, as it has been described in Chapter 2, as well

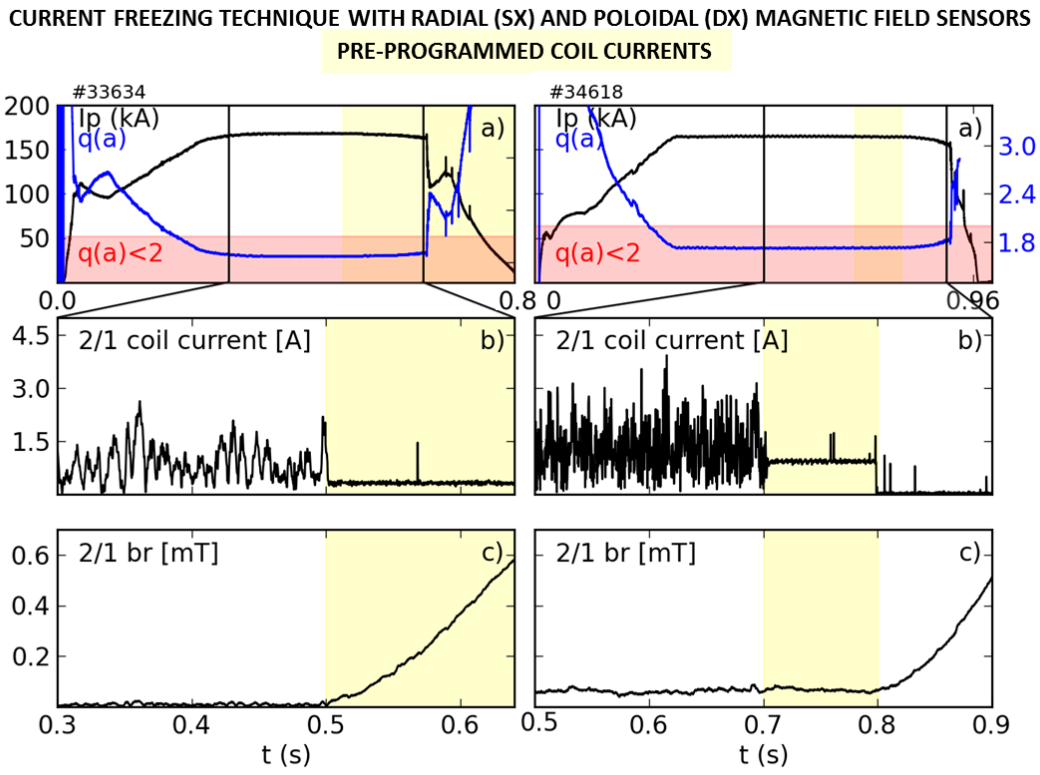

Figure 5.1: Error field correction in RFX-mod with radial (on the left) and poloidal (on the right) magnetic field sensors. Time evolution of a) the plasma current (in black) and the edge safety factor (in blue), b) the $m = 2, n = 1$ component of the coil currents, c) the $m = 2, n = 1$ component of the radial magnetic field. Pre-programmed currents replaces feedback ones in the time interval highlighted in yellow.

as to maintain the plasma stability until $t = 0.5s$. In the interval $t = [0.45, 0.5]s$ the MHD control system stores the coil current signals and evaluate their mean value, that will be applied as pre-programmed currents from $t = 0.5s$ on, as it is highlighted in yellow. As soon as the magnetic feedback control is switched off at $t = 0.5s$, the $m = 2,\ n = 1$ starts growing exponentially. This evidence could suggest that the current-driven RWM is an intrinsically unstable mode or that the error fields were not completely corrected. This second hypothesis was supported by previous DIII-D experiments in high β plasmas, where the inefficiency of the radial magnetic sensors with the DEFC technique was proved to depend on the sensor coupling to the coils [40]. As far as the validation of the DEFC technique is concerned, this result was encouraging and motivated further experiments to put light on this open issue.

Once the new thick array of poloidal magnetic field sensors has been integrated in the real-time framework, as it has been described in Chapter 3, the same experiment was repeated using the new probes. The result is reported on the right column of Fig. 5.1. In this case the MHD control system starts to store the time history of the coil currents at $t = 0.65ms$ and a time average over the next $50ms$ is computed, as in the previous experiment. The so obtained pre-programmed currents are supplied by the power system as soon as the feedback control is switched off, namely from $t = 0.7ms$. The time evolution of the $m = 2, n = 1$ component of the coil currents is shown in panel b) on the right, where the current freezing gap is highlighted with a yellow path. It is worth to note here that, differently from the previous experiment, a significant noise affects the feedback current signal, whose high frequency fluctuations are further amplified by the feedback high proportional gain. Nonetheless, as right panel c) shows, the frozen currents seem to apparently prevent the $m = 2, n = 1$ RWM growth for $100ms$, that corresponds to twice the RFX-mod shell time constant for vertical magnetic field penetration, $\tau_{WALL} \approx 50ms$ [50]. Further repetitions of this experiment widened the phenomenology with contrasting experimental evidences and sudden or delayed exponential RWM growth have been observed as well.

The results of all the current freezing experiments with both poloidal and radial magnetic field sensors are summarized in Fig. 5.2. Each point in this polar plot corresponds to a circular Tokamak plasma discharge with $q(a) = [1.5, 1.9]$ and $n_e \sim 10^{19} m^{-3}$. The $m = 2, n = 1$ amplitude and phase of the frozen coil currents are plotted in the radial and angular coordinate, respectively. The current freezing experiments with poloidal magnetic sensors are plotted in red, the ones with the radial magnetic field sensors in blue. An ensemble of entirely feedback controlled discharges are plotted in black as well, for sake of comparison. In the latter case, plasma stability is guaranteed by the Clean Mode Control scheme, that relies on the radial magnetic field sensor measurements as it has been described in Chapter 2. The same control algorithm is applied in the feedback controlled phase of the current freezing experiments with radial magnetic sensors. Thus, not surprisingly, the black and the blue points are overlapped. Conversely, the red ones, that correspond to the experiments with poloidal magnetic field sensors, are more widely spread in the third quarter, but they are prominently nearer to $\sim 230deg$, namely the phase of the RFX-mod error fields that has been measured with the compass scan technique, as it has been described in Chapter 4.

In addition, the coil currents in the freezing experiments with poloidal magnetic

sensors are characterized by higher amplitudes if they are compared with the other data series at the same edge safety factor values. This is evident in Fig. 5.3, where the mean $m = 2, n = 1$ coil current amplitude is plotted as a function of $q(a)$. Similarly to Fig. 5.2, the black points and the blue ones can be considered equivalent as far as this statistical analysis is concerned. The latter ensemble shows that the coil current amplitude increases as the current limit $q(a) = 2.$ is approached, due to the enhancement of the RWM growth rate, as it is shown in [57]. Interestingly the red data move from this trend and the magnetic feedback control with poloidal magnetic field sensors at $q(a) \simeq 1.8$ is found to prescribe coil currents whose amplitude is on average higher to the one prescribed by the feedback control with radial magnetic sensors at higher $q(a)$ values. The observed variability in the results of these preliminary experiments could be due either to the intrinsic unstable nature of the current-driven RWM, that differently from the pressure-driven one can not be prevented by eliminating the error fields, or to an

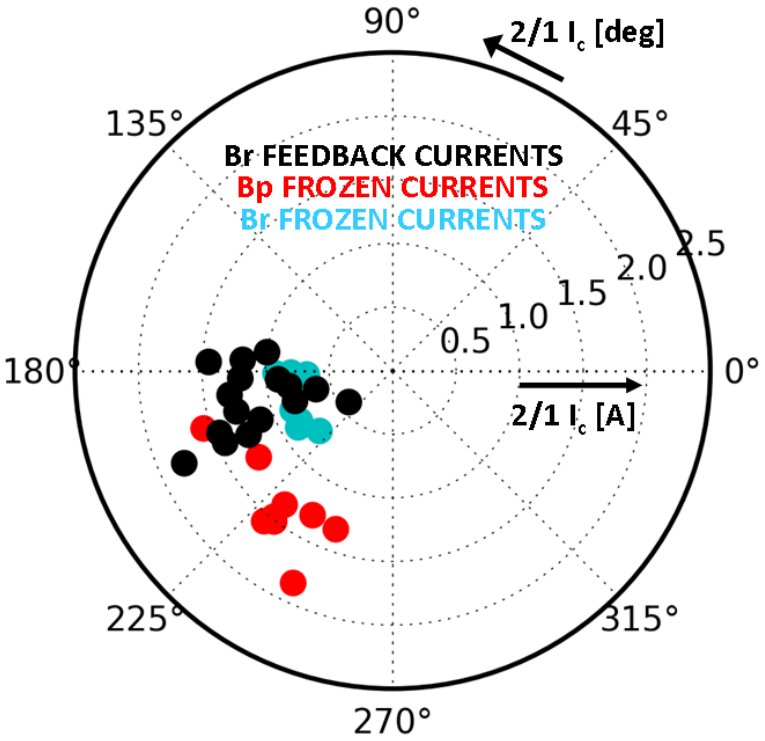

Figure 5.2: Statistical analysis on the coil currents prescribed in RFX-mod in circular Tokamak operation at $q(a) < 2$, $m = 2, n = 1$ amplitude and phase are plotted in the radial and angular coordinates, respectively.

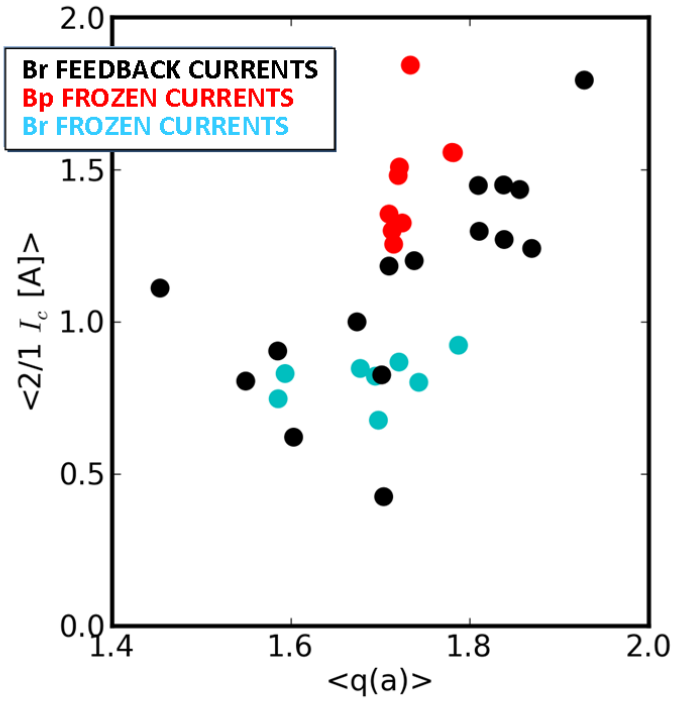

Figure 5.3: Statistical analysis on the coil currents prescribed in RFX-mod in circular Tokamak operation at $q(a) < 2$, mean $m = 2, n = 1$ coil current amplitude as a function of the edge safety factor.

error field symmetrization that can not be reproducibly guaranteed in any plasma discharge. In order to put light on this open issue, the current freezing method was improved on the basis of the DIII-D expertise on the error field correction in high β plasmas, which requires high proportional gain in the feedback phase and null coupling between the magnetic sensors and the active coils, as it has been discussed in the previous Section. Both these improvements were converted into concrete MHD control tools that could be easily embedded in the real-time MARTe framework, as it will be discussed in the next Section.

5.2.2. New real-time control tools to improve dynamic error field correction in RFX-mod

Real-time digital filter

As anticipated, high proportional gain is required for en effective error field correction based on slow magnetic feedback. In RFX-mod, the feedback control with poloidal sensors did not allow to increase arbitrarily such value because these sensors were affected by a significant noise, as it can be seen in Fig. 5.1. These magnetic probes are located on the inner surface of the copper shell, as it has been described in Chapter 2. Their bandwidth is thus limited only by the vacuum vessel eddy currents at about $1kHz$, while the radial magnetic field ones are shielded also by the shell. Fig. 5.4 shows how the unwanted noise of the poloidal magnetic field sensors, that is quantified like the standard deviation of the $m = 2, n = 1$ amplitude of the corresponding feedback coil currents, is amplified by the proportional gain.

To overcome this limit, a real-time single-pole Butterworth filter was implemented in the MARTe framework to get rid of the high frequency fluctuation in the poloidal magnetic field sensors. The frequency and the phase response of this filter with a cut-off frequency $f_c = 100Hz$ are plotted in Fig. 5.5. The Butterworth filter is known to be maximally flat, namely it does not have any ripple from $0Hz$,

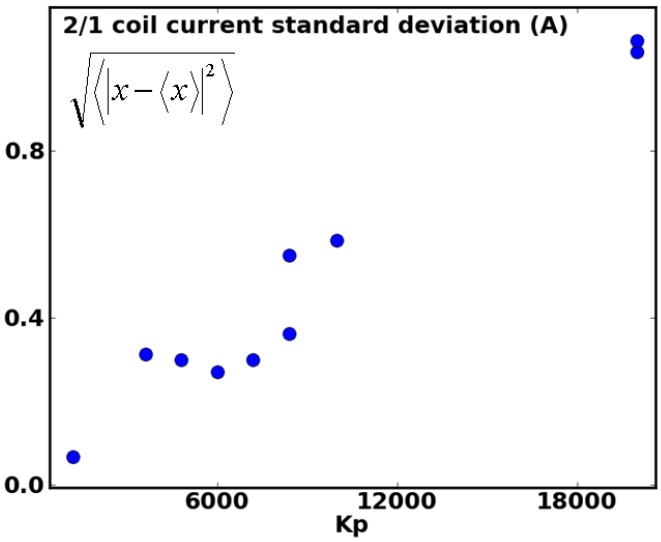

Figure 5.4: The noise amplification in the $m = 2, n = 1$ amplitude of the coil currents prescribed by the poloidal feedback control as a function of the applied proportional gain.

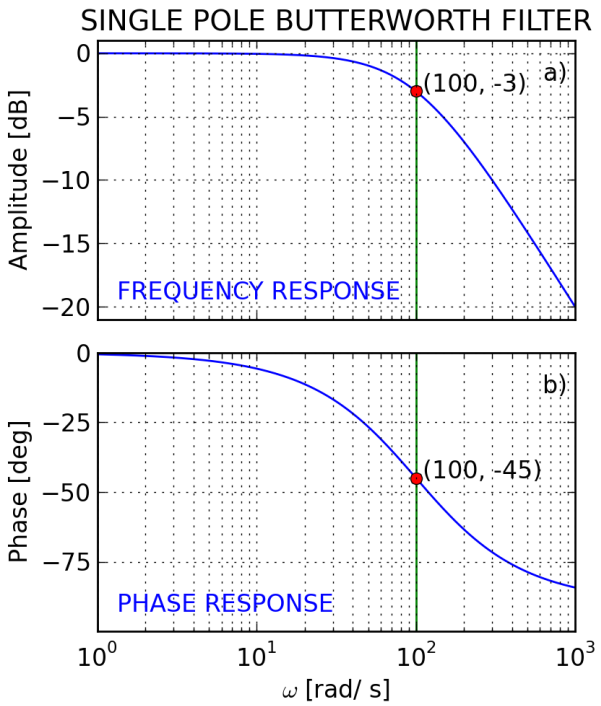

Figure 5.5: Single pole Butterworth filter frequency a) and phase b) response, the green line highlights the cut-off frequency.

the DC case, to the cut-off frequency at $-3dB$. Unluckily, this filter achieves pass band flatness at the expense of a wide transition band as the filter changes from the pass band to the stop band, indeed higher frequencies beyond the cut-off point rolls-off down to zero in the stop band at the slow rate of $20dB/decade$.

As it was described before in Chapter 3, the RFX-mod control system provides the possibility to set-up different control configurations in up to 8 time windows. The cut-off frequency of the digital filter is one of this user-defined parameters, thus it can be flexibly changed during the same discharge. Fig. 5.6 shows the effect of this filter on the $m = 2, n = 1$ amplitude of the poloidal magnetic field. The cyan signal is the reference unfiltered case, while the blue one was filtered with a $20Hz$ cut-off frequency. The filter successfully reduces the unwanted high frequency fluctuations in the signal, however it also introduces a delay $\Delta t \simeq 6ms$.

The effect of the filter on the feedback variable is to slow down the controller action. Indeed all the phenomena that take place on a timescale smaller than $\simeq 1/2\pi f_c$ are neglected. In addition, the filter delay increases with the cut-off frequency f_c. Nonetheless, stable plasma operation at $q(a) < 2$ was obtained with a $5Hz$ filter, which corresponds to a timescale of about $\sim 30ms$ that is comparable

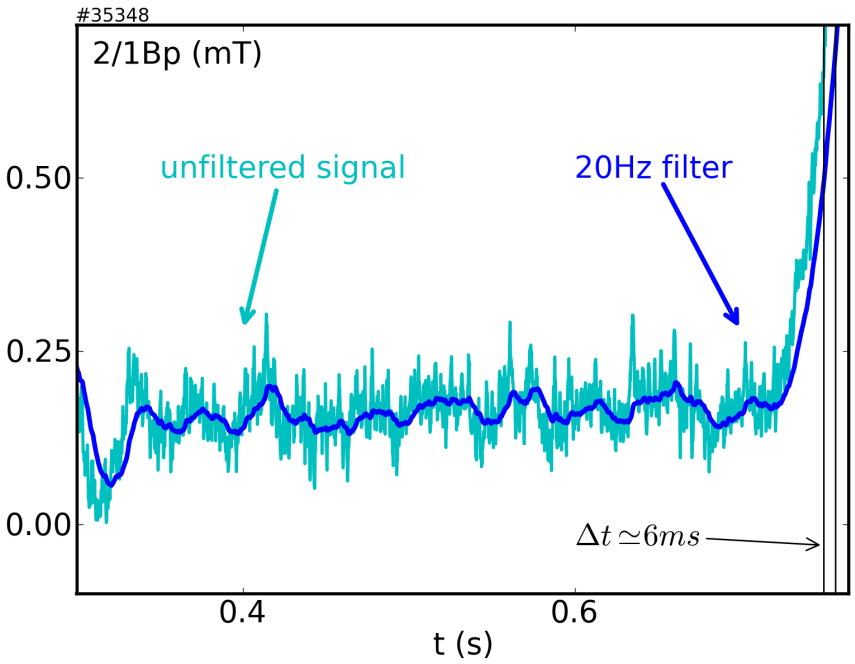

Figure 5.6: Effect of the real-time single pole Butteworth filter on the feedback variable. Time evolution of the $m = 2, n = 1$ poloidal amplitude of the magnetic field, unfiltered reference signal (light blue), 20Hz filtered one (blue).

to RWM growth rate at $q(a) \sim 1.8$.

Fig. 5.7 summarizes the results of the experiments where the MHD stability was maintained at $q(a) < 2$ using the poloidal magnetic field sensors and a feedback control with increasing proportional gain values. The plot compares similar discharges that only differ from the applied gain. Panel a) reports the time history of the plasma current and the edge safety factor in the left and right y-axis, respectively. It is worth to note here that $q(a) \simeq 1.8$. Panel b) sketched the proportional gain applied in the corresponding discharge, as the colour code suggests. The horizontal line is an empirical limit that roughly divided the stable gains from the unstable ones. Panels c) and d) show the time evolution of the $m = 2, n = 1$ amplitude and phase of the poloidal magnetic field. The figure highlights that the feedback control with poloidal sensors is able to sustain the plasma stability below $q(a) = 2$ with a relatively low gain, namely with $Kp = 8000(a.u.)$ as lower bound. The lower the proportional gain, the higher the amplitude and the slower the rotation of the feedback variable, as the last two panels show. If the gain is insufficient, like in cyan case, the amplitude of the feedback variable, i.e. the RWM one, overcome a critical threshold, the feedback action is too weak to quench the growth and the control is eventually lost.

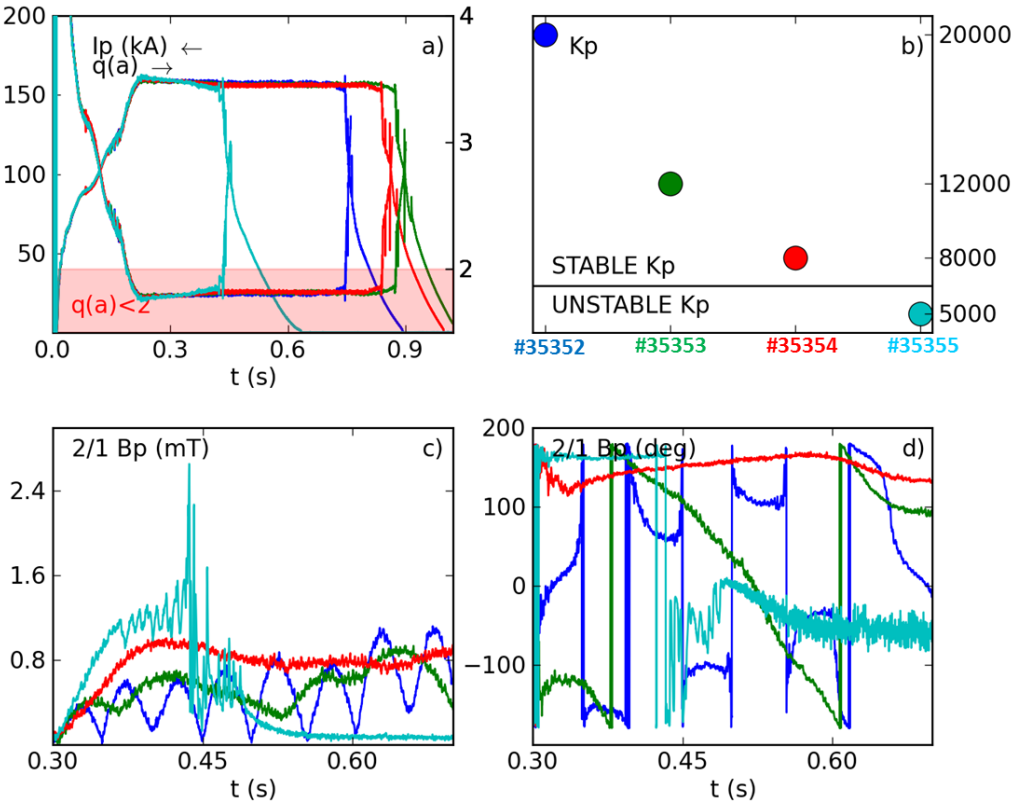

Figure 5.7: Proportional gain scan experiment with a 5Hz filtered poloidal feedback variable. a)Time evolution of plasma current and edge safety factor, b) the applied proportional gain, c) and d) time evolution of the $m = 2, n = 1$ amplitude and phase of the poloidal magnetic field.

The control strategy that corresponds to the red case in Fig. 5.7 is able to maintain the plasma stability in a very robust way. Fig. 5.8 documents how this feedback control scheme with low gain, $Kp = 8000(a.u.)$ and a relatively low cut-off frequency, $f_c = 5Hz$, is able to maintain the plasma stability at about $q(a) \simeq 1.8$ even if magnetic perturbations, like natural sawtooth oscillations or $8kA$ magnetic kicks, perturb the plasma. These perturbing quantities are reported in panel c) and d) respectively, in the form of the time evolution of a core SXR signal and the $m = 2, n = 1$ amplitude of the coil currents. The last two panels, e) and f) compares the time history of the $m = 2, n = 1$ amplitude of the poloidal magnetic field with (in black) and without (in blue) the filter action. The stabilization provided by this "slow" feedback is evident in panel f) where the growth of the RWM, that appeared as soon as the coil currents dropped, is prevented.

Remarkably, the cut-off frequency of the filter could be further lowered to $3Hz$

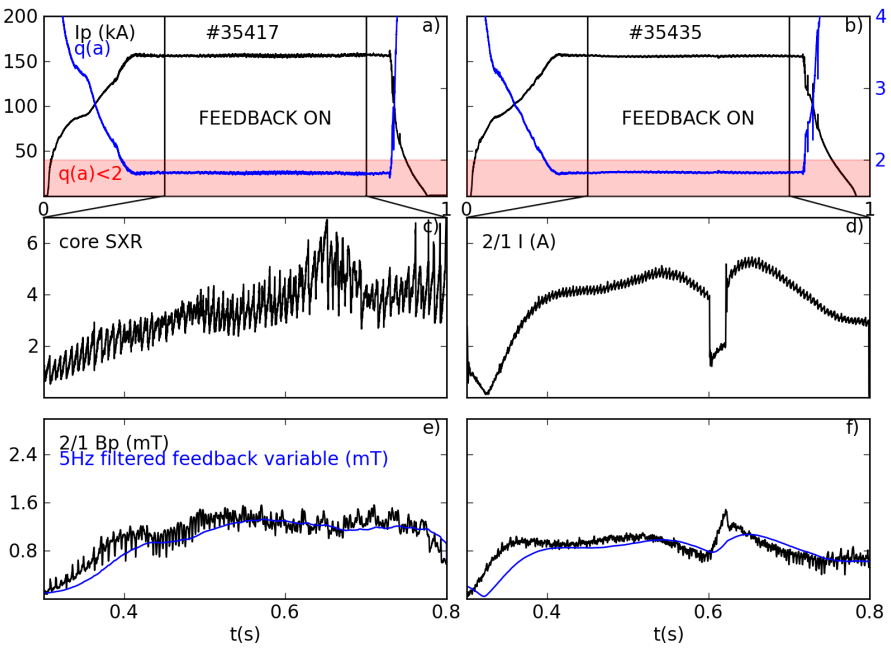

Figure 5.8: Stability proof experiments in the presence of sawteeth and externally applied magnetic kicks. Panel a) and b) time evolution of the plasma current and the edge safety factor, c) sawteeth as measured by a core SXR signal, d) $m = 2, n = 1$ coil current amplitude with a 8kA magnetic kick at $t = 0.6s$, e) f) time evolution of the $m = 2, n = 1$ poloidal magnetic field amplitude with (black) and without (blue) a 5Hz filter action.

with the same $Kp = 8000(a.u.)$ proportional gain. At this frequency the feedback control acts on a timescale $\sim 50ms$ which is longer than the RWM growth rate at this edge safety factor value ($\sim 30ms$). In this experiment, that is summarized in Fig. 5.9, the cut-off frequency of the filter was carefully reduced in consecutive time windows with a double aim. Firstly, to safely control the fast growing tearing mode, that appears before the current limit is approached, and secondly, to avoid sudden and sharp transitions in the feedback variable signal, that can originate unwanted oscillations due to the delay introduced by the filter. The figure reports the time history of the plasma current and the edge safety factor in panel a), while panels b) and c) reports the time evolution of the feedback variable, namely the $m = 2, n = 1$ amplitude and phase of the filtered poloidal magnetic field. In the first time window, $t = [0, 0.3]s$ the cut-off frequency is set to $1kHz$ to overcome the tearing mode which rotates at about $\simeq 60Hz$. In the next one, $t = [0.3, 0.45]s$, the cut-off frequency is lowered to $10Hz$, the feedback variable decreases significantly in amplitude, but it still maintains a partial rotation, probably due to the ampli-

fication of a residual tearing oscillation. Eventually, from $t = 0.45s$ on, the filter is further reduced to $3Hz$ and the $q(a) \simeq 1.8$ is safely maintained till the feedback switching off at $0.8s$. In the last time window the mean amplitude of the poloidal field increases compared to the previous one, nonetheless the feedback succeeds in maintaining the plasma stability, at least till the end of this discharge. Panel b) shows that the feedback variable seems to diminish towards the end but unluckily, due to the limited length of this last time window, it is not possible to state if it was indeed depleting rather oscillating very slowing. However, thanks to a new set-up of the power supply system, Tokamak discharges in RFX-mod can now be lengthened up to $1.2s$, thus it will be possible to repeat this experiment and put light on this open issue.

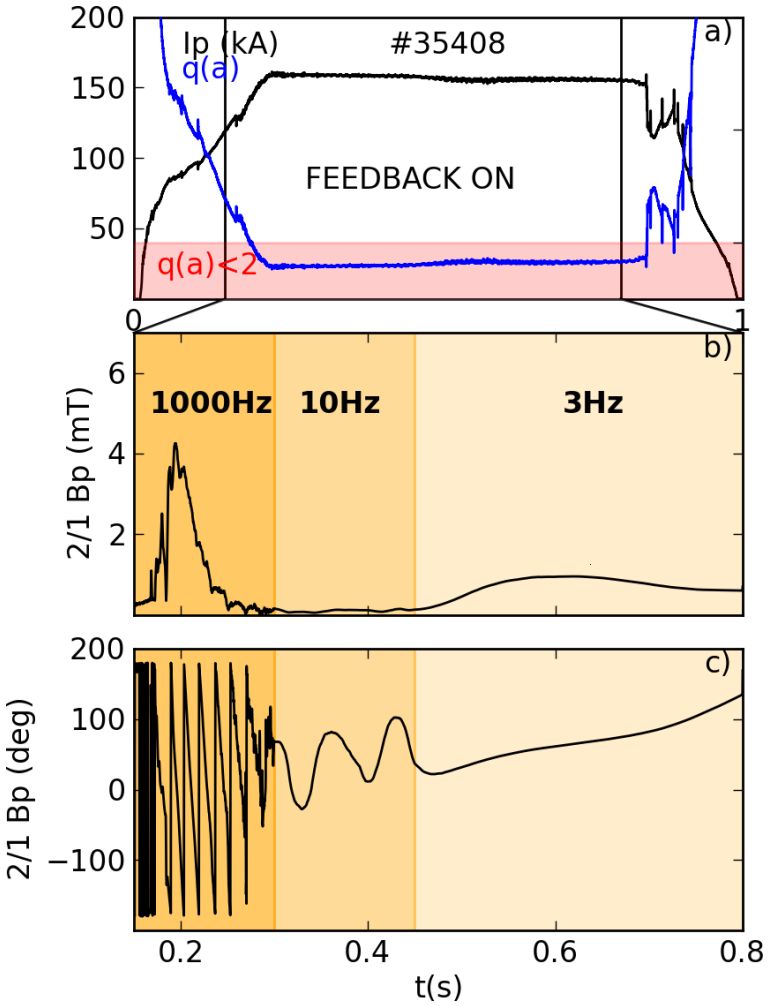

Figure 5.9: Poloidal feedback control with a 3Hz Butterworth digital filter. Time evolution of a) the plasma current and the edge safety factor, b) and c) the $m = 2, n = 1$ filtered poloidal amplitude and phase respectively.

Active coil reconfiguration

The second step to improve dynamic error field correction in RFX-mod consisted in maximizing the decoupling between the magnetic sensors and the active coils. Due to their geometry, the radial sensors are intrinsically coupled to the active saddle coils, while the poloidal ones are far less. The latter were already DC-compensated, as it has been described in Chapter 3, however a further optimization came from the flexibility to operate with a user-defined active coil configuration. This possibility was introduced by the brand-new MARTe framework and it avoided complex and time consuming hardware modifications. Indeed, as it has been described in Chapter 2, the standard $48X4$ active coil pattern can be arbitrarily modified to emulate the action of a smaller number of wider active coils, the so called *super-coils*, or to simply switch off the actuators that directly face the magnetic sensors, as it was done in the error field correction experiments. The currents prescribed by the feedback control are re-evaluated at the end of the closed loop according to the new coil configuration, and then sent to the corresponding actuator. Fig. 5.10 sketches the magnetic configuration used in these experiments together with the main discontinuities in the RFX-mod boundary geometry, namely portholes, gaps and broken saddle coils. The poloidal magnetic sensors are highlighted with red and green squares, respectively. A group of 4 active coils (the blue rectangles), that were placed in the proximity of the thick poloidal sensors, was switched off in order to minimize their coupling. In so doing the active coil coverage was reduced by 50% but the toroidal symmetry was maintained.

A series of error field correction experiments were then performed with these new control tools, with the aim to obtain clearer and conclusive results on the possible destabilizing role of the magnetic asymmetries on the RWM dynamics. The experiments consisted in exploiting simultaneously the filter, to apply a high gain feedback controller, and the reduced set of active coils reported in Fig. 5.10, to minimize the coupling between the saddle coils and the magnetic sensors. The optimizations were applied in the first part of the discharge, when the active feedback control was switched on to prescribe the coil currents necessary for the magnetic field symmetrization. At $t = 0.7s$ the active control was turned off and replaced by the passive error field correction performed with the frozen currents. The results are summarized in Fig. 5.11. This figure compares three similar discharges, where the feedback variable was filtered with decreasing cut-off frequencies, namely $100Hz, 20Hz, 10Hz$. The applied proportional gain was the same for all the dis-

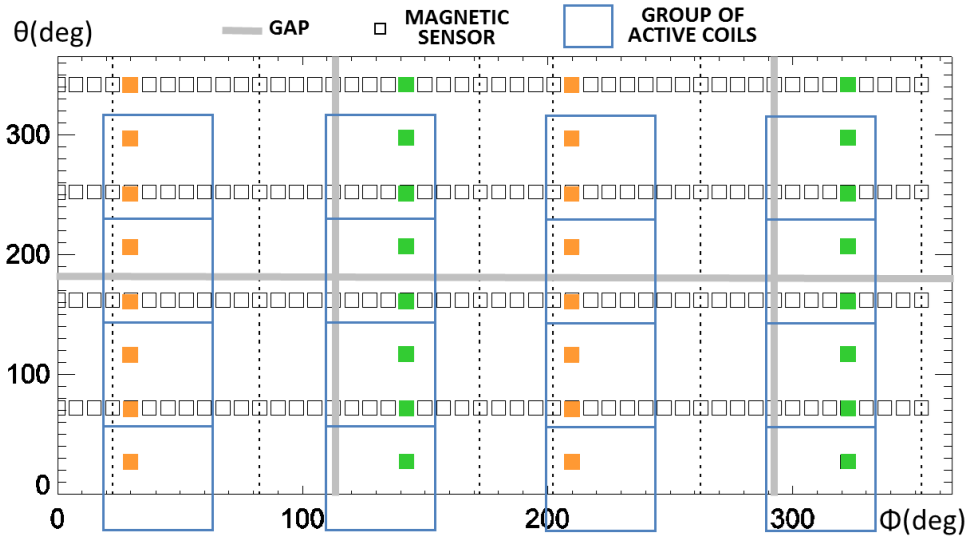

Figure 5.10: Sketch of the configuration of magnetic sensors and the reduced set of active coils used in the error field correction experiments. The blue rectangles highlights the inactive saddle coils, orange and green squares the poloidal magnetic sensors.

charges. It was scaled to take into account the half active coil coverage and carefully maximized to avoid the high gain instability. The $m = 2, n = 1$ amplitude and phase of the active coil currents are plotted in panel b) and c) respectively. Both signals are modulated by oscillations, whose frequency decreases with the cut-off one. Interestingly, this effect is equivalent to increase the proportional gain at a fix cut-off frequency as it is shown in Fig. 5.7. As a consequence, the frozen currents are not exactly the same from shot to shot, however their amplitude and phase average values are about $2A$ and $240deg$, respectively. An enlargement of the time history of the $m = 2, n = 1$ component of the poloidal magnetic field is reported in panels d) and e). The first closeup shows that the feedback variable is modulated as well, but the average value is quite similar in all discharges, the second points out the dynamics of the $m = 2, n = 1$ RWM when the feedback is switched off. In particular panel e) points out that the higher the cut-off frequency, the longer the delay with which the RWM appears as soon as the feedback is switched off at $t = 0.7s$. The delay is $\simeq 30ms$ in the blue case, namely at $f = 100Hz$, while the RWM grows instantaneously when $f = 10Hz$. Interestingly, the RWM growth rate increases with the cut-off frequency as well. Assuming that the error field correction was performed at best with these two optimizations, the

experiments discussed so far did not succeed in validating the hypothesis that the error field asymmetries were responsible for the RWM onset when the current limit $q(a) < 2$ is overcome in RFX-mod. This interpretation is supported also by the RWM linear theory, as it will be discussed in the next Section.

5.2.3. RWM linear theory interpretation of the experimental results

The apparently quiescent state of the $m = 2, n = 1$ RWM, that was experimentally observed when the feedback current were frozen and/or the filter was applied, can be explained within the standard RWM linear models. The modelling that will be discussed in this Section neglects the stabilizing effect of the plasma rotation since in RFX-mod its contribution is not significant.

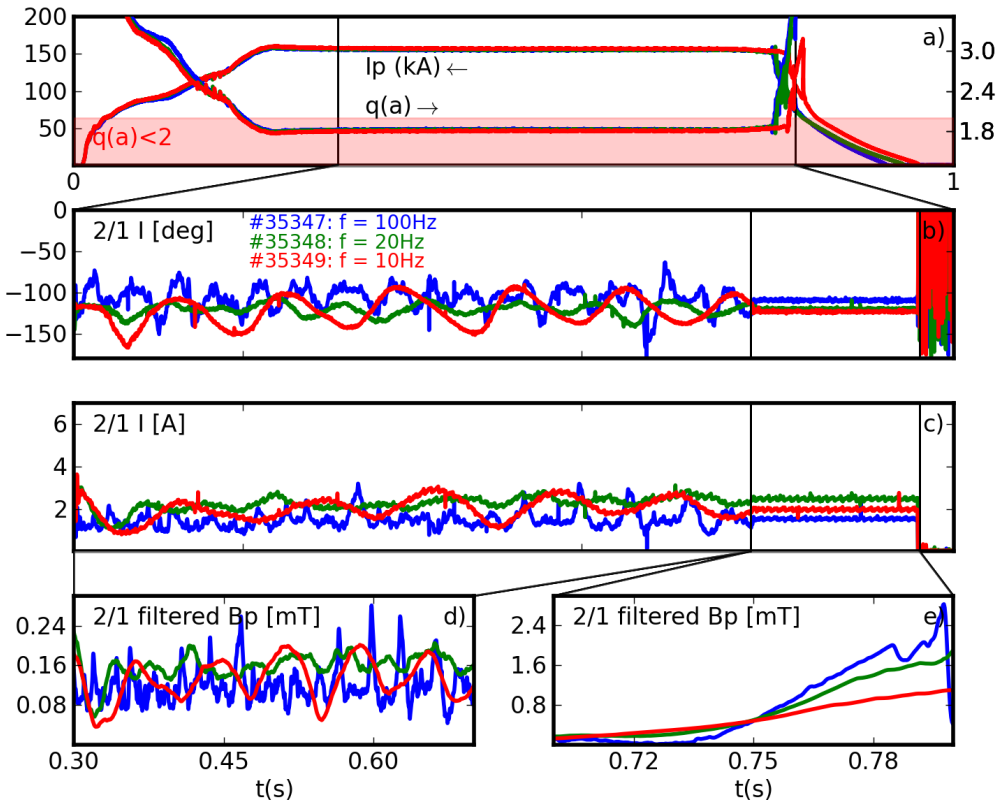

Figure 5.11: Error field correction with a reduced set of active coils and with a filtered feedback variable. Time evolution of a) the plasma current and the edge safety factor, b) and c) the $m = 2, n = 1$ coil current amplitude and phase, d) and e) zoom of the $m = 2, n = 1$ poloidal field amplitude in the presence of feedback and pre-programmed currents, respectively.

Modelling of the "current freezing" experiments

The dynamics of a linearly unstable RWM in the presence of a feedback control, that is assumed to be switched on at $t = [0, t1]$, can be simply described with a couple of equations that refer to a single harmonic m, n:

$$\begin{cases} \frac{db_r}{dt} = \gamma_0 b_r - \gamma_{VAC} b_r^{VAC} I_c \\ b_r^{VAC} I_c = b^{FEED} + b^{EF} = -K b_r + b^{EF} \;\; K \in C, Re(K) > 0, \end{cases} \tag{5.7}$$

where b_r is the m, n radial field harmonic at the shell radius, γ_0 is the RWM free growth rate, namely the one that is measured when the coil current are zero, $\gamma_{VAC} < 0$ is the current damping rate in vacuum and b_r^{VAC} is the radial amplitude produced by a unit current harmonic ($I_c = 1$) at the shell radius without plasma and shell. b^{FEED} is the magnetic field applied by the feedback and b^{EF} a constant error field that is introduced to model the effect of freezing the feedback currents. The second equivalence stands for the application of the radial field Clean Mode Control feedback algorithm during $t = [0, t1]$. The gain K is complex, the real part is positive while the imaginary one is finite to take into account the phase shift between b_r and I_c that is due to the residual sideband aliased field. The solutions of Eq. 5.7 in the three coil current regimes that characterize a typical plasma discharge of an error field experiment, namely the feedback controlled phase Eq. 5.8a, the current freezing one Eq. 5.8b and eventually the switching off of any coil currents at the end of the shot Eq. 5.8c, are:

$$\begin{cases} b_r(t) \simeq \dfrac{\gamma_{VAC} b^{EF}}{\gamma} \left(1 - e^{\gamma t}\right) & t = [0, t1] \quad (5.8a) \\ b_r(t) \simeq b_r(t_1) - \dfrac{\gamma_{VAC} b^{EF}}{\gamma_0} e^{\gamma t_1} e^{\gamma_0 (t - t_1)} & t = [t1, t2] \quad (5.8b) \\ b_r(t) \simeq \left(b_r(t_1) - \dfrac{\gamma_{VAC} b^{EF}}{\gamma_0} e^{\gamma t_1} e^{\gamma_0 (t_2 - t_1)} \right) e^{\gamma_0 (t - t_2)} & t > t2 \quad (5.8c) \end{cases}$$

where $\gamma = \gamma_0 + K\gamma_{VAC} \in C$ and $Re(\gamma) < 0$ to have a stabilized system. In the error field experiment reported in Fig. 5.1 the amplitude of the $m = 2, n = 1$ harmonic seems to remain constant while the currents are frozen. But this is not the case, indeed the feedback action in the time window $t = [0, t1]$ has a kind of persisting effect in the freezing one at $t = [t1, t2]$, that masks the growth of the RWM instability. This masking effect is due to the dominance of the constant

term $b_r(t_1)$ over the second addend, that is weighted by the factor $e^{\gamma t_1} \ll 1$. This subtlety suggested a more accurate analysis, where the constant contribution of the radial magnetic field at $t1$ instant is subtracted as an offset to the solution, in order to point out the growth of the instability. In so doing, the new solutions for the cases of Eq. 5.8b and Eq. 5.8c read as:

$$\begin{cases} b_r(t) - b_r(t_1) \simeq -\dfrac{\gamma_{VAC} b^{EF}}{\gamma_0} e^{\gamma t_1} e^{\gamma_0 (t - t_1)} & t = [t1, t2] \\ b_r(t) - b_r(t_1) \simeq \left(b_r(t_1) - \dfrac{\gamma_{VAC} b^{EF}}{\gamma_0} e^{\gamma t_1} e^{\gamma_0 (t_2 - t_1)} \right) e^{\gamma_0 (t - t_2)} - b_r(t_1) & t > t2 \end{cases}$$

It is worth to note here that the last two solutions in the last equation have a different phase due to $\gamma \in C$. Some simulations have been performed to test this new model with the RFXlocking code, that is a cylindrical, zero pressure, spectral code [94]. This code solves the single fluid MHD motion equations for toroidal and poloidal angular velocities under both viscous and electromagnetic torques developed by tearing modes, where the latter are described by Newcomb's equation. The code takes into account the radial field diffusion across the passive structures that surround the plasma and it models the feedback coil action as well. The RFXlocking simulations were performed using the RWM version of this code, which includes both vessel and the shell and the Wesson's equilibrium model for the plasma. The feedback control system is modelled as a voltage-control and it matches the characteristics of the real one, namely it has a feedback cycle frequency of $5kHz$, $1ms$ latency and it can include the sidebands aliasing. The results of these simulations are summarized in Fig. 5.12. This plot compares the amplitude of the $m = 2, n = 1$ RWM in different controlled regimes. The solid black line represents the free growth of this mode when the feedback currents are switched off, whereas the dashed one the quenching action of the feedback control. In both green and red case, a constant EF is added to reproduce the experiments. At $t = t0$ the active feedback control is switched off, the RWM starts growing immediately in the green case, that was feedback controlled till $t = t0$, with the same rate of the black solid line in the previous time window. Conversely the coil currents are frozen in the red case and the results is a RWM delayed growth.

The results confirm the masking effect of the frozen currents on the RWM dynamics and so does the experimental ones that are reported in Fig. 5.13. The figure shows the time evolution of the $m = 2, n = 1$ amplitude and phase of the

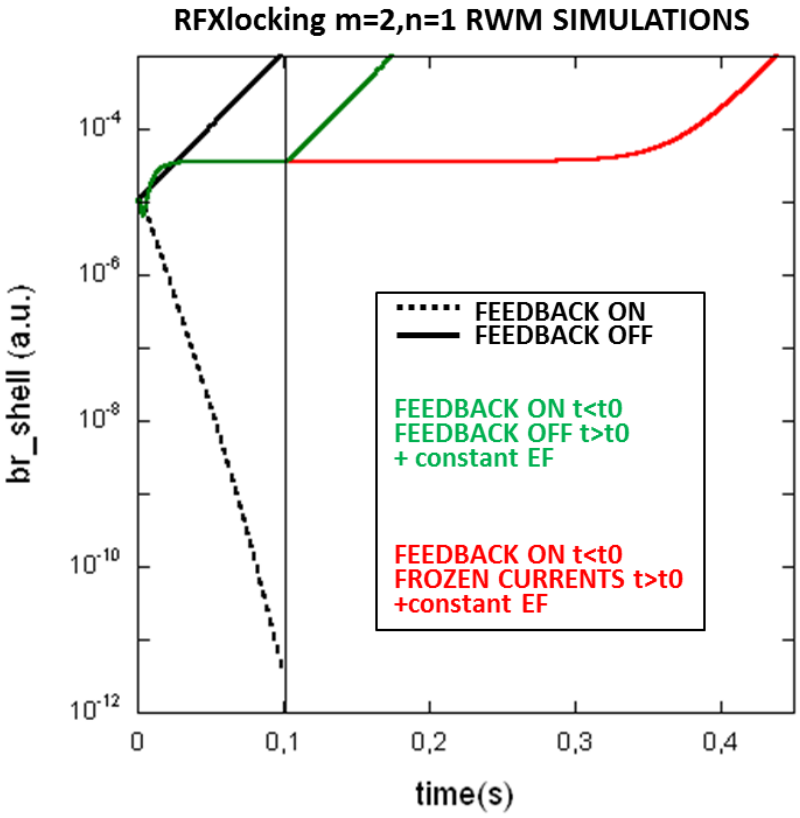

Figure 5.12: RFXlocking simulation of the time evolution of the $m = 2, n = 1$ RWM amplitude in different control regimes.

radial magnetic field, as it was measured in the error field correction experiment with poloidal sensors. The black curves are substantially the same time traces of panels b) and c) Fig. 5.1 and they are reported here again to be compared with the new results of the analysis that was suggested by the theoretical model (in blue). The y-axis logarithmic scale should foreground the exponential growth of the instability, that however seems not to appear in the black case. In addition, the phase of the radial $m = 2, n = 1$ harmonic remains constant during the whole plotted period, regardless of the different current regimes. This is the case when the feedback action masks the real dynamics of the instability. Conversely, the blue case verifies all the predictions of the model and unveils what is really going on. Indeed, the subtraction of the radial magnetic field at $t = t1$ to the measurements allows not only to reveal the RWM growth even during the pre-programmed current phase, but also the change in the phase of the same harmonic during the last two

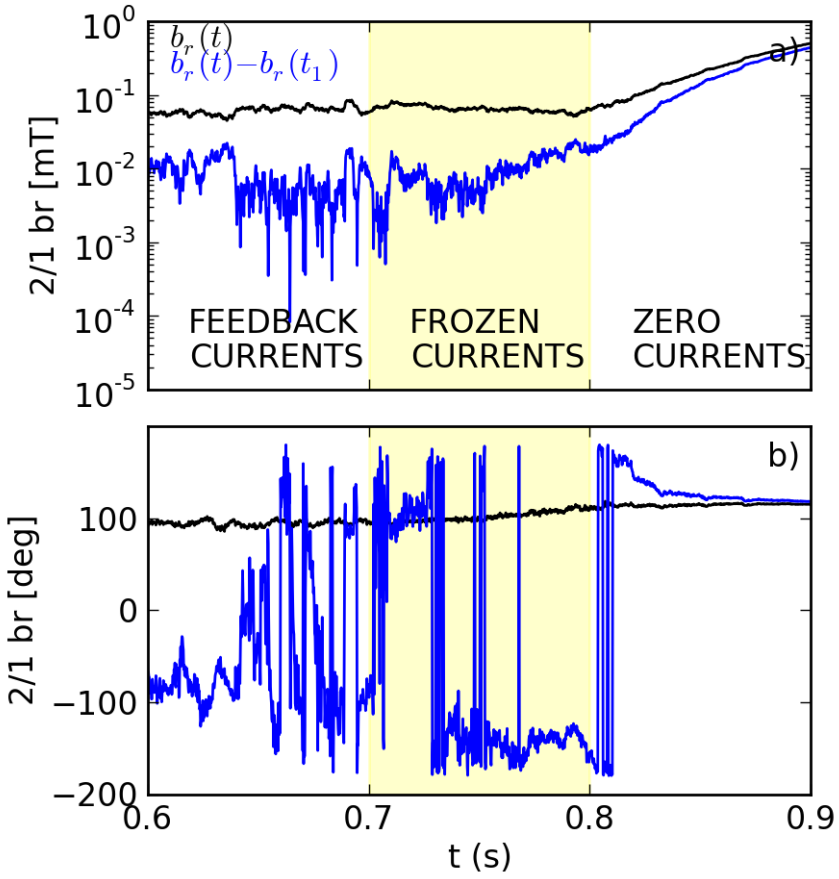

Figure 5.13: Time evolution of the $m = 2, n = 1$ a) amplitude and b) phase of the radial magnetic field. Black curves refers to the original data, the radial magnetic field at $t = t1$ is subtracted to the measurements in the blue ones.

time windows, as it was predicted by the model.

The validation of the theoretical predictions, that have been discussed in this Section, with the experimental data was verified statistically, as the comparison of Fig. 5.14 shows. In the two plot is reported the $m = 2, n = 1$ RWM growth rate as a function of the edge safety factor for three different cases, namely when the RWM grows freely as soon as the coil currents are switched off at the end of a discharge (black), when the RWM grows while the pre-programmed currents, that are prescribed by the radial feedback control, are compensating the error field (cyan) and finally the case similar to the latter but with the radial feedback control substituted by the poloidal one (red). The growth rate is evaluated with an exponential fit on the $m = 2, n = 1$ radial component of the magnetic field, while the edge safety factor is estimated as a time average over the first 10ms of the RWM growth. The growth rates in the plot on the left were obtained by a straightforward

exponential fit on the raw $m = 2, n = 1$ amplitude of the radial magnetic field. This plot shows that when the error field correction is performed with radial sensors, the $m = 2, n = 1$ RWM growth rates are comparable to the ones measured when the coil currents are switched off, and this evidence is in agreement with the known inefficiency of these sensors. Interestingly, the red points are well outside this main data trend and a noticeable variability of positive (unstable) and negative (stable) growth rates exists as well. Nonetheless the growth rates are systematically lower than the ones of the other two series at the same edge safety factor value. This is even more evident for the two slightly negative growth rates, that are evaluated in discharges where the $m = 2, n = 1$ radial magnetic field amplitude is slightly decreasing in time as in panel b) of Fig. 5.1. Globally this plot seems to suggest that the error field correction with poloidal sensors is able to effectively affect the RWM dynamics, by slowing down, or even completely quenching, its growth. But this picture changes completely if the growth rate of the same shot samples is evaluated after subtracting the masking effect of the radial field at the end of the feedback phase, $b_r(t_1)$, to the radial magnetic measurements $b_r(t)$. This was done in the plot on the right and as a result, all the data align to the main data trend regardless their identity, meaning that the error field correction does not impact the RWM dynamics in these low-q plasmas.

The theoretical predictions of the linear RWM model that was introduced in this Section were simulated with RFXlocking. The current freezing tool is emulated by adding an error component b_{err} in the feedback variable, that is split into a systematic b_0 plus a random phase noise part:

$$b_{err} = b_0(1 + \epsilon e^{i\phi_{rand}(t)}). \tag{5.10}$$

The RFXlocking simulations of the feedback masking effect with radial and poloidal sensors are reported in Fig. 5.15, in the left and right plot, respectively. The comparison of these two plots show that the dependence of the feedback behavior on the noise characteristics is independent from the used magnetic sensors, thus the radial and poloidal feedback controls are basically the same on the RFXlocking point of view. The equilibrium was chosen to reproduce a RWM growth rate of $\sim 45 s^{-1}$, which is comparable with the experimental one. In the absence of noise, the $\epsilon = 0$ black continuous line, the masking effect is important in both cases. But as the noise increases, especially at lower feedback frequencies, the effect vanishes progressively. This is evident if one compares the blue with

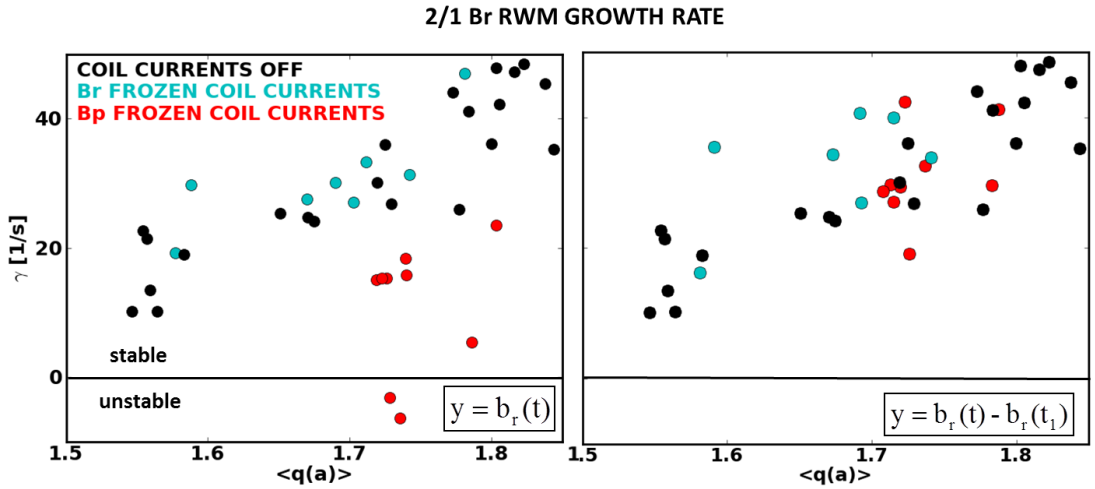

Figure 5.14: $m = 2, n = 1$ RWM growth rate as a function of the edge safety factor with (right) and without (left) the subtraction of the radial magnetic field at the end of the feedback phase in the current freezing experiments. Black points refer to the RWM free growth when the coil currents are switched off at the end of the discharge. The red and the cyan ones correspond to the growth of this instability in the presence of pre-programmed currents that are prescribed by the feedback with poloidal and radial magnetic sensors, respectively.

the green case (or the red with the orange), namely the case where the random phase of the noise changes at every feedback cycle ($5kHz$) with the one where it does it every 20 cycles ($250Hz$). In the radial feedback plot there seems to be also a dependence on the noise amplitude ϵ, that however is not reproduced in the poloidal one on the right. These simulations suggest that the different noise in the signals provided by the two sensors could play a role

Modelling of the experiments with a filtered feedback variable

The same RWM linear model presented in the previous Section can be applied to model the experimental results that were obtained in the experiments where the high frequency components were removed from the feedback variable with a single pole Butterworth filter. The equations in this regime read as:

$$\begin{cases} \frac{db_r}{dt} = \gamma_0 b_r + \gamma_{VAC} K w_r \\ \frac{1}{\omega_f}\frac{dw_r}{dt} + w_r = b_r, \end{cases} \tag{5.11}$$

where w_r is the low-pass filtered feedback harmonic, ω_f the cut-off angular frequency of the filter and K the gain that is assumed to be simply a real posi-

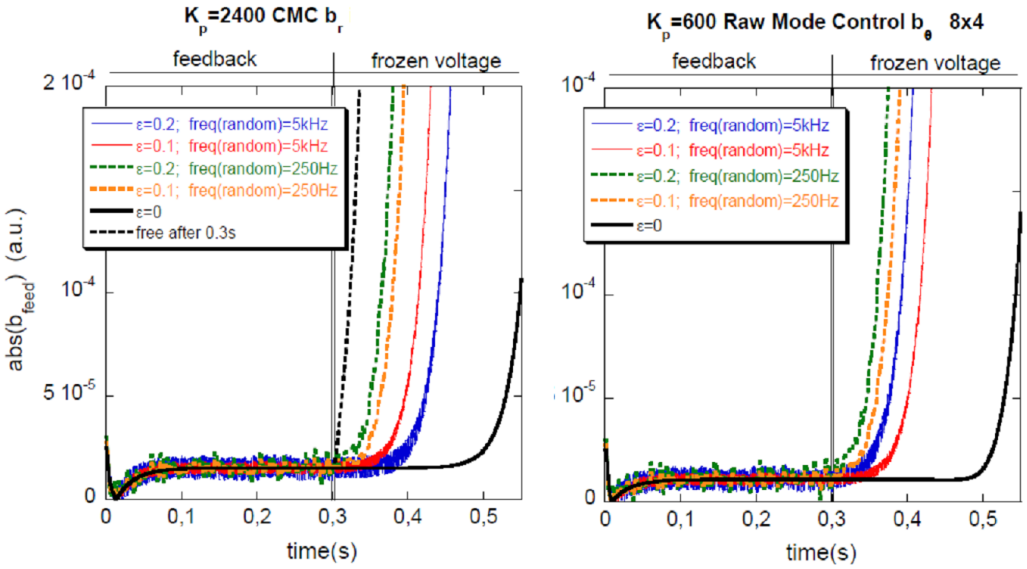

Figure 5.15: RFXlocking simulations of the feedback masking effect in the error field correction experiments. Time evolution of the feedback variable that is controlled till $t = 0.3s$ with the radial Clean Mode Control feedback algorithms in the plot on the left and with the Poloidal Control one on the right. (This figure is taken from [95]).

tive number. The eigenvalues λ of the system are the solution of a second order equation, whose solution and discriminant are:

$$\begin{cases} \lambda = \frac{\gamma_0 - \omega_f \pm \sqrt{\Delta}}{2} \\ \Delta = (\omega_f - \gamma_0)^2 + 4\omega_f(\gamma_0 + \gamma_{VAC}K). \end{cases} \tag{5.12}$$

Three different regimes can be identified:

Stable solutions $Re(\lambda) < 0, \forall Im(\lambda)$. The system is stable, this occurs when $\omega_f > \gamma_0$ and $K > K_{marg} \equiv -\gamma_0/\gamma_{VAC}$.

Marginally stable solutions $Re(\lambda) = 0, \forall Im(\lambda)$. The system admits two complex conjugate purely imaginary solutions, this occurs when $|K| \geq |K_{marg}|$ and $\omega_f = \gamma_0$

Unstable solutions $Re(\lambda) > 0, \forall Im(\lambda)$. The system admits two complex unstable solutions, this occurs when $\omega_f < \gamma_0$. The eigenvalue $\lambda = [(\gamma_0 - \omega_f)/2, \gamma_0 - \omega_f] \simeq [K > K_{marg}, K = K_{marg}]$. In this regime the mode appears with a growth rate $\lambda < \lambda_0$ and oscillates.

5.2.4. Qualitative comparison with CarMa

Numerical simulations were performed with the CarMa code [96] to model the effect of a first order filter on the radial Clean Mode Control feedback variable. This code originates from the synergy between the CARIDDI and the MARS-F codes and provides a linearized model of the RWM physics in the presence of both active and passive structures. CarMA allows a reliable and robust reconstruction of the RWM dynamics, since it includes both kinetic effects into the MHD equations and a realistic reconstruction of the structures that surrounds the plasma, with a particular attention on the effects of the 3D geometry on the mode dynamics.

Fig. 5.16 reports the results of series of simulation where an unstable mode with growth rate $\gamma \sim 120s^{-1}$ appears at $t = 0.1s$. This value is higher than the experimental one but the results of this simulations can be indicative as well. In $t = [0.1, 0.3]s$ a first order filter with cut-off angular frequency $\omega_f = 200\gamma_0$, that corresponds to $f_f \sim 3800Hz$, is applied. From $t = 0.3s$ on different cut-off frequencies are tested, namely $\omega_f = [5, 1, 1/2, 1/6]\gamma_0$ ($f_f = [95, 19, 9.5, 3.2]Hz$). The proportional gain was kept at a fixed value, $K = 12000 > K_{marg}$ in all the simulations in order to stabilize and avoid the high gain instability with any filter frequency. The time evolution of the $m = 2, n = 1$ radial amplitude, that is reported in the figure, is not affected by the filtering in the first time window, $t = [0.1, 0.3]s$, while a significant effect is observed in the last one especially in the cases where the cut-off frequency is lower than γ_0, the mode free growth rate. The marginal stability is achieved at $\omega_f = \gamma_0$ while smaller values lead to an unstable regime. The oscillations, that are always present regardless the frequency value, are due to the imaginary part of the solution. Thus the quiescent state of the mode that is observed in Fig 5.7, 5.8 and 5.9 can be an evidence of a marginally stable mode, being the applied cut-off angular frequency of the order of the free mode growth rate, especially in the former two cases where $\omega_f = 2\pi f_f \sim 30ms \sim \gamma_0$. A possible interpretation of Fig. 5.9, where the applied filter acts on time scales that are likely longer than the RWM characteristic one, is that the RWM stabilization can be apparent, since the RWM growth can be hidden by the oscillations that slowly modulate the amplitude. Longer discharges, that are now feasible in RFX-mod thanks to a new set-up of the power supply, will put light on this issue.

The new real-time tools, namely the possibility to freeze the currents prescribed by the feedback in order to apply them as pre-programmed ones during the same discharge, and the low pass single pole Butterworth filter, were tested with two

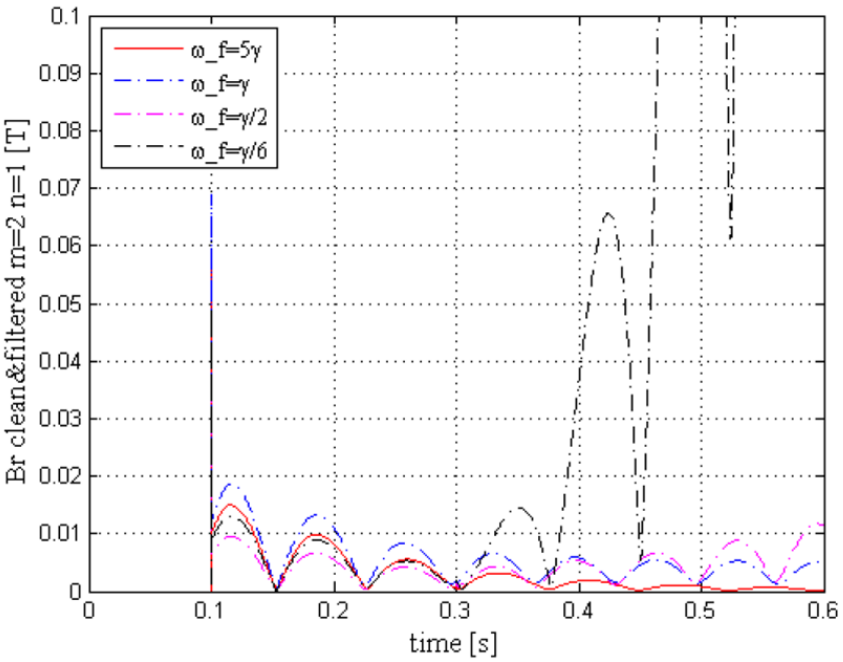

Figure 5.16: Time evolution of the $m = 2, n = 1$ radial magnetic field amplitude with different filter cutoff frequencies, marginal stability case is plotted in blue. (This figure is taken from [95]).

similar linear models. The first one relied on the RFXlocking code while the second on the CarMA one. Besides a direct comparison of these two codes is not possible, due to the significantly different growth rate assumed in the simulations ($\gamma = 45s^{-1}$ in RFXlocking and $\gamma = 120s^{-1}$ in CarMa), the predictions are in agreement with the corresponding experimental data, once the latter are treated accordingly. Both models interpreted the RWM stability, that was apparently observed in the experiment of Fig. 5.1 on the right, as an evidence of an unstable regime where the growth of the mode was masked by the action of the control tool itself. If the experimental data are analyzed as the theoretical predictions suggest, then the masking effect is unveiled and the RWM is found to be unstable even when the error fields are minimized at best.

6

Magnetic feedback sensors and control schemes for RWM control in RFX-mod

RFX-mod is equipped with a unique and sophisticated MHD control system that allows to develop feedback control algorithms based on radial, toroidal and poloidal magnetic field sensors and to test them in the challenging $q(a) < 2$ regime, whose stability is threaten by a very reproducible $m = 2,\ n = 1$ RWM. This Chapter will discuss the performance of the feedback control algorithms that have been implemented during this Thesis work, in order to contribute to the scientific debate on the optimal magnetic feedback control schemes in Tokamaks.

6.1 Feedback control in RFX-mod

Several experiments have been performed in RFX-mod running as a Tokamak to measure and correct the error fields. Chapter 5 presented and discussed the compass scan technique and the new real-time control tools that were used to compensate the magnetic field asymmetries in Tokamak plasmas. At the date of this Thesis work, despite the pursuit of more and more refined and reliable recipes, the correction of the magnetic non-axisymmetry did not succeed in stabilizing the $m = 2, n = 1$ RWM above the current limit. This implies that this mode is really linearly unstable thus a feedback control action is mandatory to drive and maintain the plasma stability at $q(a) < 2$ in the RFX-mod circular Tokamak.

Luckily, this experiment is equipped with a unique and sophisticated MHD control system, that allows to routinely operate circular Tokamak plasmas at $q(a) < 2$. As far as MHD control is concerned, appealing features of this experiment are the variety and the large number of magnetic field sensors, as well as the flexibility of its new real-time framework, that allows to implement computationally challenging feedback algorithms and to re-configure the native set of active coils.

Therefore RFX-mod can significantly contribute to the scientific debate on the optimal sensors for magnetic feedback control in Tokamaks because it offers the possibility to design complex control algorithms based on radial, toroidal and poloidal magnetic field sensors, and to test them in a very challenging but also reproducible regime.

The optimization of the feedback control schemes for RWM stabilization is an open issue in Tokamaks, that needs to be solved. Indeed the RWM instability in high β Tokamaks is stabilized by energy dissipation mechanisms that depend on plasma rotation and kinetic effects, whose roles in ITER are still under investigations [87]. Part of the interest in the fusion community is focused on the positioning and orientation of the sensors. Indeed the optimization of these two parameters allows to clearly detect the magnetic field component linked to the MHD activity and to produce a reliable and robust signal as input for magnetic feedback control algorithms.

Theoretically it has been demonstrated that a magnetic feedback system with sensors measuring the poloidal magnetic field is much better than the one with radial field sensors [63, 97]. On the experimental point of view, for example in the DIII-D device, dedicated experimental campaigns have been performed to investigate this topic. The major result is that magnetic feedback control using

the radial field sensors, both internal or external, do not prevent the onset of a pressure-driven RWM in high β plasmas. In contrast, when feedback using the poloidal field sensors was applied, such instability did not appear [40]. This result confirms the theoretical prediction.

On the other hand RFX-mod can successfully stabilize the current-driven RWM well below $q(a) = 2$ using radial magnetic field sensors and a feedback control algorithm that cleans the measurements from the sideband aliasing, as it has been shown in Chapter 2.

Several new feedback control algorithms have been implemented in real-time during this Thesis work. These rely on both radial, toroidal and poloidal magnetic field sensors, as it has been described in Chapter 3. Systematic experiments, where different control approaches have been compared in a very simple and reproducible case, namely in $q(a) < 2$ RFX-mod Tokamak plasmas, will be presented in this Chapter. A further aim will be to discuss their performance in order to contribute to the scientific debate on the optimal magnetic field sensors and control scheme for feedback control in Tokamak plasmas.

6.2 RWM feedback control with radial field sensors

6.2.1. Clean Mode Control to overcome the limits of Raw Mode Control

Before the magnetic feedback control with poloidal magnetic field sensors became available in RFX-mod, the radial sensors provided the only feedback signals in RFX-mod. The Raw Mode Control feedback scheme is seriously limited by the high number of sidebands, that are originated by the discrete nature of the active coils. The sideband contribution affects the maximum RWM growth rate value that can be stabilized by this control scheme [94]. In RFP plasmas the sideband aliasing in the measure of the unstable $m = 1, n = 6$ RWM is negligible and indeed the threshold value is $\gamma_{MAX}^{1,-6} \lesssim 220 s^{-1}$, that is considerably higher than the typical RWM growth rate in RFX-mod $\gamma^{1,-6} \simeq 25 s^{-1}$. Conversely, the characteristic $m = 2, n = 1$ RWM growth rate in $q(a) < 2$ Tokamak plasmas, that is similar to the $m = 1, n = 6$ RWM in the RFP case, is comparable to the corresponding critical value, namely $\gamma_{MAX}^{2,1} \lesssim 40 s^{-1}$. This explains why the RMC succeeds in controlling the RWMs in RFP plasmas while it fails.

The Clean Mode Control with its sideband de-aliasing algorithm was implemented to overcome this limitation and since then it has been the most extensively

used feedback control scheme in RFX-mod, running both as a RFP and as a Tokamak [55, 79, 94]. In the former case it allowed to reach plasma currents up to 2MA, in the latter routine operations up to $q(a) \simeq 1.54$.

6.2.2. Explicit Mode Control with radial sensors

The same theoretical model that predicts the RMC limitation of the maximum $m = 2, n = 1$ RWM growth rate that can be stabilized, predicts a similar result for the Explicit Mode Control. The experimental validation of the inefficiency of this control scheme, that has never been performed before, will be presented for the first time in this Section. Fig. 6.1 reports the results of a series of experiments performed in RFX-mod Tokamak circular plasmas. The performance of the EMC control was tested in 4 discharges where the plasma current was ramped down at fixed B_ϕ, to lead the edge safety factor progressively closer to $q(a) = 2$, as panel a) shows. Doing this it is possible to change the RWM growth rate since it depends on $q(a)$ as it is shown in Fig. 5.14. In the first part of each discharge, up to $t = 0.35s$, the same proportional gain $K_p = 40000(a.u.)$ is applied to safely overcome the tearing mode instability. As a result the EMC succeeds in maintaining the plasma stability while the equilibrium crosses the current limit, and it does it in a very reproducible way. In the remaining part of the discharge, up to $t = 0.8s$ that is the time when the feedback control is switched off, different proportional gains are applied.

As one expects, the higher the gain the smaller the amplitude baseline and the closer to 2 the value of the edge safety factor at which the discharge disrupts. But the latter evidence seems to hold only up to a critical gain, $K_p = 10000(a.u.)$ in these experiments. For higher gain values the performance of the discharge does not improve and indeed the cyan shot is comparable to the blue one, regardless the double proportional gain applied, whose only further effect is to induce the mode to rotate at 5Hz.

The saturation of the EMC's capabilities in stabilizing the RWM in $q(a) < 2$ Tokamak plasmas is predicted by a theoretical model as well. Fig. 6.2 shows the CarMa predictions for the performances of the different radial feedback controls implemented in RFX-mod. The plot, that reports the $m = 2, n = 1$ RWM growth rate as a function of the proportional gain, was made assuming a RWM free growth rate $\gamma = 120s^{-1}$, as the white circle at $K_p = 0(a.u.)$ signals. It is worth to note here that the assumed equilibrium does not match the experimental one. The

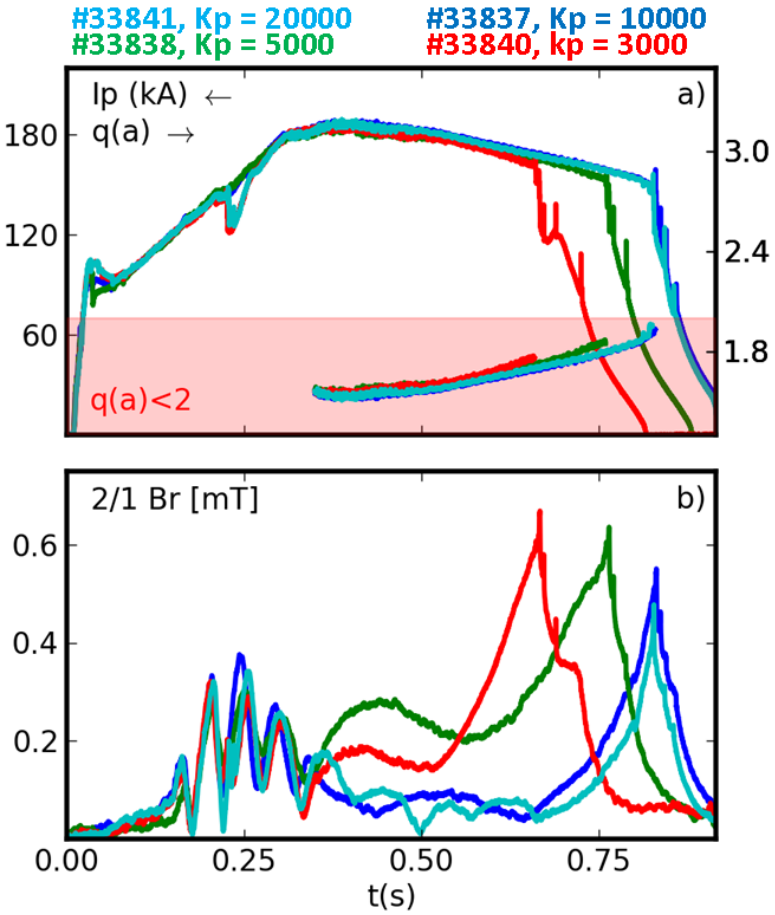

Figure 6.1: Explicit Mode Control - EMC of the $m = 2, n = 1$ RWM instability in RFX-mod circular Tokamak discharges where the plasma current is ramped down

typical experimental growth rates for this mode goes from $15s^{-1}$ to $50s^{-1}$ as Fig. 5.14 shows, thus a direct validation of this predictions is not possible.

The simulations predict that only the CMC algorithm is able to efficiently control the RWM instability in the $q(a) < 2$ regime using radial magnetic field sensors, since its growth rate is completely annihilated by increasing the proportional gain values, whereas the RMC and the EMC are found to succeed only for a slowly growing RWM, up to $\gamma \simeq [70, 40]s^{-1}$ respectively. For higher and higher gain values a saturation of the stabilizing capabilities of these control schemes occurs, that is experimentally observed as well.

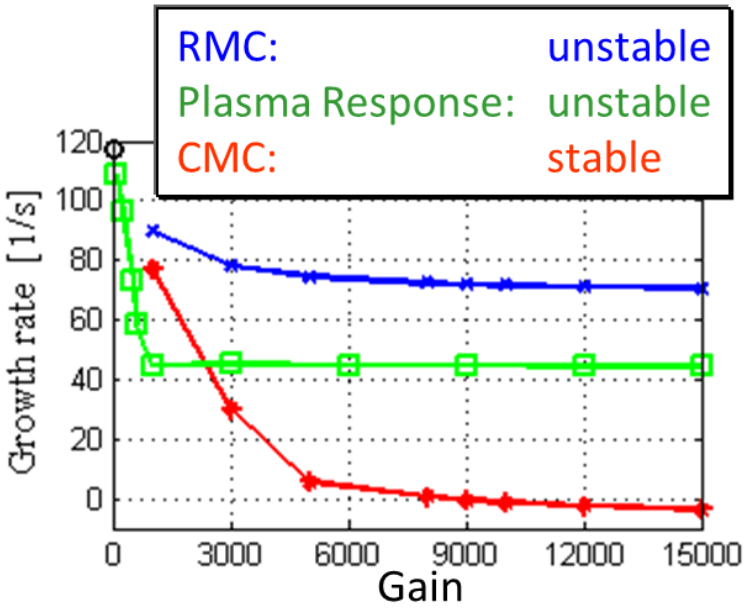

Figure 6.2: CarMa simulations of the Raw Mode Control - RMC, Explicit Mode Control - EMC and the Clean Mode Control CMC performances in RFX-mod circular Tokamak plasmas at $q(a) < 2$

In Fig. 6.3 we tried to estimate the γ critical threshold from the experimental data. Panels b) and c) show how the radial amplitude and phase of the $m = 2, n = 1$ RWM evolve as a function of the increasing edge safety factor in the 4 discharges of Fig. 6.1 from $t = 0.6s$ till the disruption. The plot in panel b) points out that the smaller the proportional gain the smaller the edge safety factor value at which the EMC looses control over the RWM instability. The amplitudes in both blue and cyan case start growing approximately together, suggesting the existence of a $m = 2, n = 1$ RWM growth rate threshold beyond which the EMC fails in maintaining the plasma stability. In these experiments the EMC seems to succeed up to $q(a) \lesssim 1.7$, that corresponds to $\gamma \simeq 30s^{-1}$, as panel a) indicates. This experimental estimate is smaller but compatible with the theoretical one, besides the latter was based on a RWM growth rate of $120s^{-1}$.

In order to further characterize the EMC control, a proportional gain scan experiment has been performed at $q(a) \simeq 1.55$. In this regime the $m = 2, n = 1$ growth rate is sufficiently small for the EMC control to be effective if an adequate proportional gain is applied. Fig. 6.4 reports the time evolution of a) the plasma current and the edge safety factor in the primary and secondary y-axis, respectively, and in panels b) and c) the $m = 2, n = 1$ amplitude and phase of the radial

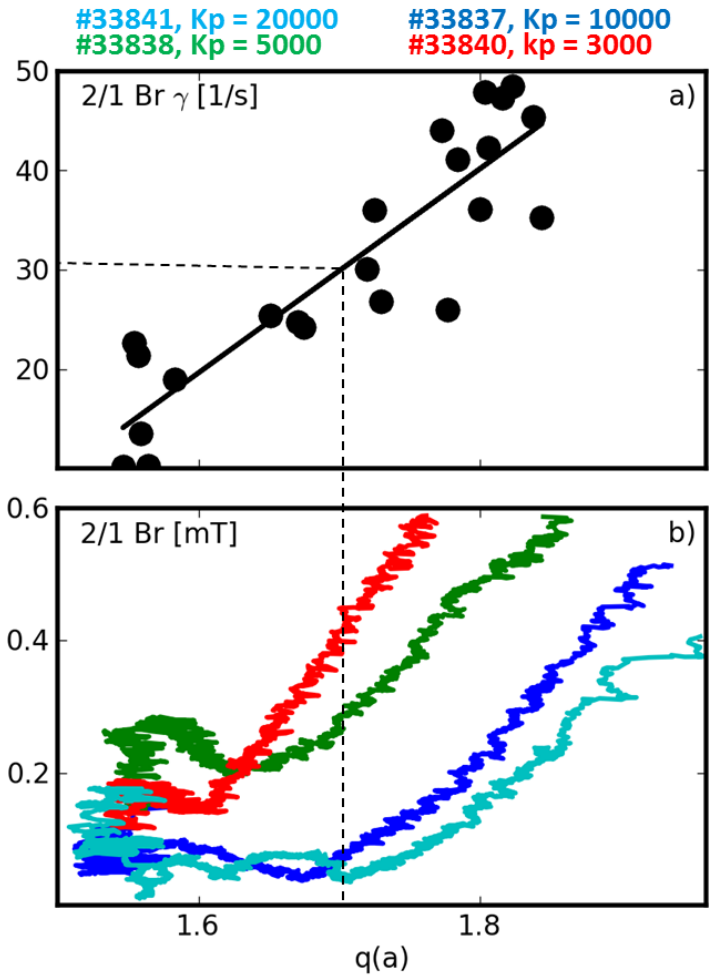

Figure 6.3: The $m = 2, n = 1$ RWM growth rate threshold with the Explicit Mode Control

magnetic field. The EMC feedback control is on in the time interval $t = [0.6, 0.8]s$ for all the discharges except for the blue one, that survives without the active control for $0.15s$, that is the time necessary for the slowly growing RWM to reach an amplitude high enough to trigger the disruption. The proportional gain in the green case, $K_p = 5000(a.u.)$, results to be insufficient to avoid the instability growth whereas the one of the red case, $K_p = 10000(a.u.)$, succeeds, meaning that the minimum stabilizing gain for this regime is between these two values. Once again, a similar performance is observed by doubling the gain as the comparison of the red and cyan shots documents, however panel c) shows that no rotation is induced in this case. The results of all these experiments suggest that removing

the aliasing in the radial measurements by subtracting the entire vacuum coils' field, as the EMC algorithm does, is not a successful strategy for RWM control. Probably this may depend on the unfavorable ratio between the magnetic field produced by the coils and the plasma one.

6.3 Feedback control with poloidal sensors

The brand-new feedback control scheme with poloidal sensors, whose real-time implementation was presented in Chapter 3, has been tested in a gain scan experiment similar to the EMC's one in Fig. 6.4 in the RFX-mod circular Tokamak

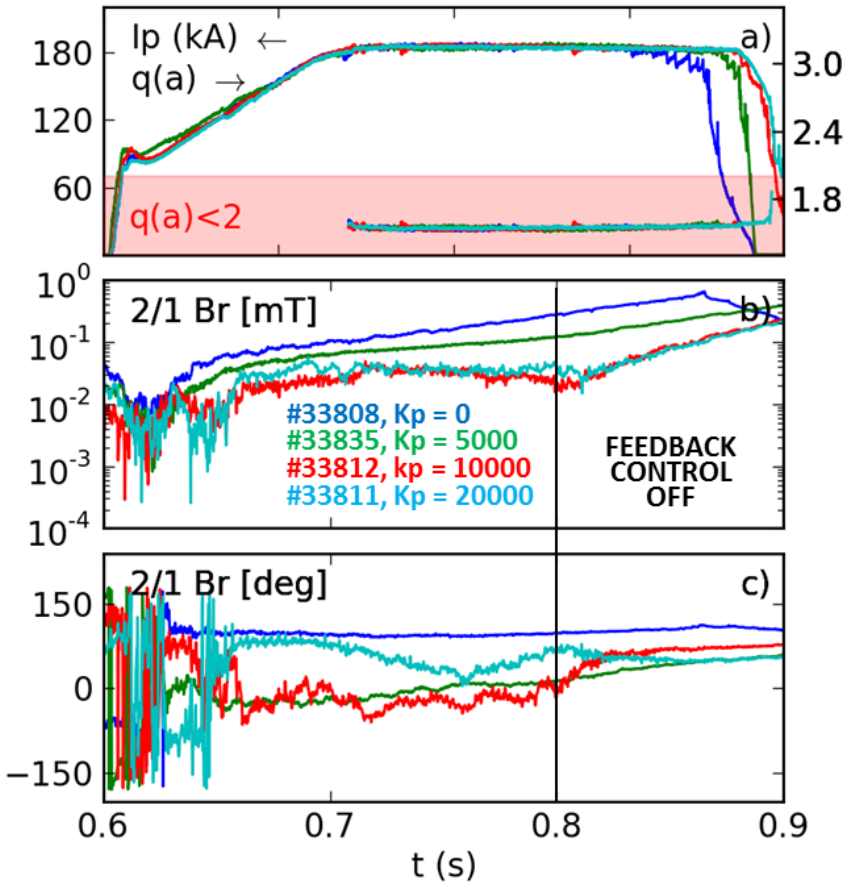

Figure 6.4: Proportional gain scan experiments in the RFX-mod circular Tokamak discharges with the Explicit Mode Control - EMC.

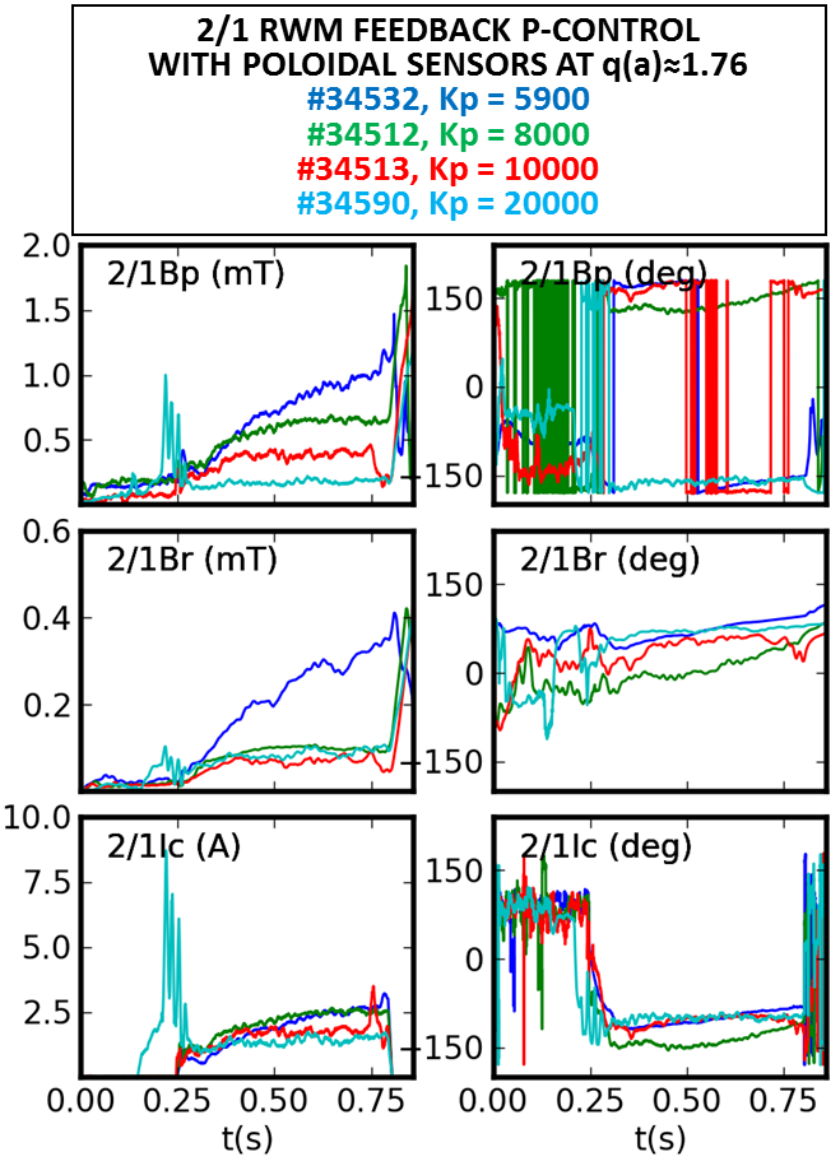

Figure 6.5: Proportional gain scan experiments in the RFX-mod circular Tokamak discharges with the poloidal field control scheme.

discharges at $q(a) \simeq 1.76$. The results of this experiment are reported in Fig. 6.5, that compares the performance of this approach with increasing proportional gains. The figure plots the $m = 2, n = 1$ amplitude and phase of the poloidal and radial magnetic field and of the coil currents. The feedback control is switched on until $t = 0.8s$. The RWM growth is slowed down but not completely suppressed in the blue case, which corresponds to the minimum gain $K_p = 5900(a.u.)$, whereas

an effective stabilization is obtained with gains $K_p \gtrsim 8000(a.u.)$. The higher gain values tested in these experiments resulted in a smaller feedback variable amplitude, the poloidal one, without inducing any high gain instabilities even at the highest gain $K_p = 20000(a.u.)$. It is worth to note here that besides the poloidal field component changes according to the efficiency of the proportional controller the radial and the coil currents' one do not change significantly. The results of this gain scan experiment suggests that $K_p = 20000(a.u.)$ is a good choice for the proportional gain for this control scheme since it is able to maintain the plasma stability against both tearing mode and the RWM one.

6.4 Comparison of radial and poloidal sensor performances

To directly compare the performance of radial and poloidal feedback control schemes in RFX-mod, the EMC, CMC and the poloidal field control have been tested in similar circular Tokamak discharges at $q(a) \simeq 1.76$. The results of these experiments are summarized in Fig. 6.6 that reports the $m = 2, n = 1$ spectral component of the poloidal magnetic field, the radial one and of the coil currents. The three feedback control schemes have been tested with the optimal proportional gain for the chosen equilibrium and all of them succeed in controlling the RWM instability till the end of the pre-programmed feedback window. The EMC, here plotted in blue, is the less efficient algorithm compared to the others since it requires higher currents that however, are just able to keep the RWM amplitude at a relative large amplitude while making the $m = 2, n = 1$ mode rotate.
Interestingly, the CMC and the poloidal field control, that are plotted in green and red, respectively, have a comparable effect. The poloidal field control prescribes coil currents that are slightly higher than the CMC's ones and besides its radial magnetic amplitude remains at a finite value, the poloidal one has basically the same magnitude of the CMC's one.

The results of the RFX-mod experiments, that have been presented in this Chapter, suggest that the active control of the $m = 2, n = 1$ RWM in $q(a) < 2$ circular Tokamak plasma can be performed with the 192 radial sensors as well as with the 32 poloidal ones. The sideband aliasing in the magnetic measurements is unavoidable in any fusion device, due to finite number of the actuators. However, it limits the performance of the radial feedback control more significantly than the poloidal one.

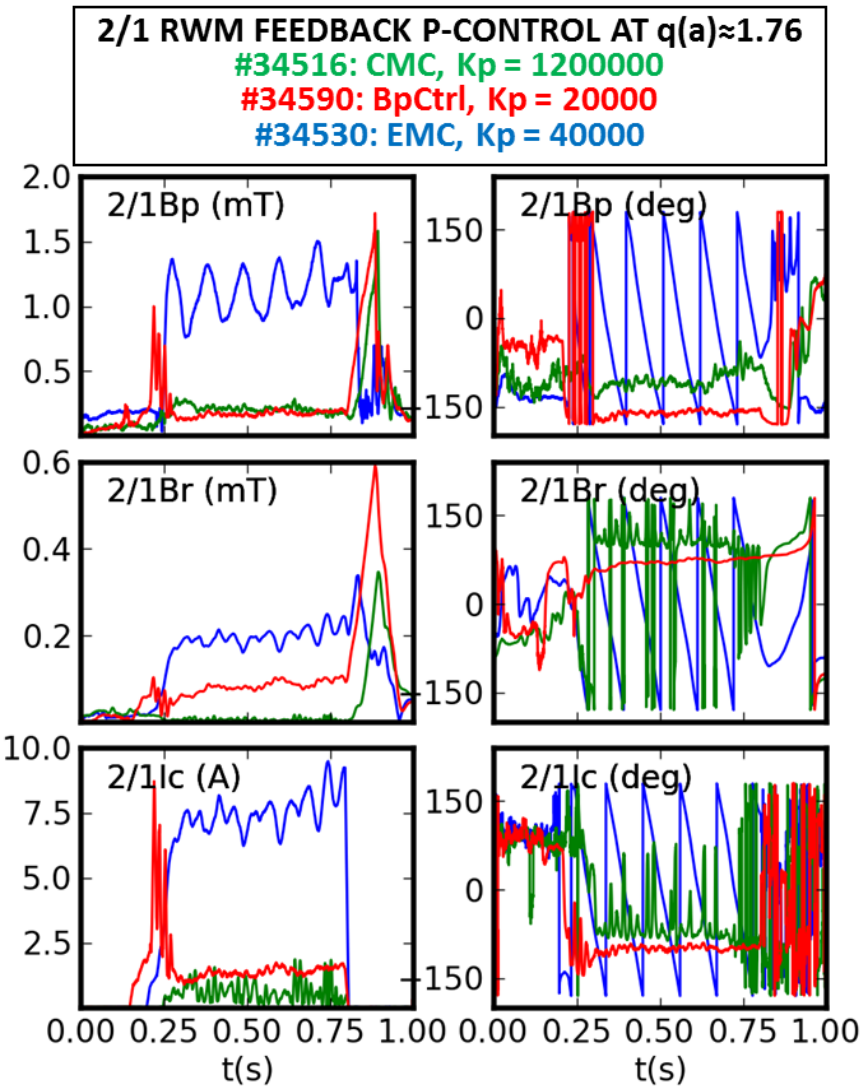

Figure 6.6: Performance comparison of radial and the poloidal feedback control schemes in RFX-mod.

The main disadvantage of the radial CMC algorithm stands in the necessity of a model-based real-time estimate of the sidebands' contribution that is then subtracted to the spectra of the radial magnetic field measurements. In RFX-mod this requirement is satisfied by a real-time algorithm that implements an analytical model that is based on a circular geometry. The radial sensors are located outside the vacuum vessel, thus their measurements are effectively shielded by unwanted high frequency fluctuations. Moreover this location will protect them by the harsh enviroment of future fusion reactors and eases a lot their maintenance too.

6.4. Comparison of radial and poloidal sensor performances

The poloidal sensors, that are installed inside the vacuum vessel, have been generally preferred over the external radial ones in many Tokamak experiments. The sideband aliasing in the poloidal sensors is weaker than in the radial ones thanks to the cancellation of the vacuum coil harmonics for this former field component. As a result, the RMC and EMC algorithms behave essentially in the same way. Being closer to the plasma, a poloidal sensor captures more readily the plasma dynamics. Unluckily its promptness comes at the expense of its highly noisy signal, that sometimes needs to be opportunely processed before being used. The feedback algorithm, however, is less complex than the radial ones and this is an important advantage as far as the real-time implementation is concerned.

In RFX-mod, the poloidal feedback control scheme uses the magnetic measurements from 32 locations only. Beside this, the two sets of sensors show similar performances. However, on the point of view of a fusion reactor, the radial ones, that are located outside the vacuum vessel, will be a probable choice.

7

Helical states in RFX-mod controlled with 3D fields

In RFX-mod Ohmic Tokamak plasmas both $m = 2,\ n = 1$ Resistive Wall Mode - RWM and the $m = 2,\ n = 1$ Tearing Mode - TM, that routinely appear in $q(a) < 2$ and $q(a) > 2$ plasmas, respectively, have a mitigating effect on sawteeth when they grow to small non disruptive amplitudes. This evidence suggested a new pioneering approach to investigate the dynamics of sawteeth: the application of external three-dimensional magnetic fields. This Chapter will present and discuss the RFX-mod experiments where this method has been applied to probe the interaction of the applied magnetic fields with internal MHD dynamics and to mitigate the sawtooth instability.

7.1 Interaction between sawteeth and MHD modes like TM and RWM

The plasma in a fusion experiment is a complex non-linear system, whose dynamics is the result of the interplay of several instabilities that can coexist together. Usually their interaction is not desirable since it can deteriorate the plasma stability by triggering other unstable modes. For instance, sawteeth can provide the seed islands for the onset of NTMs [98]. But, interestingly, some instabilities can have a mitigating effect on others. Such as in the so called Frequently Interrupted Regime - FIR, where the nonlinear coupling between a $m = 4,\ n = 3$ and a $m = 1,\ n = 1$ mode reduces the $m = 3,\ n = 2$ NTM amplitude on a very short time scale, providing a natural preemptive NTM avoidance [99].

In RFX-mod running as an Ohmic Tokamak both $m = 2,\ n = 1$ Resistive Wall Mode (RWM) and the $m = 2,\ n = 1$ Tearing Mode (TM), that routinely appear in $q(a) < 2$ and $q(a) > 2$ plasmas, respectively, are found to interact with the sawtooth instability. The experimental evidence of this effect is documented in Fig. 7.1. The RWM and the TM case are plotted on the left and on the right, respectively. Panel a) reports the time evolution of the plasma current, b) the edge safety factor, c) the $m = 2,\ n = 1$ amplitude of the radial magnetic field normalized to the equilibrium one and d) a core Soft X-Ray (SXR) signal. Panel c) shows that a RWM promptly appears when the feedback control is switched off at $t = 0.35s$, but the effect on the sawtooth oscillations is observed only after $\simeq 50ms$, namely as soon as the RWM amplitude becomes high enough. In this experiment the sawtooth oscillations progressively diminish, till disappearing completely. When $B_r^{2,1}/B_{t0} \gtrsim 0.1\%$ both axisymmetric equilibrium and the plasma performance are sensibly affected as well.

A similar effect is noticed in $q(a) > 2$ plasmas with a TM instead of a RWM. In the experiment reported on the right, a $m = 2,\ n = 1$ rotating tearing mode eventually locks to the wall. As long as its amplitude increases prior to the plasma disruption, the sawtooth oscillations disappear. The mitigation in this case occurs more rapidly than in the RWM experiment, due to the shorter characteristic timescale of the TM instability. This effect has been documented also in COMPASS-C, here the application of $m = 2,\ n = 1$ magnetic perturbations causes the error field penetration. The sawteeth are suppressed because an internal $m = 1$ kink sideband of a $m = 2,\ n = 1$ island develops via toroidal coupling as soon as the mode penetration occurs. Indeed, before mode penetration, the

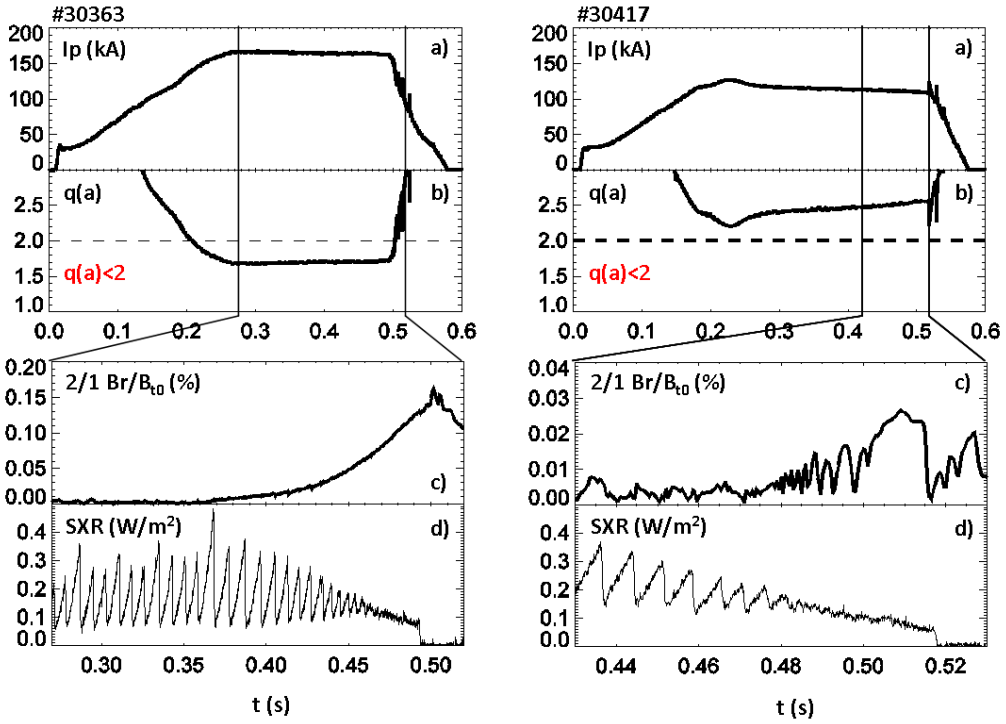

Figure 7.1: RWM (on the left) and TM (on the right) mitigating effect on the sawtooth instability in RFX-mod. Time history of a) the plasma current, b) the edge safety factor and c) the $m = 2, n = 1$ amplitude of the radial magnetic field normalized to the equilibrium field.

$m = 2$ RMP field and its toroidally coupled sidebands are restricted to regions lying outside their own resonant surfaces and thus cannot affect the plasma core [86].

7.2 $n = 1$ external magnetic field to tailor the sawtooth dynamics

The results of all these experiments suggested a new pioneering approach to investigate the sawtooth instability, namely to replace the role of the RWM and the TM instabilities with external three-dimensional magnetic fields having a strong $n = 1$ component.

RFX-mod is a highly suitable device to test this approach because such $n = 1$ magnetic perturbation can be induced in two different ways. The former exploits the possibility to apply in feed forward external magnetic perturbations with user defined helicity. The latter its unique capability to guarantee stable Tokamak

plasma operation at $q(a) < 2$ while keeping the amplitude of the unstable $m = 2,\ n = 1$ RWM at finite values using magnetic feedback.

The target of these experiments is a Tokamak circular plasma at $q(a) < 2$, similar to the one that has been described in Chapter 2, whose plasma stability is guaranteed during the whole flat top by the Clean Mode Control (CMC) feedback algorithm on the $m = 2,\ n = 1$ radial magnetic field harmonic.

A paradigmatic example of the first method is reported in Fig. 7.2. Here a $m = 1, n = 1$ magnetic perturbation of $0.6mT$ slowly rotating at $10Hz$ has been applied in the interval $t = [0.4, 0.7]s$, as it is shown in panels b) and c). Besides the amplitude being just 0.04% of the equilibrium magnetic field B_0, the overall effect on the sawtooth instability is clear and significant. The time evolution of a soft X-ray (SXR) chord passing through the plasma core, that is plotted in panel a), shows that the sawtooth amplitude and period decrease as soon as the perturbation is switched on. In addition, as the $m = 1, n = 1$ mode is rotated in the laboratory frame, a $m = 1, n = 1$ helical core deformation is observed by a fan of SXR lines of sight spanning an entire poloidal cross-section, whose contour plot is reported in panel d).

A similar effect can be obtained with the second method, namely by keeping the $m = 2, n = 1$ RWM at a finite amplitude rather than completely annihilating it. Fig. 7.3 compares two similar discharges where the feedback control was devoted either to fully nullify the RWM amplitude, in black, or to maintain it to about 0.05% of the main equilibrium magnetic field at a fixed rotation frequency of $10Hz$. The amplitude and phase of the resulting $m = 2,\ n = 1$ radial magnetic field are plotted in panel a) and b), respectively.

The SXR contour plot in panel c) refers to the latter case and it does not reveal any particular activity in the plasma core, except for the residual sawtooth oscillations. Conversely the contour plot in panel d), that corresponds to the former case, shows that the discrete sawtoothing activity is replaced by a stationary $n = 1$ deformation in the plasma core, that is locked to the applied $m = 1, n = 1$ magnetic perturbation. Indeed in this case, the $m = 2,\ n = 1$ and $m = 2,\ n = 1$ radial magnetic field phases rotate together, which means that the two modes are coupled by toroidicity.

In order to investigate the role of the perturbation amplitude on the helical deformation in the plasma core further experiments were carried out. In these experiments, the amplitude of the $m = 2, n = 1$ RWM is controlled at finite but increasing constant values in different discharges, as it is shown in panel a) of Fig.

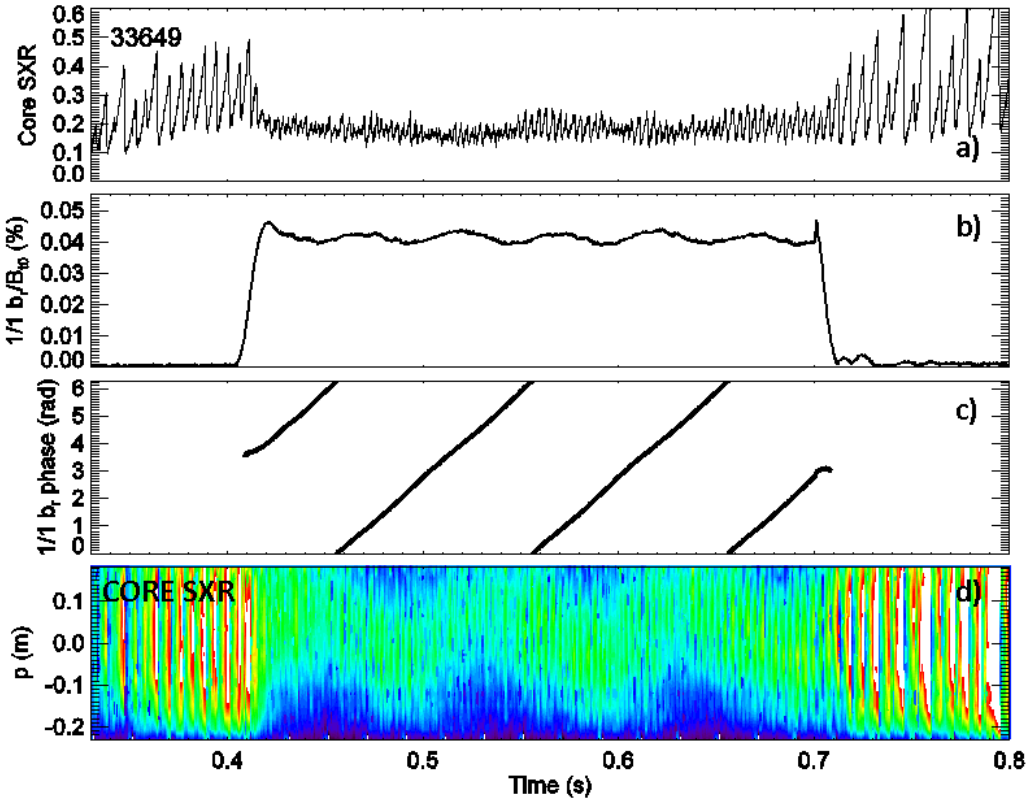

Figure 7.2: Effect of $m = 1, n = 1$ externally applied magnetic perturbation on a sawtoothing plasma in RFX-mod. a) Core soft X-ray (SXR) signal, b) time evolution of the $m = 1, n = 1$ amplitude, c) time evolution of the $m = 1, n = 1$ phase, d) contour plot of a fan of SXR lines of sight passing through the plasma core.

7.4. The helical deformation of the plasma core, whose time evolution is plotted in panel b), is quantified as the displacement from the torus axis of the centroid of every SXR line of sight that spans the plasma core. This panel shows that the higher the amplitude of the magnetic perturbation, the wider the deformation of the equilibrium, at least up to a critical value. The threshold value can be easily inferred from plot c) that reports the average of the displacement for every perturbation amplitude, indeed any 3D field stronger than $\simeq 0.05\% B_0$ would result in the same helical deformation.

These results are highly reproducible and strongly depend on the amplitude of the $m = 2, n = 1$ component of the magnetic field. Fig. 7.5 summarizes the results of a statistic analysis that was carried out on 22 similar Tokamak discharges with $I_p = [148, 157]kA$, $q(a) = [1.75, 1.9]$ and $n_e = [1, 2.5]10^{19} m^{-3}$. The plots in

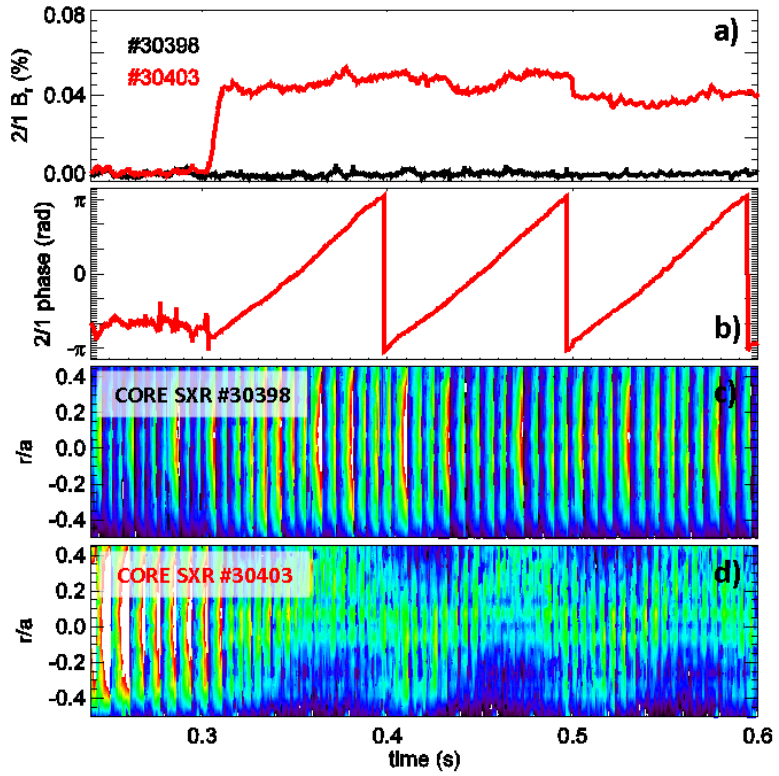

Figure 7.3: Effect of a finite $m = 2, n = 1$ rotating magnetic perturbation on the sawtooth activity in RFX-mod. The reference discharge without any 3D magnetic field in black and with a small perturbation on red. Time evolution of a) and b) $m = 2, n = 1$ amplitude and phase, c) and d) the contour plot of a fan of SXR lines of sight in the plasma core for the black and red case, respectively.

panels a) and b) report the sawtooth amplitude and frequency as functions of the $m = 2, n = 1$ radial magnetic field amplitude normalized to the equilibrium field. Both quantities, that were inferred from the measure of a SXR line of sight passing through the plasma core, are correlated with the perturbation amplitude. The amplitude of sawteeth decreases with the $m = 2, n = 1$ perturbation amplitude, while their frequency increases leading to an overall mitigation of their effect. No major deleterious effects on confinement are observed in these discharges. Thus controlling the $m = 2, n = 1$ mode at finite amplitude in $q(a) < 2$ plasmas has the twofold advantage of counteracting the RWM instability and mitigating the sawtooth one.

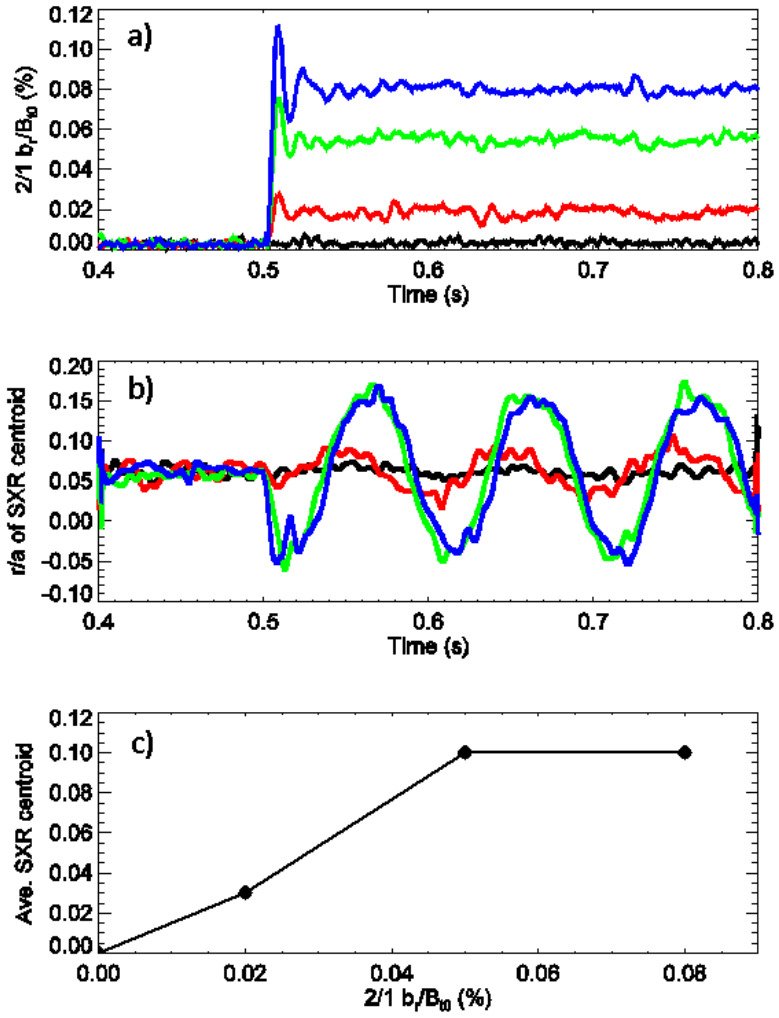

Figure 7.4: Critical magnetic perturbation amplitude and helical deformation of the plasma core. Time evolution of a) the $m = 2, n = 1$ radial amplitude normalized to the main equilibrium field, b) the SXR centroid displacement and c) its averaged value for every perturbation amplitude.

Interestingly, a similar effect is observed also in $q(a) > 2$ plasmas. Fig. 7.6 enriches the experiment reported in Fig. 7.1 with a SXR contour plot focused on the plasma core, highlighting its helical deformation towards the end of the discharge. The faster TM dynamics partially hides the transition towards the helical equilibrium, nonetheless the sawtooth mitigation actually occurs as the time history of a single SXR line of sight, that is reported in panel b), clearly

documents.

This experimental evidence in $q(a) > 2$ plasmas suggests a new disruption avoidance technique. Indeed the appearance of a stationary $m = 1, n = 1$ kink and the mitigation of the periodic oscillations in a otherwise sawtoothing plasma, can be interpreted as precursor events of a plasma disruption. If these evidences are modelled in real-time with a predictive code, then it will be possible to embed a controller that prescribes preemptive actions to avoid or, at least, to mitigate the disruptive event. This development can be carried out with the RAPTOR code as it will be extensively discussed in Chapters 9 and 10.

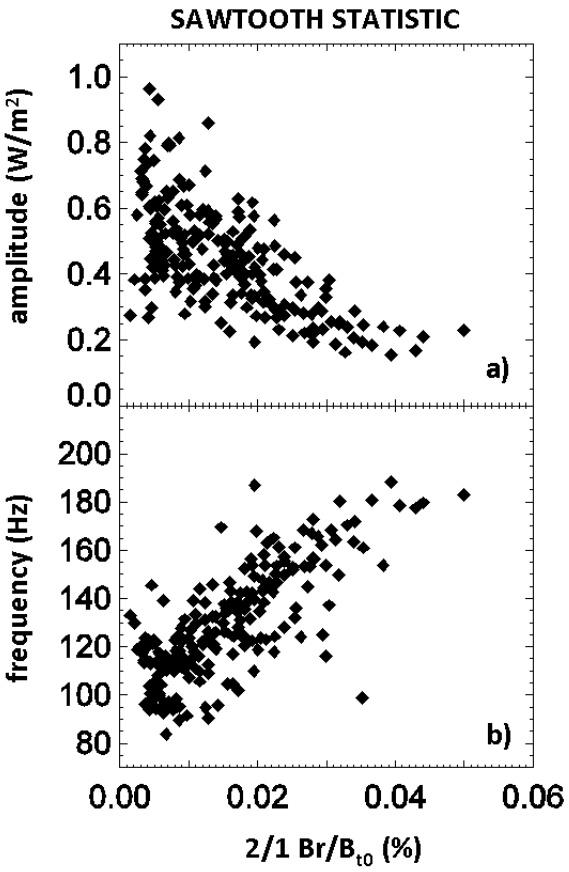

Figure 7.5: Statistical analysis on the interaction of a $m = 2, n = 1$ unstable mode with the sawtooth instability. Sawtooth amplitude a) and frequency b) as functions of the $m = 2, n = 1$ radial mode amplitude normalized to the equilibrium field.

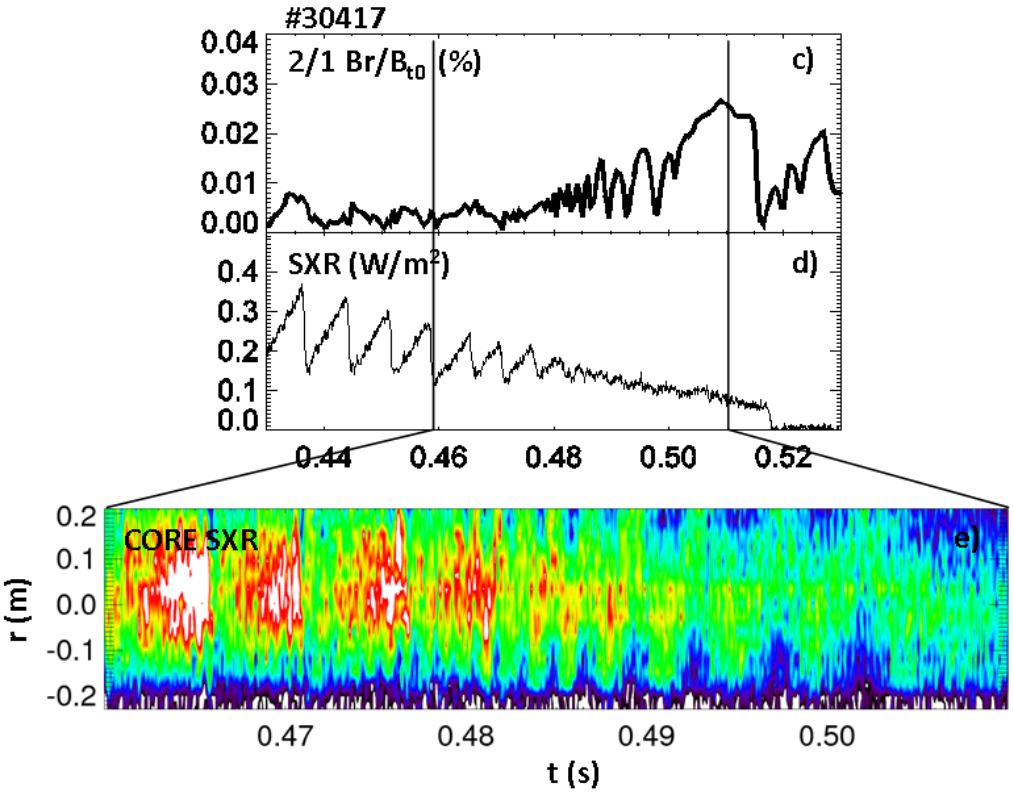

Figure 7.6: Coupling of a locked TM with the sawtooth instability. Time evolution of a) the $m = 2, n = 1$ TM amplitude, b) SXR line of sight in the plasma core and c) the SXR contour plot.

7.2.1. PIXIE3D nonlinear MHD simulations well reproduce the experimental evidences

Three-dimensional magnetic fields with a strong $n = 1$ component can reproducible mitigate the sawtooth oscillation in low edge safety factor RFX-mod Tokamak plasmas. This experimental evidence, together with the helical deformation of the plasma core equilibrium, are qualitatively well reproduced by numerical simulations with PIXIE3D [100], a visco-resistive nonlinear MHD code.
Circular Ohmic Tokamak simulations have been carried out in toroidal geometry, with fixed on-axis Lundquist number ($S = 10^5$) and Prandtl number ($P = 30$), where the two parameters are defined as:

$$S = \frac{\mu_0 L V_A}{\eta}, \tag{7.1}$$

where L is the length scale of the simulated phenomenon, $V_A = B/\sqrt{\mu_0 n m_i}$ is the Alfvén velocity and η the plasma resistivity, and:

$$P = \frac{v}{k}, \tag{7.2}$$

being v and k the kinematic viscosity and the thermal diffusivity, respectively. In these simulations, the aspect ratio is similar to the RFX-mod one, $R/a = 4$, and the initial axisymmetric equilibrium is characterized by an edge safety factor profile with the values on-axis and at the edge respectively of $q(0) = 0.8$ and $q(a) = 1.8$. In addition to this, the boundary conditions of the code have been conveniently modified in order to apply finite 3D magnetic fields at the plasma wall. All the simulations presented here have been performed by neglecting the plasma rotation, but efforts to include it are currently on going. The results of PIXIE3D simulations for the experiments carried out in RFX-mod are summarized in Fig. 7.7.

The figure summarizes the results of four different simulations, where the helicity and the amplitude of the $n = 1$ magnetic perturbations, that have been applied at the wall located in b such that $b/a = 1.1$, have been changed. Panels a, c) report the time evolution and the profile of the on-axis safety factor, the same quantities are plotted for the on-axis radial amplitude of the $m = 1, n = 1$ internal kink mode in panels b, e) and the maximum of the $m = 2, n = 1$ radial amplitude in c, f) ones.

The colour code corresponds to the four simulations. The black case represents the reference scenario, where the application of no external perturbation results in the typical sawtooth dynamics that appears with a narrow $m = 2, n = 1$ island at the plasma edge, as it is shown in the corresponding Poincaré plot in panel c). The island is due to the toroidal coupling between the $m = 1, 2, n = 1$ modes. In the blue case a $m = 2, n = 1$ external perturbation with 0.1% amplitude relative to edge toroidal field is applied. As a result, both sawtooth amplitude and period decrease. The width of the $m = 2, n = 1$ island increases as a consequence of the applied magnetic perturbation and the overlap with the $m = 3, n = 2$ island originates a chaotic layer at the plasma edge as it can be seen in panel i). The green case corresponds to a magnetic perturbation with the same amplitude but $m = 1, n = 1$ helicity. Thanks to a more direct effect on the $m = 1, n = 1$ internal kink mode, this last choice results to be more effective in quenching the sawtooth instability and furthermore it does not trigger any magnetic chaos at the edge,

panel h). Interestingly no evidence of this enhanced efficiency has been observed yet, and experimentally the application of $m = 1, 2, n = 1$ magnetic perturbations gives apparently the same results. In the last case, the red one, the normalized amplitude of the $m = 1, n = 1$ perturbation has been increased up to 0.3%, this value allows the full suppression of the sawtooth oscillations and triggers a steady-state helical configuration of the plasma core, as it can be inferred from the panel j). Here again, the toroidal coupling between the $m = 1, 2, n = 1$ mode originates a stochastic layer in the plasma edge.

PIXIE3D is a valuable tool that qualitatively reproduces the experimental trend but unluckily, for the moment, it is still neglecting the contribution of the plasma rotation, which can come into play in the observed sawtooth mitigation. Indeed the braking effect of non-resonant $n = 1$ externally applied magnetic field has been recently documented in similar RFX-mod Tokamak plasmas [101]. It has been found that a small increase of the perturbation amplitude of around 0.13%, referred to the equilibrium field, leads to a reduction of the toroidal plasma flow of about 50%, while the poloidal one remains unaffected. Since it is well known that the higher the plasma rotation, the longer the sawtooth period [102], it is likely that the observed plasma braking is playing a role in the observed sawtooth mitigation, in addition to the transition towards a helical equilibrium in the plasma core.

The results of the experiments carried out in RFX-mod motivated similar ones in DIII-D, these will be presented and discussed in Chapter 8.

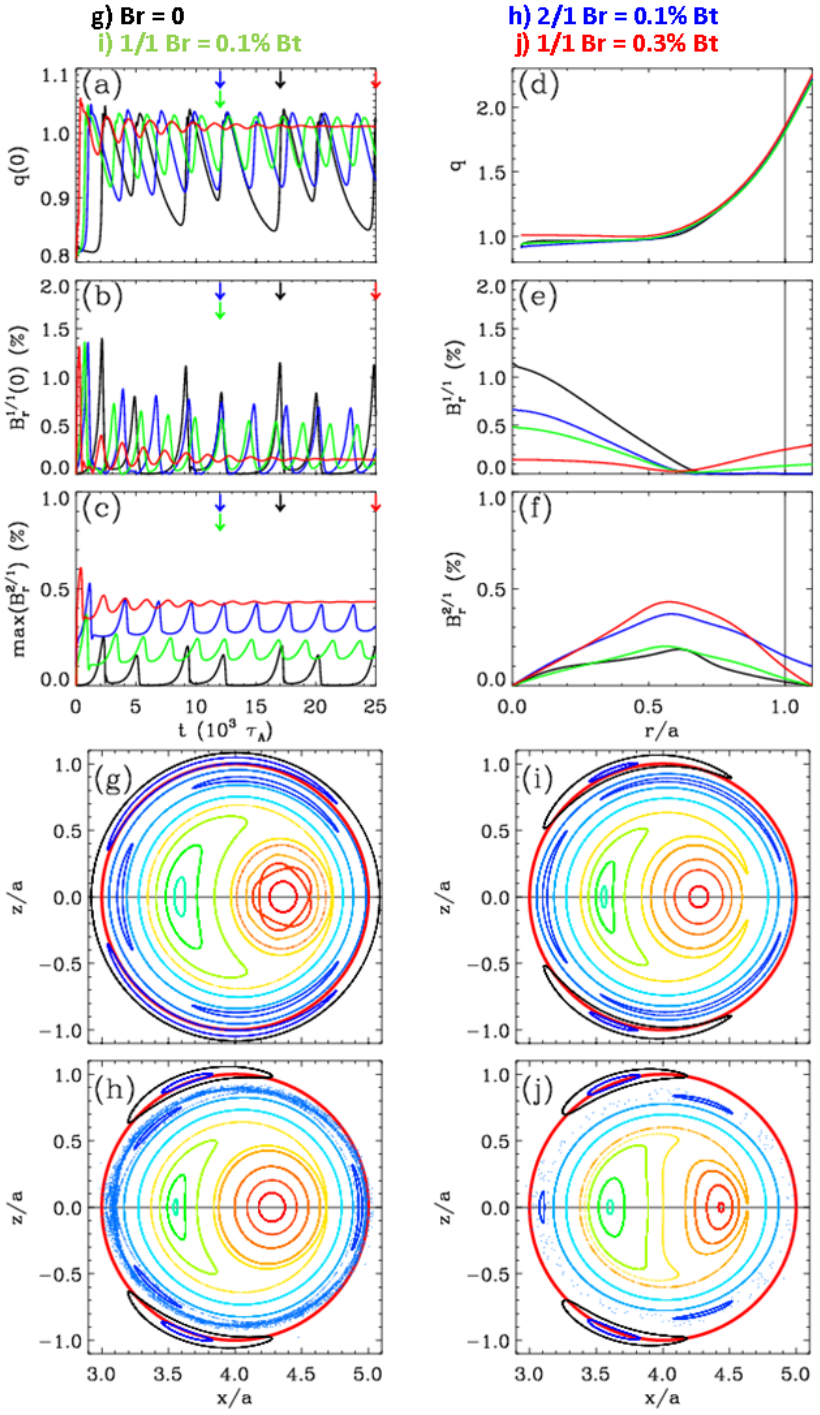

Figure 7.7: PIXIE3D simulations of sawtooth suppression in RFX-mod. a,d) On-axis safety factor time evolution and profile, b,e) on-axis radial amplitude of the $m = 1, n = 1$ internal kink mode time evolution and profile, c,f) maximum of the $m = 2, n = 1$ radial amplitude time evolution and profile g-j) PoincarÃÍ plots of the magnetic equilibria for the cases tagged in the legend above.

8

Coupling of external 3D fields and sawteeth in DIII-D

The mitigating effect of 3D magnetic fields on the sawtooth dynamics, that has been initially studied in RFX-mod, has stimulated further investigations in DIII-D L-mode Tokamak plasmas at low q_{95} values. These experiments show that an effective coupling of the 3D field with sawteeth can both mitigate this instability and induce a NTV torque on the plasma core. These results will be presented and discussed in this Chapter.

8.1 I-Coil phasing scan dynamically changes the poloidal magnetic field spectrum

The success of the RFX-mod results that have been presented in Chapter 7 motivated similar experiments in DIII-D L-mode plasmas at low q_{95} values. This regime has been recently explored in the DIII-D Tokamak, that allowed stable operation at safety factor $q_{95} \simeq 1.9$ in divertor plasmas, by feedback controlling the resistive wall mode for 150 growth times [46, 57].

The plasma target of the experiments that will be discussed in this Chapter is summarized in Fig. 8.1. This figure reports the time history of the plasma current in panel a), the electron density in b) and the safety factor with the $q_{95} < 2$ stability limit highlighted in red in c). It is worth to note here that the latter is slightly above 2.

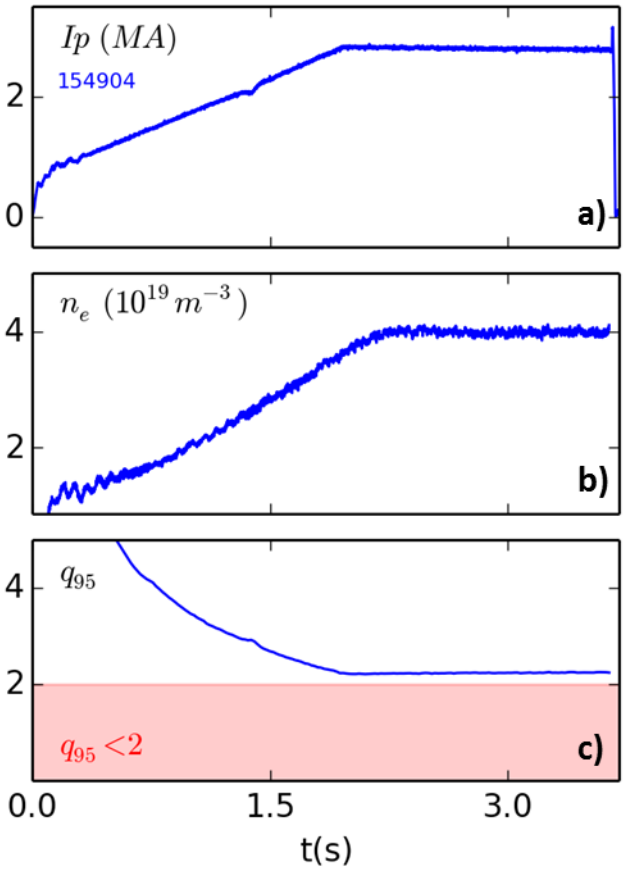

Figure 8.1: Reference plasma target for 3D magnetic field experiments in DIII-D. a) Plasma current, b) plasma density and c) safety factor with the $q_{95} < 2$ stability limit highlighted in red.

In the DIII-D experiments, $n = 1$ magnetic perturbations have been applied both with I and C coils, the latter have been also used to maintain the plasma stability at q_{95} just above 2 with pre-programmed currents for error field correction. The poloidal harmonic content of the applied $n = 1$ magnetic perturbation changes according to the value of the differential phasing between the upper and lower set of I-coils, which can be driven independently both in phase and amplitude. The applied poloidal spectra and its coupling with the internal $n = 1$ kink can be simulated with the Ideal Perturbed Equilibrium Code - IPEC [103]. This code solves free-boundary ideal MHD equilibria when axisymmetric equilibria are perturbed by small non-axisymmetric perturbations. In doing this, it predicts the plasma response based on DCON and VACUUM.

An extensive simulation work performed with IPEC in the design phase of the experiments allowed to identify the I-coil configuration which maximizes the coupling with the $n = 1$ kink mode. The I-coil phasing is defined as the phase difference between the upper and lower I-coils, the applied magnetic spectrum depends on this value. An I-coil phasing of $\sim 200deg$ phasing is necessary to maximize the $n = 1$ plasma coupling, while the $n = 1$ vacuum harmonic is maximized at $\sim 100deg$.

The IPEC predictions have been validated experimentally by dynamically changing the lower I-coil phase, while keeping the upper I-coil one constant. The current amplitudes were constant too. With this simple method it is possible to vary continuously the applied poloidal harmonic spectra in a single discharge to study the effects of the perturbation on the plasma response in the same plasma conditions.

Fig. 8.2 summarizes the main findings of this experiment. Panel a) shows the time evolution of the $n = 1$ component of both I-coil phasing (red), and the phase of the plasma response (blue), that is measured by the set of poloidal magnetic probes located at the midplane of the low-field side of the Tokamak, as it has been described in Chapter 2. The $n = 1$ component of the plasma response, that is reported in panel b), is modulated in amplitude by the I-coil phasing. The maximum plasma response is measured at around $t = 2.8s$. This evidence is consistent with the IPEC prediction. The sawtooth frequency and the plasma rotation in the plasma core are plotted in panel c). Both quantities result to be modulated by the applied perturbation, in particular when the plasma response increases the sawtooth frequency increases as well, while the plasma rotation velocity drops, as it is highlighted by the shaded rectangle in the figure. The sawtooth frequency increases by 50% and the rotation is reduced by 70%, but it is not fully nulled.

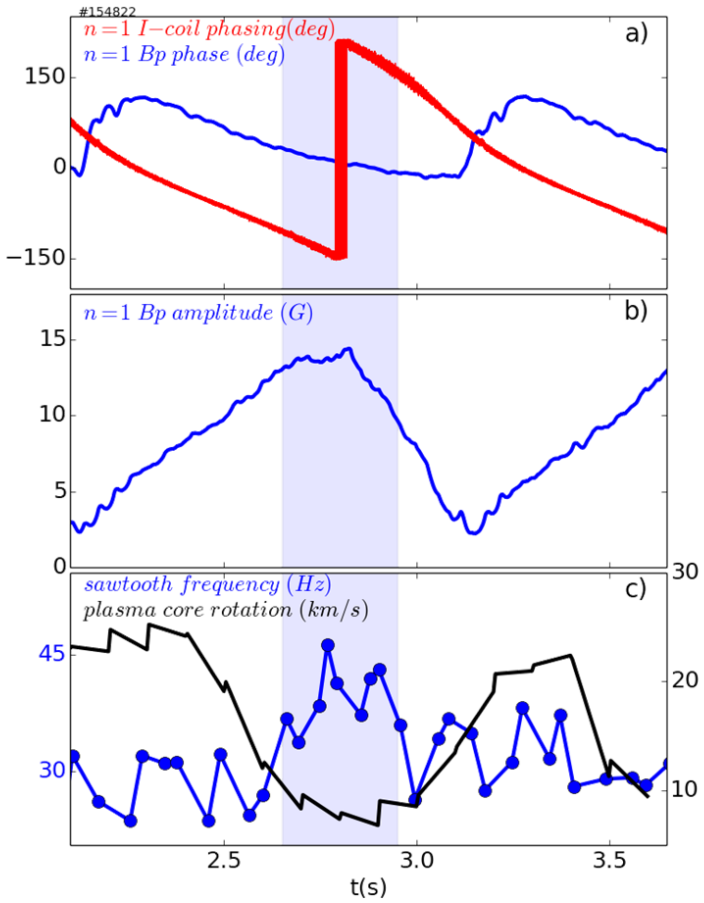

Figure 8.2: DIII-D I-Coil phase scan experiment. Time evolution of a) the $n = 1$ phase of the poloidal magnetic field (blue) and of the I-Coil currents (red), b) the $n = 1$ amplitude of the poloidal magnetic field, c) the sawtooth frequency and the plasma rotation in the core on the primary and secondary y-axis, respectively.

Similarly to RFX-mod, this experiment confirms that the most effective way to affect the sawtooth dynamics is to increase the coupling between the external and the internal $n = 1$ kink.

8.2 $n = 1$ magnetic perturbation brakes core rotation

In order to investigate the plasma dynamics in more stationary conditions, dedicated shots were performed by keeping the I-coil phasing at constant values, namely $20deg$, $100deg$, $200deg$, $280deg$, and increasing the current in the I-coil up to $\sim 2kA$. The results of these experiments are summarized in Fig. 8.3. The

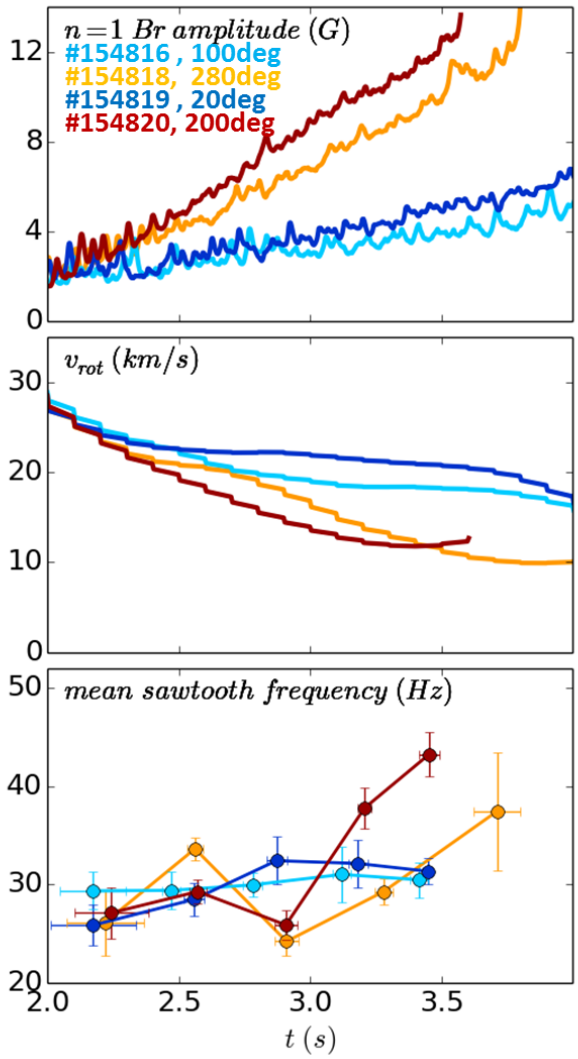

Figure 8.3: Time evolution of a) the $n = 1$ component of the poloidal magnetic field (primary y-axis) and of the I-coil current (secondary y-axis), b) plasma rotation velocity, c) mean sawtooth frequency.

panels report the time evolution of f a) the $n = 1$ component of the poloidal magnetic field (primary y-axis) and of the I-coil current (secondary y-axis), b) the plasma rotation velocity, c) the sawtooth frequency averaged over about six sawtooth periods.

The $n = 1$ coupling in vacuum is maximized at 100 deg (light blue), at this I-coil phasing value all the quantities mentioned above seem to be quite insensitive to the applied field. Similar results have been obtained with the I-coil phasing that minimizes the coupling with the global kink at $24deg$, here plotted in blue. But one

can notice a simultaneous increase of the plasma response, the drag in the plasma rotation and the mean sawtooth frequency in the orange case that corresponds to the phasing which minimizes the n=1 coupling in vacuum. The most evident effect is measured at $200deg$, the value that IPEC predicts to maximize the $n = 1$ coupling with the global kink. At this value the plasma response is the highest, the plasma rotation depletes the most and the sawteeth are more frequent than the ones in all the other cases.

A deeper analysis on the last case, the one with the largest effect on sawteeth, revealed that only the inner plasma volume slows down as the perturbation grows in amplitude. Fig. 8.4 reports the time evolution of the plasma current (black) and q_{95} (blue) in panel a), together with a zoom of the electron temperature (black), as it has been measured by a central Electron Cyclotron Emission (ECE) diagnostic, and the $n = 1$ component of the I-coil currents of the applied magnetic perturbation (blue) in panel c). Panel d) and e) report the sawtooth frequency and the energy confinement time, respectively. It is worth to note here that the application of the external magnetic field during the stationary phase of the plasma flat-top had a clear mitigating effect on the sawtooth instability, whose amplitude and period start decreasing when the I-coil current is higher than 1.3kA. A second interesting effect of the field appeared in the plasma rotation, whose profile is reported in panel b) for different time instants as the colour code suggests. From this plot it is clear that the higher the perturbation amplitude, the lower the plasma rotation in the inner plasma volume. But besides this significant braking, the energy confinement time remains constant, as it can be seen in panel e) and so the normalized β, not shown here, does, meaning that the perturbation is not deteriorating the plasma confinement at least in L-mode.

The robustness of the technique is confirmed by Fig. 8.5, which is a representative example of a series of experiments where the applied magnetic field was repeatedly switched on and off. The figure reports the time evolution of a) the plasma current (black) and q_{95} (blue), together with an zoom of b) the $n = 1$ component of the I-coil current amplitude (black, primary y-axis) and phase (blue, secondary y-axis), c) the central electron temperature, d) sawtooth frequency and e) the EFIT equilibria in the two time instants indicated with a black and pink dashed line, respectively, in panel a). This plot shows that the applied magnetic field has a reproducible effect on the sawtooth instability without any strong impact on the plasma equilibrium as the comparison of the EFIT reconstructions at the minimum and maximum field amplitude points out. The time evolution

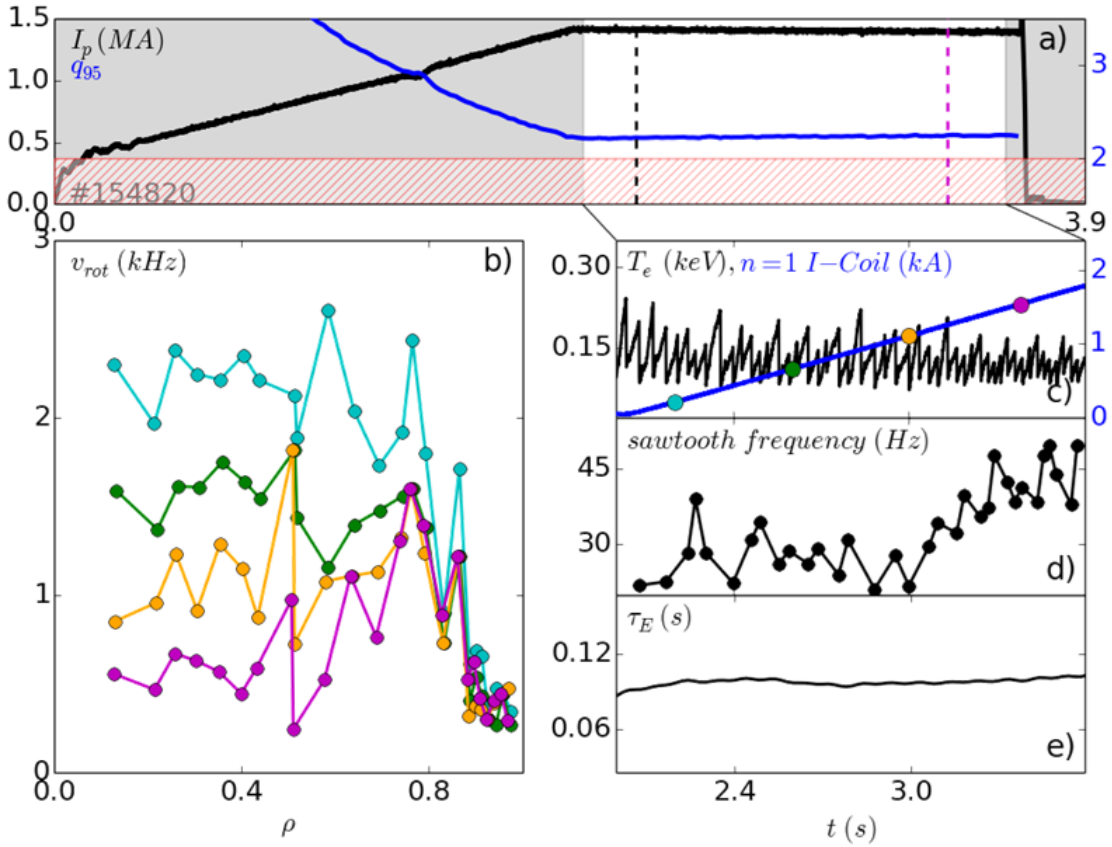

Figure 8.4: Time evolution of a) the plasma current (black) and the q_{95} (blue), b) plasma rotation profile in 4 different time instants, an zoom of c) the central electron temperature (black, primary y-axis) and the $n = 1$ component of the I-coil current (blue, secondary y-axis), d) sawtooth frequency and e) energy confinement time.

of the plasma rotation results to be modulated by the applied ON-OFF magnetic perturbation as well.

The global effect of the applied $n = 1$ magnetic perturbation on the plasma rotation profile, as it was measured by the charge exchange recombination spectroscopy, is reported in Fig. 8.6 for the three different cases discussed above, namely Fig. 8.2, Fig. 8.4 and Fig. 8.5. Panels a) and b) refer to the minimum and maximum $n = 1$ coupling with the global kink, respectively. The comparison of these two plots points out clearly the essential role of the coupling in the observed plasma braking. The plasma rotation profile is strongly modulated in both plots in panel c) and d), in the former the modulation is due to the switching on and off of the magnetic perturbation, that is applied in the same condition of panel b), while in the latter the tuning results from the dynamically changing $n = 1$

coupling that is obtained in the phasing scan experiment.

8.3 Non-linear dependence of the plasma rotation on the $n = 1$ magnetic perturbation

Further analyses performed with Ideal Perturbed Equilibrium Code IPEC point out that the dependence of the plasma rotation on the coupling is not linear. Fig. 8.7 shows the time evolution of the angular momentum, the applied I-coil currents

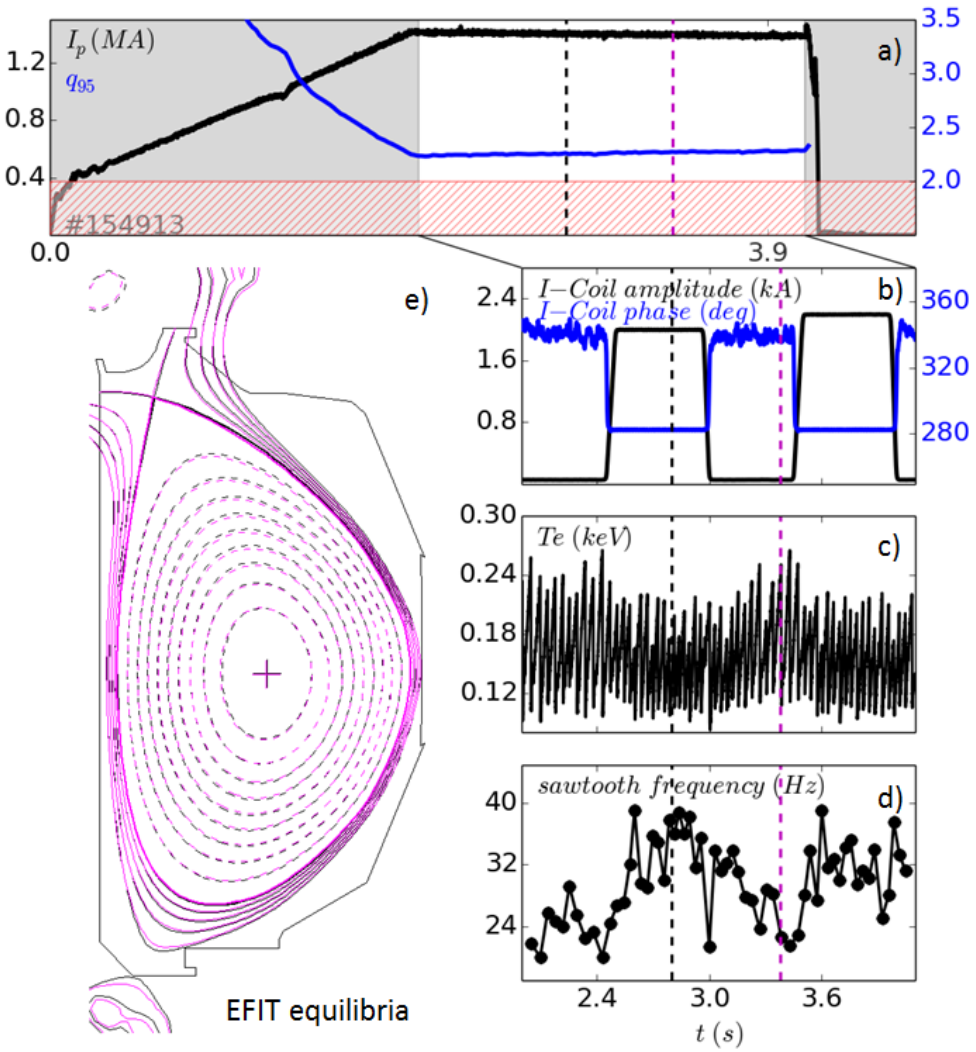

Figure 8.5: Time evolutions of a) the plasma current (black) and the q_{95} (blue), an zoom of b) the $n = 1$ component of the I-coil current amplitude (black, primary y-axis) and phase (blue, secondary y-axis) c) the central electron temperature, d) sawtooth frequency and e) the EFIT equilibria in the two time instants identified with a black and pink dashed line in panel a).

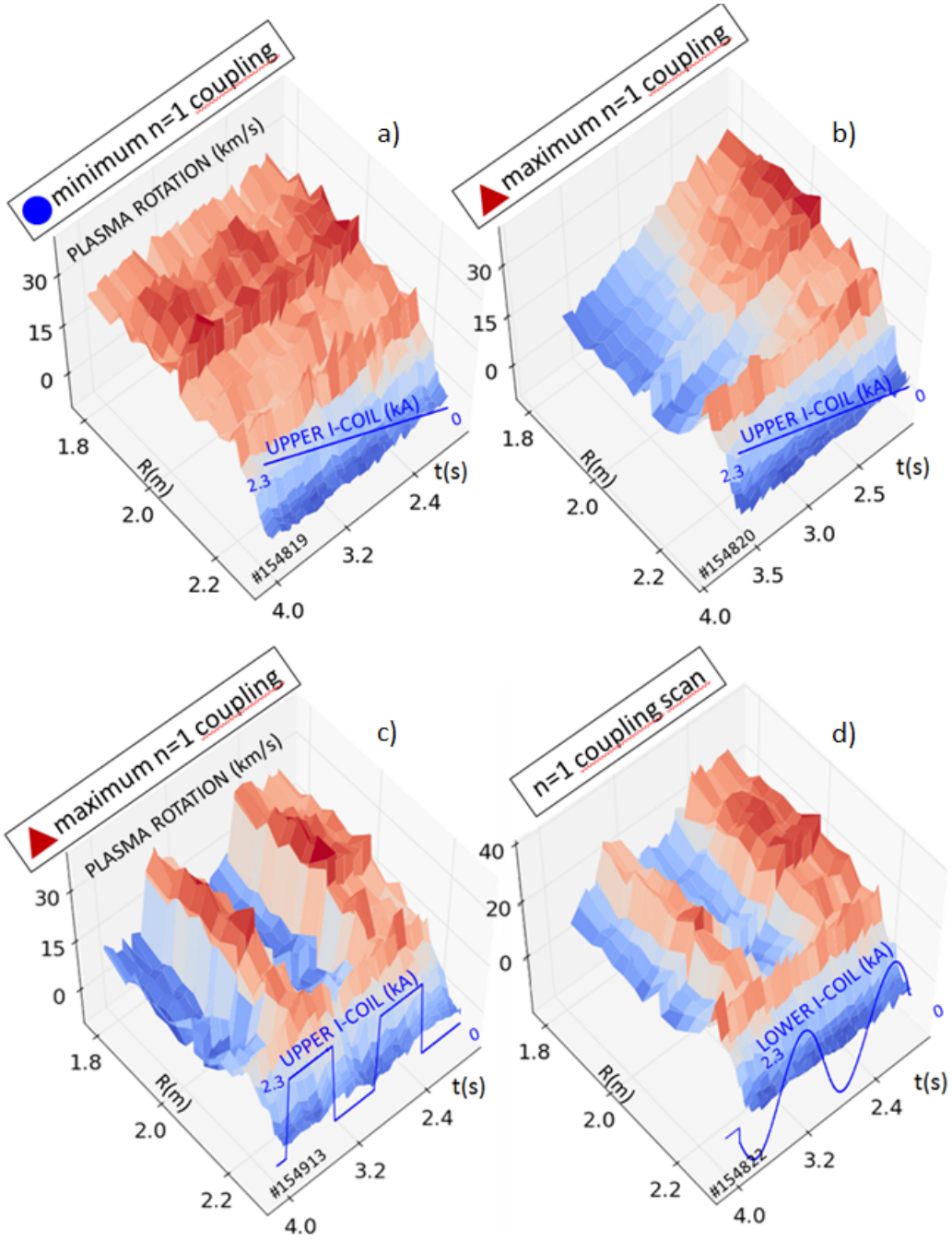

Figure 8.6: Time evolutions of the plasma rotation profiles for different I-coil phasing set-ups. a) minimum $n = 1$ coupling with the global kink, b) maximum $n = 1$ coupling with the global kink, c) maximum $n = 1$ coupling with the global kink in ON-OFF experiments, d) dynamically changing $n = 1$ coupling in the I-coil phasing scan experiment.

and the so called overlap, an IPEC estimate of the resonant field coupling that includes the plasma response. This plot shows that at the minimum coupling, the

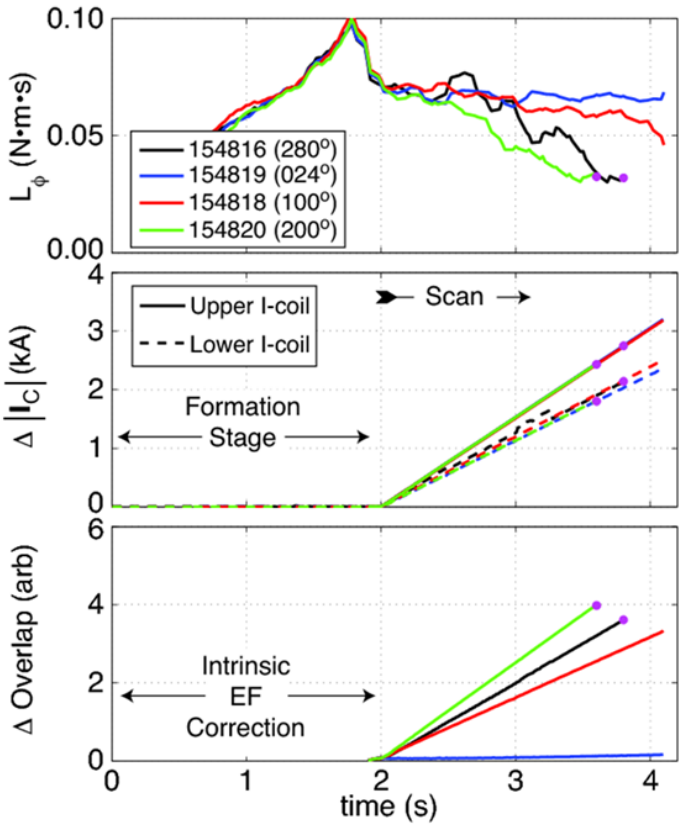

Figure 8.7: Time evolutions of a) the plasma angular momentum, b) the upper and lower I-coil currents, c) the IPEC overlap.

blue case, the angular momentum remains basically constant. As the coupling increases the momentum starts decreasing as expected, but interestingly it does it in a non-linear way. Indeed the red case is breaking less than expected. The reason why this happens is still currently under investigation.

In order to put light on the mechanisms that may explain the observed plasma braking, some numerical simulations were performed with the Perturbed Equilibrium Nonambipolar Transport - PENT code [104] to estimate the contribution of the Neoclassical Toroidal Viscosity - NTV torque. The synergy between IPEC and PENT codes allows to obtain a picture of the plasma, that accounts for the NTV torque, the resonant field coupling and the vacuum poloidal spectrum, as function of the applied I-coil phasing as it is depicted in panel a), b) and c) of Fig. 8.8, respectively. These simulations show that the higher the coupling the stronger the NTV torque, thus it is likely that this force is contributing to the observed braking in the plasma core. In addiction, the reconstruction of the vacuum

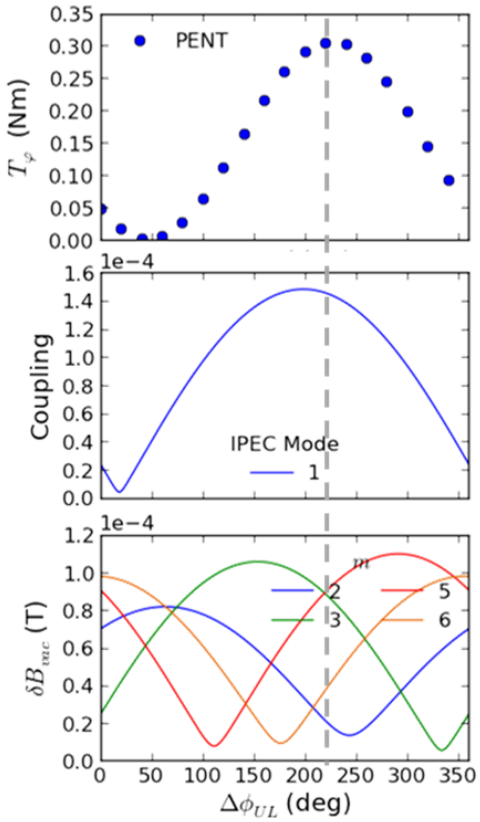

Figure 8.8: IPEC/PENT reconstruction of a) the NTV torque, b) the resonant field coupling, c) the vacuum poloidal spectrum as function of the applied I-coil phasing.

poloidal spectrum confirms the important role of the plasma response, indeed the blue $m = 2$ vacuum harmonic is peaked quite far from $200deg$ which is the phasing that maximizes it.

The figure reported in Fig. 8.9 summarizes the main results of the experiments performed in diverted DIII-D plasmas. The angular coordinate in the polar plot corresponds to the I-coil phasing values tested during the experiments. The two inner rings are the results of IPEC/PENT simulations, as highlighted by the grey shade. The first one represents the coupling between the internal kink and the applied $n = 1$ magnetic field, the second one the NTV torque. The outer ring is the $n = 1$ component of the poloidal magnetic field as it has been measured during the I-coil phasing scan experiment in shot #154822. The colour bar with the relative amplitudes of the different quantities is reported below. The maxima of the three above mentioned quantities are well aligned at around $200deg$, meaning that the plasma response and the plasma braking in the core are strongly correlated with the

coupling effectiveness. The four contour plots located along the edges correspond to the 2D map of the plasma response at different I-coil phasing values, as it is indicated in the figure. If one follows the evolution of these contours as the I-coil phasing is changing, it is easy to notice that the plasma response amplification is well parametrized by the $n = 1$ coupling. The plasma response is localized in the core and the structure remains constant during the phase scan suggesting the dominant contribution of a single eigenstructure.

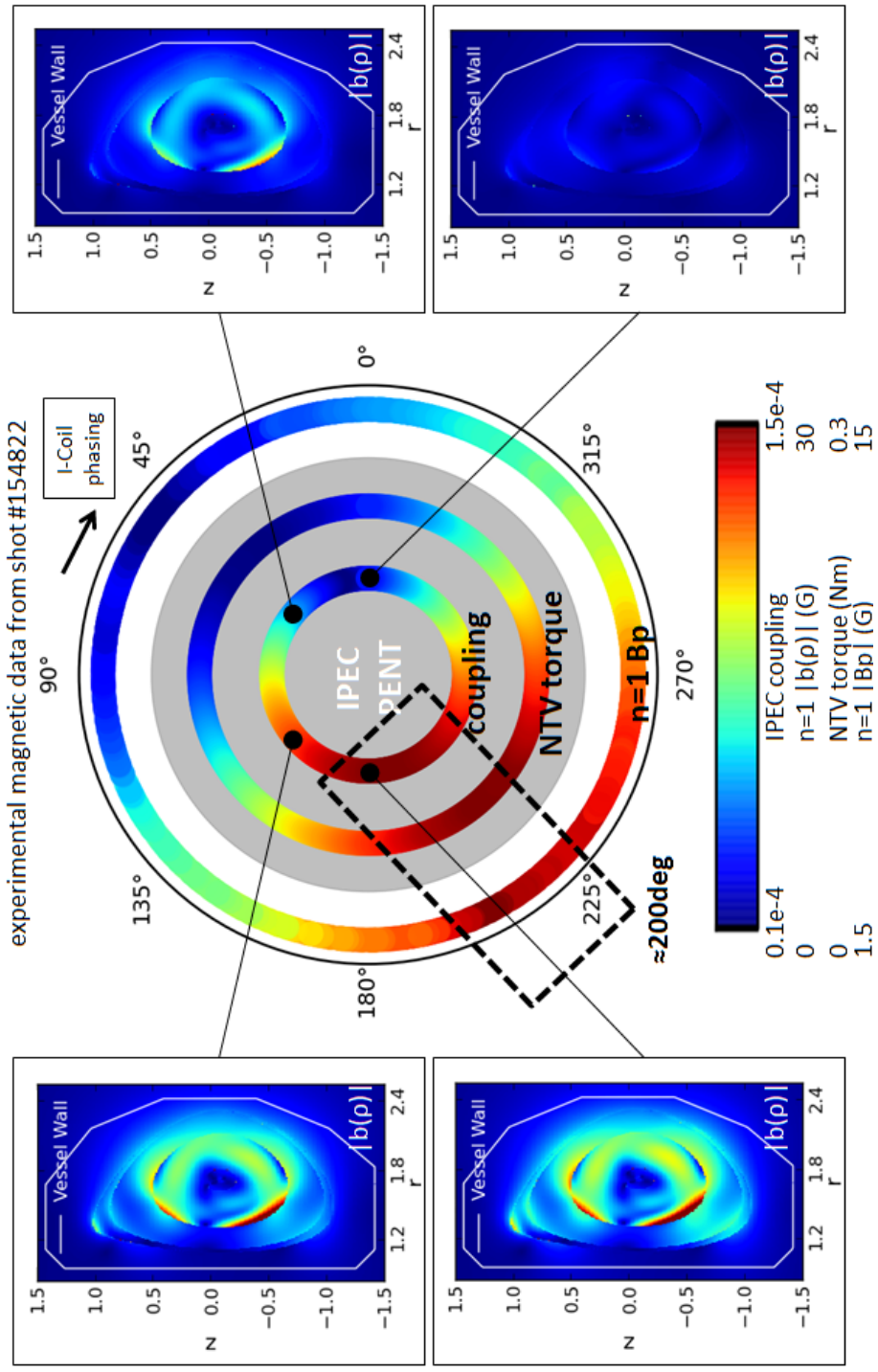

Figure 8.9: Summary of DIII-D experiment results. Polar plot, from inside to outside: the $n = 1$ coupling between the applied 3D magnetic field and the kink mode, the NTV torque and the $n = 1$ component of the poloidal magnetic field as it has been measured during the I-coil phasing scan experiment in shot #154822. Contour plots along the edges: the 2D plasma response at four different I-coil phasing values.

8.3. Non-linear dependence of the plasma rotation on the $n = 1$ magnetic perturbation

II

INTEGRATED REAL-TIME MODELLING OF PLASMA DYNAMICS AND SAWTOOTH CONTROL

9

Real-time plasma state reconstruction with RAPTOR

A safe and efficient plasma operation of a fusion device requires a real-time control of many plasma parameters. Part of them, like the radial profile of the current density, are generally not accurately measured in experiments. Moreover future reactors will rely only on a limited number of diagnostic measurements due to the harsh environment of their vacuum vessel, where generally many diagnostic components are located. This partial knowledge of the plasma state can be completed if the missing data are reconstructed from the available measurements with a simplified model, that has to be complex enough to reproduce all the plasma dynamics but light enough to be embedded in a real-time framework. Once this is achieved, the new data can be used to supervise and actively control the plasma state. The real-time RApid Plasma Transport simulatOR - RAPTOR [F. Felici, Nuclear Fusion, 51, 083052 (2011)] state observer algorithm is a possible answer for this call. This Chapter will provide an overview on this model-based plasma state reconstruction algorithm and it will describe its recent integration in the ASDEX Upgrade Discharge Control System.

9.1 Overview on the RAPTOR code

The real-time state observer RApid Plasma Transport simulatOR - RAPTOR algorithm was originally developed, tested and validated on the TCV Tokamak, as reported in [105, 106] and it has been recently implemented in the real-time control system of the ASDEX Upgrade Tokamak [107]. This algorithm combines many diagnostic data with the predictions of a real-time transport code that provides a rapid but accurate profile evolution. Thanks to this synergy, an accurate picture of the plasma state can be obtained every few ms. A summary of the main features of the RAPTOR code will be provided in this Section.

The code evolves two plasma profile quantities, the electron temperature $T_e(\rho, t)$ and the poloidal magnetic flux, $\psi(\rho, t)$, by solving two coupled 1D profile diffusion equations - PDEs. The poloidal flux diffusion equation reads as:

$$\sigma_{//}\frac{\partial \psi}{\partial t} = \frac{R_0 J^2}{\nu_0 \rho}\frac{\partial}{\partial \rho}\left(\frac{G}{J}\frac{\partial \psi}{\partial \rho}\right) - \frac{V'}{2\pi\rho}(j_{bs} + j_{aux}). \tag{9.1}$$

While the electron transport equation:

$$V'\frac{\partial}{\partial t}(n_e T_e) = \frac{\partial}{\partial \rho} G_1 V' n_e \chi_e \frac{\partial T_e}{\partial \rho} + V' P_e. \tag{9.2}$$

In the first equation: $\sigma_{//}$ is the neoclassical conductivity, ψ is the poloidal magnetic flux, R_0 the plasma major radius and $J = T/R_0 B_0$, being $T(\psi) = RB_\Phi$, is the normalized poloidal current flux function that accounts for the diamagnetic or paramagnetic plasma behavior. $\rho = \sqrt{\Phi/\pi B_0}$ identifies a flux surface on the basis of its contained toroidal flux. This quantity be considered as an effective minor radius indeed for a circular Tokamak with a uniform magnetic field B the two quantities coincide. $G_2 = \frac{V'}{4\pi^2}\left\langle \frac{(\nabla\rho)^2}{R^2} \right\rangle$, $V' = \frac{\partial V}{\partial \rho}$ while j_{bs} and j_{aux} are the bootstrap current density and the current drive one, respectively. In the second equation $G_1 = \langle (\nabla\rho)^2 \rangle$, χ_e the heat diffusivity and P_e the power density to the electrons.

The spatial discretization for the PDEs is carried out in RAPTOR with finite elements. This choice, that distinguishes this transport code from others, like ASTRA [108] or JETTO [109], has many advantages like the flexible choice of basis functions, the possibility to implement a non-uniform mesh and to reduce the order of the PDEs by integrating by parts. The basis functions are non-periodic cubic B-splines, whose main feature is the continuity up to the second order derivative. With this choice the PDEs are converted into ordinary differential equations -

ODEs in the basis function space. All the other kinetic plasma profiles, namely the ion temperature T_i, the electron n_e and the ion n_i densities are maintained fixed during the simulation but their time evolution corresponds to the measured one.

The version of the code used in this Thesis work assumes that the flux surface geometry and the enclosed toroidal magnetic flux do not vary in time, but the former approximation has been recently overcome in a new release of the code.

Besides its lightweight, RAPTOR is able to reproduce the plasma dynamics even in advanced Tokamak scenarios because its model includes plasma resistivity, bootstrap current and auxiliary current drive sources as well. The evolution of the former two quantities is obtained by solving neoclassical equations while the non-inductive current drive is modelled by assuming a known spatial distribution that is modulated in time by the actuator power and by a user defined current drive efficiency [106].

In order not to impact on the computational time, the auxiliary heating sources are analytically parametrized as weighted Gaussian distributions. Generally, the width and peak radial position of the curves are fixed user-defined parameters but they can varying in time as well, if any measure is available in real-time.

The RAPTOR transport model is simplified too. The only driving term for the heat flux is the electron temperature gradient, while any convective transport is neglected. These approximations result in a closed-form expression of the heat diffusivity χ_e that reads as:

$$\chi_e = \chi_{neo} + c_{ano}\rho q F(s) + \chi_{central} e^{-\rho^2/\delta_0^2}. \tag{9.3}$$

The neoclassical diffusion term is represented by χ_{neo}, the anomalous diffusion is ruled by the constant c_{ano} and the safety factor q, which takes into account the reduced transport that is generally observed at higher plasma currents, and by the term $F(s)$, that models the improved confinement at low negative shear. Eventually, $\chi_{central}$ and δ_0 are ad-hoc terms that reproduce the experimentally observed flatness of the kinetic profiles in the plasma core. RAPTOR can provide either interpretative or predictive estimates of the plasma state. In the former case it solves only the poloidal flux equation, whereas the evolution of all the other quantities of the model, like the electron temperature and all the other kinetic profiles are inferred from the real-time diagnostic measurements. In the latter, RAPTOR solves a system of two coupled PDEs that rules the evolution

of both poloidal flux and the electron temperature. The simulations presented in this Thesis work refer to this second option.

9.1.1. Integration of RAPTOR in a real-time control framework

In the real-time state observer algorithm, RAPTOR is combined with the experimental data. The minimum set of diagnostic measurements, that are required in real-time to solve the poloidal flux transport equation, includes the plasma current and the electron temperature profile.
The code needs then to be embedded in a real-time framework, where the state observer algorithm is integrated in an active control system as Fig. 9.1 sketches. The actuator command signals, that drive the plasma dynamics in a real experiment, act as references for the state observer algorithm as well. The latter combines them with other pre-processed real-time data, that come from the real-time diagnostics, to fasten the convergence of the code and to give an accurate estimate of the plasma state. The eventual mismatches between the simulated data and the measured ones can be used to estimate the residuals that can signal either diagnostic faults or the imminence of a disruption, to adapt the model parameters in real-time or to supervise the plasma dynamics with the action of an active feedback control.

But the real-time simulation of the plasma state has many other advantages, indeed it can yield information on an arbitrary spatial and temporal scale beyond the sample time and the spatial resolution provided by the diagnostic systems. It

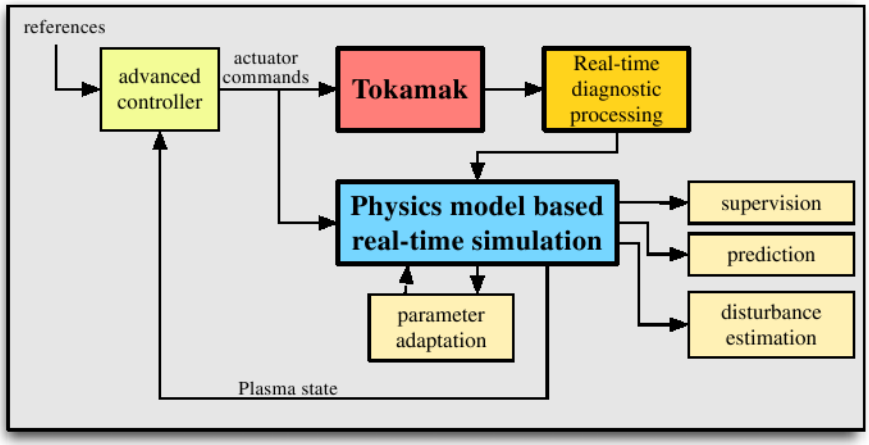

Figure 9.1: Diagram illustrating the envisaged role of a real-time simulation in a Tokamak real-time control scheme. (This figure is taken from [105]).

can automatically filter the data noise when it is not compatible with physically expected variations in the measured signals and it provides an optimized estimation of all those plasma parameters that are not known a-priori in the model, since diagnostic measurements can be compared with the simulated ones to tune them.

One of the main appealing features of a real-time simulator is the possibility to use as a feedback variable quantities that are not directly measurable. Moreover, a real-time simulator guarantees a higher level supervision of the plasma performance compared to a standard feedback control system that relies only on the diagnostic measurements. Indeed a simulator can detect and cope with any diagnostic fault, while maintaining a safe plasma operation and maximizing the quality of the data output. Its potentialities, concerning the plasma control, include also the possibility to perform predictive simulations that, maintaining the plasma state inside its safety limits, allows to mitigate or even avoid plasma disruptions.

9.2 RAPTOR in the ASDEX Upgrade control system

The state observer algorithm and the RAPTOR code were embedded in TCV [105, 106] but they been recently integrated in the ASDEX Upgrade real-time control system too. A C code was generated by the MATLAB SIMULINK tool and then compiled into an application for the ASDEX Upgrade Discharge Control System - DCS. The final real-time framework is depicted in Fig. 9.2.

In order to provide an accurate estimate of the plasma state at each time step, RAPTOR needs real-time input data as well as additional diagnostic measurements for the real-time correction of its predictions. In ASDEX Upgrade, all these data make up almost 150 real-time signals.

Among these, there are 60 channels of the ECE diagnostic, that are used to correct the model prediction at any time step, the DCR diagnostic that provides the electron density profile for the estimate of T_e, the bootstrap current and many other quantities, the real-time measure of the plasma current that sets the start and the end of the simulation and constraints the magnetic equilibrium, the NBI and the EC auxiliary heating signals and eventually the toroidal magnetic field and the real-time Grad-Shafranov solver that allows RAPTOR to vary the magnetic flux surface geometry in real-time.

Similarly, RAPTOR generates a large number of output signals, that are summarized in the green boxes on the right. Among these the time evolution of the safety factor, the electron temperature and the density profiles, but also many

other quantities that are useful to monitor and control the plasma dynamics, like the magnetic shear profile that is closely related to the sawtooth instability as it will be discussed in Chapter 10.

9.2.1. RAPTOR benchmark with the ASTRA code

As it has been discussed above, in order to be fast enough to run in real-time, the physic model on which the RAPTOR code is built is much simpler than the one of other transport codes, like ASTRA. Despite RAPTOR contains less physics details, it is able to reproduce the same results of more complex codes. A benchmark with ASTRA has been performed in this Thesis work for an ASDEX Upgrade shot.

The main parameters of the shot simulated in Fig. 9.3 are $I_p \simeq 1MA$, $q_{95} \simeq 4$ and $n_e \simeq 8 \cdot 10^{19} m^{-3}$. The figure shows the time evolution of the plasma current and density, the additional power sources, the electron temperature and the on-axis safety factor on the left, while the radial profile of the different quantities at the time instant identified with the black line is reported on the right. The first 4 panels correspond to the input data of the RAPTOR simulation. The radial profile of the EC power sources has been configured with TORBEAM [110], that provides the ASDEX Upgrade EC power heating set up, while the nominal power

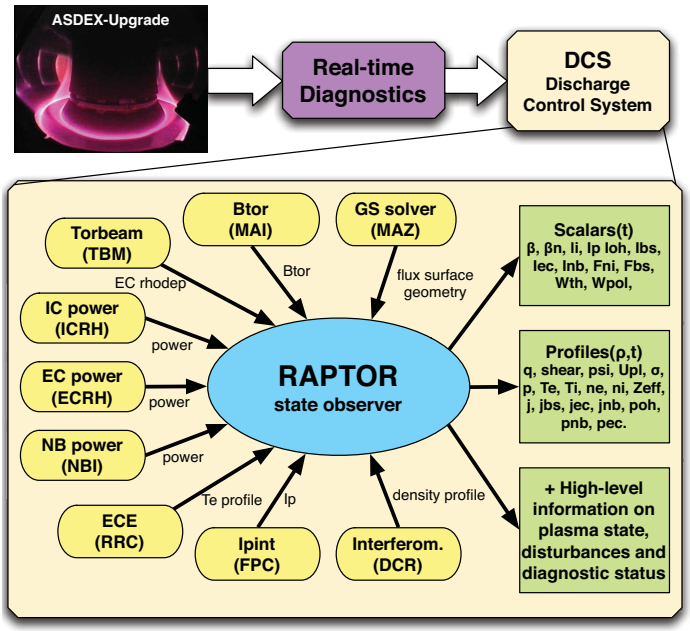

Figure 9.2: ASDEX Upgrade implementation of the state-observer algorithm. (This figure is taken from [107]).

is the measured one. The auxiliary heating systems are analytically parametrized by weighted Gaussian distributions, whose width and location of the peak of the deposition are user-defined parameters. These can either be fixed or change at every time step if the corresponding time evolution is provided. The former option has been used in this simulation. It is worth to note here that, differently from ASTRA, the equilibrium is not changing in time as well.
Both EC and NBI additional heating systems are switched on slightly after 1s. As a consequence, the electron temperature T_e increases. The temperature panel shows that the P_{EC} and P_{NBI} fast gradients are recovered more quickly in RAPTOR than in ASTRA but, eventually the two codes converge to the same value. The reconstruction of the radial profiles are highly compatible as well, proving the reliability of the former code.

9.2.2. Real-time simulation of an ASDEX Upgrade shot

An example of real-time RAPTOR simulation is reported in Fig. 9.4. This plot compares the RAPTOR predictions with the raw experimental measurements and the corresponding offline profile reconstructions. The two data sets are plotted in blue and red respectively. The panels of the first two rows report the time history of some plasma quantities, namely the plasma current, the loop voltage, the electron density and temperature, the EC, NBI and Ohmic power and the corresponding currents. The sixth panel plots the time evolution of the innovation, that is a parameter that estimates the difference between the predicted and the experimental diagnostic measurements[107]. The last three panels show the radial profiles of the safety factor and the magnetic shear, the electron temperature and density at the time instant identified with the black dashed line.

The RAPTOR reconstruction of the electron temperature and density profiles benefits from the real-time availability of the ECE and DCR measurements in ASDEX, while the one of the safety factor relies only on the flux transport model predictions. As a consequence, the former kinetic profiles match quite well the ECE and the Thomson data, that are reported with circles and squares, respectively, while the q profile slightly disagrees with the one evaluated with the off-line Grad-Shafranov solver CLISTE in the plasma centre.

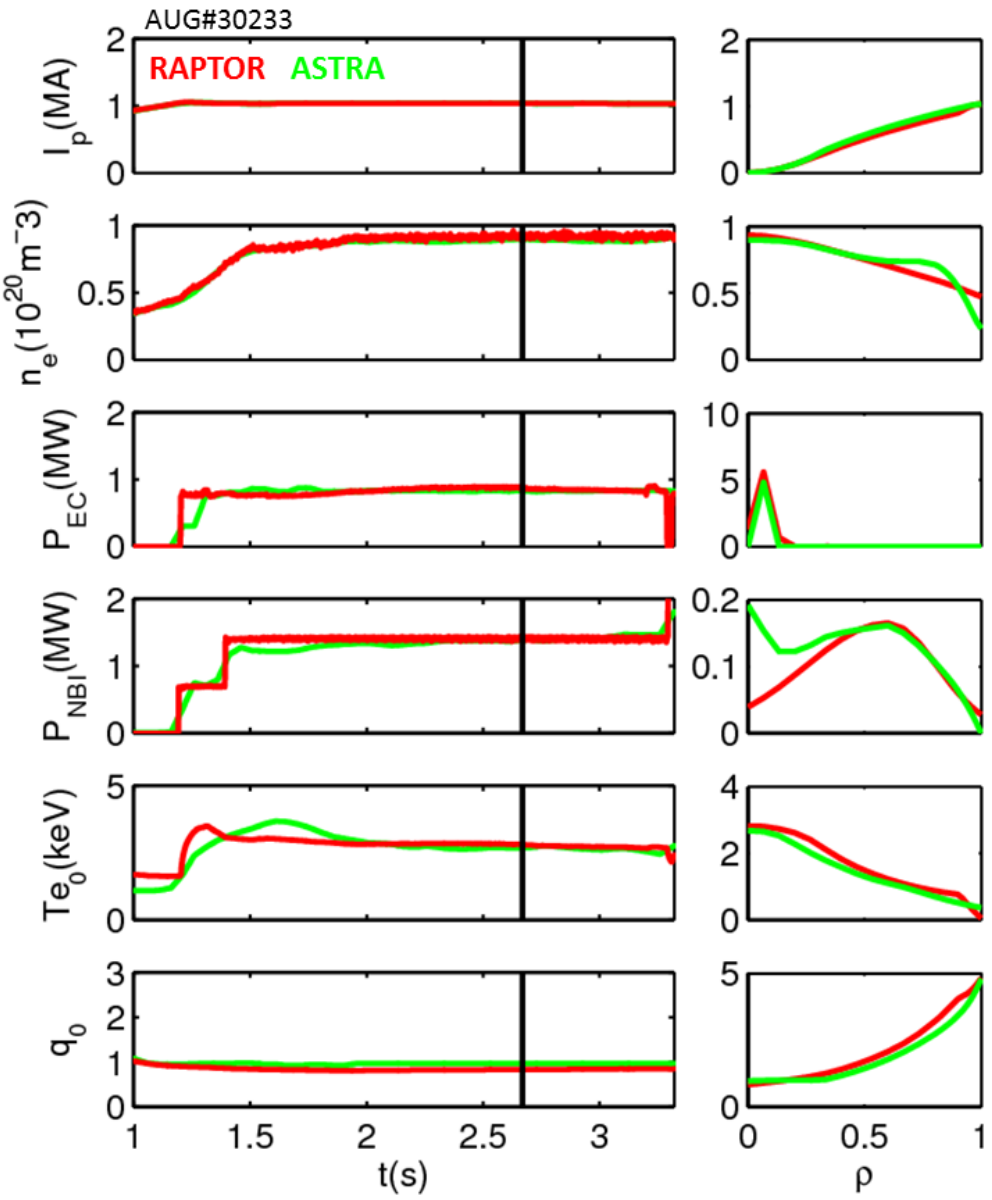

Figure 9.3: RAPTOR (red) and ASTRA (green) benchmark for an ASDEX Upgrade discharge.

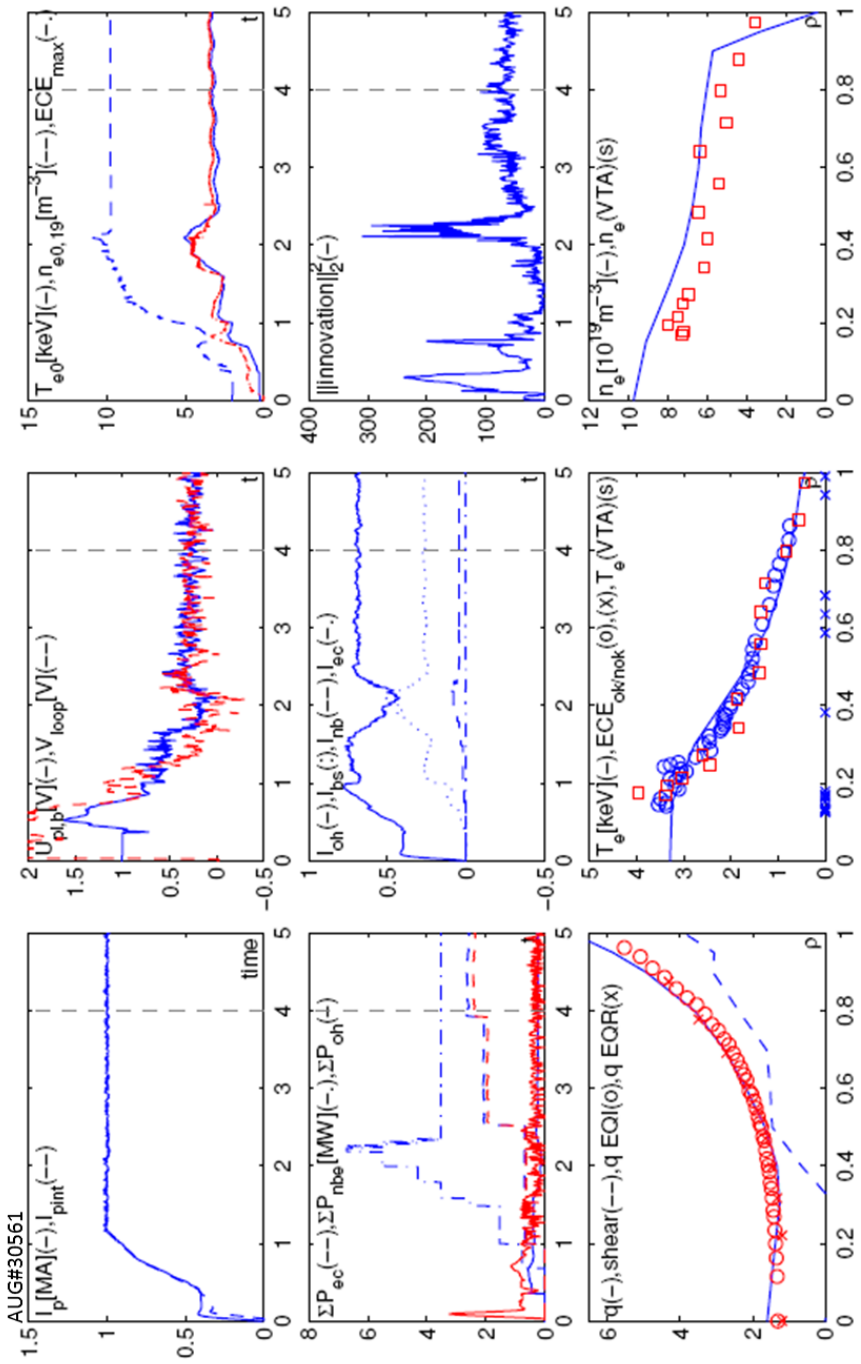

Figure 9.4: The performance of the real-time state observer algorithm in ASDEX Upgrade. The RAPTOR outputs (blue) are compared with off-line experimental data (red).(This figure is taken from [107]).

10

Real-time modelling of the sawtooth instability in RAPTOR

A new module inside the RAPTOR code has been developed during this Thesis, which evolves in real-time the Porcelli's sawtooth model, to include the effects of the sawtooth crashes on the safety factor and electron temperature profiles. This new module is able to provide a reliable prediction of the time averaged sawtooth period in real-time. Thanks to this new module, RAPTOR can now be used to design and control sawtooth locking or pacing experiments using ECRH to avoid NTMs, whose seed islands can be provided by sawteeth. But it can also be used in the direct NTM control with ECCD, due to the improved estimate of the safety factor profile. The description of this module, together with the results of some simulations of ASDEX Upgrade shots, will be discussed in this Chapter.

10.1 Criterion for the sawtooth crash

The crash of a sawtooth oscillation is triggered by the onset of an $m = 1, n = 1$ kink mode, whose dynamics is influenced by many factors besides the MHD ones, like the collisionless kinetic effects related to high energy and thermal particles or non-ideal effects localized in the narrow layer around $q = 1$.

A heuristic model predicts a sawtooth crash when one of the following criteria is satisfied [111] :

$$-\delta\hat{W}_{core} > C_h \omega_{dh} \tau_A, \tag{10.1}$$

$$-\delta\hat{W} > \frac{1}{2}\omega_{\phi i}\tau_A, \tag{10.2}$$

$$-C_\rho \hat{\rho} < -\delta\hat{W} < \frac{1}{2}\omega_{\phi i}\tau_A \text{ and } \gamma_{eff} > \frac{1}{C_*}\sqrt{\omega_{*i}\omega_{*e}}. \tag{10.3}$$

where ω_{dh} is the magnetic drift frequency of the ions, $\tau_A = \sqrt{3R/v_A}$ is the Alfvén time, c_h, c_ρ and c_* are constants of order unity, γ_{eff} is the effective growth rate of the resistive internal kink mode and $\hat{\rho} = \rho_i/r_1$. Two equations rule the change in the kink mode potential energy, namely $\delta W_{core} = \delta W_{MHD} + \delta W_{KO}$ and $\delta W = \delta W_{core} + \delta W_h$, where δW_{KO} is the change in the mode energy due to the collisionless thermal ions, δW_h is the change in energy due to the fast ions and δW_{MHD} is the ideal fluid mode drive.

In auxiliary heated plasmas the three criteria can be replaced by a single one [17] :

$$s_1 > max\left(s_{crit} = \frac{4\delta W}{\xi_0^2 \epsilon_1^2 R B^2 c_{\hat{\rho}} \hat{\rho}}, s_{crit(\omega_*)}\right). \tag{10.4}$$

Once a sawtooth is triggered, the equilibrium is evolved according to a reconnection model that can either be complete, as the one proposed by Kadomtsev, or incomplete. The two models will be described in the following.

10.2 Magnetic reconnection models

10.2.1. Kadomtsev's complete reconnection model

The Kadomtsev's model [112] is built upon two assumptions. Firstly, the magnetic surfaces with equal helical flux ψ_* reconnect and secondly, the toroidal flux is

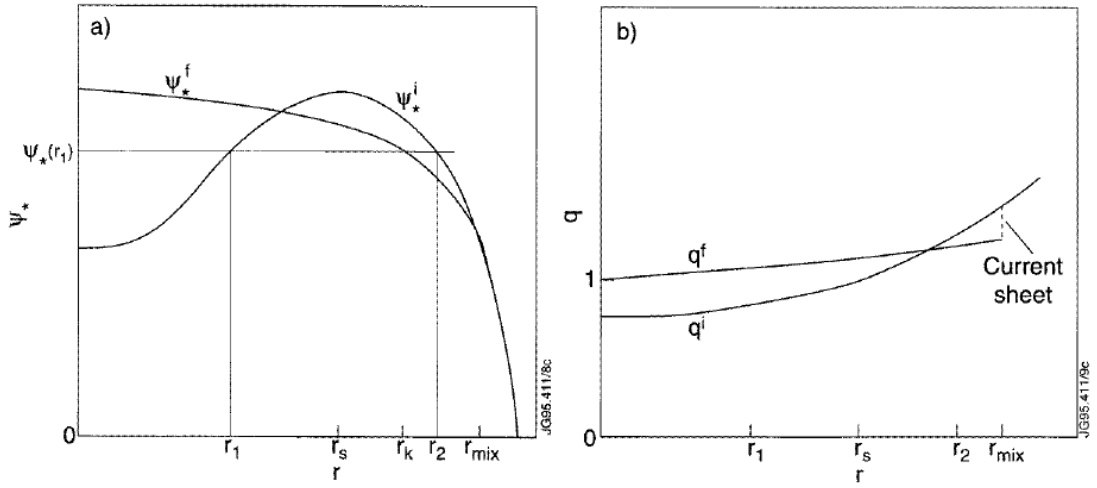

Figure 10.1: Magnetic helical flux before and after a complete reconnection process, according to the Kadomtsev's model: (a) Helical flux function before (ψ_*^i) and after (ψ_*^f) the sawtooth crash. (b) Magnetic winding index before (q^i) and after (q^f) the sawtooth crash. (This figure is taken from [111]).

conserved in the reconnection, that in cylindrical approximation corresponds to the conservation of the cross-sectional area between the reconnecting surfaces. Within these approximations, the normalized flux reads as:

$$\psi_*(r^2) = \int_0^r (q^{-1} - 1) dr'^2. \tag{10.5}$$

Its profile together with the one of the safety factor, is depicted in Fig. 10.1 before and after a sawtooth crash.

Before the crash $\psi_*(r)$ has its maximum at r_s, namely at the $q = 1$ surface. For any r_1 there is a radius $r_2 > r_s$ such that $\psi_*^i(r_1) = \psi_*^i(r_2)$. These are the two surfaces that reconnect during a sawtooth crash.

In so doing an $m = 1$ island grows so that each flux surface within r_s moves towards this radius and beyond till touching and reconnecting with the external surface at r_2 that has an equal helical flux, as it is reproduced in panel b) of Fig. 10.2.

As a consequence of the toroidal flux conservation, the area A_X, that is enclosed inside the separatrix, has to equal the annular one between the initial positions of the two reconnecting surfaces and this equivalence has to hold even after the reconnection, when the area deforms till the process completes. Eventually, when the poloidal symmetry is restored, each reconnected surface becomes a circle of radius $r_k^2 = r_2^2 - r_1^2$ with $\psi_*^f(r_K) = \psi_*^i(r_1) = \psi_*^i(r_2)$, as it is shown in panel a) of

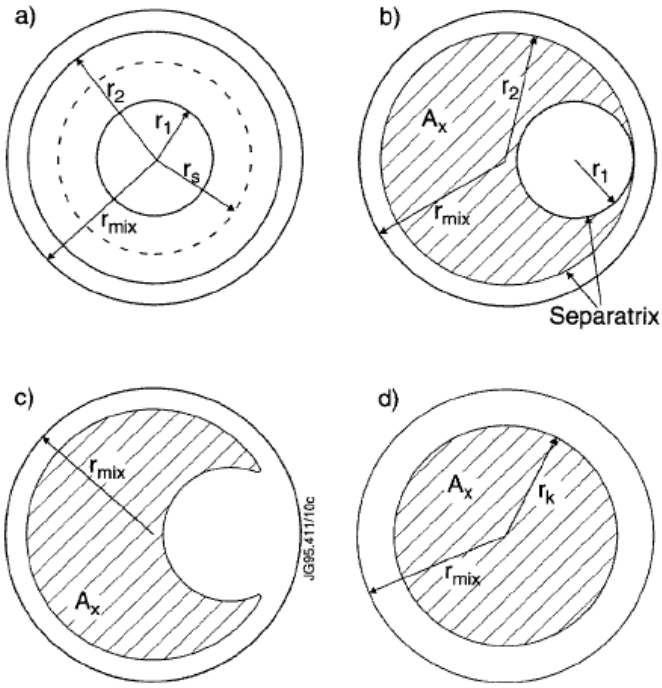

Figure 10.2: Magnetic surfaces during a complete reconnection process, according to the Kadomtsev's model. (a) Helical flux surfaces before reconnection starts. (b) The flux surface originally at $r = r1$ reconnects with the flux surface originally at $r = r2$. (c) At a later time, the island separatrix of (b) has deformed into a croissant-shaped surface, maintaining a constant area A_X . (d) Reconnection is completed, with the original magnetic axis reconnecting with the surface at $r = r_{mix}$. The new axis is the O-point of the $m = 1$ magnetic island. (This figure is taken from [111]).

Fig. 10.1. In this model, the magnetic flux surface at the magnetic axis reconnects with other one at the mixing radius so that $\psi^i_*(0) = \psi^i_*(r_{mix})$, the initial magnetic axis disappears and it is replaced by the O-point of the new expanding $m = 1$ island.

The reconnection event modifies the q profile only inside the mixing radius. The final safety factor profile has two distinctive features, firstly $q(0) = 1$ and secondly, a discontinuity at $r = r_{mix}$, which corresponds to a negative current sheet that rapidly vanishes due to the resistive diffusion in the first part of the increasing phase of the next sawtooth.

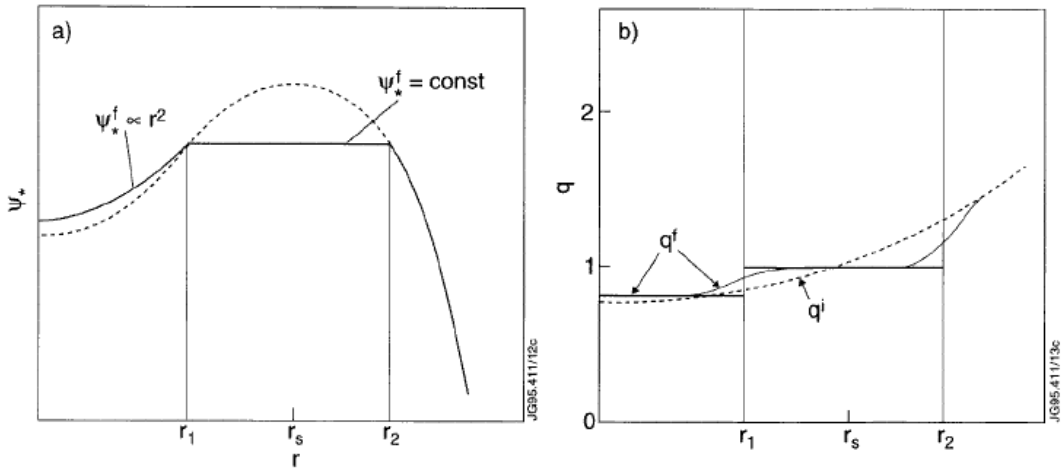

Figure 10.3: Magnetic helical ïňĆux and winding index before and after an incomplete reconnection process. (This figure is taken from [111]).

10.2.2. Porcelli's incomplete reconnection model

As soon as detailed soft X-ray measurements became available, the Kadomtsev's model resulted not to be sufficient to explain the observed experimental data. Indeed the expansion of the magnetic island was observed to be suddenly interrupted by a secondary instability and the q-profile on-axis remained below unity after the thermal crash [113]. In order to model these evidences a heuristic incomplete reconnection model was proposed by Porcelli.

The basis of this new model are the same of the previous one, the difference consists in assuming that a widespread magnetic turbulence rises as soon as the magnetic island reaches a critical width w_{crit}. As Fig. 10.3 shows, the reconnecting surfaces are $\psi^i_*(r_1) = \psi^i_*(r_2)$ such that $r_2 - r_1 = w_{crit}/2$

The model assumes that the plasma core and the magnetic island relaxes differently and that a new magnetic axis forms as soon as the poloidal symmetry is restored. In the inner core, $r = [0, r_1]$, a Taylor relaxation process occurs, that preserves the helicity of the initial flux surface at r_1 and shapes the final poloidal flux into a parabolic function, the q profile flattens correspondingly. Inside the critical island, $r = [r_1, r_2]$, the relaxed surfaces are assumed to have the same helical flux $\psi^f_*(r) = \psi^i_*(r_1)$ and as a result $q(r) = 1$. In this model the mixing radius corresponds to r_2 which is larger than the $q = 1$ one but smaller than the mixing radius predicted by Kadomtsev. Similarly to the complete one, this model predicts two current sheets at the $r = r_1, r_2$ that rapidly vanishes. The resulting safety factor profile is characterized by $q(0) < 1$ and a shoulder of low magnetic

shear around the $q = 1$ surface.

10.3 Sawtooth module in the RAPTOR code

As it has been discussed so far, the sawtooth instability strongly impacts the plasma profiles, especially the safety factor and the electron temperature ones. In order to achieve a more reliable picture of the plasma state, the RAPTOR code has been recently developed during this Thesis work to simulate in real-time both complete and the incomplete reconnection model. The advantages provided by this module are many as well as the potentialities, as it will be discussed at the end of this Section.

RAPTOR can automatically detect a sawtooth crash in real-time from the diagnostic measurements, but it can also simulate it. A sawtooth crash is triggered in the simulation whenever the magnetic shear s at the $q = 1$ surface overcomes a user-define threshold, $s_{crit} \simeq 0.2$. The magnetic shear is defined as:

$$s = \frac{r}{q}\frac{dq}{dr} = -\frac{r}{\iota}\frac{d\iota}{dr},$$

and its value at the $q = 1$ surface is obtained with an interpolation on the iota values close to the $\iota = 1$ threshold. The estimation of the magnetic shear is highly sensitive to the spatial grid of the model, that has to be simplified very carefully. At the present state, the real-time RAPTOR in ASDEX Upgrade has a mesh of 16 points, that seems to be the optimal compromise between spatial resolution and computational time. A second critical aspect in the magnetic shear computation at the $q = 1$ surface are the non-monotonic iota profiles where the equality $\iota = 1$ is satisfied in more than one radial position. In this case the code takes into account the outer radius where ι crosses unity.

As soon as the magnetic shear reaches the critical limit, a second module is called to simulate the reconnection of the magnetic surfaces and the evolution of the radial profiles. The complete or incomplete reconnection model is chosen on the basis of an user-defined parameter. In the second case the critical width of the magnetic island is an additional free parameter of the model. In order to simulate the reconnection at best, the code maps the poloidal magnetic flux into a denser grid of 1001 points. This choice allows a better matching of the reconnecting surfaces with the same magnetic flux values, as it has been described in the previous Section.

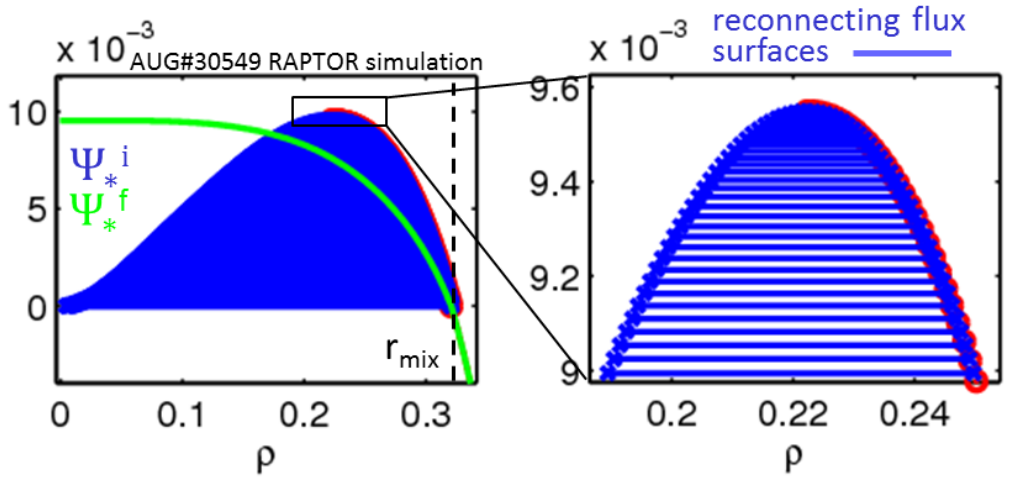

Figure 10.4: Magnetic helical flux profiles in the RAPTOR simulation of a sawtooth in the ASDEX Upgrade shot #30549

Fig. 10.4 shows the ψ_* profile evaluated by RAPTOR before (in blue) and after (in green) a sawtooth crash, that occurs in the ASDEX Upgrade shot #30549. In this simulation the magnetic flux surfaces reconnect according to the complete model. The first panel shows that the final ψ_*^f profile differs from the initial one ψ_*^i only inside the mixing radius, that is represented here with a dashed line. The second panel reports a zoom of the initial profile in the neighborhood of the maximum. The blue and red circles represent the magnetic flux surfaces in the $\rho_1 = [0, \rho_{MAX}]$ and $\rho_2 = [\rho_{MAX}, \rho_{mix}]$ range, respectively. The new ψ_*^f profile is evaluated by associating at each radial position $\rho_k = \sqrt{(\rho_2^2 - \rho_2^2)}$ the ψ_*^i value that connects each ρ_1 and ρ_2, that is represented here by parallel blue lines.

Whenever a sawtooth occurs, RAPTOR updates its vector state, that contains the poloidal magnetic flux and the electron temperature profiles, with the corresponding values that are evaluated on the basis of the new ψ_*^f. The other kinetic profiles, like the electron density and the pressure one, are evaluated by satisfying the requirement of the energy and particle conservation before and after a sawtooth crash.

The results of Kadomtsev's complete reconnection model in a RAPTOR predictive simulation of the ASDEX Upgrade shot #30549 are summarized in Fig. 10.5. The figure reports the time evolution of the plasma current, the NBI and the EC power, that are plotted with a continuous and a dashed line respectively, the electron temperature and the on-axis safety factor. The RAPTOR output is plot-

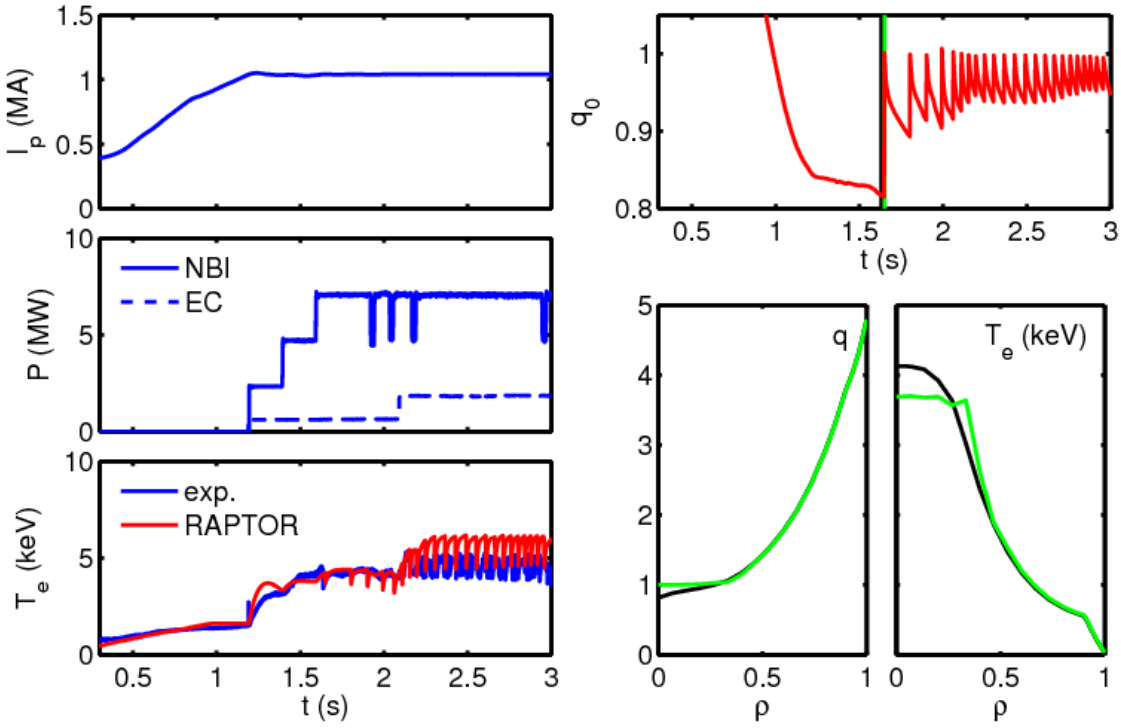

Figure 10.5: Porcelli complete reconnection module simulation in RAPTOR.

ted in red, while the experimental data in blue. The time history of the electron temperature shows that the natural sawtooth period is forced to decrease from $t = 2s$ on by the destabilizing effect of an additional EC launcher that is pointed towards the plasma core. The sawtooth in the experiment are more frequent and irregular than the simulated ones, but globally RAPTOR succeeds in reproducing the trend. The two radial profiles on the bottom right show the safety factor and the electron temperature before (in black) and after (in green) a sawtooth crash, as it is highlighted by the two lines with the same colour code in the time evolution of the on-axis safety factor that is reported in the upper panel. The simulated profiles correctly reproduce the typical plasma dynamics after a sawtooth crash in the plasma core, namely the safety factor jump from $q(0) < 1$ to $q(0) > 1$ and the electron temperature profile flattening due to the mixing the of the hot plasma near the magnetic axis with the cooler one beyond the $q = 1$ surface.

10.4 RAPTOR simulations of an ASDEX Upgrade sawtooth locking experiment

If the sawtooth criterion Eq. 10.4 holds, then the sawtooth oscillation can be deliberately triggered or postponed by increasing or hindering the growth of the local magnetic shear around the $q = 1$ surface. One of the most robust technique, that is currently used in nowadays Tokamaks to locally modifying the magnetic shear profile, exploits the Electron Cyclotron Resonance Heating - ECRH system. This auxiliary heating system can deposit either heating or current in a very localized position. Indeed, if the EC waves are launched with an additional toroidal component, then they can result in an electron cyclotron driven current either parallel (co-ECCD) or anti-parallel (counter-ECCD) to the Ohmic power. Both ECRH and ECCD acts on the magnetic shear profile. The former modifies the local resistivity and thus the local current profile. The latter moves the $q = 1$ surface when it is injected close to it, the magnetic shear changes accordingly and with it the probability to trigger a sawtooth crash [17] .

If the deposition is localized outside the $q = 1$ surface, it has a stabilizing effect on the sawtooth instability since its effect is to slow down the magnetic shear, that is found to naturally increase after a sawtooth crash at the $q = 1$ surface. Conversely a deposition inside this surface speeds up the growth of the magnetic shear and destabilizes the sawtooth oscillations [17, 114].

This method is very effective, but it requires a precise radial deposition of the EC power, since the $q = 1$ surface sets a very narrow and sharp transition between the stabilizing and the destabilizing regime. Generally, the radial position of the $q = 1$ surface is not known a-priori but it can be detected by radially sweeping the EC power from the torus axis towards the plasma edge or it can be inferred by the sawtooth inversion radius measured by an ECE diagnostic.

The sawtooth destabilization, that has been discussed in Fig. 10.5, is followed by a sawtooth locking experiment, whose results are reported in Fig. 10.6. The figure shows the time evolution of the NBI and the EC power and the corresponding radial deposition of the different launchers, as the colour code suggests. In this experiment an EC launcher is pointed well inside the $q = 1$ surface (red), while the power of the remaining ones (blue and green) is pulsed and it is deposited outside, but very close, to this surface with the aim to stabilize and lock the sawteeth. The sawtooth locking period is increased in consecutive time windows in the range $T_{LOCK} = [70, 100, 140]ms$, while the duty cycle is fixed at 80%. The

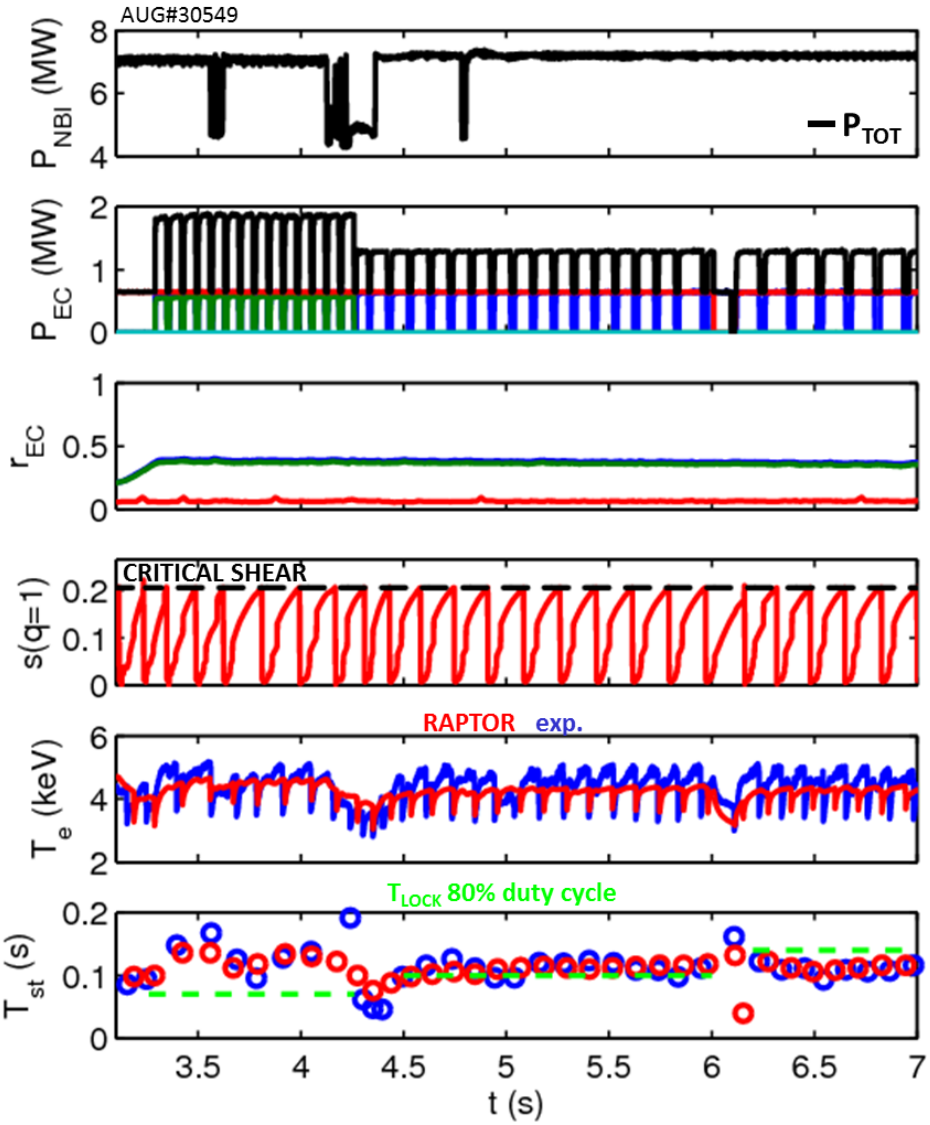

Figure 10.6: Sawtooth locking experiment in ASDEX Upgrade and comparison with the RAPTOR predictions (red)

last two panels compare the measured electron temperature and the sawtooth period (blue) with the RAPTOR predictions (red), the former being inferred from the ECE diagnostic. The agreement of the two time histories is remarkably good, but both of them succeed in locking the oscillations only in the mid window, as the overlap with the green dashed lines, that represent T_{LOCK}, suggests.

The success or the failure of a sawtooth locking experiment depends on the radial deposition of the EC power and on the right choice of the period and the

duty cycle of the pre-programmed EC square waveforms. Dedicated simulations have been performed to investigate on these two issues and they will be presented in the following.

The deposition radius of the two pulsed EC launchers in Fig. 10.6 was fixed at $r \simeq 0.36$ on the basis of a preliminary shot, where the inversion radius was localized at $\rho = 0.3$. A RAPTOR simulation is performed to simulate an EC power sweeping in the experimental conditions of the $AUG\#30549$ shot, namely with the same plasma current, electron density and NBI power of this discharge. The results are summarized in Fig. 10.7. An EC launcher, here plotted in red, supplies $0.6MW$ to the plasma core while a second one, that is plotted in blue, deposit $1.3MW$ in the range $r_{EC} = [0.2, 0.6]$. The critical magnetic shear is fixed at $s_{crit} = 0.2$ as in the simulation in Fig. 10.6. The last two panels, that report the time evolution of the electron temperature on the axis and the sawtooth period, show the effect of the EC power deposition on the sawtooth instability. As soon as the blue EC launcher approaches the $q = 1$ surface, its stabilizing effect lengthens the sawtooth period that is maximized at $\rho = 0.32$. At larger radii, namely from $t \gtrsim 4s$, the EC stabilizing effect saturates.

The sensitivity of the sawtooth instability on the radial deposition of the EC power is highlighted in Fig. 10.8 that reports the period of the oscillations as a function of r_{EC}. The maximum sawtooth period $T_{MAX} = 216ms$ occurs when $r_{EC} = 0.33$, this confirms that the experimental deposition radius $r_{EC,exp} = 0.36$ in Fig. 10.6 is a wise choice. The saturated efficiency of the outer EC deposition is observed from $r_{EC} \gtrsim 0.45$

In order to further characterize the sawtooth period response as a function of the EC deposition radius and the effect of the deposited power on the dynamics of the $q = 1$ surface, a RAPTOR simulation has been performed where where the EC power sweeping has been repeated twice by crossing the $q = 1$ surface in the two directions, namely back and forth from the torus axis towards the edge, as it is reported in fourth panel of Fig. 10.9. In this simulation, all the input signals are the same of Fig. 10.7 except for this quantity that is ramped up from $r_{EC} = 0.2$ to $r_{EC} = 0.4$ in $t = [3, 4.75]s$, kept constant at $r_{EC} = 0.4$ in a short time window and eventually ramped down from $r_{EC} = 0.4$ to $r_{EC} = 0.2$ in $t = [5.25, 7]s$. In so doing the EC power is deposited from inside the $q = 1$ surface towards the outside in the first window, as it has been done in Fig. 10.7, constantly outside the $q = 1$ surface in the second window that smooths the transition between the two sweeps, and from outside to inside the $q = 1$ surface in the last one. The last panel shows

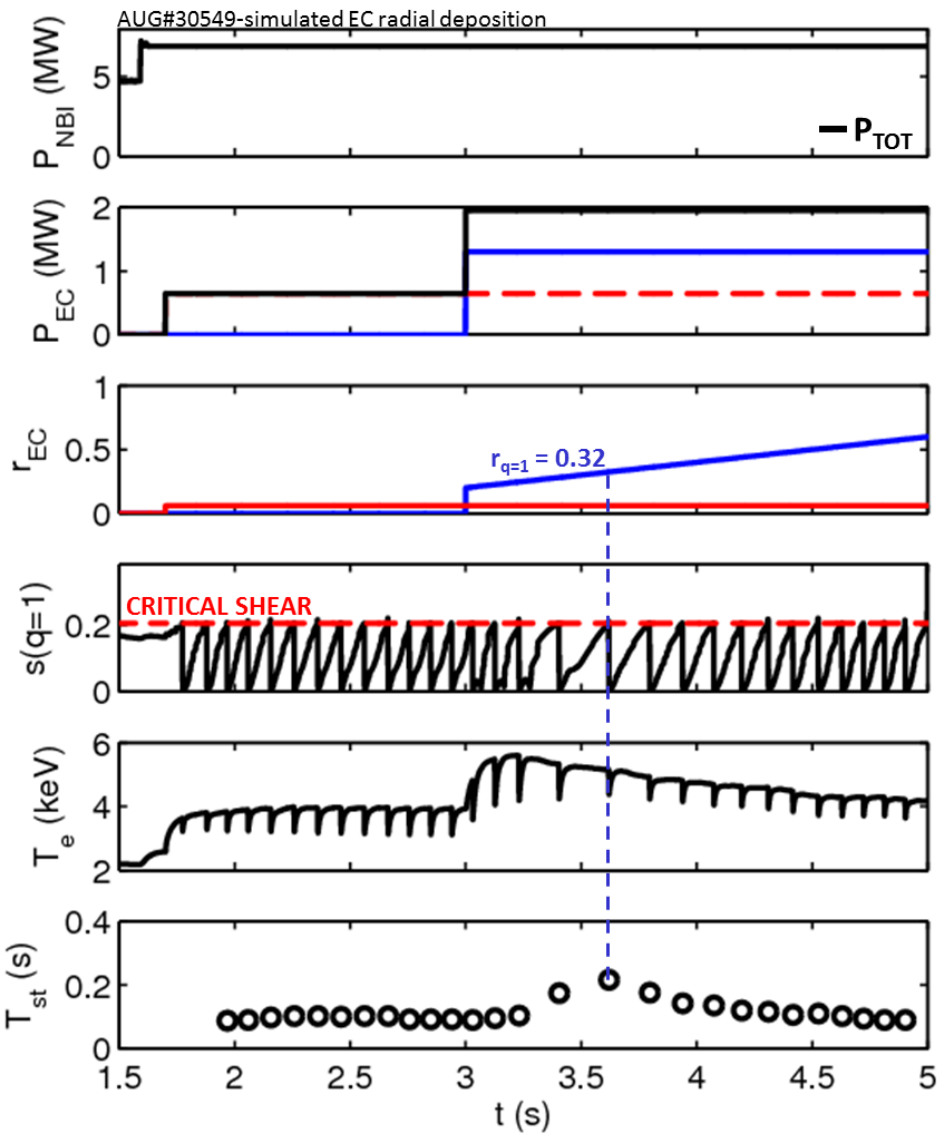

Figure 10.7: RAPTOR simulation of an EC power radial sweeping experiment for the ASDEX Upgrade shot *AUG*#30549. Time evolution of the NBI and the EC power, the EC power deposition radius, the magnetic shear and the critical threshold in red, the electron temperature on the plasma axis and the sawtooth period.

that the sawtooth period is modulated in time, as it has been described above, in the first and third time windows, when the EC radius is changing, Interestingly, the response dynamics of the oscillation period is not exactly the same in the two sweeps, not only the maximum period of the second sweep is higher than the one in the first, but also the position of the $q = 1$ surface changes in the two cases.

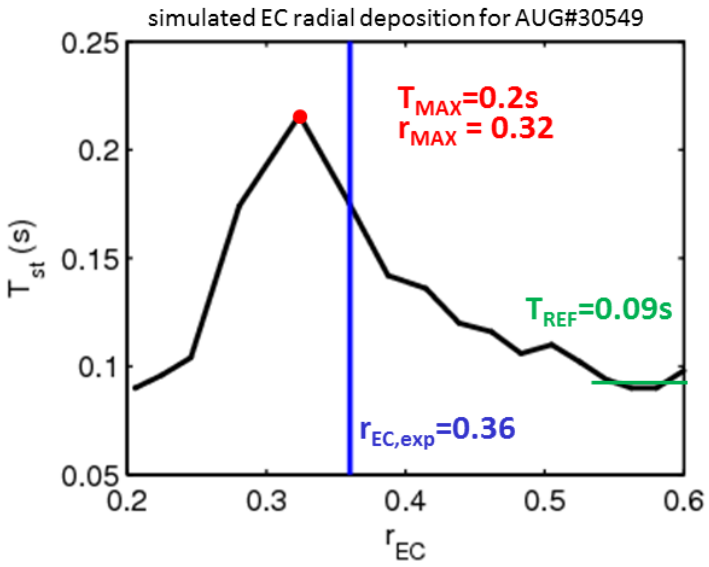

Figure 10.8: RAPTOR simulation of an EC power radial sweeping experiment for the ASDEX Upgrade shot *AUG*#30549. The sawtooth period as a function of the EC power deposition radius.

The difference between the two sweeps is foregrounded in Fig. 10.10, where the sawtooth period is plotted as a function of the EC deposition radius in the two cases. The first sweeping is plotted with a continuous line while the second with a dashed one. By comparing the two curves is evident that in the second case, namely when the power is deposited towards the plasma core, the $q = 1$ surface moves towards a smaller radius. This hysteresis process, that has been experimentally observed as well [115, 116] is due to the redistribution of the plasma current due to the off-axis EC power deposition that shifts the $q = 1$ surface. Conversely, The period remains constant at $T_{ref} = 0.12s$ in the transition between the two sweeps. It is worth to note here that in this simulation the plasma radius is swept more rapidly than in Fig. 10.7, as a result this nominal values the reference sawtooth period, as well as the maximum one, in the first sweep is slightly higher than the one in Fig. 10.8.

10.4.1. Reproducibility of the RAPTOR simulated sawteeth

In order to characterize the reproducibility of the sawteeth that are locked at $T_{lock} = 0.1s$ a RAPTOR simulation has been performed. In this simulation all the input signals are constant and have the same nominal values of the ones in Fig.

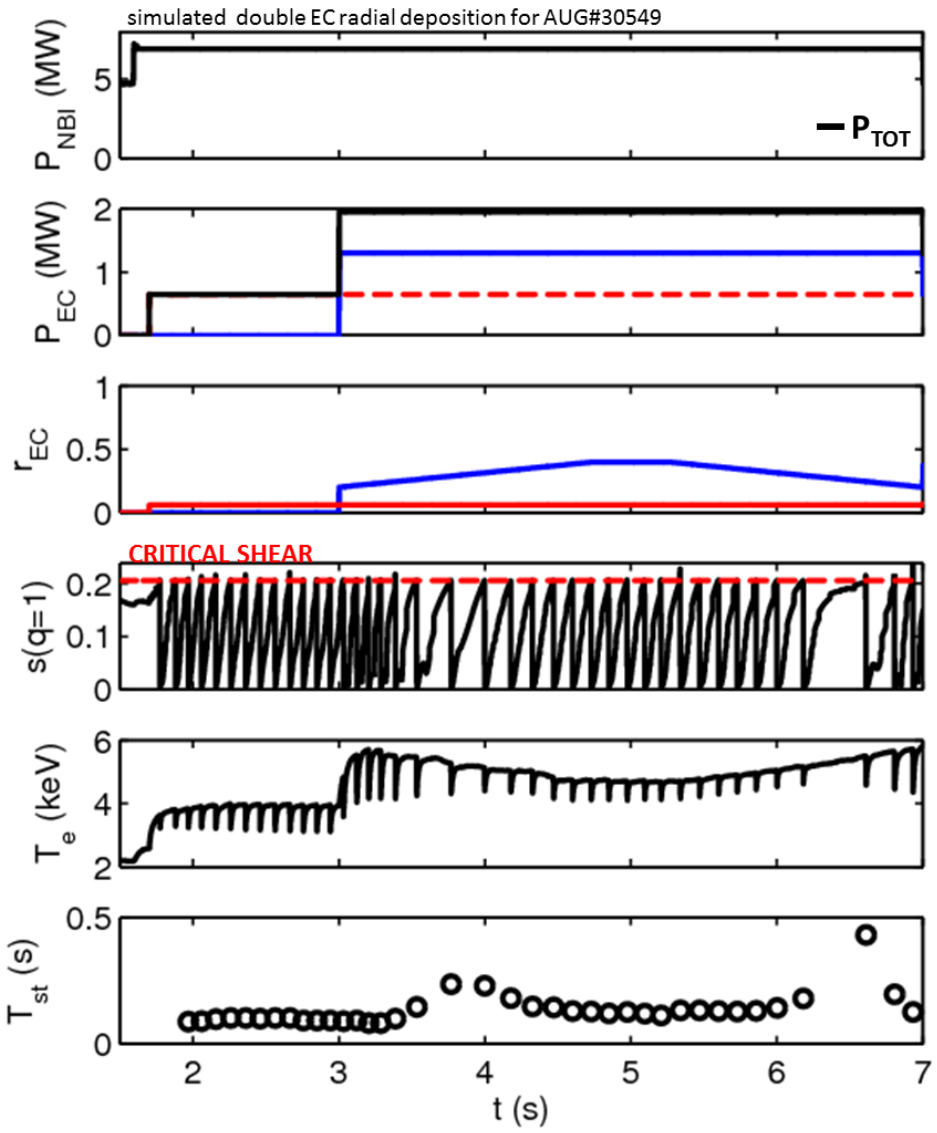

Figure 10.9: RAPTOR simulation of two EC power sweeps, the first one from inside to outside of the $q = 1$ surface, the second one in the opposite direction. Time evolution of the NBI and the EC power, the EC power deposition radius, the magnetic shear and the critical threshold in red, the electron temperature on the plasma axis and the sawtooth period.

10.6, except for the pulsed waveforms of the two EC launchers, whose $T_{lock} = 0.1s$ and duty cycle $DC = 80\%$ are kept fixed for the entire discharge. In so doing a wide ensemble of locked sawteeth can be obtained. Once the simulation has overcome an initial transient regime, 14 oscillations are taken into account and overplotted to quantify the spread in terms of magnetic shear, electron temperature and period.

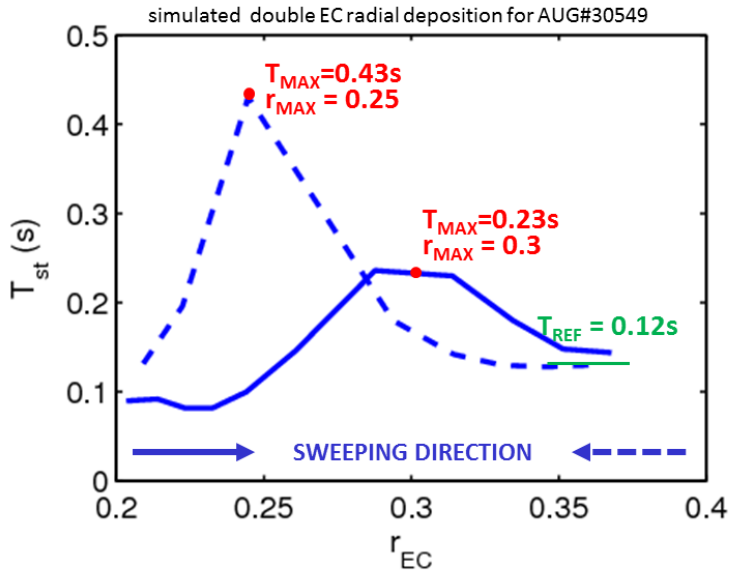

Figure 10.10: The sawtooth period as a function of the EC power deposition radius in a RAPTOR simulation where the first EC sweep is performed from inside to outside of the $q = 1$ surface (continuous line), while the second one in the opposite direction (dashed line).

As Fig. 10.11 shows, the variation in the sawtooth period is obviously the same in the two quantities and it is around 2%. A similar relative width is observed in the magnetic shear, namely $\Delta s = 3\%$, conversersely the electron temperature evolution during the sawtooth ramping phase is not as much as reproducible as the latter one, being $\Delta T_e = 15\%$. These differences are likely to be reduced by increasing the thickness of the spatial grid.

As it was discussed above the reproducibility of the sawtooth oscillations that is documented in Fig. 10.11, was obtained using constant input data. In order to quantify the effect on the RAPTOR predictions of the noise in the electron density measurements, whose signals are generally subjected to fluctuations due to the challenging control of this quantity, a series of simulations with increasing noise in the electron density measure have been performed and the results are summarized in Fig. 10.12.

This figure compares the RAPTOR outputs, in terms of the electron density profile and the time evolution of the electron temperature and the sawtooth period, in four different simulations, as the first panel on the left shows. The noise in the n_e signal is completely suppressed in the red case, maintained as the experiment

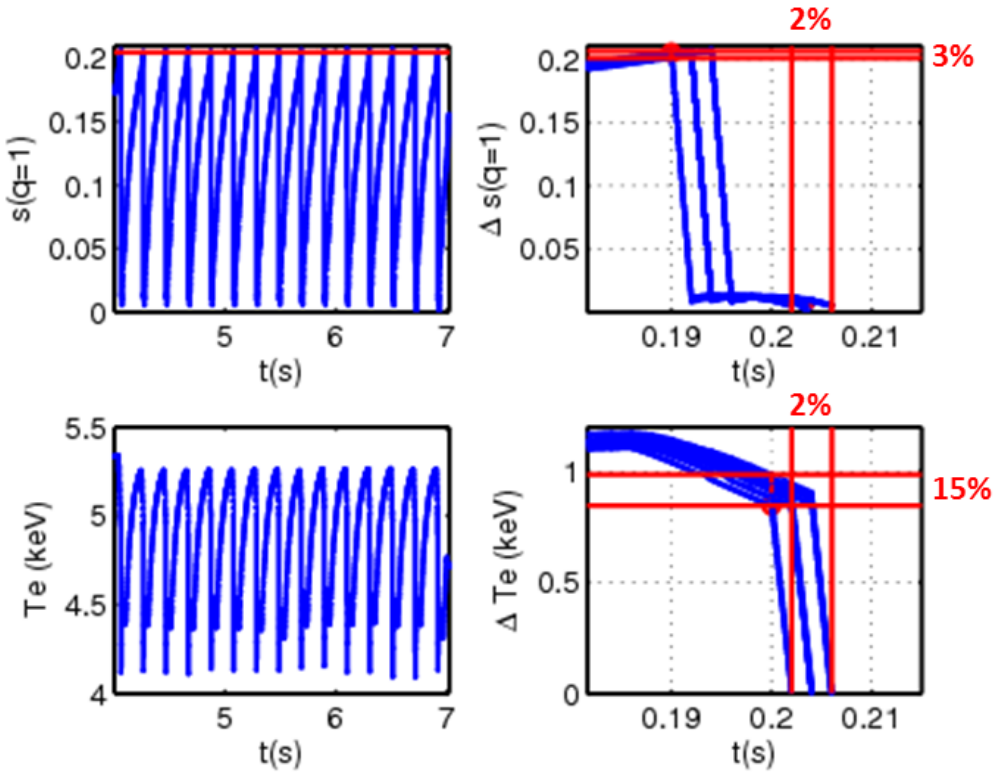

Figure 10.11: Reproducibility of the locked sawteeth that are simulated by RAPTOR in terms of the magnetic shear (upper panels) and the electron temperature (bottom panels). Red lines define the spread in the corresponding quantities.

in the black one or artificially increased by 0.01% and 0.1% in the green and blue curves. The comparison of the corresponding profiles and the time evolution of the other quantities suggests that up to a noise level of 0.1% the impact on the RAPTOR predictions, as far as the sawtooth dynamics is concerned, is negligible. significant deviations, especially on the density profile evaluation are obtained with higher noise values as the blue curves point out.

10.5 RAPTOR in the RFX-mod control system

The real-time RAPTOR simulator is currently embedded in the TCV [105] and ASDEX Upgrade [107] control system, but in the next future it is going to be integrated in RFX-mod too. As it has been discussed in Chapter 3, the RFX-mod control system has recently moved to the real-time MARTe framework that

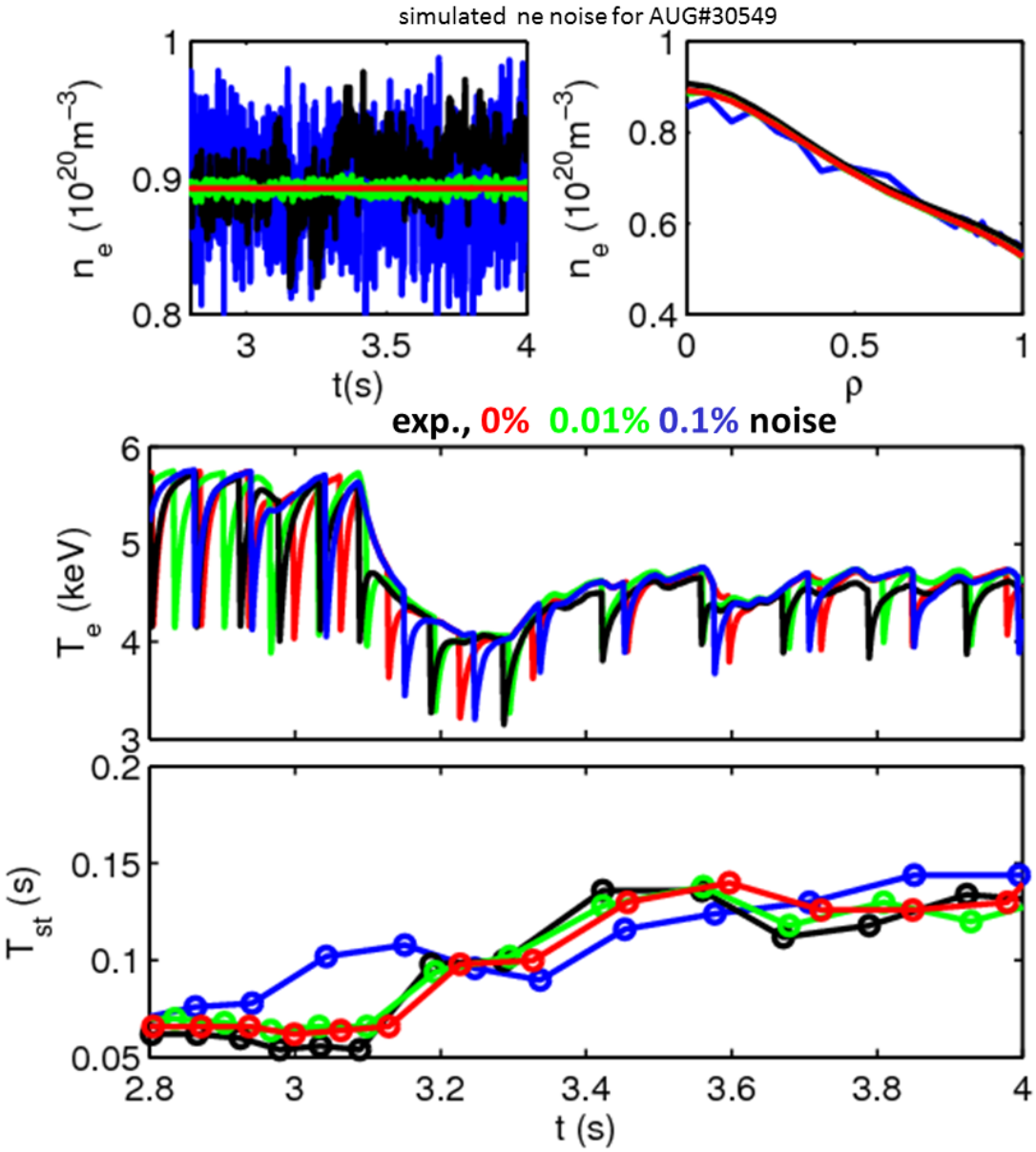

Figure 10.12: Effect of increasing noise in the electron density measurements on the RAPTOR simulations of locked sawteeth.

is used in many other Tokamak experiments, among these the JET one. All these experiments will benefit from the expertise that will be gained in porting the RAPTOR code into RFX-mod.

The magnetic equilibrium in RFX-mod, as far as the plasma shape and position are concerned, can be feedback controlled in real-time, as it has been described in Chapter 1. A measure of the safety factor profile, or the one of the electron

temperature and the plasma density, are not available in real-time at the moment. Thus the integration of RAPTOR in RFX-mod will provide a model-based estimate for all these missing data and will broaden the potentialities of the active feedback control of both magnetic equilibrium and MHD instabilities.

Thanks to the new real-time sawtooth model, that has been implemented in RAPTOR during this Thesis work as it will be discussed in Chapter 10, the dynamics of this instability and its effects on the plasma profiles can be predicted in real-time. With this brand new tool the interpretative RAPTOR simulator can be exploited to predict a plasma disruption in RFX-mod by monitoring the dynamics of the sawteeth during the discharge. Indeed, as it has been discussed in Chapter 7, the growth of both a $m = 2, n = 1$ RWM or a tearing mode in $q(a) < 2$ or $q(a) > 2$ sawtoothing Tokamak plasmas, respectively, is accompanied by a mitigation of the sawtooth oscillations, that eventually disappear towards the end of the discharge. Preventive actions can be prescribed in time by the active control system if an increasing mismatch between the RAPTOR predictions and the measured data is detected.

As it has been discussed before, the RAPTOR state observer algorithm requires the real-time measure of a minimum set of diagnostics. In RFX-mod the plasma current is already available in the real-time framework, while the integration of all the other signals is currently going on. In particular the electron temperature will be provided by the double filter SXR diagnostic [117], while the electron density will be inferred by the temperature and the diamagnetic β real-time measure. Eventually, the sawtooth crash detector will be implemented on a core SXR signal. Part of the future development of this Thesis work will deal with the development and the commissioning of the new MARTe code that will be necessary to embed RAPTOR and all its input and output data in the RFX-mod real-time framework.

As a preparatory work, a CHEASE equilibrium, that reproduces the RFX-mod circular Tokamak one, has been tested in an offline RAPTOR simulation. The results, that have been obtained for a Ohmic Deuterium plasma discharge (#35376), are reported in Fig. 10.13.

This figure compares the experimental data, that are reported in blue, with the RAPTOR simulated outputs, in red. The panels a-d) on the left column shows the time evolution of the plasma current, the q_{95} and the on-axis electron temperature. The remaining ones e-h) on the right report the radial profile of the corresponding quantity on the left, except for panel e) that shows the radial profile of the heat diffusivity and panel g) that reports the one of the electron density. In

this simulation, the transport coefficients ($c_{ano} = 9$, $\delta_0 = 0.25$, $\chi_{e,central} = 10$) and the critical magnetic shear threshold for the sawtooth trigger ($s_{1,crit} = 0.36$), have been chosen to match the experimental data namely the electron temperature in the core $T_{e0} \simeq 0.4keV$ and the sawtooth period $T_{st} \simeq 10ms$. It is worth to notice here that this demonstrative example is just the first preliminary result that has been obtained with RAPTOR in RFX-mod. Besides this, the agreement between the simulated data and the experimental ones is good and promising. An extensive validation of the code with other RFX-mod shots with $q(a)$ both both above and below 2 is going to be carried out in the future development of this Thesis work.

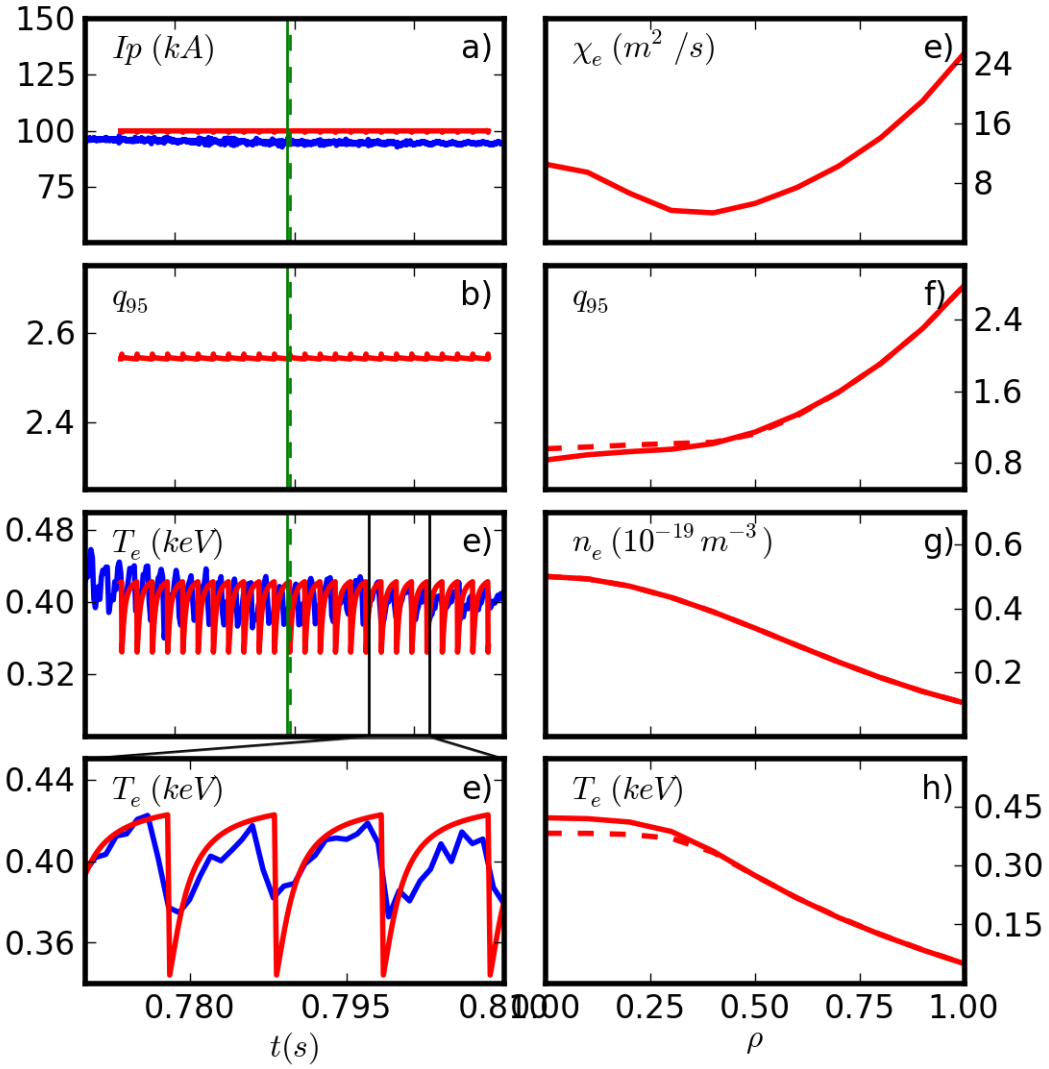

Figure 10.13: A offline RAPTOR simulation (red) of a RFX-mod Ohmic circular Tokamak discharge (blue). The time evolution of the plasma current, the q_{95}, and of the electron density and temperature is reported on the left column. The radial profiles of the heat diffusivity and of the corresponding quantities on the left are reported on the right column. The continuous and the dashed curves correspond to the profiles before and after a sawtooth crash, that occurs at $t = 0.716s$ as the green lines indicate

Conclusions and future work

This Thesis work developed the knowledge on the active control of MHD instabilities with an interdisciplinary approach, whose physics and engineering aspects were investigated initially in RFX-mod at Consorzio RFX, Padua, Italy, and then in larger Tokamaks, namely DIII-D at General Atomics, San Diego, USA, and ASDEX Upgrade at Max-Planck-Institute für Plasmaphysik in Garching, Germany. A summary of the original contributions of this work will be provided in this final Chapter.

RWM control and EF correction in RFX-mod

This work contributed to the upgrade of the RFX-mod MHD control system, by dealing with its integration in the new real-time MARTe framework and its final deployment. The enhanced potentialities of the MHD control system, that allows now to design and test more computationally challenging algorithms, were exploited to develop new feedback control schemes based on radial, toroidal and poloidal magnetic field sensors. The latter were embedded in real-time during this Thesis as well, allowing to compare for the first time in RFX-mod the performance of the MHD control schemes based on radial magnetic field sensors with the poloidal ones. The testbed was the challenging $q(a) < 2$ regime, that is threatened in RFX-mod by a highly reproducible $m = 2, n = 1$ RWM. The experiments carried out during this Thesis proved that poloidal and radial magnetic field sensors have similar performances, provided that the aliased sideband contribution is removed from the latter. This result is promising, since the harsh environment of the future fusion reactors will not allow to install poloidal magnetic field sensors inside the vacuum vessel. Thus the radial magnetic field sensors, being installed outside it, can be a valuable alternative.

During this Thesis, the RWM control was attempted with another control

strategy, the DEFC. This technique, that consists in compensating the magnetic asymmetries with pre-programmed currents, was originally developed for high β plasmas in DIII-D and was tested for the first time in the RFX-mod in $q(a) < 2$ Tokamak plasmas. The optimization of the technique in this regime was extensively pursued with both poloidal and radial magnetic field sensors. Besides this, it failed in stabilizing the $m = 2, n = 1$ RWM. This result suggested that, differently from a pressure-driven RWM in high β plasmas, the current-driven one in low q plasmas is a linearly unstable mode. RFXlocking and CarMa simulations confirmed that the onset of this instability in RFX-mod does not depends on the error fields in this device, which however are small. The latter have been measured for the first time during this Thesis work as well in both circular and D-shaped Tokamak plasmas with the compass scan technique.

Coupling of external 3D fields and sawteeth

The experimental evidence that in RFX-mod boyh RWM and TM can couple with sawteeth, suggested an innovative approach to study the sawtooth instability, namely the application of external 3D magnetic fields with a strong $n = 1$ component that well couples with these modes. In RFX-mod these fields were applied in $q(a) < 2$ Tokamak plasmas either in the form of $m = 1, n = 1$ magnetic perturbations or by keeping the $m = 2, n = 1$ RWM at finite amplitude. In both cases, they caused a reduction of both the sawtooth amplitude and period, that was found to be correlated with the amplitude of the applied perturbation, and they led to an overall mitigating effect on this instability. The sawtoothing internal kink mode eventually disappeared and was replaced by a stationary $m = 1,\ n = 1$ helical equilibrium without an increase in disruptivity. However toroidal rotation was significantly reduced in these plasmas too, thus it is likely that the sawtooth mitigation in RFX-mod is due to the combination of the helically deformed core and the reduced rotation. These experimental results were qualitatively well reproduced by PIXIE3D, a visco-resistive non-linear MHD code.

The success of the RFX-mod experiments motivated similar ones in DIII-D L-mode Tokamak plasmas with q_{95} just above 2. In these experiments the $n = 1$ magnetic perturbations, that were applied with the I-coils, succeeded in reproducing the sawtooth mitigation that was originally observed in RFX-mod. A significant rotation braking in the plasma core was also observed in DIII-D, probably due to the effect of the NTV torque, as PENT simulation suggested. In the

future, further experiments where the loss of plasma momentum will be externally supplied, for instance with NBI injection, will put light on the mechanism that drive the sawtooth mitigation when $n = 1$ magnetic fields are applied in DIII-D. The results of the experiments carried out both in RFX-mod and DIII-D showed that an appreciable effect on sawteeth can be obtained if the plasma response from the $n = 1$ external kink coupled to the $m = 1, n = 1$ internal kink is sufficiently high. This seems to occur in the low q regime investigated in these devices. A similar effect may be expected at high β values, close to the no-wall limit. In the future it will be interesting to extend these experiments in high β scenarios, exploiting the pressure-driven plasma response to couple the external 3D fields to the internal sawtoothing kink.

RAPTOR and the first step towards an integrated control

This Thesis work further investigated the sawtooth instability and its active control in ASDEX Upgrade, where the real-time state observer RAPTOR algorithm has been recently installed. This code, that reconstructs the plasma state in real-time by combining the diagnostic measurements with the predictions of a simplified transport model, was developed to include a new module that evolves Porcelli's sawtooth model. Thanks to this contribution, RAPTOR is now able to predict in real-time the sudden sawtooth crashes, to correctly reproduce the magnetic reconnection of the magnetic flux surfaces, as well as the effect on all the other plasma profiles. In ASDEX Upgrade this new sawtooth model can be used to design and control in real-time sawtooth locking and pacing experiments, as well as to investigate new control strategies to counteract NTMs, whose seed island can be provided by sawteeth. But it can also be used to optimize existing control techniques, like the NTM's control with ECCD that should benefit from the improved estimate of the safety factor profile.

The real-time state observer RAPTOR algorithm is about to be embedded in RFX-mod too, where it will broaden the potentialities of its active feedback control. The expertise that will be gained in porting RAPTOR in RFX-mod can be exploited in all the other fusion experiments that embed the MARTe framework, like JET. Furthermore, RFX-mod with its highly reproducible $m = 2, n = 1$ current-driven RWM in $q(a) < 2$ Tokamak plasmas will offer a challenging testbed where to develop new control strategies aiming at stabilizing the current-driven RWM, mitigating sawteeth and avoiding disruptions. Eventually, these strategies

can be exported to advanced Tokamak scenarios. The development of new integrated control strategies will be pursued in ASDEX Upgrade as well, where the active control of the MHD instabilities could rely on its heating and current drive systems as further actuators.

Bibliography

[1] J. P. Freidberg. *Plasma Physics and Fusion Energy*. Cambridge University Press, 2007. Cambridge Books Online.

[2] J. Wesson and D. J. Campbell. *Tokamaks*. International Series of Monographs on Physics. OUP Oxford, 2011.

[3] A. R. Choudhuri. *The Physics of Fluids and Plasmas: An Introduction for Astrophysicists*. Cambridge University Press, 1998.

[4] ITER. Iter website, 2015.

[5] H. R. Strauss. The dynamo effect in fusion plasmas. *Physics of Fluids (1958-1988)*, 28(9):2786–2792, 1985.

[6] S. Cappello, D. Bonfiglio, and D. F. Escande. Magnetohydrodynamic dynamo in reversed field pinch plasmas: Electrostatic drift nature of the dynamo velocity fielda). *Physics of Plasmas (1994-present)*, 13(5):056102, 2006.

[7] C. Piron. Study of magnetic reconnection events in fusion plasmas. Master's thesis, Padova, 2011.

[8] S. Ortolani and D. D. Schnack. *Magnetohydrodynamics of plasma relaxation*, volume 156. World Scientific, 1993.

[9] L. Spitzer. The stellarator concept. *Physics of Fluids*, 1(4):253, 1958.

[10] EUROfusion. Eurofusion website, 2015.

[11] H. Ji and S.C. Prager. *Magnetohydrodynamics*, 38:191–210, 2002.

[12] T. G. Cowling. The magnetic field of sunspots. *Monthly Notices of the Royal Astronomical Society*, 94:39–48, 1933.

[13] V. Igochine. *Active Control of Magneto-hydrodynamic Instabilities in Hot Plasmas*. Springer Series on Atomic, Optical, and Plasma Physics. Springer Berlin Heidelberg, 2014.

[14] T. C. Hender et al. Chapter 3: Mhd stability, operational limits and disruptions. *Nuclear Fusion*, 47(6):S128, 2007.

[15] E. J. Strait. Stability of high beta tokamak plasmas*. *Physics of Plasmas (1994-present)*, 1(5):1415–1431, 1994.

[16] M. Greenwald, J. L. Terry, S. M. Wolfe, S. Ejima, M. G. Bell, S. M. Kaye, and G. H. Neilson. A new look at density limits in tokamaks. *Nuclear Fusion*, 28(12):2199, 1988.

[17] I. T. Chapman. Controlling sawtooth oscillations in tokamak plasmas. *Plasma Physics and Controlled Fusion*, 53(1):013001, 2011.

[18] H. R. Strauss. The dynamo effect in fusion plasmas. *Physics of Fluids (1958-1988)*, 28(9):2786–2792, 1985.

[19] R. Fitzpatrick and E. Rossi. Control of tearing modes in toroidal fusion experiments using designer error fields. *Physics of Plasmas (1994-present)*, 8(6):2760–2770, 2001.

[20] L. Piron. *Improved feedback contro of MHD instabilities and error fields in reversed field pinch and tokamak*. PhD thesis, Padova, 2011.

[21] R. J. Buttery, S. Günter, G. Giruzzi, T. C. Hender, D. Howell, G. Huysmans, R. J. La Haye, M. Maraschek, H. Reimerdes, and O. Sauter. Neoclassical tearing modes. *Plasma Physics and Controlled Fusion*, 42(12B):B61, 2000.

[22] H. R. Wilson. Neoclassical tearing modes. *Fusion Science and Technology*, 53:152–60, 2008.

[23] O. Sauter, E. Westerhof, M. L. Mayoral, B. Alper, P. A. Belo, R. J. Buttery, A. Gondhalekar, T. Hellsten, T. C. Hender, and D. F. Howell. Control of neoclassical tearing modes by sawtooth control. *Physical Review Letters*, 88(10):105001, 2002.

[24] S. Coda, L. G. Eriksson, M. Lennholm, J. Graves, T. Johnson, J. H. Brzozowski, M. DeBaar, D. F. Howell, S. Jachmich, and V. Kiptily. Ntm prevention by iccd control of fast-ion-stabilised sawteeth. In *34th European Physical Society Conference on Plasma Physics, Warsaw, Poland*, pages 90–90, 2007.

[25] B. Esposito, G. Granucci, M. Maraschek, S. Nowak, A. Gude, V. Igochine, E. Lazzaro, R. McDermott, E. Poli, and J. Stober. Avoidance of disruptions at high β_n in asdex upgrade with off-axis ecrh. *Nuclear Fusion*, 51(8):083051, 2011.

[26] D. A. Humphreys, J. R. Ferron, R. J. La Haye, T. C. Luce, C. C. Petty, R. Prater, and A. S. Welander. Active control for stabilization of neoclassical tearing modesa). *Physics of Plasmas (1994-present)*, 13(5):056113, 2006.

[27] E. Kolemen, R. Ellis, R. J. La Haye, D. A. Humphreys, J. Lohr, S. Noraky, B. G. Penaflor, and A. S. Welander. Real-time mirror steering for improved closed loop neoclassical tearing mode suppression by electron cyclotron current drive in diii-d. *Fusion Engineering and Design*, 88(11):2757–2760, 2013.

[28] R. J. Hastie. Sawtooth instability in tokamak plasmas. *Astrophysics and space science*, 256(1-2):177–204, 1997.

[29] I.T. Chapman, R. Scannell, W. A. Cooper, J. P. Graves, R. J. Hastie, G. Naylor, and A. Zocco. Magnetic reconnection triggering magnetohydrodynamic instabilities during a sawtooth crash in a tokamak plasma. *Physical Review Letters*, 105(25):255002, Dec 2010.

[30] R. J. La Haye and O. Sauter. Threshold for metastable tearing modes in diii-d. *Nuclear Fusion*, 38(7):987, 1998.

[31] M. F. F. Nave, S. Ali-Arshad, B. Alper, B. Balet, H. J. De Blank, D. Borba, C. D. Challis, M. G. Von Hellermann, T. C. Hender, G. T. A. Huysmans, W. Kerner, G. J. Kramer, F. Porcelli, J. O'Rourke, L. Porte, G. J. Sadler, P. Smeulders, A. C. C. Sips, P. M. Stubberfield, D. Stork, R. Reichle, J. A. Wessom, and W. Zwingmann. Mhd activity in jet hot ion h mode discharges. *Nuclear Fusion*, 35(4):409, 1995.

[32] A. Y. Aydemir. Mechanism for rapid sawtooth crashes in tokamaks. *Physical Review Letters*, 59:649–652, Aug 1987.

[33] J. P. Graves, R. J. Hastie, and K. I. Hopcraft. The effects of sheared toroidal plasma rotation on the internal kink mode in the banana regime. *Plasma Physics and Controlled Fusion*, 42(10):1049, 2000.

[34] A. Pochelon, F. Hofmann, H. Reimerdes, C. Angioni, R. Behn, R. Duquerroy, I. Furno, P. Gomez, T.P. Goodman, M.A. Henderson, A. Martynov, P. Nikkola, O. Sauter, and A. Sushkov. Plasma shape effects on sawtooth/internal kink stability and plasma shaping using electron cyclotron wave current profile tailoring in tcv. *Nuclear Fusion*, 41(11):1663, 2001.

[35] X. T. Ding, Y. Q. Liu, G. C. Guo, E. Y. Wang, K. L. Wong, L. W. Yan, J. Q. Dong, J. Y. Cao, Y. Zhou, J. Rao, Y. Yuan, H. Xia, Y. Liu, and HL-1M group. Observation of internal kink instability purely driven by suprathermal electrons in the hl-1m tokamak. *Nuclear Fusion*, 42(5):491, 2002.

[36] P. Martin, L. Marrelli, A. Alfier, F. Bonomo, D. F. Escande, P. Franz, L. Frassinetti, M. Gobbin, R. Pasqualotto, P. Piovesan, D. Terranova, and RFX mod team. A new paradigm for rfp magnetic self-organization: results and challenges. *Plasma Physics and Controlled Fusion*, 49(5A):A177, 2007.

[37] R. Lorenzini, E. Martines, P. Piovesan, D. Terranova, P. Zanca, M. Zuin, A. Alfier, D. Bonfiglio, F. Bonomo, and A. Canton. Self-organized helical equilibria as a new paradigm for ohmically heated fusion plasmas. *Nature Physics*, 5(8):570–574, 2009.

[38] M. S. Chu and M. Okabayashi. Stabilization of the external kink and the resistive wall mode. *Plasma Physics and Controlled Fusion*, 52(12):123001, 2010.

[39] E. J. Strait, J. Bialek, N. Bogatu, M. Chance, M. S. Chu, D. Edgell, A. M. Garofalo, G. L. Jackson, T. H. Jensen, L. C. Johnson, J. S. Kim, R. J. La Haye, G. Navratil, M. Okabayashi, H. Reimerdes, J.T. Scoville, A. D. Turnbull, M. L. Walker, and DIII-D Team. Resistive wall stabilization of high-beta plasmas in diii-d. *Nuclear Fusion*, 43(6):430, 2003.

[40] A. M. Garofalo, T. H. Jensen, L. C. Johnson, R. J. La Haye, G. A. Navratil, M. Okabayashi, J. T. Scoville, E. J. Strait, D. R. Baker, J. Bialek, M. S. Chu, J. R. Ferron, J. Jayakumar, L. L. Lao, M. A. Makowski, H. Reimerdes, T. S. Taylor, A. D. Turnbull, M. R. Wade, and S. K. Wong. Sustained

rotational stabilization of diii-d plasmas above the no-wall beta limit. *Physics of Plasmas (1994-present)*, 9(5):1997–2005, 2002.

[41] A. M. Garofalo, E. J. Strait, L. C. Johnson, R. J. La Haye, E. A. Lazarus, G. A. Navratil, M. Okabayashi, J. T. Scoville, T. S. Taylor, and A. D. Turnbull. Sustained stabilization of the resistive-wall mode by plasma rotation in the diii-d tokamak. *Physical Review Letters*, 89:235001, Nov 2002.

[42] J. Bialek, A. H. Boozer, M. E. Mauel, and G. A. Navratil. Modeling of active control of external magnetohydrodynamic instabilities. *Physics of Plasmas (1994-present)*, 8(5):2170–2180, 2001.

[43] Y. Q. Liu, M. S. Chu, I. T. Chapman, and T. C. Hender. Toroidal self-consistent modeling of drift kinetic effects on the resistive wall mode. *Physics of Plasmas (1994-present)*, 15(11):–, 2008.

[44] J. W. Berkery, S. A. Sabbagh, H. Reimerdes, R. Betti, B. Hu, R. E. Bell, S. P. Gerhardt, J. Manickam, and M. Podestá. The role of kinetic effects, including plasma rotation and energetic particles, in resistive wall mode stability. *Physics of Plasmas (1994-present)*, 17(8):–, 2010.

[45] D. Yadykin, Y. Q. Liu, and R. Paccagnella. Effects of kinetic resonances on the stability of resistive wall modes in reversed field pinch. *Plasma Physics and Controlled Fusion*, 53(8):085024, 2011.

[46] P. Piovesan, J. M. Hanson, P. Martin, G. A. Navratil, F. Turco, J. Bialek, N. M. Ferraro, R. J. La Haye, M. J. Lanctot, M. Okabayashi, C. Paz-Soldan, E. J. Strait, A. D. Turnbull, P. Zanca, M. Baruzzo, T. Bolzonella, A. W. Hyatt, G. L. Jackson, L. Marrelli, L. Piron, and D. Shiraki. Tokamak operation with safety factor q95$<$2 via control of mhd stability. *Physical Review Letters*, 113:045003, Jul 2014.

[47] Y. Q. Liu, A. Kirk, and E. Nardon. Full toroidal plasma response to externally applied nonaxisymmetric magnetic fields. *Physics of Plasmas (1994-present)*, 17(12):–, 2010.

[48] M. Baruzzo, T. Bolzonella, Y. Q. Liu, G. Manduchi, G. Marchiori, A. Soppelsa, M. Takechi, and F. Villone. Rwm control studies on rfx-mod with a limited set of active coils. *Nuclear Fusion*, 52(10):103001, 2012.

[49] G. Rostagni. *Fusion Engineering and Design*, 25:301–313, 1995.

[50] P. Sonato, G. Chitarin, P. Zaccaria, F. Gnesotto, S. Ortolani, A. Buffa, M. Bagatin, W. R. Baker, S. Dal Bello, P. Fiorentin, L. Grando, G. Marchiori, D. Marcuzzi, A. Masiello, S. Peruzzo, N. Pomaro, and G. Serianni. Machine modification for active {MHD} control in {RFX}. *Fusion Engineering and Design*, 66-68(0):161 – 168, 2003. 22nd Symposium on Fusion Technology.

[51] P. Zaccaria, S. Dal Bello, and D. Marcuzzi. *Fusion Engineering and Design*, 66-68:289–293, 2003.

[52] G. Manduchi, A. Luchetta, A. Soppelsa, and C. Taliercio. The new feedback control system of rfx-mod based on the marte real-time framework. In *Real Time Conference (RT), 2012 18th IEEE-NPSS*, pages 1–5, June 2012.

[53] T. Bolzonella, V. Igochine, S. C. Guo, D. Yadikin, M. Baruzzo, and H. Zohm. Resistive-wall-mode active rotation in the rfx-mod device. *Physical Review Letters*, 101(16):165003, 2008.

[54] P. Zanca et al. Avoidance of tearing modes wall-locking in a reversed field pinch with active feedback coils. *Plasma Physics and Controlled Fusion*, 51(1):015006, 2009.

[55] P. Zanca, L. Marrelli, R. Paccagnella, A. Soppelsa, M. Baruzzo, T. Bolzonella, G. Marchiori, P. Martin, and P. Piovesan. Feedback control model of the m=2, n=1 resistive wall mode in a circular plasma. *Plasma Physics and Controlled Fusion*, 54(9):094004, 2012.

[56] P. Martin, M. E. Puiatti, P. Agostinetti, M. Agostini, J. A. Alonso, V. Antoni, L. Apolloni, F. Auriemma, F. Avino, and A. Barbalace. Overview of the rfx-mod fusion science programme. *Nuclear Fusion*, 53(10):104018, 2013.

[57] J. M. Hanson, J. M. Bialek, M. Baruzzo, T. Bolzonella, A. W. Hyatt, G. L. Jackson, J. King, R. J. La Haye, M. J. Lanctot, L. Marrelli, P. Martin, G. A. Navratil, M. Okabayashi, K. E. J. Olofsson, C. Paz-Soldan, P. Piovesan, C. Piron, L. Piron, D. Shiraki, E. J. Strait, D. Terranova, F. Turco, A. D. Turnbull, and P. Zanca. Feedback-assisted extension of the tokamak operating space to low safety factora). *Physics of Plasmas (1994-present)*, 21(7):–, 2014.

[58] J. L. Luxon. A design retrospective of the diii-d tokamak. *Nuclear Fusion*, 42(5):614, 2002.

[59] A. M. Garofalo, M. S. Chu, E. D. Fredrickson, M. Gryaznevich, T. H. Jensen, L. C. Johnson, R. J. La Haye, G. A. Navratil, M. Okabayashi, J. T. Scoville, E. J. Strait, A. D. Turnbull, and DIII-D Team. Resistive wall mode dynamics and active feedback control in diii-d. *Nuclear Fusion*, 41(9):1171, 2001.

[60] T. E. Evans et al. *Nature Physics*, 2:1745–2473, 2006.

[61] M. Okabayashi et al. In *25th IAEA Fusion Energy Conference*, 2014. 25h IAEA Fusion Energy Conference, Saint Petersburg, Russian Federation, October 2014, IAEA.

[62] J. D. King, E. J. Strait, R. L. Boivin, D. Taussig, M. G. Watkins, J. M. Hanson, N. C. Logan, C. Paz-Soldan, D. C. Pace, D. Shiraki, M. J. Lanctot, R. J. La Haye, L. L. Lao, D. J. Battaglia, A. C. Sontag, S. R. Haskey, and J. G. Bak. An upgrade of the magnetic diagnostic system of the diii-d tokamak for non-axisymmetric measurements. *Review of Scientific Instruments*, 85(8):–, 2014.

[63] M. Okabayashi, J. Bialek, M. S. Chance, M. S. Chu, E. D. Fredrickson, A. M. Garofalo, M. Gryaznevich, R. E. Hatcher, T. H. Jensen, and L. C. Johnson. Active feedback stabilization of the resistive wall mode on the diii-d device. *Physics of Plasmas (1994-present)*, 8(5):2071–2082, 2001.

[64] A. S. Welander, E. Kolemen, R. J. La Haye, N. W. Eidietis, D. A. Humphreys, J. Lohr, S. Noraky, B. G. Penaflor, R. Prater, and F. Turco. Advanced control of neoclassical tearing modes in diii-d with real-time steering of the electron cyclotron current drive. *Plasma Physics and Controlled Fusion*, 55(12):124033–124038, 2013.

[65] I. T. Chapman, R. J. La Haye, R. J. Buttery, W. W. Heidbrink, G. L. Jackson, C. M. Muscatello, C. C. Petty, R. I. Pinsker, B. J. Tobias, and F. Turco. Sawtooth control using electron cyclotron current drive in iter demonstration plasmas in diii-d. *Nuclear Fusion*, 52(6):063006, 2012.

[66] A. Herrmann and O. Gruber. Asdex upgrade: Introduction and overview. *Fusion science and technology*, 44(3):569–577, 2003.

[67] Asdex Upgrade. Asdex upgrade website, 2014. [Online; accessed 3-January-2015].

[68] W. Suttrop, O. Gruber, S. Günter, D. Hahn, A. Herrmann, M. Rott, T. Vierle, U. Seidel, M. Sempf, B. Streibl, E. Strumberger, D. Yadikin, O. Neubauer, B. Unterberg, E. Gaio, V. Toigo, and P. Brunsell. In-vessel saddle coils for mhd control in asdex upgrade. *Fusion Engineering and Design*, 84(2-6):290 – 294, 2009. Proceeding of the 25th Symposium on Fusion Technology (SOFT-25).

[69] W. Treutterer, R. Cole, K. Lüddecke, G. Neu, C. Rapson, G. Raupp, D. Zasche, and T. Zehetbauer. Asdex upgrade discharge control system - a real-time plasma control framework. *Fusion Engineering and Design*, 89(3):146 – 154, 2014. Design and implementation of real-time systems for magnetic confined fusion devices.

[70] G. Manduchi, A. Barbalace, A. Luchetta, A. Soppelsa, C. Taliercio, and E. Zampiva. Upgrade of the rfx-mod real time control system. *Fusion Engineering and Design*, 87(12):1907 – 1911, 2012. Proceedings of the 8th {IAEA} Technical Meeting on Control, Data Acquisition, and Remote Participation for Fusion Research.

[71] G. Manduchi, A. Luchetta, A. Soppelsa, and C. Taliercio. The new feedback control system of rfx-mod based on the marte real-time framework. *Nuclear Science, IEEE Transactions on*, 61(3):1216–1221, June 2014.

[72] G. Manduchi, A. Luchetta, A. Soppelsa, and C. Taliercio. From distributed to multicore architecture in the rfx-mod real time control system. *Fusion Engineering and Design*, 89(3):224 – 232, 2014. Design and implementation of real-time systems for magnetic confined fusion devices.

[73] A. C. Neto, F. Sartori, F. Piccolo, R. Vitelli, G. De Tommasi, L. Zabeo, A. Barbalace, H. Fernandes, D. F. ValcaÌĄrcel, and A. J. N. Batista. Marte: A multiplatform real-time framework. *Nuclear Science, IEEE Transactions on*, 57(2):479–486, April 2010.

[74] A. C. Neto, D. Alves, L. Boncagni, P. J. Carvalho, D. F. ValcaÌĄrcel, A. Barbalace, G. De Tommasi, H. Fernandes, F. Sartori, E. Vitale, R. Vitelli, and L. Zabeo. A survey of recent marte based systems. *Nuclear Science, IEEE Transactions on*, 58(4):1482–1489, Aug 2011.

[75] A. Soppelsa, T. Bolzonella, R. Cavazzana, G. Manduchi, G. Marchiori, L. Marrelli, P. Martin, P. Piovesan, C. Piron, L. Piron, C. Taliercio, and P. Zanca. Organization of the mhd control algorithms in the new control system of rfx-mod. In *Symposium on Fusion Technology (SOFT), 2012 18th*, September 2012.

[76] G. Manduchi, L. Marrelli, G. Marchiori, P. Piovesan, L. Piron, A. Soppelsa, P. Zanca, A. Barbalace, M. Baruzzo, D. Bonfiglio, R. Cavazzana, D. Fabris, Y. Q. Liu, A. Luchetta, N. Marconato, C. Piron, C. Taliercio, and F. Villone. Development of mhd active control in the rfx-mod rfp. In *IAEA Fusion Conference, 2012 24th*, October 2012.

[77] W. Just, D. Reckwerth, E. Reibold, and H. Benner. Influence of control loop latency on time-delayed feedback control. *Physical Review E*, 59:2826–2829, Mar 1999.

[78] M. Frigo and S. G. Johnson. The fastest fourier transform in the west. Technical report, DTIC Document, 1997.

[79] P. Zanca, L. Marrelli, G. Manduchi, and G. Marchiori. Beyond the intelligent shell concept: the clean-mode-control. *Nuclear Fusion*, 47(11):1425, 2007.

[80] K. H. Burrell, T. E. Evans, E. J. Doyle, M. E. Fenstermacher, R. J. Groebner, A. W. Leonard, R. A. Moyer, T. H. Osborne, M. J. Schaffer, and P. B. Snyder. Elm suppression in low edge collisionality h-mode discharges using n= 3 magnetic perturbations. *Plasma Physics and Controlled Fusion*, 47(12B):B37, 2005.

[81] H. Reimerdes, A. M. Garofalo, E. J. Strait, R. J. Buttery, M. S. Chu, Y. In, G. L. Jackson, R. J. La Haye, M. J. Lanctot, and Y. Q. Liu. Effect of resonant and non-resonant magnetic braking on error field tolerance in high beta plasmas. *Nuclear Fusion*, 49(11):115001, 2009.

[82] R. Fitzpatrick. Interaction of tearing modes with external structures in cylindrical geometry (plasma). *Nuclear Fusion*, 33(7):1049, 1993.

[83] A. H. Boozer. Error field amplification and rotation damping in tokamak plasmas. *Physical Review Letters*, 86(22):5059, 2001.

[84] J. E. Menard, R. E. Bell, D. A. Gates, S. P. Gerhardt, J. K. Park, S. A. Sabbagh, J. W. Berkery, A. Egan, J. Kallman, S. M. Kaye, B. LeBlanc, Y. Q. Liu, A. Sontag, D. Swanson, H. Yuh, W. Zhu, and NSTX Research Team. Progress in understanding error-field physics in nstx spherical torus plasmas. *Nuclear Fusion*, 50(4):045008, 2010.

[85] A. M. Garofalo, R. J. La Haye, and J. T. Scoville. Analysis and correction of intrinsic non-axisymmetric magnetic fields in high-beta diii-d plasmas. *Nuclear Fusion*, 42(11):1335, 2002.

[86] T. C. Hender, R. Fitzpatrick, A. W. Morris, P. G. Carolan, R. D. Durst, T. Edlington, J. Ferreira, S. J. Fielding, P. S. Haynes, J. Hugill, I. J. Jenkins, R. J. La Haye, B. J. Parham, D. C. Robinson, T. N. Todd, M. Valovic, and G. Vayakis. Effect of resonant magnetic perturbations on compass-c tokamak discharges. *Nuclear Fusion*, 32(12):2091, 1992.

[87] E. J. Strait, R. J. Buttery, T. A. Casper, M. S. Chu, J. M. Hanson, A. M. Garofalo, Y. Gribov, R. J. La Haye, H. Reimerdes, M. J. Schaffer, and F. A. Volpe. Measurement of tokamak error fields using plasma response and its applicability to iter. *Nuclear Fusion*, 54(7):073004, 2014.

[88] F. A. Volpe, L. Frassinetti, R. Brunsell, J. R. Drake, and K. E. J. Olofsson. Error field assessment from driven rotation of stable external kinks at extrap-t2r reversed field pinch. *Nuclear Fusion*, 53(4):043018, 2013.

[89] J. T. Scoville and R.J. La Haye. Multi-mode error field correction on the diii-d tokamak. *Nuclear Fusion*, 43(4):250, 2003.

[90] R. J. Buttery, M. De' Benedetti, T. C. Hender, and B. J. D. Tubbing. Error field experiments in jet. *Nuclear Fusion*, 40(4):807, 2000.

[91] S. M. Wolfe, I. H. Hutchinson, R. S. Granetz, J. Rice, A. Hubbard, A. Lynn, P. Phillips, T. C. Hender, D. F. Howell, R. J. La Haye, and J. T. Scoville. Nonaxisymmetric field effects on alcator c-moda). *Physics of Plasmas (1994-present)*, 12(5):–, 2005.

[92] E. M. Hollmann, P. B. Aleynikov, T. Fülöp, D. A. Humphreys, V. A. Izzo, M. Lehnen, V. E. Lukash, G. Papp, G. Pautasso, F. Saint-Laurent, and J. A. Snipes. Status of research toward the iter disruption mitigation system. *Physics of Plasmas (1994-present)*, 22(2):–, 2015.

[93] L. Piron, J. M. Hanson, Y. In, G. Marchiori, L. Marrelli, P. Martin, M. Okabayashi, P. Piovesan, H. Reimerdes, and A. Soppelsa. Improved dynamic response of magnetic feedback in rfx-mod and diii-d. *Plasma Physics and Controlled Fusion*, 53(8):084004, 2011.

[94] P. Zanca, G. Marchiori, L. Marrelli, L. Piron, and RFX mod team. Advanced feedback control of magnetohydrodynamic instabilities: comparison of compensation techniques for radial sensors. *Plasma Physics and Controlled Fusion*, 54(12):124018, 2012.

[95] P. Zanca and G. Marchiori. Considerations on the frozen coils' current and filtered-feedback experiments on m=2, n=1 control. *RFX-mod Nota Tecnica*, FC(87), 2014.

[96] G. Marchiori, M. Baruzzo, T. Bolzonella, Y. Q. Liu, A. Soppelsa, and F. Villone. Dynamic simulator of rwm control for fusion devices: modelling and experimental validation on rfx-mod. *Nuclear Fusion*, 52(2):023020, 2012.

[97] A. Bondeson, Y. Q. Liu, C. M. Fransson, B. Lennartson, C. Breitholtz, and T. S. Taylor. Active feedback stabilization of high beta modes in advanced tokamaks. *Nuclear Fusion*, 41(4):455, 2001.

[98] A. Gude, S. Günter, S. Sesnic, and ASDEX Upgrade Team. Seed island of neoclassical tearing modes at asdex upgrade. *Nuclear Fusion*, 39(1):127, 1999.

[99] S. Günter, M. Maraschek, M. de Baar, D. F. Howell, E. Poli, E. Strumberger, C. Tichmann, and ASDEX Upgrade team. The frequently interrupted regime of neoclassical tearing modes (fir-ntms): required plasma parameters and possibilities for its active control. *Nuclear fusion*, 44(4):524, 2004.

[100] D. Bonfiglio, L. Chacon, and S. Cappello. Nonlinear three-dimensional verification of the specyl and pixie3d magnetohydrodynamics codes for fusion plasmas. *Physics of Plasmas (1994-present)*, 17(8):–, 2010.

[101] L. Piron, D. Bonfiglio, P. Piovesan, B. Zaniol, F. Auriemma, L. Carraro, L. Chacon, L. Marrelli, M. Valisa, M. Veranda, and M. Zuin. 3d magnetic fields and plasma rotation in rfx-mod tokamak plasmas. *Nuclear Fusion*, 53(11):113022, 2013.

[102] I. T. Chapman, T. C. Hender, S. Saarelma, S. E. Sharapov, R. J. Akers, N. J. Conway, and MAST Team. The effect of toroidal plasma rotation on sawteeth in mast. *Nuclear Fusion*, 46(12):1009, 2006.

[103] J. K. Park, A. H. Boozer, and A. H. Glasser. Computation of three-dimensional tokamak and spherical torus equilibria. *Physics of Plasmas (1994-present)*, 14(5):–, 2007.

[104] N. C. Logan, J. K. Park, K. Kim, Z. Wang, and J. W. Berkery. Neoclassical toroidal viscosity in perturbed equilibria with general tokamak geometry. *Physics of Plasmas (1994-present)*, 20(12):122507, 2013.

[105] F. Felici, O. Sauter, S. Coda, B. P. Duval, T. P. Goodman, J. M. Moret, J. I. Paley, and TCV Team. Real-time physics-model-based simulation of the current density profile in tokamak plasmas. *Nuclear Fusion*, 51(8):083052, 2011.

[106] F. Felici. *Real-Time Control of Tokamak Plasmas: from Control of Physics to Physics-Based Control*. PhD thesis, SB, Lausanne, 2011.

[107] F. Felici et al. First results of real-time plasma state reconstruction using a model-based dynamic observer on asdex-upgrade. In *41st EPS conference on Plasma Physics*, June 2014.

[108] G. Pereverzev and P. N. Yushmanov. Astra automated system for transport analysis in a tokamak. Technical report, Max-Planck-Institut fuer Plasmaphysik, Garching (Germany), 2002.

[109] G. Cenacchi and A. Taroni. Jetto a free boundary plasma transport code. Technical report, ENEA, Rome (Italy), 1988.

[110] E. Poli, A. G. Peeters, and G. V. Pereverzev. Torbeam, a beam tracing code for electron-cyclotron waves in tokamak plasmas. *Computer Physics Communications*, 136(1):90–104, 2001.

[111] F. Porcelli, D. Boucher, and M. N. Rosenbluth. Model for the sawtooth period and amplitude. *Plasma Physics and Controlled Fusion*, 38(12):2163, 1996.

[112] B. B. Kadomtsev. *Reports on Progress in Physics*, 50:115, 1987.

[113] V. Igochine, J. Boom, I. Classen, O. Dumbrajs, S. Günter, K. Lackner, G. Pereverzev, and H. Zohm. Structure and dynamics of sawteeth crashes in asdex upgrade. 17(12):122506, 2010.

[114] C. Angioni, T. P. Goodman, M. A. Henderson, and O. Sauter. Effects of localized electron heating and current drive on the sawtooth period. *Nuclear Fusion*, 43(6):455, 2003.

[115] J. I. Paley, J. Berrino, S. Coda, N. Cruz, B. P. Duval, F. Felici, T. P. Goodman, Y. Martin, J. M. Moret, F. Piras, A. P. Rodriques, B. Santos, C. A. F. Varandas, and TCV Team. Real time control of plasmas and ecrh systems on tcv. *Nuclear Fusion*, 49(8):085017, 2009.

[116] T. P. Goodman et al. In *19th IAEA Fusion Energy Conference*, 2002. 19th IAEA Fusion Energy Conference, Lyon, France, October 2002, IAEA.

[117] A. Alfier, R. Pasqualotto, G. Spizzo, A. Canton, A. Fassina, and L. Frassinetti. Electron temperature profiles in rfx-mod. *Plasma Physics and Controlled Fusion*, 50(3):035013, 2008.

Acknowledgements

It is a pleasure to thank the many people who made this Thesis possible.

I wish to thank my Supervisor, Prof. Piero Martin, and to my Tutors Dr. Lionello Marrelli and Dr. Paolo Piovesan. They constantly gave me the important guidelines and precious suggestions for my research work.

I thank Dr. Gabriele Manduchi for help with MARTe which was the starting point of my research and for his friendly support during all this time.

I am grateful to Consorzio RFX, where most of this Thesis was made, for having given me the possibility to work in a very stimulating group and to develop my research work in collaboration with DIII-D, ASDEX Upgrade and TCV. It has been a very formative experience to visit these experiments, where I found an extraordinary scientific environment. In particular I would like to thank Andrea Garofalo, Carlos Paz-Soldan and Jeremy Hanson, Olivier Sauter and Federico Felici for their precious support.

I also would like to thank all my lab mates for providing a stimulating and fun environment in which to learn and grow.

I wish to thank my long-term friend Stefania for her support, company and entertainment and Matteo, for his overqualified experitise in text editing and punctuation.

I am also very thankful to my sister, Lidia for her unvaluable support, to piccolo Pippo tenero eroe for his fluffiness, and Matteo. Lastly, and most importantly, I wish to thank my parents, Luigina Morosin and Dino Piron, my uncle Adolfo for the moral support and my aunt Gemma and my uncle Piero for being my second family.